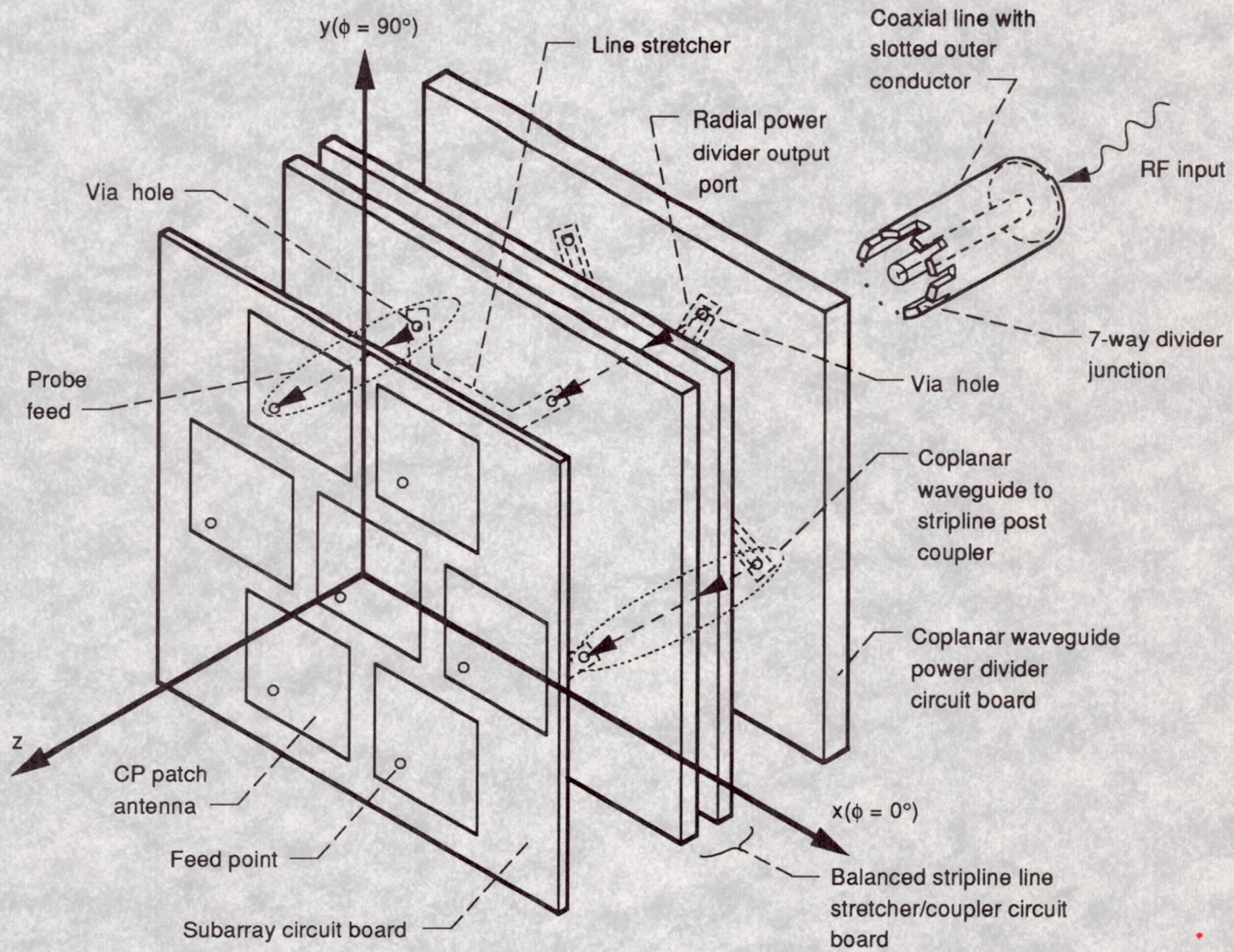


4-28-92
E6447

NASA Technical Memorandum 105159

Solid State Technology Branch of NASA Lewis Research Center Third Annual Digest



June 1990–June 1991
Lewis Research Center

PREFACE TO THE THIRD ANNUAL SOLID STATE
TECHNOLOGY BRANCH DIGEST

The Solid State Technology branch has added personnel again this year. Two new additions to the branch roster, Dr. Felix Miranda and Ms. Crystal Cabbage, both majored in physics before coming to the branch. Each has been assigned to the investigation of some aspect of high temperature superconductivity, an indication of the branch's (and NASA's) continuing interest in the topic.

This volume represents one year's (June 1990-June 1991) production of research publications. Reprints are organized into three sections: microwave circuits, both hybrid and MMIC; materials and device work; and superconductivity. In a number of cases, comparisons with last year's digest will indicate a transition of some technologies - from material/device work to circuit work or from circuit work to subsystem work. The focus in the area of fiber optic control of RF circuits has moved almost entirely to a system effort with research being conducted almost entirely by our sister organization, the Antenna and RF Systems Branch. Consequently, only one paper in this area will appear in the journal this year. In general, this type of transition is a reflection of the avowed NASA policy to carry out a focussed research and technology program, and to shorten the elapsed time from research to insertion.

The first section of the journal deals with microwave circuits, both MMIC and hybrid. Although not yet reflected in publications, the frequency range under investigation was expanded significantly during the reporting period with the award of a contract to TRW for the development of a monolithic W-band, low-noise amplifier and mixer based on InGaAs/InP technology. Although NASA has not yet identified a need for this frequency range, it is clear that the antenna size and power level required for transmission of a reasonable data rate during a manned interplanetary mission would be too large at any lower frequency. Other circuit work, carried out in collaboration with the Antenna Systems Branch, continues to investigate the application of coplanar waveguide technology to a variety of antenna feed systems and coupling schemes. This section also includes a paper which, although it describes work using high temperature superconductors, appeared to have the design of microwave circuitry as a major thrust. The feeling of the editors is that this is another indication of technologies "working their way up the readiness scale."

The second section of the journal contains papers devoted to development of new heterojunction materials and devices. During this last period, testing focus was on InGaAs/InP materials and devices, research was carried out in collaboration with the University of Michigan. The evaluation of MODFET materials, both InP- and GaAs-based, by means of ellipsometry remained a major

research area. During the reporting period, a major facility, a cryogenic RF probe station, was designed and fabricated. Although completed too late to be reflected in this journal, this unique facility should have a major impact on work in the upcoming year.

Finally, high temperature superconductivity continued to provide the focus for a significant fraction of the branch staff. A wide range of activities, from film deposition to microwave circuit design, were undertaken and reported. In this area too, however, the last year has seen events which will significantly focus research efforts. Lewis Research Center and the Jet Propulsion Laboratory have agreed to undertake a cooperative effort aimed at the design, fabrication, testing, and delivery of a superconducting receiver system as a candidate for the Navy's second High Temperature Superconducting Space Experiment (HTSSE-2).

In addition to these articles, Kul Bhasin and Regis Leonard were responsible for editing the proceedings of an SPIE Symposium on Monolithic Microwave Integrated Circuits for Sensors, Radar, and Communications Systems, which took place in Orlando in April, 1991.

THIRD ANNUAL SOLID STATE TECHNOLOGY BRANCH DIGEST

Contents

Section One

MMIC And Hybrid Microwave Circuits

Microwave Integrated Circuits for Space Applications by Regis F. Leonard and Robert R. Romanofsky	3
Comparative Study of Bolometric and Non-Bolometric Switching Elements for Microwave Phase Shifters by Massood Tabib-Azar, Kul B. Bhasin, and Robert R. Romanofsky	13
Design of an Optically Controlled K _a -band GaAs MMIC Phased-Array Antenna by Richard R. Kunath, Paul C. Claspy, Mark A. Richard, and Kul B. Bhasin	23
A Seven Patch Hexagonal CP Subarray with CPW/Stripline Feed Network by R.N. Simons, R.Q. Lee, and G.R. Lindamood	29
Coplanar-Waveguide/Microstrip Probe Coupler and Applications to Antennas by R.N. Simons and R.Q. Lee	39
New Coplanar Waveguide/Stripline Feed Network for Seven Patch Hexagonal CP Subarray by R.N. Simons, R.Q. Lee, and G.R. Lindamood	41
New Channelised Coplanar Waveguide to Rectangular Waveguide Post and Slot Couplers by R.N. Simons	45
Theoretical and Experimental Characterization of Coplanar Waveguide Discontinuities for Filter Applications by Nihad I. Dib, Linda P. B. Katehi, George E. Ponchak, and Rainee N. Simons	49

Section Two

Development Of Hetrojunction Materials And Devices

Ellipsometric Study of InGaAs MODFET Material by S.A. Alterovitz, R.E. Sieg, H.D. Yao, P.G. Snyder, J.A. Woollam, J. Pamulapati, and P.K. Bhattacharya	61
Low-Temperature Microwave Characteristics of Pseudomorphic $\text{In}_x\text{Ga}_{1-x}\text{As}/\text{In}_{0.52}\text{Al}_{0.48}\text{As}$ Modulation-Doped Field-Effect Transistors by R. Lai, P. K. Bhattacharya, S.A. Alterovitz, A.N. Downey, and C. Chorey	65
Modeling $\text{Al}_x\text{Ga}_{1-x}$ as Optical Constants as Functions of Composition by Paul G. Snyder, John A. Woollam, Samuel A. Alterovitz, and Blaine Johs	69
Dielectric Function of InGaAs in the Visible by S.A. Alterovitz, R.E. Sieg, H.D. Yao, J.A. Wollam, J. Pamulapati, P.K. Bhattacharya, and P.A. Sekula-Moise	71

Section Three

High Temperature Superconductivity

Superconducting Microwave Electronics at Lewis Research Center by Joseph D. Warner, Kul B. Bhasin, and Regis F. Leonard	79
High Temperature Superconductive Microwave Technology for Space Applications by R.F. Leonard, D.J. Connolly, K.B. Bhasin, J.D. Warner, and S.A. Alterovitz	89
Emerging Applications of High-Temperature Superconductors for Space Communications by Vernon O. Heinen, Kul B. Bhasin, and Kenwyn J. Long	101

Analysis of Microstrip Lines with Alternative Implementations of Conductors and Superconductors by K.-S. Kong, H.-Y. Lee, C.M. Chorey, and K.B. Bhasin	111
An Experimental Study of High TC Superconducting Microstrip Transmission Lines at 35 GHz and the Effect of Film Morphology by C.M. Chorey, K.B. Bhasin, J.D. Warner, J.Y. Josefowicz, D.B. Rensch, and C.W. Nieh	115
Microwave Response of High Transition Temperature Superconducting Thin Films by Felix A. Miranda	121
Determination of Surface Resistance and Magnetic Penetration Depth of Superconducting $\text{YBa}_2\text{Cu}_3\text{O}_{7-\delta}$ Thin Films by Microwave Power Transmission Measurement by K.B. Bhasin, J.D. Warner, F.A. Miranda, W.L. Gordon, and H.S. Newman	123
Properties of Large Area $\text{ErBa}_2\text{Cu}_3\text{O}_{7-x}$ Thin Films Deposited by Ionized Cluster Beams by L.L. Levenson, M. Stan, and K.B. Bhasin	127
Temperature Dependence of the Anisotropy in Magnetic Relaxation in $\text{YBa}_2\text{Cu}_3\text{O}_{7-x}$ Thin Films by S. Vitta, M.A. Stan, and S.A. Alterovitz	131
Dependence of the Critical Temperature of Laser-Ablated $\text{YBa}_2\text{Cu}_3\text{O}_{7-\delta}$ Thin Films on LaAlO_3 Substrate Growth Technique by Joseph D. Warner, Kul B. Bhasin, and Felix A. Miranda	135
Electromigration Failure in $\text{YBa}_2\text{Cu}_3\text{O}_{7-x}$ Thin Films by S. Vitta, M.A. Stan, J.D. Warner, and S.A. Alterovitz	139
Ellipsometric Study of $\text{YBa}_2\text{Cu}_3\text{O}_{7-x}$ Laser Ablated and Co-Evaporated Films by S.A. Alterovitz, R.M. Sieg, J.D. Warner, M.A. Stan, and S. Vitta	143
Millimeter-Wave Surface Resistance of Laser-Ablated $\text{YBa}_2\text{Cu}_3\text{O}_{7-\delta}$ Superconducting Films by F.A. Miranda, W.L. Gordon, K.B. Bhasin, and J.D. Warner	149

Biographies

Samuel A. Alterovitz	155
Christopher M. Chorey	155
Alan M. Downey	156
Edward J. Haugland	156
Thomas J. Kascak	157
Regis F. Leonard	157
Rafael A. Mena	158
Carlos R. Morrison	158
George E. Ponchak	159
John J. Pouch	159
Robert R. Romanofsky	160
Samuel E. Schacham	160
Ajit K. Sil	161
Rainee N. Simons	161
Mark A. Stan	162
Stephan Stecura	162
Susan R. Taub	163
Joseph D. Warner	163

***SECTION
ONE***

***MMIC AND HYBRID
MICROWAVE CIRCUITS***

MICROWAVE INTEGRATED CIRCUITS FOR SPACE APPLICATIONS

Regis F. Leonard and Robert R. Romanofsky

NASA Lewis Research Center
21000 Brookpark Road
Cleveland, Ohio 44135

Monolithic microwave integrated circuits (MMICs), which incorporate all the elements of a microwave circuit on a single semiconductor substrate, offer the potential for drastic reductions in circuit weight and volume and increased reliability, all of which make many new concepts in electronic circuitry for space applications feasible, including phased array antennas.

Over the last ten years, NASA has undertaken an extensive program aimed at development of MMICs for space applications. The first such circuits targeted for development were an extension of work begun earlier in hybrid (discrete component) technology in support of the Advanced Communication Technology Satellite (ACTS). As a result it focussed on power amplifiers, receivers and switches at ACTS frequencies. More recent work, however, has focussed on frequencies appropriate for other NASA programs and emphasizes advanced materials in an effort to enhance efficiency, power handling capability, and frequency of operation or noise figure to meet the requirements of space systems.

MONOLITHIC MESFET CIRCUITS

Background

This work has been carried out under contract with Texas Instruments, Rockwell, and Minneapolis Honeywell and Hughes. It is aimed at ACTS-like applications namely, communications satellites which feature multiple, electronically steerable beams. Such a system would ideally be implemented using phased array antennas with lightweight, low volume distributed transmitters and receivers and lightweight monolithic phase shifters rather than the extensive network of ferrite phase shifters and switches used by ACTS. The initial stages of development therefore were aimed at the development of the monolithic circuitry required for such a system. Carried out between approximately 1983 and 1987 and featuring transmitter frequencies of 20 GHz and receiver frequencies of 30 GHz, as required for the satellite portion of the system, the program utilized as a basic device the GaAs metal/semiconductor field effect transistor (MESFET). The program produced a number of developments, each of which consisted of one or more monolithic chips. Some of these are described here.

Ku-Band Amplifier

The space station proximity communications system is intended to provide communications within a radius of several 10's of kilometers of the space station. Users would include free flying experimental platforms, the orbital maneuvering vehicle (OMV), and astronauts in EVA. The original planning for this system utilized frequencies in Ku-band. It is not clear at this time whether that assignment will be maintained, inasmuch as there exists possible interference with commercial, fixed satellite services. Nevertheless, several chips have been developed at 13-15 GHz to accommodate this application. The most challenging of these was a variable power amplifier intended primarily for use by astronauts during EVA. The system design requires approximately 1 watt of output power. Power variability is necessary because of the wide variation in range experienced by the astronaut. Of course, high efficiency is also a prime consideration. The development of the chip was undertaken by Texas Instruments in January 1987. Their design is a four stage monolithic circuit using dual gate GaAs MESFET technology. The chip is shown in Figure 1.

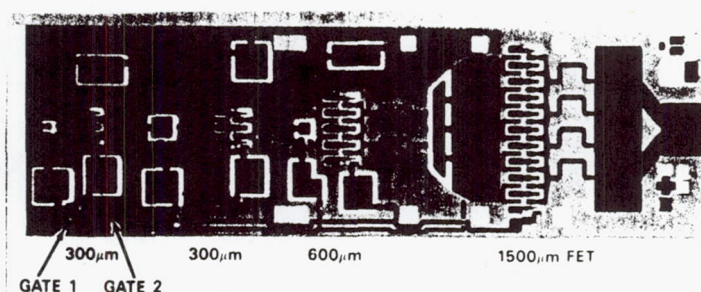


FIGURE 1. 15 GHZ MONOLITHIC VARIABLE POWER AMPLIFIER

The performance of the amplifier, compared to the design goals, is shown in Table 1.

TABLE 1.
15 GHZ HIGH EFFICIENCY VARIABLE POWER AMPLIFIER

	<u>DESIGN GOAL</u> <u>PERFORMANCE</u>	
CENTER FREQ./BANDWIDTH (GHZ)	2.0/14.0	2.0/17.0
GAIN (dB)	15.0	29.6
MAX POWER OUTPUT (W)	1.0	.92
EFFICIENCY AT MAX POWER (%)	35	30
FINAL STAGE GATE WIDTH (MM)	---	1.5

20 GHz variable power amplifier

Since, ideally, a phased-array antenna should be able to vary the phase and the amplitude of each antenna element independently, one desirable module for such a system would be a variable power amplifier. Because of the stringent limitations on power consumption imposed by a space system, it is desirable to maintain insofar as possible the efficiency of a power amplifier while adjusting output power. For this reason, the contractor (Texas Instruments) chose a dual gate FET as the basic device for design of this chip, and adjusted the device bias to obtain variable output. The topology of the amplifier closely resembles the Ku-band amplifier illustrated earlier. This was one of the earliest MMICs developed under the NASA program. A summary of its performance compared to design goals is shown in Table 2.

TABLE 2
TEXAS INSTRUMENTS 20 GHZ VARIABLE POWER AMPLIFIER

	<u>DESIGN GOAL</u>	<u>PERFORMANCE</u>
BANDWIDTH (GHZ)	2.5	2.5
MAX POWER OUTPUT (W)	0.5	0.25
EFFICIENCY AT MAX OUTPUT (%)	15	< 10
GAIN (dB)	20	20
4TH STAGE GATE WIDTH (MM)	----	1.2

High power 20 GHz amplifier

A second 20 GHz chip focussed entirely on the production of the maximum possible 20 GHz power in a monolithic chip. Once more the contractor was Texas Instruments. This effort resulted in a three stage amplifier using single gate FETs. In order to achieve the desired power output, each stage features multiple parallel gates (as many as 32 for the output stage). The chip performance is summarized in Table 3.

TABLE 3.
TEXAS INSTRUMENTS 20 GHZ HIGH POWER AMPLIFIER

	<u>DESIGN GOAL</u>	<u>PERFORMANCE</u>
BANDWIDTH	2.5	2.5
MAX POWER OUTPUT (W)	2.5	>2.0
EFFICIENCY AT MAX POWER (%)	20	16
GAIN (dB)	15	18
LAST STAGE GATE WIDTH (MM)	----	3.6

20 GHz integrated transmitter module

Ultimately, one desires to incorporate all the elements of a transmitter module (phase shifter, variable power amplifier, and power amplifier) on a single chip. The advantages of such high level integration include: improved reliability, compactness, potential performance enhancements, and reduced cost. Such a project was pursued under contract with Rockwell. The chip produced a 21 dBm output power with 15 dB gain. A picture of the module developed under this effort is shown in Figure 2.

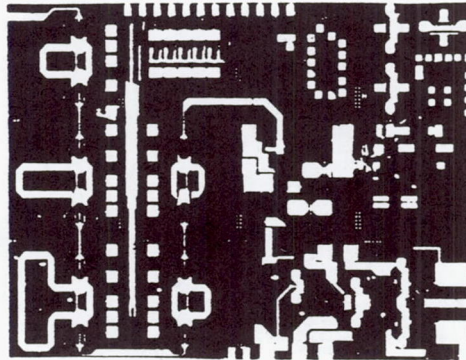


FIGURE 2. Rockwell 20 GHz Transmit Module

30 GHz integrated receiver

Active phased arrays have been proposed for a number of NASA applications, including: array feeds for deep space communications, multiple-beam satellite communications, hemispherical coverage multiple access communications for space station Freedom, orbital debris tracking for space station Freedom, and adaptive arrays for distorted reflector compensation. To enable the practical implementation of scanning arrays, the complexities of device and antenna integration must be solved. As a preliminary step, prototype 30 GHz receiver modules were developed by Hughes and Honeywell. Honeywell developed an interconnected MMIC receiver for which all functions were performed at the RF frequency. The device consisted of a two-stage 0.25 by 100 micron gate FET low noise amplifier (LNA), a two-stage dual-gate gain control amplifier, and a four bit switched-line/loaded-line phase shifter. The receiver produced a noise figure of 14 dB at maximum gain (13 dB) and achieved full 360 degree phase coverage in nominally 11.25 degree increments. Ultimately, the LNA would require six stages of amplification, which would reduce the noise figure, in principle, to about 5 dB. Hughes was directed to implement phase shift control at the LO frequency and gain control at the IF. The advantage of this approach is that the array beam forming network can be implemented at lower frequencies, albeit the benefit could be offset by the need for a mixer at each antenna element. In fact, the mixer was perhaps the most troublesome component in both designs, providing a best case conversion loss of 8 dB.

HIGH PERFORMANCE MONOLITHIC CIRCUITS

Background

It is clear that all of the GaAs MESFET-based modules, although they constituted benchmark achievements at these frequencies, suffered from many of the same problems as the earlier hybrid implementations of solid state technology. For the power devices, their efficiencies make their use marginal for space applications, except in very limited numbers, such as would be required if they were used as a driver for a higher efficiency final stage. An attempt to use multiple chips with any kind of combining would lead to prohibitively large prime power requirements. For receiver modules, the noise figures obtained using MESFET technology are not competitive with that which can be attained using discrete devices and custom-tuned circuits. However, recent advances in semiconductor materials, enabled by the development of molecular beam epitaxy (MBE) techniques, have drastically improved the performance which basic devices can achieve. Typically, power-added efficiencies near 50% can be obtained for a single device at frequencies near 30 GHz. While device noise figures less than 1 dB are possible at 60 GHz.

At the present time NASA Lewis is sponsoring the development of monolithic chips based on heterojunction devices. Two of these at 32 GHz are for possible use in the space (transmitter) portion of the deep space communications network. The third and fourth at 60 GHz are intended for application to intersatellite communications, such as might be required by Advanced TDRSS or lunar/Mars exploration. A fifth chip will operate at 95 GHz, with potential applications in interplanetary communications, or in earth-observation systems.

32 GHz Amplifiers

In another application the NASA deep space communications network is considering a conversion to Ka-band. The primary motivation for such a change is the significant increase in antenna gain (for a fixed aperture size) and the corresponding decrease in power requirements (for a fixed data rate). Increased antenna gain, however, implies smaller beams and therefore more stringent pointing requirements. Such a situation, of course, is ideal for implementation of an electronically steerable phased array, which does not disturb other critically-pointed spacecraft instruments (experiments or sensors) in the way a mechanically steered antenna would. To support breadboard evaluations of such a system, 32 GHz power amplifier modules are under development. The contractors executing these efforts are Texas Instruments and Hughes Aircraft. The TI work has been under way since May, 1985, and is near completion, while the Hughes effort was initiated in June 1988.

TI proposed and originally designed amplifiers using GaAs MESFET technology, but was directed, after approximately 18 months work, to concentrate on heterojunction devices. Specifically, they have investigated AlGaAs/GaAs HEMT structures and pseudomorphic InGaAs/GaAs structures. At this point it is clear that the pseudomorphic technology

outperforms both the AlGaAs HEMT and the GaAs MESFET technology by a significant margin at 32 GHz. The specific pseudomorphic structure which TI has adopted is shown in Figure 3.

GaAs Cap Layer 400 Å	
$\text{Al}_{0.23}\text{Ga}_{0.77}\text{As}$	2×10^{18} 500 Å
$\text{In}_{0.15}\text{Ga}_{0.85}\text{As}$	2×10^{18} 100 Å
GaAs	2×10^{18} 80 Å
GaAs Buffer 1 μm	
Substrate	

FIGURE 3. Texas Instruments' Pseudomorphic Power Amplifier Structure

The performance parameters for two of the pseudomorphic chips developed under this program are shown in Table 5.

TABLE 5.
TEXAS INSTRUMENTS 32 GHZ MONOLITHIC POWER AMPLIFIER
PERFORMANCE

	<u>3-STAGE AMP</u>	<u>1-STAGE AMP</u>
BANDWIDTH (GHZ)	2.0	2.0
GAIN (dB)	23	4.6
GATE LENGTH (μm)	0.25	0.25
FINAL STAGE GATE WIDTH (MM)	.25	.25
POWER OUTPUT (mW)	190	460
EFFICIENCY (%)	30	24

The layout of the three-stage 2.6 mm by 1.2 mm MMIC amplifier is shown in figure 4.

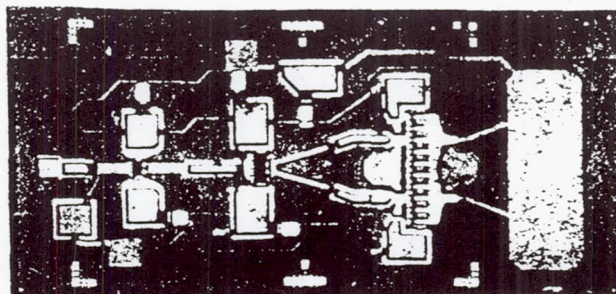


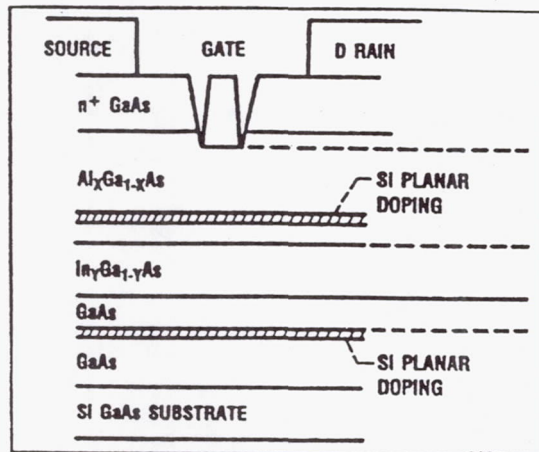
FIGURE 4. TI's 3-STAGE MONOLITHIC 32 GHZ AMPLIFIER

In a parallel 32 GHz effort Hughes Aircraft Corporation's Microwave Products Division and Malibu Research Laboratories are collaborating on the development of a 32 GHz variable power amplifier. The design goals for this chip are shown in Table 6.

TABLE 6.
DESIGN GOALS FOR HUGHES 32 GHZ VARIABLE POWER AMPLIFIER

BANDWIDTH (GHz)	2.0
MAX POWER OUTPUT (mW)	150
EFFICIENCY AT MAX POWER(%)	40
GAIN AT 1 DB COMP. (dB)	15.0

The Hughes contract, like most such developments at this time is to be carried out in several phases. These will consist of (1) the optimization of a single gate device design, (2) the development of a single stage amplifier, (3) the development of a dual gate device, (4) the design, fabrication, and test of a three-stage, single gate amplifier, and finally, (5) a three stage dual gate amplifier. In the 16 months that the Hughes team has been under contract, they have carried out the first two phases. The epitaxy which they have selected for the basic device is similar to that utilized by TI, except that Hughes has elected not to dope the active layer. It does, however, utilize a single active InGaAs layer with donors on each side. The structure and performance parameters for the basic 32 GHz device are shown in Figure 5.



FREQUENCY	32.0
GAIN*	4(5) dB
POWER OUTPUT*	222(123)mW
EFFICIENCY*	23(41)%
GATE WIDTH	300 uM
GATE LENGTH	0.2 uM

*tuned for max power(eff)

Figure 5. Structure and Performance of Hughes 32 GHz Power MODFET

This device has been incorporated into a single stage amplifier which exhibited an output power of 125 mW at 21 % efficiency with 5.5 dB gain. This amplifier is intended as the third stage of the final monolithic module. These results represent the first iteration of this chip, and significant improvement is expected before the program ends.

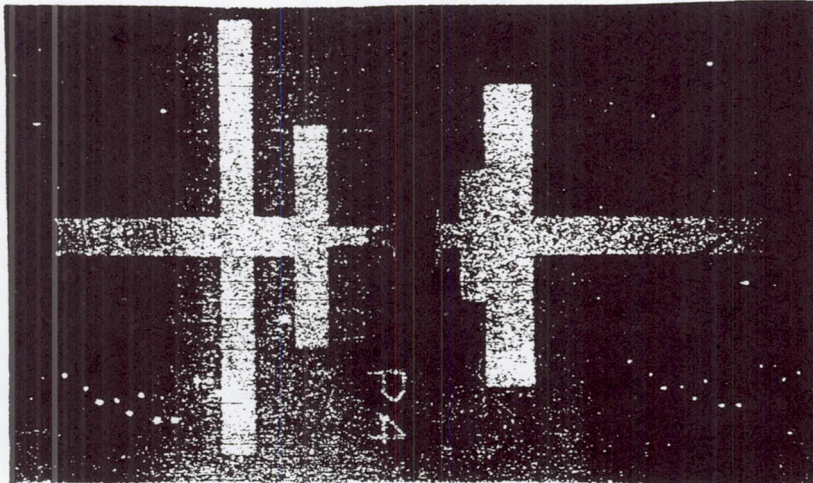
60 GHz Amplifiers

In addition, under the same contract, Hughes is developing a 60 GHz monolithic power amplifier. The justification for this program is eventual application in intersatellite links. Although NASA's plans for the Advanced Tracking and Data Relay Satellite (ATDRS) do not presently call for 60 GHz crosslinks, it seems likely that if such technology were available it would eventually find application in that area. The performance goals for the program, are shown below in Table 7.

TABLE 7. Performance Goals for Hughes' Pseudomorphic 60 GHz Power Amplifier

BANDWIDTH (GHz)	2.0
MAX POWER OUTPUT (W)	0.1
GAIN (dB)	15
EFFICIENCY (%)	30.0

At 60 GHz Hughes is using the same basic pseudomorphic device structure as at 32 GHz, although the gate lengths have been shortened somewhat (0.1 to 0.15 μm). The layout and the performance achieved for a single stage amplifier are shown in Figure 6. The chip is approximately 1.5 mm long. As in the 32 GHz module, the amplifier shown is intended as the third (high power) stage of the completed monolithic amplifier.



POWER OUT	112 mW
GAIN	6 dB
EFFICIENCY	26%

FIGURE 6. Hughes Single Stage Monolithic 60 GHz Amplifier

FUTURE ACTIVITIES

Phased Array Development

The 32 GHz power amplifier modules developed by Texas Instruments and described here are scheduled to be incorporated into a breadboard transmitter array antenna which will also utilize phase shifters developed under NASA Lewis sponsorship. This work is being carried out at NASA's Jet Propulsion Laboratory, where a two dimensional array is expected to be completed late in calendar year 1990.

The Hughes work at both 32 Ghz and 60 Ghz is probably at least a year away from being used even in a breadboard system. Although the contract is scheduled for completion in early 1991, it has yet to address what has been one of the major difficulties in the fabrication of a multistage power amplifier - inadequate large signal device models. It has been a common experience for a designer to develop excellent individual stage amplifiers, which meet all the requirements of the overall power and gain budget, only to find that the multistage module performance falls far short of the program requirements. Consequently, it appears optimistic to expect that Hughes will complete their development by 1991. 1992 would appear to be more realistic. At that time, it is anticipated that a 60 GHz breadboard array will be built, either at JPL or at NASA Lewis. As with the Ka-band array, it will utilize monolithic phase shifters which are being developed in parallel at Hughes.

W-Band Receiver

The most recent MMIC developmental effort is the production of a 94 GHz receiver. Potential applications include deep-space communications, radiometry, and orbital debris tracking radar. Goals of the program include a noise figure of 3.5 dB and a gain of 18 dB. It is anticipated that the ambitious goals of this program will necessitate a technology based on InP, rather than traditional GaAs.

REFERENCES

1. Saunier, P.; Tserng, H. Q.; and Kim, B.: Monolithic Gallium Arsenide Variable Power Amplifier. NASA CR 180814, 1987.
2. Higgins, J. A.: 20 GHz Monolithic Transmit Modules. NASA CR 182134, 1987.
3. Geddes, J.; Mondal, J.; Contolatis, T.; and Sokolov, V.: 30 GHz Monolithic Receive Module. NASA CR 185198, 1989.
4. Liu, L.; Lin, C.; Kessler, J.; and Wang, S.: A 30 GHz Monolithic Receiver. IEEE Microwave and Millimeter-Wave Monolithic Circuit Symposium Digest, 1986, pp. 41-44.

**COMPARATIVE STUDY OF BOLOMETRIC AND NON-BOLOMETRIC
SWITCHING ELEMENTS FOR MICROWAVE
PHASE SHIFTERS**

**Massood Tabib-Azar
Case Western Reserve University
Department of Electrical Engineering and Applied Physics
Cleveland, Ohio 44106**

and

**Kul B. Bhasin and Robert R. Romanofsky
National Aeronautics and Space Administration
Lewis Research Center
Cleveland, Ohio 44135**

ABSTRACT

This paper compares the performance of semiconductor and high- T_c superconductor switches as they are used in delay-line-type microwave and millimeter-wave phase shifters. We compare such factors as their ratios of the off-to-on resistances, parasitic reactances, power consumption, speed, input-to-output isolation, ease of fabrication, and physical dimensions. Owing to their almost infinite off-to-on resistance ratio and excellent input-to-output isolation, bolometric superconducting switches appear to be quite suitable for use in microwave phase shifters; their only drawbacks are their speed and size.

We also discuss the SUPERFET, a novel device whose operation is based on the electric field effect in high- T_c ceramic superconductors. Preliminary results indicate that the SUPERFET is fast and that it can be scaled; therefore, it can be fabricated with dimensions comparable to semiconductor field-effect transistors.

I. INTRODUCTION

Phase shifters are an indispensable part of phased-array microwave antenna systems. There are many different realizations of phase shifters, which can be broadly divided into analog and digital types [1]. Here we confine ourselves to only digital and planar configurations. Specifically, we will discuss microstrip line phase shifters [2].

Three parameters can be altered to cause a phase shift in an electromagnetic wave traveling on a microstrip line. These are velocity [3], path length [1], and reactance [4] (or the load in a transmission line that effectively changes the group velocity). Changing the velocity or path length is straightforward. Changing reactances is more involved and it is usually so frequency sensitive that it is rarely used except where frequency-dependent phase shift is sought. Changing the wave velocity is relatively easy in a traditional waveguide; so it is used extensively with rectangular waveguides, though not in microstripline-based systems. Inducing a change in the wave velocity requires an electro-optic substrate such as GaAs, whose permittivity or refractive index can be altered by an external electric field (only recently has attention been given to this approach [5]). Routing the microwave through paths of different length (delay lines) is a practical way of inducing phase shift that we will consider in more detail.

Figure 1 shows a delay line phase shifter that uses electronic switches to route the microwave through different paths. Ideally, these switches would have an infinite off-to-on resistance ratio and would not interfere with the propagation of the microwave; also there would be no interaction between the control signal of the switch, and the microwave. In the following sections, we will discuss semiconductor and superconductor switches and we will compare their performances.

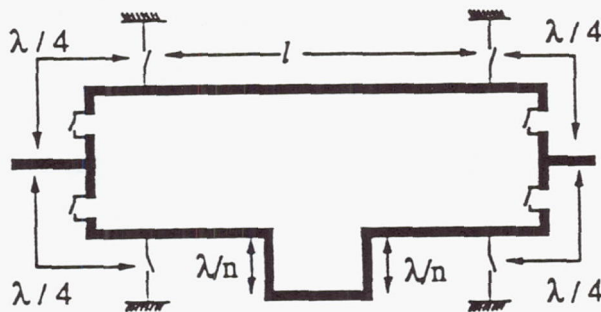


Figure 1 Delay line Phase shifter.

II. SEMICONDUCTOR SWITCHES

PIN diodes [6] and field effect transistors [7] are used as semiconductor switches in delay-line phase shifters. PIN diodes are also used as varactors in analog phase shifters, as are FETs in amplifier-type phase shifters. Dual-gate FETs [8] have become popular in analog phase shifters because a single device can both amplify and switch a signal; essentially they are dc-gain-controlled microwave amplifiers and phase shifters.

PIN Diodes. PIN diodes are extensively discussed in the literature (for example, see reference 1). They are minority-carrier devices and, therefore, their power consumptions are high. They have a storage delay time of 0.2 μ s and "on" resistance of 0.5-5 Ω [9,10], but are relatively lossy with an "off" resistance of 1-4 M Ω and capacitance of 0.4-0.8 pF [9,10]. The physical dimensions of a low-power PIN diode in the

unpackaged planar form is approximately $25\mu\text{m} \times 100\mu\text{m}$. However, since they require a biasing circuit their overall effective dimensions are much larger.

MESFETs and MISFETs. These devices have been developed extensively in recent years, and they are used in microwave monolithic integrated circuits (usually GaAs based) successfully. They are majority-carrier devices and require little power. They have an "on" resistance of $0.5\text{-}5\ \Omega$ [9,10], but are lossy with an "off" resistance of $1\text{-}40\ \text{K}\Omega$ and drain-to-source capacitance of $0.4\text{-}0.8\ \text{pF}$ [9,10]. Their switching speed is as high as $0.1\ \text{ns}$. Low-power FETs in the unpackaged planar form are $100\mu\text{m} \times 100\mu\text{m}$. However, since they require a biasing circuit, their overall effective dimensions are much larger.

III. SUPERCONDUCTING SWITCHES

Superconductor switches that can be used in phase shifters are of the following types: (1) bolometric devices heated by light [11,12] or by an overlay polysilicon or metallic heater, (2) devices photonically controlled by laser excitation [13], (3) magnetic field effect devices controlled by the magnetic field of an inductor loop [14], (4) transverse electric field effect devices controlled by charging a gate electrode [15-21], and (5) longitudinal electric field effect devices controlled by current density [21].

Bolometric Devices. In Figure 2a, we show a phase shifter that uses superconducting-normal-superconducting switches in place of FET/diode switches. The switches are fabricated from high temperature thin films of $\text{YBa}_2\text{Cu}_3\text{O}_{7-x}$. The switches operate in the bolometric mode with the film near its transition temperature. Radiation from a light source raises the temperature higher than the film's T_C and consequently causes the film to become resistive. When the light is on the microwave signal travels past the switch; it is reflected when the light is off. To achieve the desired phase shift, the paired switches on the same side are illuminated. Figure 2b shows the predicted behavior for a phase shifter with an R_S

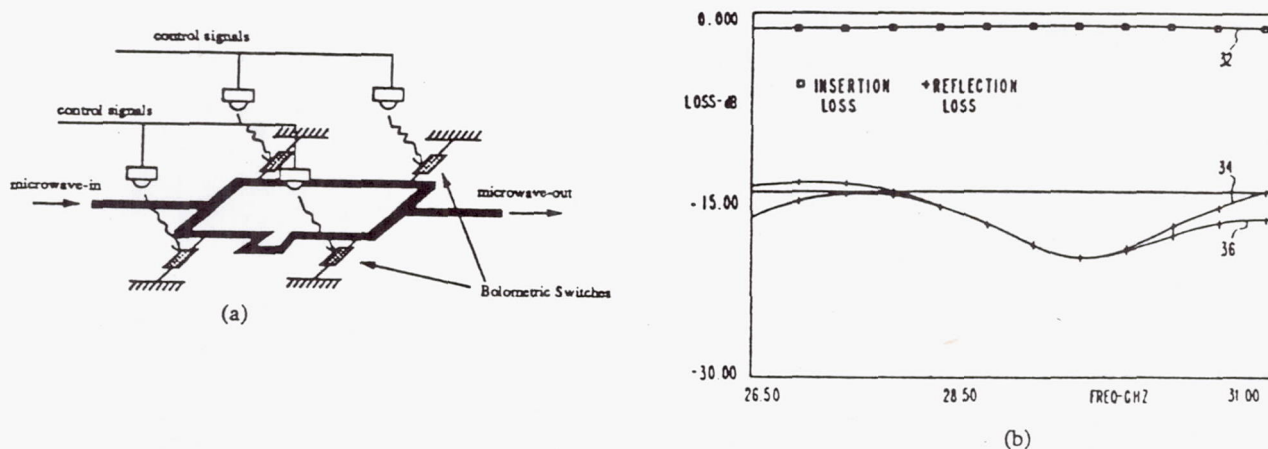


Figure 2 a) A delay line phase shifter with bolometric switches. b) Insertion and reflection losses of a delay line phase shifter that uses superconducting switches.

value that is the same as gold at 77 K (0.1Ω) and having a R_S of 1Ω in the normal state. It has an exceptionally narrow insertion loss envelope and excellent return loss.

Bolometric switches have an "on" resistance of nearly 0Ω and an "off" resistance of $0.1\text{-}4 \text{ k}\Omega$. In microwave application, their kinetic inductance and skin resistance must also be taken into account in calculating their "on" impedance. These switches are approximately $25\mu\text{m} \times 1000\mu\text{m}$. Their speeds, however, are very low-around 1s. They can be redesigned, however, to be as fast as $10\mu\text{s}$ [12]

We have fabricated the above phase shifter and we now discuss the bolometric response of one of its switches. Figure 3 shows the resistance versus temperature curve of this switch. The transition width is somewhat large-about 1 K. This is mainly due to the very narrow channel. Figure 3 also shows the bolometric response of this switch. We will report the microwave characteristics of this phase shifter in the future.

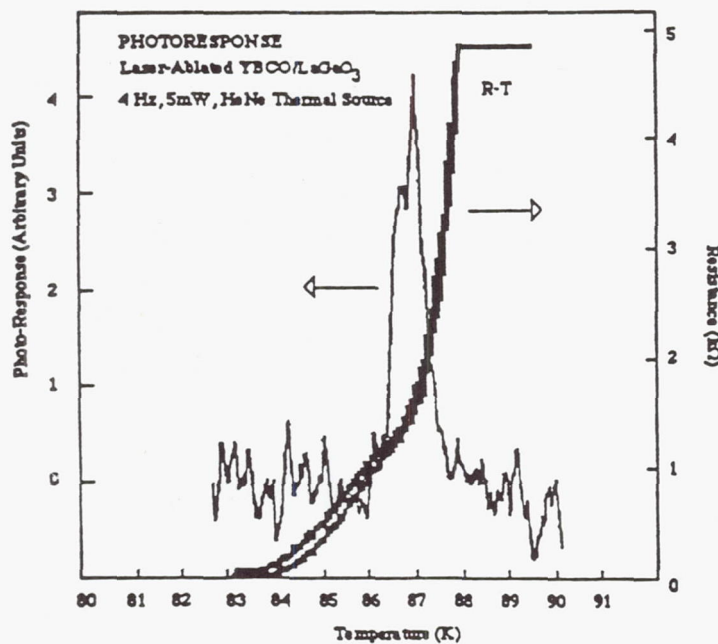


Figure 3 Resistance versus temperature graph (solid line) and the bolometric response of a superconducting switch. To obtain the bolometric response, the device was illuminated with a 5mW HeNe laser that was chopped at 4 Hz. The channel width was $10 \mu\text{m}$ and the channel length was 0.5 mm .

A typical fabrication sequence starts with the growth of the HTS film, followed by its patterning, etching, and metallization. Growth of the $\text{YBa}_2\text{Cu}_3\text{O}_{7-x}$ films on microwave substrates is discussed in references 23-26. Patterning is discussed comprehensively in reference 25.

Bolometric devices are quite easy to fabricate. After the film is grown, it is patterned and the bolometer is defined. Then the devices are annealed in an oxygen rich environment to increase the oxygen content in the film and to compensate for any losses that might have occurred in the previous stages. In reference 25 we discussed the side effects of the patterning of HTS $\text{YBa}_2\text{Cu}_3\text{O}_{7-x}$ films comprehensively. We

concluded that patterning lowers the T_c of the film by only a fraction of a degree-for all practical purposes, negligible. A more significant problem is the potential non-uniformity of T_c over the film. In the case of the bolometric devices, where all the devices are thermally biased near their transition temperature, a spatial non-uniformity in T_c is not acceptable and local control over the bias temperature may be required. The degree of the spatial non-uniformity of T_c depends on the growth technique. In laser ablated-films, non-uniformity of T_c is only fraction of a degree over a 1 cm^2 wafer.

As growth techniques mature, highly uniform films will become a reality and the scatter of T_c of these devices may soon be within $1/10$ of a degree for a 1 cm^2 microwave circuit. Meanwhile, we may solve this problem by locally tailoring the T_c of a device by laser heating, which causes a preferential oxygen loss in the HTS film of the device and therefore lowers its T_c . This technique can be used to lower the T_c of all the devices on a wafer accurately to 77 K so that rather inexpensive liquid nitrogen can be used directly without a temperature control unit.

Photonic Devices. Non-equilibrium optical excitation can be used to switch the state of a superconductor to normal conductivity [13]. In the case of ceramic superconductors, the coupling cross section between the photons and charge carriers is not known yet. It is not clear whether this cross section is large enough to allow the useful employment of this excitation process in superconducting switches. The speed of such a device, however, will surpass all other devices discussed here.

Magnetic Field Effect Devices. In these devices, an inductive loop generates a magnetic field parallel to the a-b plane of a $\text{YBa}_2\text{Cu}_3\text{O}_{7-x}$ film as shown in Figure 4. $\text{YBa}_2\text{Cu}_3\text{O}_{7-x}$ is a type II superconductor and vortices can be easily generated in it by relatively low magnetic fields [14]. A vortex containing a quantum of magnetic flux in the presence of a current leads to dissipation of energy in the film, so vortices can be generated to effectively increase the resistivity of the film or to destroy its superconductivity.

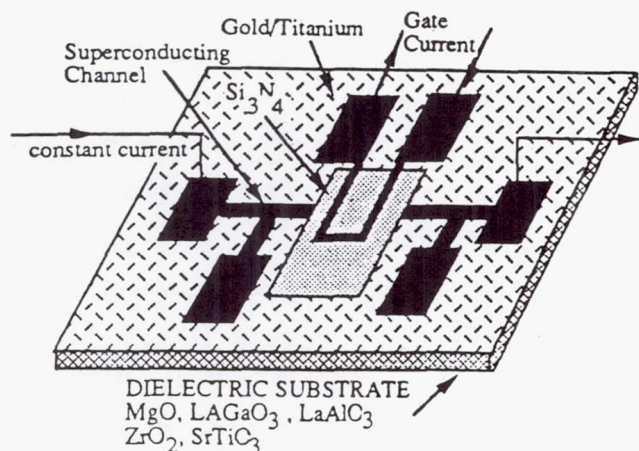


Figure 4 Schematic of a magnetically controlled superconducting switch.

Transverse Electric Field Effect Devices. These devices operate on a principle very similar to that of FET devices, where the electric field effect controls the conductivity of the channel. Because T_C is a function of the carrier density in superconductors [15-22], we propose to control T_C by electrostatically controlling the surface charge density of a superconducting channel [21]. The feasibility of this idea has already been demonstrated in normal superconductors [15-17]. In normal superconductors, T_C is a weak function of the electric field. However, in ceramic superconductors T_C can be made to be a strong function of an applied electric field because the normal carrier densities in these materials are an order of magnitude less than in metallic superconductors. Moreover, carrier density in ceramics can be tailored by doping [22].

Figure 5a shows a superconducting electric field-effect device [21]. This structure consists of a thin channel a few thousand Å thick and 5-50µm wide, consisting of the superconducting material with two pads at each end to allow four point resistance measurements. Ohmic contacts were made directly to the superconductor by attaching 2 mil gold wires with a wedge wire bonder. A Schottky contact was made to the superconductor structure midway along the channel by depositing on the sample 10nm of titanium followed by 200nm of gold by evaporation. It is believed that interaction of titanium with the oxygen in the superconducting material is responsible for the Schottky behavior. Patterning of this contact was done by the lift-off technique.

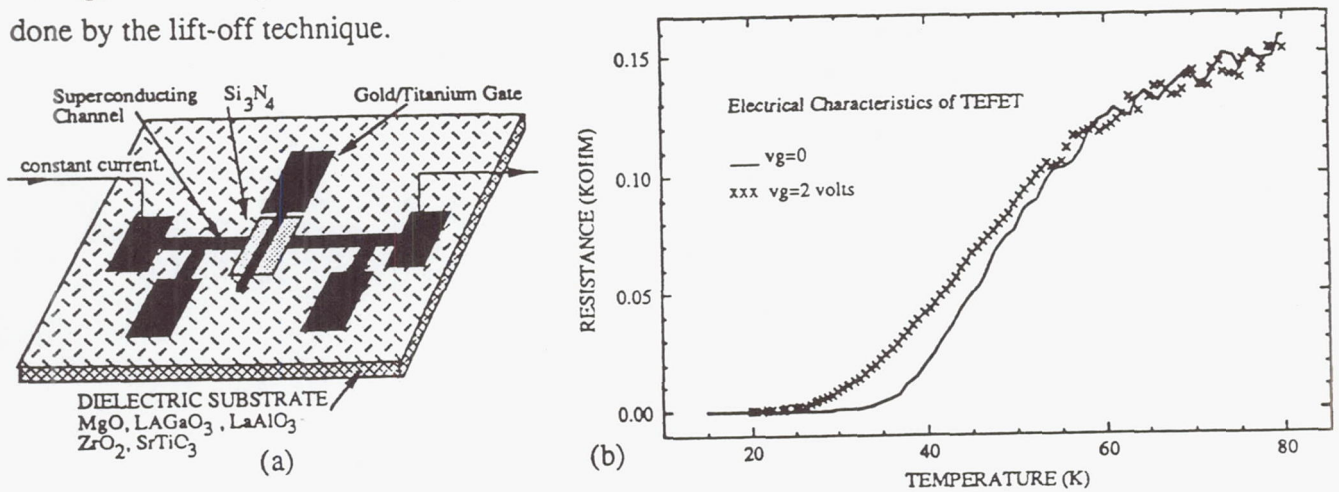


Figure 5 a) Schematic of an electric field-effect superconducting transistor. b) The resistance versus temperature characteristics of the electric field-effect transistor with two different gate biases of 0 and 2 volts. The channel current was 0.5 mA. The channel width was 10 µm and its thickness was 2000 Å. The gate width was 10 µm.

The AC resistance of the channel at 1kHz was measured as a function of temperature while different DC voltages were applied across the Schottky contact and the ground pads (see Figure 5b). As Figure 5b

shows, the transition temperature of the channel can be lowered considerably by this voltage. For this device, the influence on the transition temperature is due to the critical current being exceeded by the applied gate voltage. We are now refining our fabrication procedure to take advantage of weak links between the superconducting grains and to modulate the current by modifying the intergranular barrier heights using the electric field effect. This device can switch between a zero resistance and several hundred Ohms if it is maintained just below the transition temperature at T_s (Figure 5b).

Field-effect switches have an "on" resistance of 0Ω and an "off" resistance of $0.1-4 \text{ k}\Omega$. In microwave application, their kinetic inductance and skin resistance must also be taken into account in calculating their "on" impedance. These switches are about $50\mu\text{m} \times 1000\mu\text{m}$, and they can easily be scaled down to the size of a typical semiconductor FET.

Fabrication of the active field-effect superconducting device is slightly more involved than that of a bolometric device, because it requires an insulating layer between its channel and gate. However, the lift-off technique has been conveniently used to define the insulating layer, as discussed in reference 21. Since the gate voltage or current (in the case of magnetic field effect devices) can be used to change the channel resistance, the requirement of spatial uniformity of T_c is not as stringent for field-effect devices as it is for the bolometric devices.

Longitudinal Electric Field Effect Devices. A pseudo-three-terminal switch is shown in Figure 6. In this device, exceeding the critical current density between the gate and the source turns off the superconducting drain-to-source channel. This device offers very poor input-to-output isolation (almost zero) and excellent off-to-on resistance ratio (almost infinity). It is also extremely easy to fabricate and does not require a heat or light source. Current sources have large impedances; for this device to work, the impedance of the switch in both the "on" and "off" states must be smaller than that of the biasing circuit at microwave frequencies.

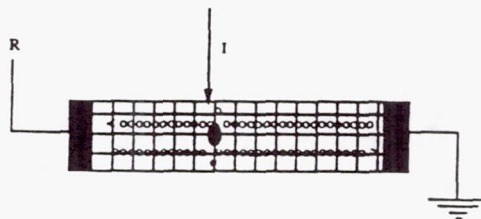


Figure 6 Schematic of a longitudinal electric field-effect device.

IV. DISCUSSION & CONCLUSION

To compare the performance of the above devices, we show their pertinent parameters in Table I. In this table "speed" is the inherent switching speed of the corresponding device. The off-to-on resistance ratio is denoted by " R_{off}/R_{on} " and is measured at dc. For bolometric devices, R_{off}/R_{on} is not infinite because these devices are thermally biased slightly above their zero-resistance state for maximum responsivity. The capacitance in the off state is denoted by " C_{off} " and is measured at 1MHz. A more relevant parameter in analysing the superconducting microwave switch is its kinetic inductance and skin resistance. We have not considered these here. High-frequency considerations will only result in somewhat lower off-to-on impedance ratios. The power needed to turn on a device is denoted by "P." This power is only an estimate and, therefore, it is discussed qualitatively. The isolation between the input (control signal) and the output (microwave) is denoted by "in/out isolation." For bolometric and photonic devices, the input-output isolation is very large, almost infinite. Size is denoted qualitatively, taking into account the entire circuit. The complexity of the switching circuit and its fabrication are also described qualitatively, lightly taking into account the fabrication steps and issues. Table I shows that the bolometric switches are very easy to fabricate and that they offer excellent input-to-output isolation as well as a good off-to-on resistance ratio. Their only drawback is their speed. Non-bolometric superconducting switches, on the other hand, are very fast.

TABLE I

Device	Speed (ns)	$\frac{R_{off}}{R_{on}}$	C_{off} (pF)	Power	in/out isol.	Size	Circuit /Fabric.
PIN	200	4×10^6	0.4	high	small	med.	high
MESFET	<1	8×10^4	0.4	med	small	small	med.
MISFET	<1	10^5	0.2	low	large	small	med.
Bolometric	10^4	$> 10^7$	< 0.1	high	∞	med.	low
Photonic	10^{-3}	∞	< 0.1	low	∞	med.	high
LEFET [#]	0.1	∞	< 0.1	med.	low	med.	med.
TEFET [§]	1	$> 10^7$	0.4	low	high	med.	med.

Longitudinal Electric Field-Effect Transistor.

§ Transverse Electric Field-Effect Transistor.

ACKNOWLEDGEMENT: The work reported here is partially supported by NASA Lewis Research Center Grant #NCC3-203, and by Reliance Electric Co. Grant # RC-471035. Discussions with Mr. Howard Jordan of Reliance have been very beneficial. Joe Warner of NASA has provided us with HTS films, and Chris Choery of NASA has helped us in different phases of the fabrication of the phase shifter. From NASA's fabrication laboratory, Joe Meola, Bruce Viergutz, Nick Varljay, Donna Bohman, and Chuck Hulbert have all contributed to the fabrication of the phase shifter. Professors Sheldon Gruber and John Angus of CWRU have been very supportive of M. Tabib-Azar in his efforts to set up a device characterization laboratory at CWRU. S. Max Golem has carefully edited this manuscript.

V. REFERENCES

1. R. Stockton and A. I. Sreenivas, "Semiconductor Control Devices: Phase Shifters and Switches," from the Handbook of Microwave and Optical Components. Edited by K. Chang, John Wiley & Sons, New York, Vol. 2, p.p. 230-262 (1990).
2. E. H. Fooks and R. A. Zakarevicius, Microwave Engineering Using Microstrip Circuits, Prentice Hall, Inc. Englewood Cliffs, New Jersey (1990).
3. R. E. Collin, Foundations for Microwave Engineering, McGraw-Hill, New York (1966).
4. J. F. White, "Diode Phase Shifters for Array Antennas." IEEE Transaction on Microwave Theory and Techniques, Vol. MTT-22 (6), pp. 658-674 (1974).
5. M. E. McKaughan and F.C. Jain, "Analysis of a Novel Monolithic GaAs MIS Phase Shifter." Conference Digest of Thirteenth International Conference on Infrared and Millimeter Waves of SPIE, p.p. 330-331 (1988).
6. J. F. White, "Semiconductor Control Devices: PIN Diodes," from the Handbook of Microwave and Optical Components. Edited by K. Chang, John Wiley & Sons, New York, Vol. 2, pp. 192-229 (1990).
7. R. S. Pengelly, Microwave Field-Effect Transistors- Theory, Design and Application, John Wiley & Sons, New York, second edition (1986).
8. J.L. Vorhaus, R.A. Pucel, and Y. Tajima, "Monolithic Dual-Gate GaAs FET Digital Phase Shifter." IEEE Trans. on Electron Devices, Vol. ED-29, No. 7, pp. 1078-1093 (1982).
9. Catalog of Fujitsu's Microwave Semiconductor Devices, Fujitsu Limited, Chiyoda-ku, Tokyo, Japan (1989).
10. Catalog of Toshiba's Microwave Semiconductor Devices, MATCOM Inc., Palo Alto, Cal. (1987).
11. T. G. Stratton, et. al., "High-Temperature Superconducting Microbolometer." Appl. Phys. Lett. 57 (1), p. 99 (1990).

12. Q. Hu and P. L. Richards, "Design analysis of a High T_c Superconducting Microbalometer," *Appl. Phys. Lett.* 55 (23), p. 2444 (1989).
13. K. Tanabe, Y. Enomoto, M. Suzuki, T. Iwata, and A. Yamaji, "Nonbolometric Infrared Detection in $La_{2-x}Sr_xCuO_4$ and $YBa_2Cu_3O_y$ Epitaxial Thin Films." *Japanese Journal of App. Phys.*, Vol. 29 (3), pp. L 466- L 469 (1990).
14. D. P. McGinnis, J. B. Beyer, and J. E. Nordman, "Vector S-Parameter Measurements of the Superconducting Vortex Flow Transistor." *IEEE Transactions on Electron Devices*, Vol. 35 (2), p.p. 240243 (1988).
15. T.G. Berlincourt, "Large shifts of transition temperature with electric charging predicted for superconducting semiconductors," *Physics Letters*, Vol. 29A, No. 6, pp. 308-309 (1969).
16. H.L. Stadler, "Changing properties of metals by ferroelectric polarization charging," *Physical Review Letters*, Vol. 14, No. 24, pp. 979-981 (1965).
17. R.E. Glover and M.D. Sherrill, "Changes in superconducting critical temperature produced by electrostatic charging," *Physical Review Letters*, Vol. 5, No. 6, pp. 248-250 (1960).
18. T. Nishino, M. Miyake, Y. Harada, and U. Kawabe, "Three-terminal superconducting device using a si single-crystal film," *IEEE Electron Device Letters*, Vol. EDL-6, No. 6, pp. 297-299 (1985).
19. T.D. Clark, R.J. Prance, and A.D.C. Grassie, "Feasibility of hybrid Josephson field effect transistors," *J. Appl. Phys.* 51(5), pp. 2736-2743 (1980).
20. W.J. Gallagher, "Three-terminal superconducting devices," *IEEE Trans. on Magnetics*, Vol., Mag-21, No. 2, pp. 709-716 (1985).
21. M. Tabib-Azar et. al., "Three Terminal Superconducting Field-Effect Transistor Fabricated Using $YBa_2Cu_3O_7$ Laser Ablated Thin Film," to be published.
22. T. Penney, M. W. Shafer and B. L. Olson, *Physica C*, Vol. 65, pp. 162-164 (1989).
23. J. D. Warner, J. E. Meola and K. A. Jenkins: "Superconductivity and Applications," Edited by H. S. Kivak, Y. H. Koo and D. T. Shaw, Plenum Press, New York, NY, pp. 163-169 (1989).
24. J.D. Warner, K.B. Bhasin, N.C. Varaljay, D.Y. Bohman and C.M. Chorey, "Growth and Patterning of Laser Ablated Superconducting YBa_2Cu_3O Films on $LaAlO_3$ Substrates," *NASA TM #102346* (1989).
25. J. D. Warner, K.B. Bhasin, M.A. Stan, S. Vitta, M. Tabib-Azar and N. S. Shoemaker, "Growth, Characterization, Patterning and Application of Laser Ablated Superconducting $YBa_2Cu_3O_7$ Films on $LaAlO_3$ Microwave Substrate." To appear in *Advanced Materials*.
26. M. Tabib-Azar, F.A. Miranda, N. Shoemaker, K.B. Bhasin, and J.D. Warner, "Detection of Weak Links in High-Temperature Superconducting Thin Films by Microwave Power Transmission Measurements." To be submitted to *Physica A*.

Design of an Optically Controlled K_a-band GaAs MMIC Phased-Array Antenna

Richard R. Kunath, Paul C. Claspy*, Mark A. Richard* and
Kul B. Bhasin

NASA Lewis Research Center, Space Electronics Division
Cleveland, Ohio 44135

* Case Western Reserve University, Department of Electrical
Engineering, Cleveland, Ohio 44106

1. INTRODUCTION

Phased-array antennas long have been investigated to support the agile, multibeam radiating apertures with rapid reconfigurability needs of radar and communications. With the development of the Monolithic Microwave Integrated Circuit (MMIC), phased array antennas having the stated characteristics are becoming realizable. However, at K-band frequencies (20-40 GHz) and higher, the problem of controlling the MMICs using conventional techniques either severely limits the array size or becomes insurmountable due to the close spacing of the radiating elements necessary to achieve the desired antenna performance.

Investigations have been made that indicate using fiber optics as a transmission line for control information for the MMICs provides a potential solution [ref. 1]. By adding an optical interface circuit to pre-existing MMIC designs, it is possible to take advantage of the small size, lightweight, mechanical flexibility and RFI/EMI resistant characteristics of fiber optics to distribute MMIC control signals. This paper will describe the architecture, circuit development, testing and integration of optically controlled K-band MMIC phased-array antennas.

2. PHASED-ARRAY ANTENNA ARCHITECTURE

NASA Lewis Research Center's Space Electronics Division has been investigating using MMICs in K-band phased-array antennas. Due to the 0.6 lambda radiating element spacing required to eliminate grating lobes in the front radiating hemisphere (+, - 90°), the distance between elements is 5mm (200 mils) at 30 GHz. The previous MMIC development at NASA-Lewis [ref. 2] has yielded devices at this frequency. The device of greatest importance, the phase shifter, is approximately 250x125 mils in dimension. This size rivals that of the radiating element and consequently forces equally close spacing of the MMICs. Spacings this close do not allow for conventional interconnects to be used. Therefore, a decision to exploit fiber optics was made and a contract to develop a low power, high speed OptoElectronic Interface Circuit (OEIC) was begun by Honeywell's Science Center in 1986 [ref. 3].

3. HYBRID OEIC DEVELOPMENT

A hybrid OEIC was delivered for verification in 1989. The circuit features an optical receiver comprised of an interdigitated (2um finger width, 5um finger spacing) PIN photodiode and a three-stage (~10dB/stage), capacitively-coupled, differential Low Noise Amplifier (LNA) with approximately 100mW of power consumption [fig. 1]. The hybrid OEIC design used a second circuit design under a second NASA contract [ref. 4] to provide 1:16 demultiplexing and GaAs to TTL logic level level shifting. The hybrid design requires external clocking, synchronization and level shifting to complete the interface to the 30GHz MMIC phase shifter. As configured,

the hybrid OEIC takes a serial optical input and demultiplexes it into 16 TTL level outputs. The maximum data rate that the optical receiver can support is 1Gbps; however, the demultiplexer limits the data rate to only 300Mbps.

4. HYBRID OEIC TESTING AND EVALUATION

As detailed in reference 3, the hybrid OEIC performance was tested and verified. The inherent delay between the optical and electrical interface signals is accommodated for using adjustable time-delay pulse generators. The MMIC phase shifters require 0 and -6 volt switching levels which are provided for by external CMOS analog multiplexers. Two different characterization/verification tests were made as described below.

The first test evaluated the hybrid OEIC characteristics and functionality [fig. 2]. A 64-bit NRZ-format word was cycled, and after external clock and synchronization signal timing was adjusted, the corresponding TTL level output bit signals were measured. The optical power required to obtain repeatable performance was $>200\mu\text{W}$, and the overall power consumption (dependant on termination impedance and demultiplexer output magnitude) was measured to be as low as 120mW.

The second test used the hybrid OEIC together with a 30GHz MMIC phase shifter. Employing an interferometric technique, the switching of the phase shifter by the hybrid OEIC could be measured by monitoring the constructive and destructive interference effects at the interferometer output with a crystal detector [fig. 3]. The external level shifter limited the test switching frequency to 2MHz; however, the use of this technique verified the hybrid OEIC's abilities to control the 45° , 90° and 180° bits of the phase shifter.

5. MONOLITHIC OEIC

While a fully monolithic OEIC was the anticipated deliverable from the OEIC contract, a materials processing problem prevented the successful development of the low power demultiplexer which inevitably led to a hybrid approach using a known, working demultiplexer (slower in speed and higher in power consumption). Further investigation by Honeywell into the processing problem finally led to the fabrication of usable fully monolithic devices [fig. 4]. The new devices feature the integrated optical receiver as before but require only an external clock signal. Synchronization is generated internally on the OEIC.

Future generations of fully monolithic OEIC designs will be augmented to provide enhanced performance and functionality. The current fully monolithic OEIC still requires a delay adjustable external clocking signal and when used in a phased-array of an appreciable size, will require adjustable delays for each MMIC in the array to account for the signal delay to the distributed MMIC elements. This can partly be corrected for by encoding the clock signal into the data stream and adding the necessary decoding circuits to the OEIC. Also, the OEIC is not a "smart" device. As it is currently configured, it relies upon the circuit sending it data to sort out its data from the data being sent to other OEIC/MMIC modules.

Distributed intelligence architectures as mentioned above are a relatively new concept for phased-array antennas, which heretofore relied upon single point array control. However, the OEIC circuitry is perfectly suited to combine all of these functions together. The design techniques to allow for independent address decoding, on-chip "look-up tables" and autonomous control are well-known and could be implemented in future OEIC/MMIC generations. NASA plans to investigate distributed intelligence architectures in future designs.

6. PLANNED INTEGRATION AND TESTING

The critical issue to address in utilizing the OEIC in phased-array antennas is how to integrate the OEIC into

the overall array architecture. NASA is designing and planning to evaluate techniques to address the integration issues. Leveraging off a NASA-Lewis program to develop MMIC packaging and characterization techniques above 20GHz [ref. 5], a package to house a new generation of 32GHz MMIC phase shifters will be designed and fabricated.

Because the OEIC requires no ground plane for operation, it can be isolated from the ground plane necessary for both the MMIC and the radiating patch antenna. A carrier has been designed to mount the fully monolithic OEIC on, which minimizes the number of bias and external control signals [fig. 5]. The OEIC carrier is then epoxied onto the lid of the MMIC phase shifter package. This "piggy-back" approach results in two levels of wire bonds from the OEIC carrier [figs. 6 & 8]. One set of bonds connect the OEIC carrier to the top surface bias/clock distribution board, while a second set of bonds connect the OEIC data output lines to the MMIC package. Although it is not desirable to have two-level wire bonding, it is believed that "flip-chip" and via hole connection techniques could be used to eliminate these problems, and stable, reliable connections would be realized.

In order to test the integrated OEIC, NASA will design and build (in-house) an optical transmitter/controller suitable to control up to a 16 element optically controlled MMIC phased-array antenna. The transmitter/controller will use LEDs as channel signal sources and will provide for external clocking signal delays. When complete, the phased-array will be tested by measuring the antenna beam performance as the antenna is optically/electronically steered.

7. CONCLUSIONS

This paper has presented and discussed the use of fiber optic distribution of control signals in K_a -band MMIC phased-array antennas. Through the development of OEICs and their subsequent combination with previously developed MMICs, it has been shown that a potential solution to distributing control information to MMICs in closely-spaced arrays is possible. Further, a plan to integrate OEICs into MMIC phased-array antennas has been outlined, and future modifications to the OEIC have been discussed.

8. REFERENCES

1. Richard R. Kunath and Kul B. Bhasin, "Optically Controlled Phased-Array Antenna Technology for Space Communication Systems", Proceedings of the SPIE Optoelectronics and Laser Applications in Science and Engineering Symposium (O/E LASE '88), January 1988.
2. K. B. Bhasin and D. J. Connolly, "Advances in Monolithic Microwave Integrated Circuit Technology for Space Communications Systems," IEEE Transactions on Microwave Theory Techniques, Volume MTT-34, pp. 994-1001, 1986.
3. Kul B. Bhasin, et al, "A High Speed G_aA_s Optoelectronic Integrated Circuit for Control of a G_aA_s Monolithic K_a -band Phase Shifter", IEEE Photonics Technology Letters, Volume 1, No. 11, November 1989.
4. NASA Contract #NAS3-24676, "Development of Gallium Arsenide High-Speed, Low-Power Serial Parallel Interface Modules", Executive Summary and Final Report, May 1988.
5. Robert R. Romanofsky and Kurt A. Shalkhauser, "Universal Test Fixture for Monolithic mm-Wave Integrated Circuits Calibrated With an Augmented TRD Algorithm", NASA Technical Paper 2875, March 1989.

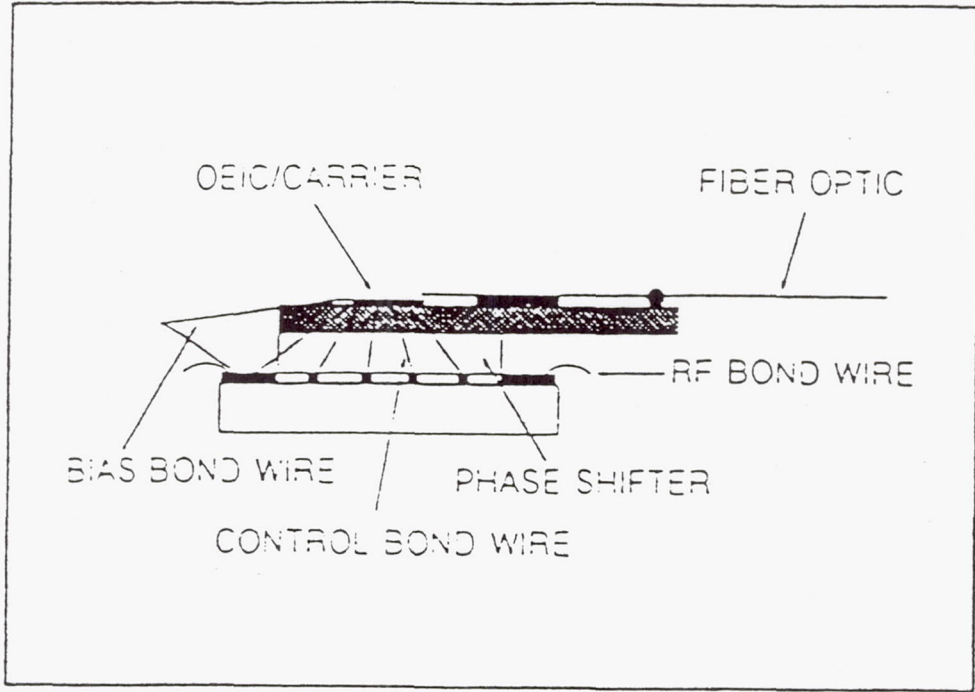


Figure 7. Close-up view of proposed "piggy-back" OEIC integration

A SEVEN PATCH HEXAGONAL CP SUBARRAY WITH CPW/STRIPLINE FEED NETWORK

R.N. Simons
Sverdrup Technology, Inc.
Lewis Research Center Group
Brook Park, Ohio 44142

R.Q. Lee
National Aeronautics and Space Administration
Lewis Research Center
Cleveland, Ohio 44135

G.R. Lindamood*
University of Akron
Akron, Ohio 44325

ABSTRACT

A seven element microstrip subarray of hexagonal geometry has been designed and tested at S-band frequencies. The microstrip patch antenna is excited at a single feed position using a direct probe type connection to generate a circularly polarized (CP) wave. The RF power is coupled to these feed positions by a novel coplanar waveguide/stripline feeding network. The paper describes the subarray architecture and the feed network in detail. The measured results include the feed network characterization as well as the radiation patterns of the subarray.

INTRODUCTION

Microstrip patch antennas have many salient features such as low cost, light weight, thin profile, conformability and ease of fabrication which makes them attractive for satellite communications applications. These antennas can be excited to radiate linearly polarized or circularly polarized (CP) waves using only a single feed. For linear polarization, a rectangular patch antenna is excited with the feed located near the center of one edge to achieve proper impedance matching. To generate CP waves without the use of phase shifters or hybrid couplers, a nearly square patch must be used with the feed position determined as given in [1].

This paper describes the architecture of a seven patch hexagonal CP planar subarray (Fig.1). The seven patches are fed in equal amplitude and phase by a novel probe type feed network. The feed is formed by a multi-layer network which is realized using a combination of coplanar waveguide (CPW) and balanced stripline.

*Summer Student Intern at NASA Lewis Research Center.

FEED SYSTEM DESIGN AND PERFORMANCE

The feed system consists of a 7-way radial CPW power divider network [2], a balanced stripline line stretcher and a CPW to stripline coupler. The RF power to the radial CPW power divider network (Fig.2) is fed by a coaxial line. The axis of the coaxial line and the plane of the CPW circuit are orthogonal. Thus the inner conductor of the coaxial line meets the junction formed by the intersecting center strip conductors of the CPW. The outer conductor of the coaxial line is slotted and meets the ground planes of the CPW. In this manner, the seven radial CPW lines are excited in equal amplitude and phase [2]. The measured return loss at the coaxial input port, the power coupled to any one of the seven output ports and the isolation between any two output ports are shown in Figures 3(a) thru 3(c). At the design frequency of 2.2875 GHz, the measured insertion loss is only 0.15 dB more than the 8.45 dB theoretically expected for a seven way divider. The return loss and the isolation are better than 10 dB and 15 dB respectively.

The output signal from the power divider is coupled to a balanced stripline line stretcher by a post coupler. The line stretcher equalizes the path length to each of the seven patch antennas. Finally, the signal from the line stretcher is coupled to the patch antennas by a second post coupler which also works as a probe feed. Figure 4(a) shows a CPW to a balanced stripline post coupler. In this coupler, the center strip conductor of the CPW and the strip conductor of the stripline are electrically connected by a metal post. The metal post enters the stripline through an aperture in the ground plane. The ground plane of the CPW and the stripline are connected together by bond wires and shorting pins. The preliminary measured characteristics of the coupler are presented in Figure 4(b). The insertion loss and return loss of the coupler are about 0.4 dB and 12 dB at 2.2875 GHz.

SUBARRAY DESIGN AND PERFORMANCE

The patches (4.45 x 4.39 cms) are arranged in a triangular lattice to form a hexagonal geometry with an edge to edge spacing of 0.43 inches. The assembled subarray and the feed and power divider network are shown in Figs. 5(a) and 5(b) respectively. The measured radiation patterns of the array at 2.325 GHz for the $\phi = 0^\circ$ and $\phi = 90^\circ$ planes are shown in Figs. 6(a) and 6(b) respectively. The measured on axis axial ratio for the LHCP is 1.5 dB and the 3dB beam widths are 36° in both planes. The gain of the antenna as determined from the beam widths is 13 dB. The measured return loss at the coaxial input port of the array is better than 15 dB at the design frequency and is shown in Fig.7.

CONCLUSIONS

The design and performance characteristics of a CPW/Stripline feed network have been presented. A seven patch hexagonal CP subarray fed with this feed network has demonstrated excellent CP patterns.

REFERENCES

1. Y. T. Lo, B. Engst and R. Q. Lee, "Simple Design Formulas for Circularly Polarized Microstrip Antennas," IEE Proc., Microwaves, Antennas and Propagation, Vol.135, Pt.H, No.3, pp.213-215, June 1988.
2. R. N. Simons and G. E. Ponchak, "Coax-to-Channelized Coplanar Waveguide In-Phase N-Way, Radial Power Divider," Electronics Letters., Vol.26, No.11, pp.754-755, May 1990.

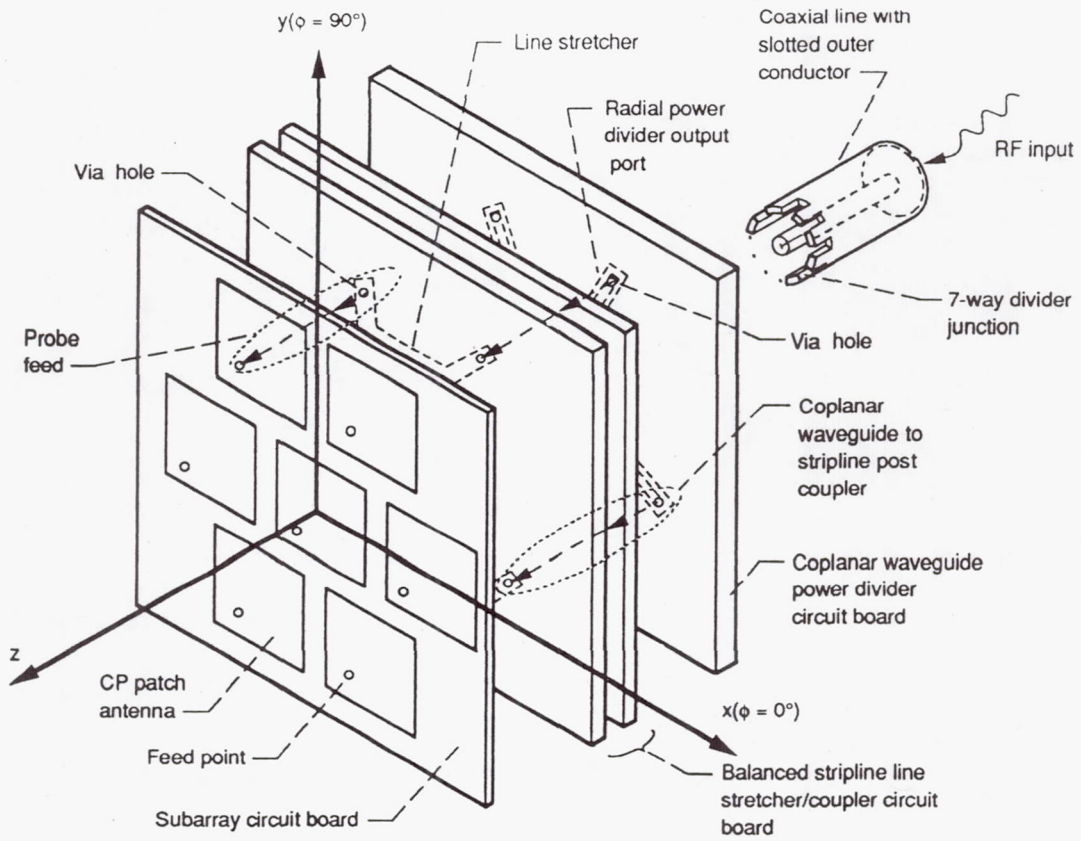


Figure 1.—Array schematic.

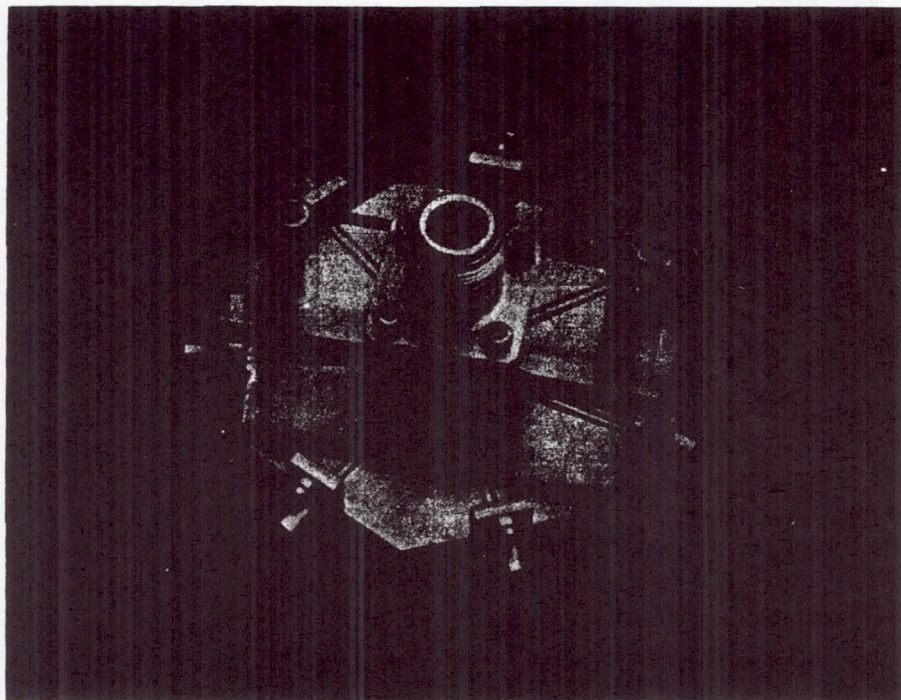
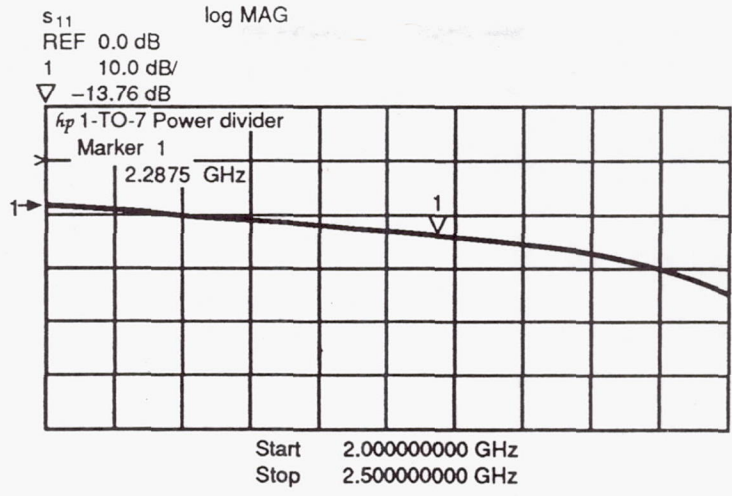
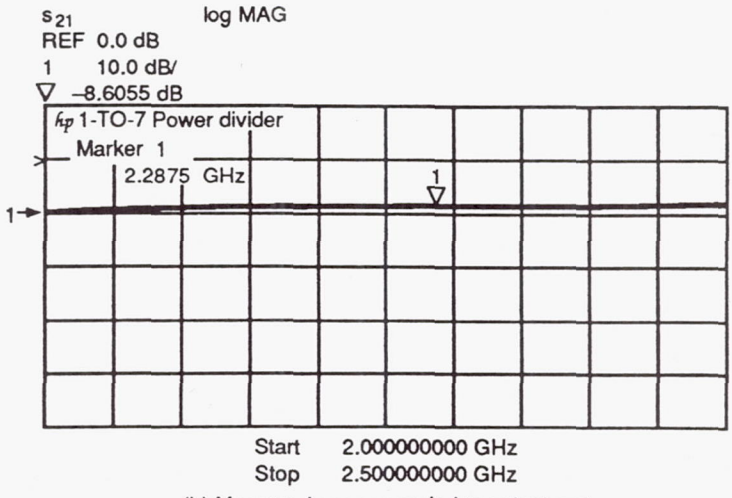


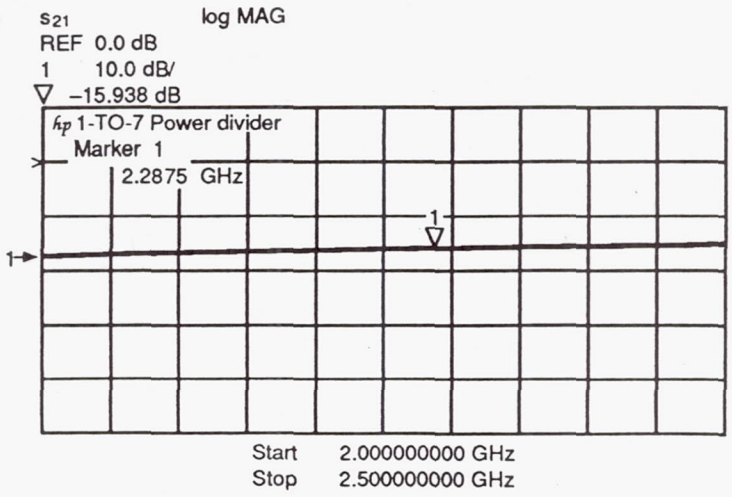
Figure 2.—Radial coax-to-CPW 1:7 power divider.



(a) Measured reflection coefficient at the coaxial input port.

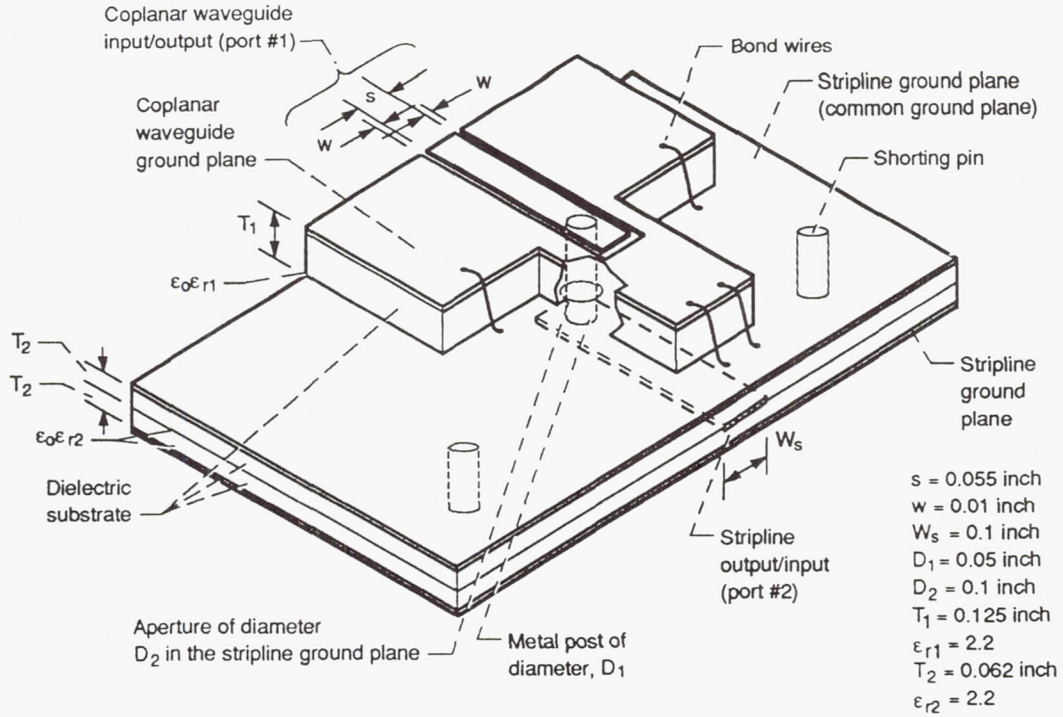


(b) Measured power coupled to output port.

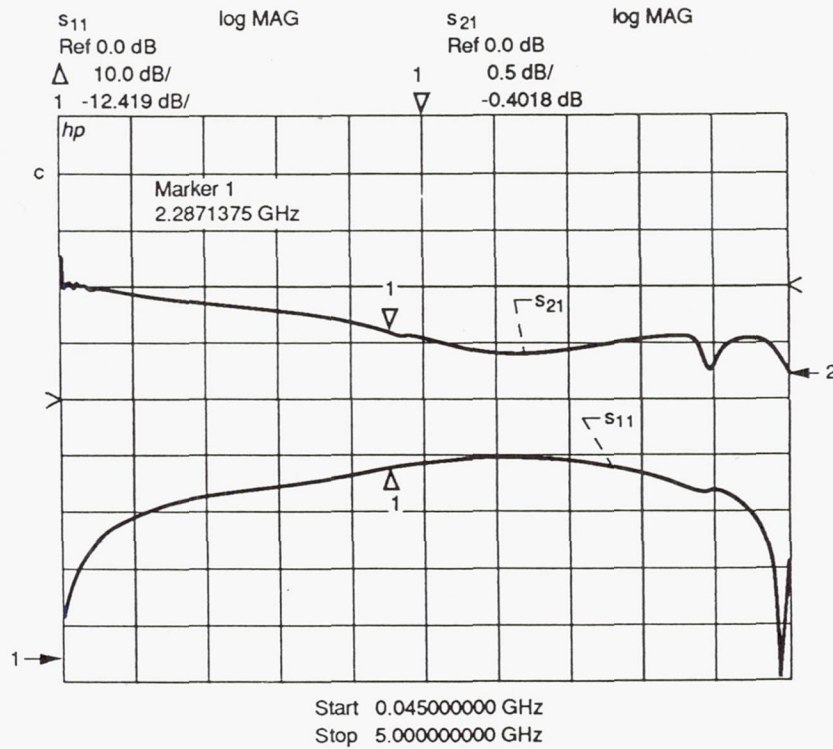


(c) Measured isolation between output ports.

Figure 3.—Coax-to-coplanar waveguide 1:7 power divider.

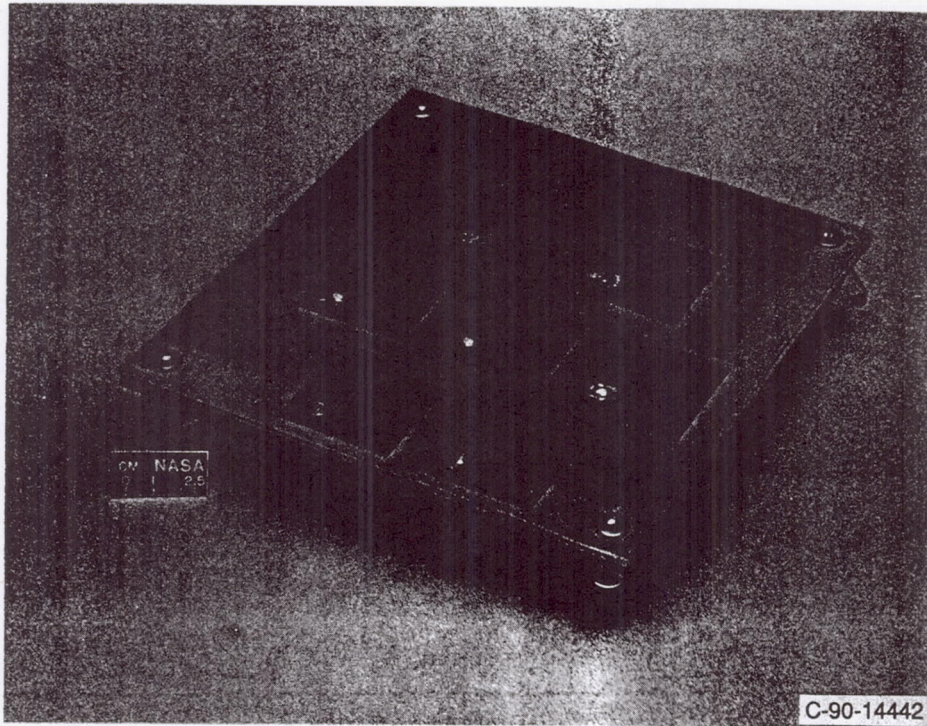


(a) CPW-to-stripline post coupler.

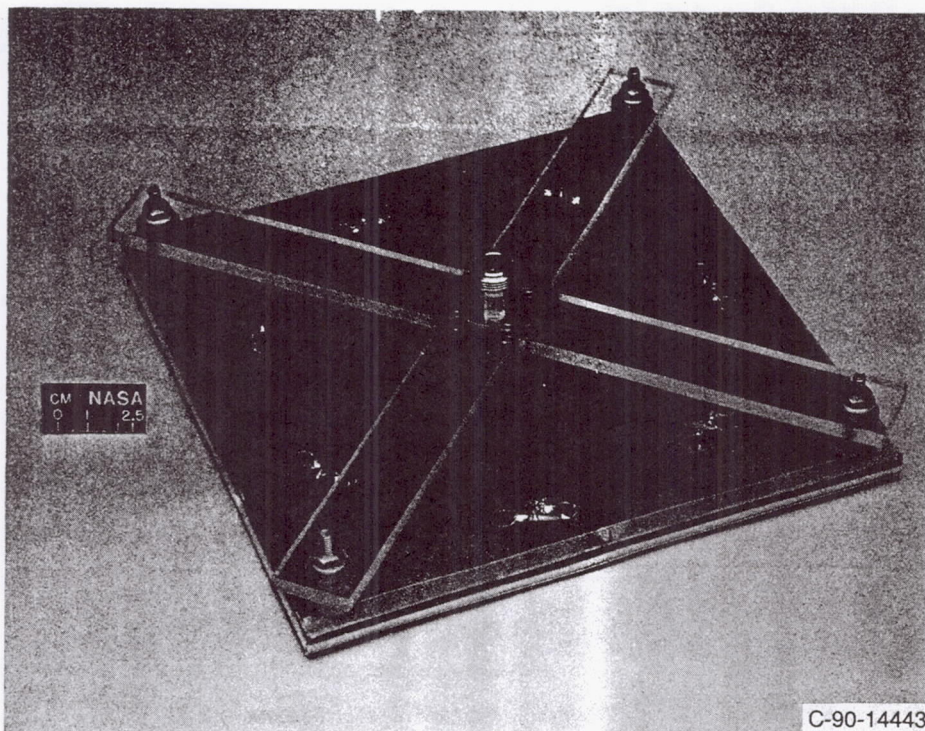


(b) Measured coupler characteristics.

Figure 4.



(a) Assembled array antenna.



(b) Feed and power divider network.

Figure 5.

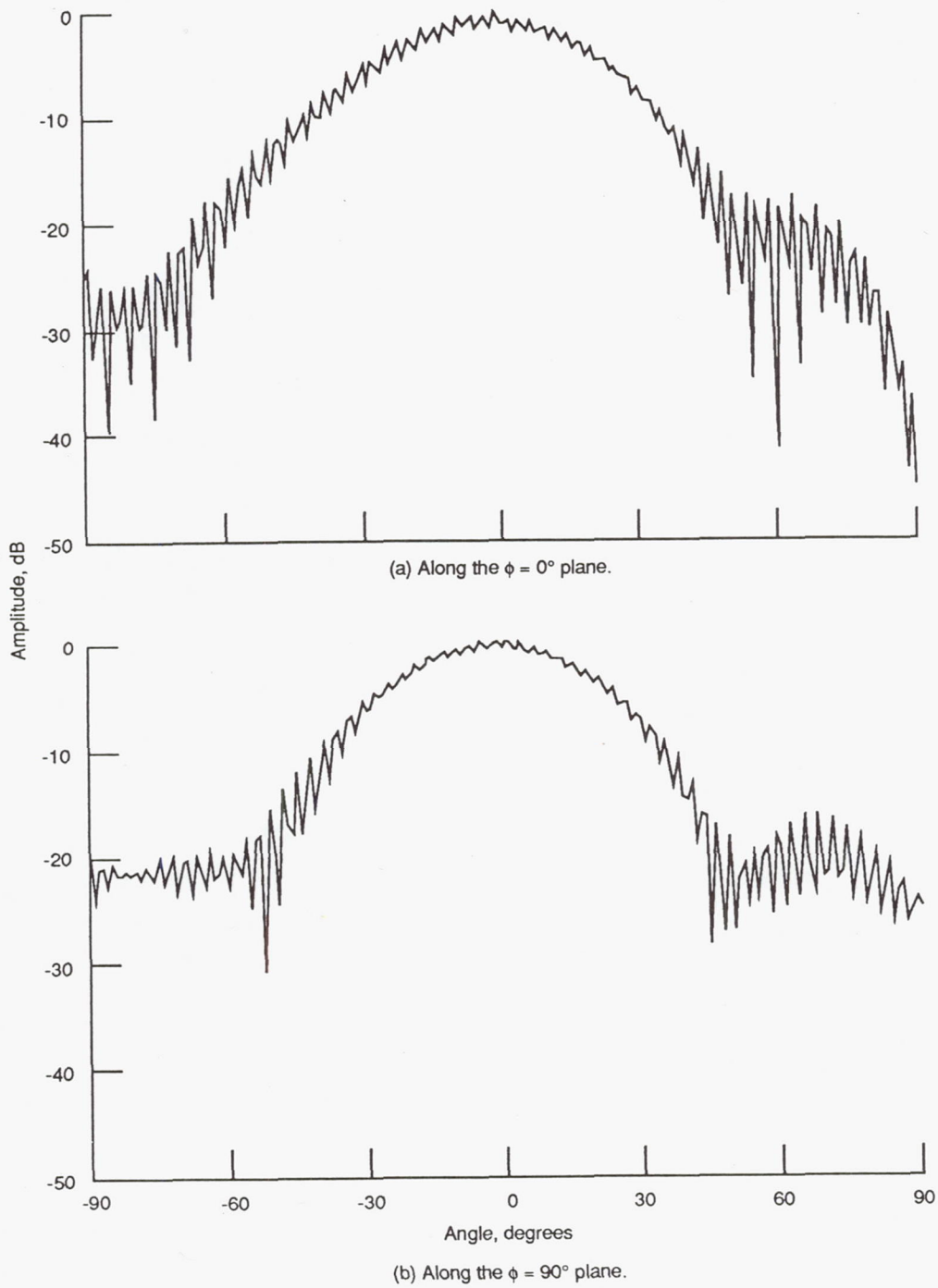


Figure 6.—Measured radiation patterns.

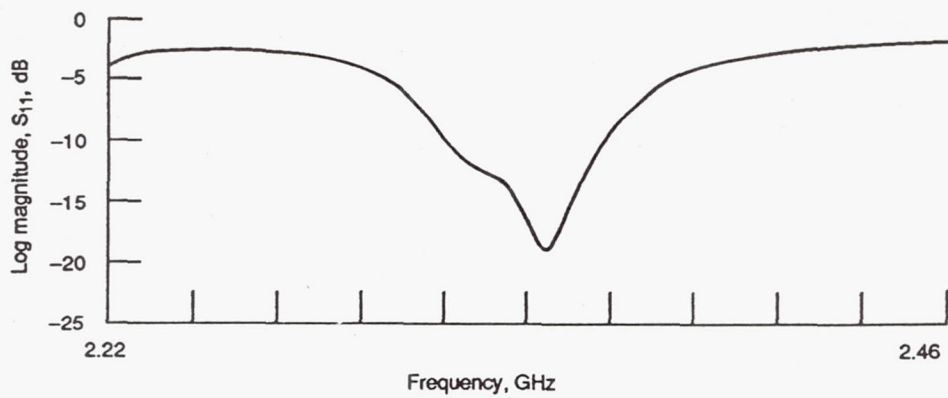


Figure 7.—Measured return loss at the coaxial input port.

COPLANAR-WAVEGUIDE/MICROSTRIP PROBE COUPLER AND APPLICATIONS TO ANTENNAS

Indexing terms: Microstrip, Antennas

A method to couple microwave power from a coplanar waveguide to a microstrip line on opposite sides of a ground plane is demonstrated. The coupler uses a metallic post which passes through an aperture on the ground plane connecting the strip conductor of the coplanar waveguide to the microstrip line. The measured insertion loss and return loss are about 1 dB and 10 dB, respectively, across the frequency range of 0.045–6.5 GHz. To demonstrate potential applications of the coupler as a feeding network for a microstrip patch array, measured radiation patterns of two rectangular patch antennas with a direct coplanar-waveguide/microstrip feed and with a proximity coupled coplanar-waveguide/microstrip feed are presented.

Introduction: The coplanar waveguide (CPW) has several advantages over conventional planar transmission lines which makes the CPW ideally suited for microwave integrated circuit components.^{1,2} At the same time, there is a growing interest in microstrip antennas because of their advantages over conventional antennas.³ In phased arrays for satellite communications systems, some of the requirements that have to be met are small size, light weight, thin profile, and high efficiency. To satisfy these requirements, it is important that the components for various circuit functions, the feed network and the radiators are fully integrated. In addition, it is equally important to completely shield the circuits and the feed system from electromagnetic interference (EMI) and electromagnetic pulse (EMP). A simple solution to this problem is to build the system using mixed transmission media such as a combination of CPW and microstrip line.

In this paper, a novel integration technique by which microwave power is coupled from a CPW to a microstrip line located on the opposite sides of a ground plane is demonstrated. Also, the radiation pattern of two rectangular patch antennas integrated with a direct CPW/microstrip feed and with a proximity or electromagnetically coupled CPW/microstrip feed are presented.

In a phased array, the coupler has the advantage of integrating a CPW feed network with active and passive circuit components to a microstrip-based radiating system. In addition, the microstrip ground plane in the coupler serves several useful functions. Firstly, it acts as a natural shield for the feed network against EMI and EMP. Secondly, it acts as an addi-

tional heatsink for active devices and provides mechanical strength to the thin structure.

Coupler and patch antenna integration: A CPW to microstrip line coupler is shown in Fig. 1. The CPW and the microstrip line share a common ground plane that has an aperture. The coupler is formed by a metal post which passes through the

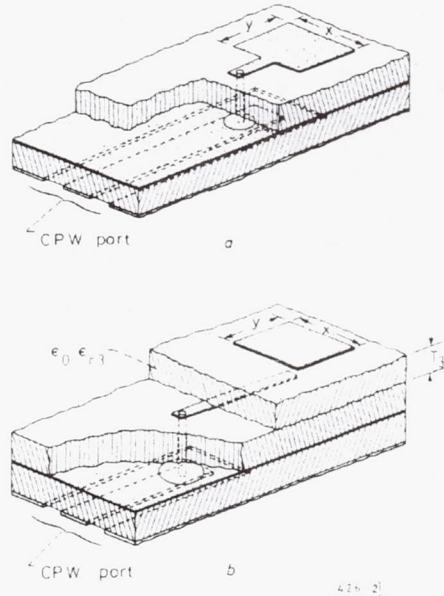


Fig. 2 Schematic diagram illustrating integration of a rectangular patch antenna

- a Direct coplanar-waveguide/microstrip feed
 $x = 52.58 \text{ mm}$ $y = 44.32 \text{ mm}$
- b Proximity coupled coplanar-waveguide/microstrip feed
 $x = 52.58 \text{ mm}$ $y = 44.32 \text{ mm}$ $T_3 = 0.25 \text{ mm}$ $\epsilon_{r3} = 2.2$

aperture and contacts the strip conductors of the CPW and the microstrip line, respectively. A pair of wire bonds located adjacent to the post tie the CPW ground planes and the microstrip ground planes to a common potential. The thickness and dielectric constant of the substrate are typical of those used in CPW circuits and microstrip patch radiators. The characteristic impedance of the CPW is 70Ω which is

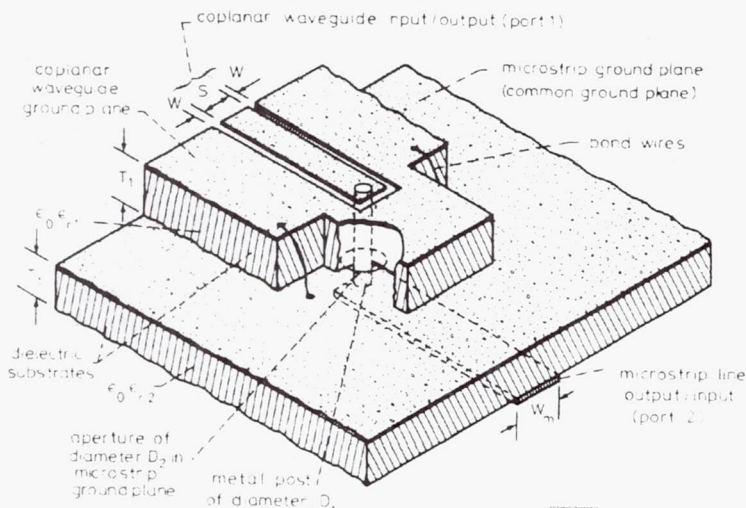


Fig. 1 Schematic diagram illustrating coplanar-waveguide to microstrip probe coupler

- $S = 1.14 \text{ mm}$ $W = 0.25 \text{ mm}$ $W_m = 0.76 \text{ mm}$
- $D_1 = 1.02 \text{ mm}$ $D_2 = 2.54 \text{ mm}$ $T_1 = 3.18 \text{ mm}$
- $\epsilon_{r1} = 2.2$ $T_2 = 0.25 \text{ mm}$ $\epsilon_{r2} = 2.2$

chosen to provide a good match to the characteristic impedance of the 50Ω microstrip line.⁴ The diameters of the aperture and the metal post were experimentally optimised to obtain the best insertion loss characteristics. It is worth noting that the post diameter turns out to be greater than the microstrip line width; however, this is essential for obtaining a low insertion loss characteristic.

The integration of a rectangular patch antenna with a direct CPW/microstrip feed and proximity coupled CPW/microstrip feed is schematically illustrated in Fig. 2. The dimensions of the patches are chosen to resonate at about 2.2 GHz and each has a linear polarisation which is parallel to the plane of the antenna. The substrate parameters for Fig. 2 are same as those in Fig. 1.

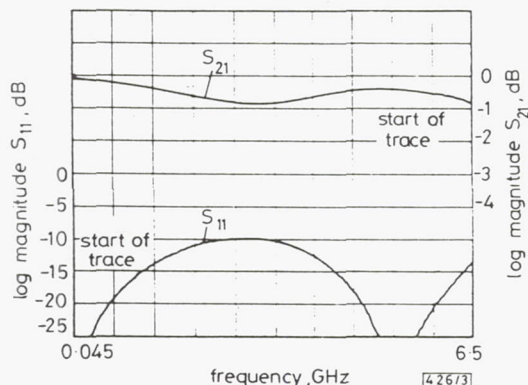


Fig. 3 Measured insertion loss and return loss of coupler

Experimental results: The measured insertion loss of the coupler over a wide frequency band extending from 0.045 to 6.5 GHz is shown in Fig. 3. The measured insertion loss which is less than 1 dB includes the losses occurring in the junction, the attenuation of the short length of CPW and microstrip line on either sides of the junction and that of the two coaxial connectors used at the input and output ports. Also superimposed on Fig. 3 is the return loss which is better than 10 dB across the band and is independent of the measurement port.

The measured radiation patterns of the microstrip patch antennas are presented in Fig. 4. It is observed that the two methods of excitation result in essentially identical radiation patterns.

Conclusion and discussions: A novel technique to couple microwave power from a CPW to a microstrip line located on the opposite sides of a ground plane and its application to patch antennas has been demonstrated. Because of its low loss and wide bandwidth, the coupler has potential applications in feed systems of wideband antennas such as spirals and log periodic arrays. As a concluding remark it may be mentioned that monolithic implementation of the coupler using semiconductor via hole technology would result in much smaller size with reduced parasitics and therefore have potential applications at millimetre-wave frequencies.

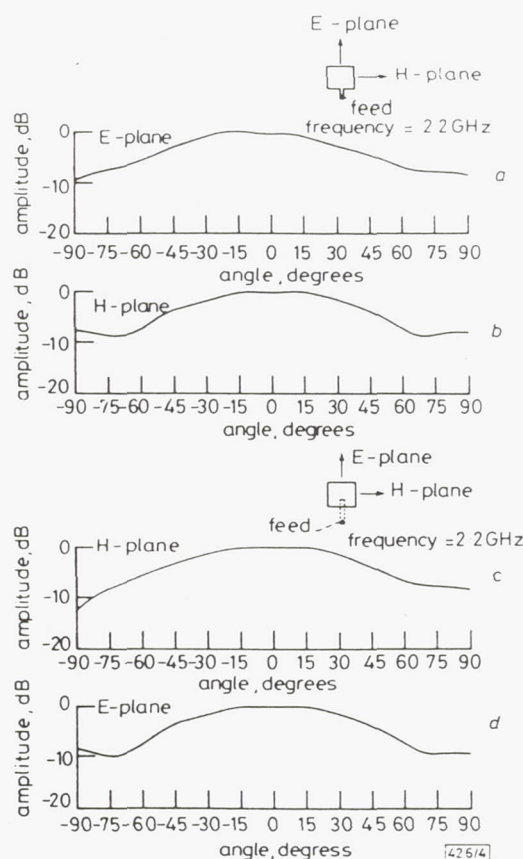


Fig. 4 Measured E- and H-plane radiation pattern of patch antenna

- a, b Antenna excited directly by coplanar-waveguide/microstrip feed
- c, d Antenna excited by proximity coupled coplanar-waveguide/microstrip feed

R. N. SIMONS
R. Q. LEE

22nd October 1990

NASA Lewis Research Center
Mail Stop 54-5
21000 Brookpark Road
Cleveland, OH 44135, USA

References

- 1 GUPTA, K. C., GARG, R., and BAHL, I. J.: 'Microstrip lines and slot-lines' (Artech House, Inc., Norwood, 1979), Chap. 7
- 2 SIMONS, R. N., and PONCHAK, G. E.: 'Coax-to-channelised coplanar waveguide in-phase, n-way, radial power divider', *Electron. Lett.*, 1990, **26**, pp. 754-755
- 3 LO, Y. T., and LEE, S. W.: 'Antenna handbook' (Van Nostrand Reinhold Co., New York, 1988), Chap. 10
- 4 SIMONS, R. N., and PONCHAK, G. E.: 'Modeling of some coplanar waveguide discontinuities', *IEEE Trans.*, 1988, **MTT-36**, pp. 1796-1803

NEW COPLANAR WAVEGUIDE/STRIPLINE FEED NETWORK FOR SEVEN PATCH HEXAGONAL CP SUBARRAY

Indexing terms: Waveguides, Striplines and stripline components, Antennas

A novel CPW-to-stripline post coupler is demonstrated. This device couples the output power from a coax-to-CPW inphase seven-way radial power divider to a balanced stripline line stretcher and together forms a multilayer probe-type feed network. The feed network excites a seven patch hexagonal circularly polarised (CP) subarray. The measured return loss and insertion loss of the coupler are better than 17 dB and 0.25 dB at the design frequency of 2.875 GHz. The measured on-axis axial ratio for the left hand circular polarisation (LHCP) is 1.5 dB and the 3 dB beam widths are 36° in the principal planes of the subarray. The gain of the subarray is 13 dB. The input return loss of the subarray is better than 10 dB.

Introduction: In satellite communications beam-to-beam isolation and frequency reuse are important requirements which can be achieved with orthogonal polarisation. For reflector antenna systems, polarisation diversity has been achieved by the use of complex beamforming networks. Although, the reflector type antennas are efficient they suffer from several disadvantages. Microstrip patch antenna arrays on the other hand have many salient features such as low cost, light weight, thin profile, conformability and ease of fabrication¹ and are therefore actively pursued.

This Letter describes the architecture of a seven patch hexagonal CP planar subarray. The seven patches are fed in equal amplitude and phase by a novel probe type feed network. The probe feed avoids the use of phase shifters or hybrid couplers to generate a circularly polarised wave and hence is simple to fabricate. The feed is formed by a multilayer network which is realised using a combination of coplanar waveguide (CPW), balanced stripline and coaxial line. $y(\phi = 90^\circ)$

Feed network and subarray design: Fig. 1 illustrates the multilayer construction of the seven patch hexagonal CP subarray. The feed network for this array consists of a coax-to-CPW inphase seven-way radial power divider² and a balanced stripline line stretcher on separate dielectric substrates coupled by a post coupler. Fig. 2 illustrates the CPW-to-balanced stripline post coupler. In this coupler, the centre strip conductor of the CPW and the stripline are electrically connected by a metal post through an aperture in the ground plane. The diameters of the aperture and the metal post were experimentally optimised to obtain the best insertion loss characteristics. The thickness and relative permittivity of the dielectric substrate are typical of those used in CPW and stripline circuits. The ground plane of the CPW and the stripline are connected together by bond wires and shorting pins to ensure equipotential of both surfaces. The line stretcher is a 50 Ω line whose length is chosen so as to equalise the distance of separation between the radial CPW output ports and the feed points of the hexagonal subarray. The patches are nearly square (44.5 × 43.9 mm) and are arranged in a triangular lattice to form a hexagonal geometry with an edge-to-edge spacing of 10.899 mm along the $\phi = 0^\circ$ plane and 10.991 mm along the $\phi = 90^\circ$ plane. The feed position is determined as explained in Reference 3. The patch array is fabricated on a dielectric substrate of thickness and relative permittivity of 0.508 mm and 2.1, respectively.

Feed network and subarray performance: The measured return loss (S_{11}) and insertion loss (S_{21}) of the post coupler are better than 17 dB and 0.25 dB, respectively, at the design frequency of 2.875 GHz and are illustrated over a wide band of fre-

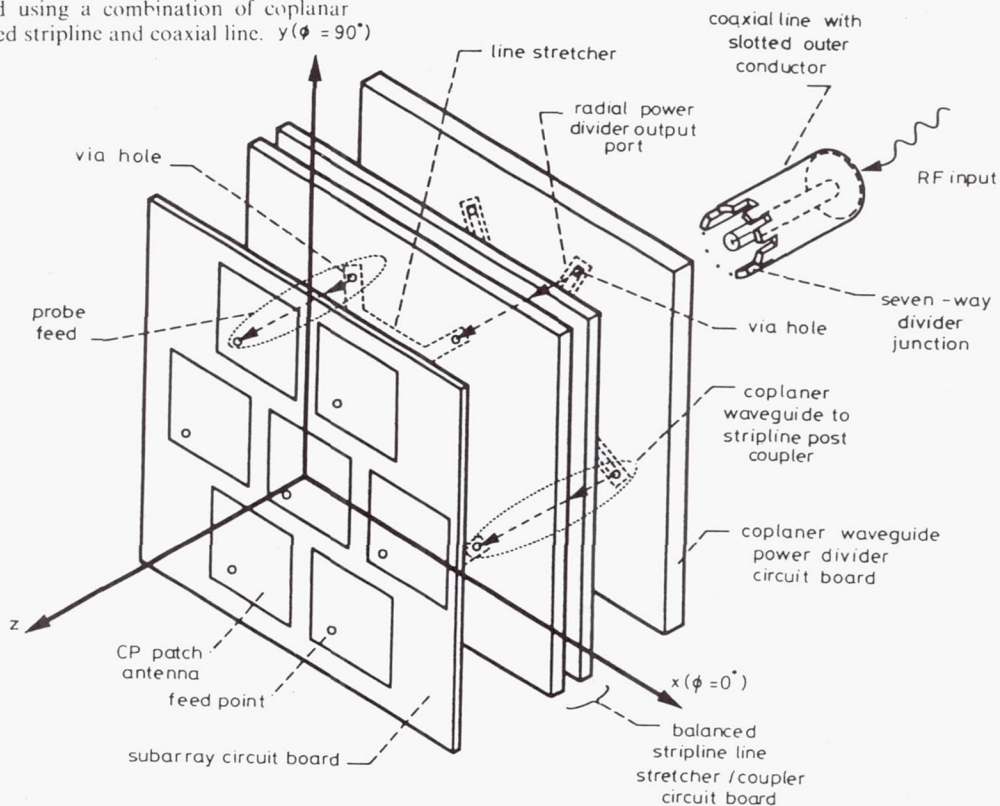


Fig. 1 Schematic diagram illustrating multilayer construction of seven patch hexagonal CP subarray

Reprinted from *ELECTRONICS LETTERS* 14th March 1991 Vol. 27 No. 6 pp. 533-535

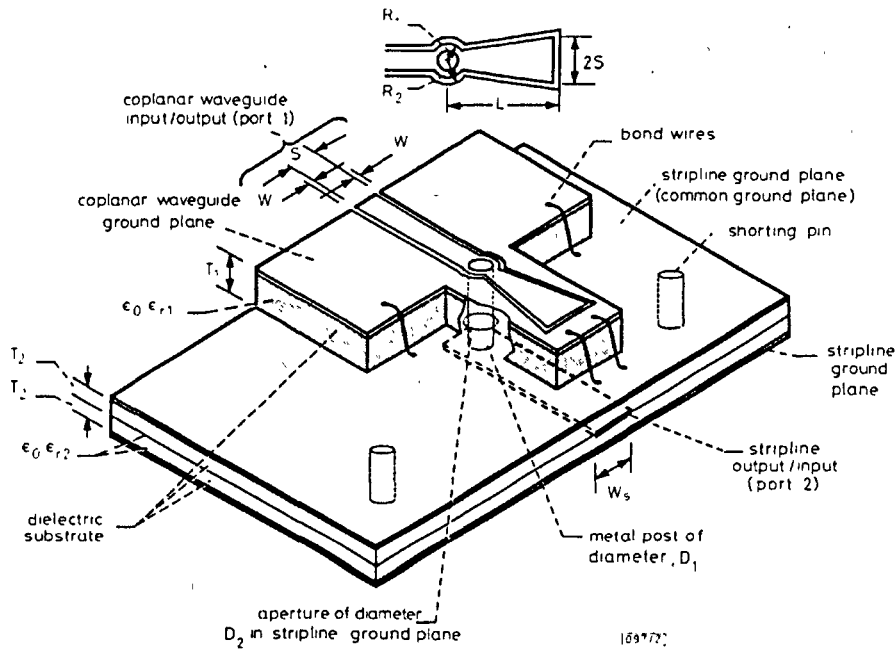


Fig. 2 Schematic diagram illustrating CPW-to-balanced stripline post coupler

$S = 1.397 \text{ mm}$ $W = 0.254 \text{ mm}$ $W_1 = 2.54 \text{ mm}$
 $D_1 = 1.27 \text{ mm}$ $D_2 = 2.54 \text{ mm}$ $T_1 = 3.175 \text{ mm}$
 $\epsilon_{r1} = 2.2$ $T_2 = 1.5748 \text{ mm}$ $\epsilon_{r2} = 2.1$
 $R_1 = 1.397 \text{ mm}$ $R_2 = 1.651 \text{ mm}$ $L = 5.969 \text{ mm}$

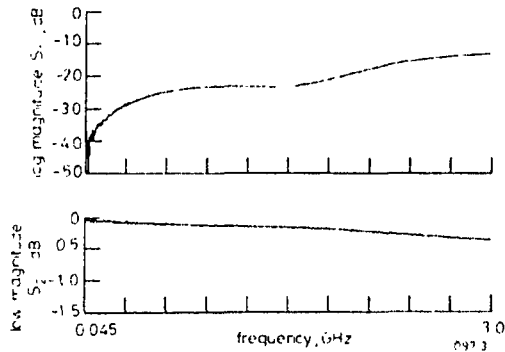


Fig. 3 Measured insertion loss (S_{21}) and return loss (S_{11}) of post coupler

frequencies in Fig. 3. The measured far-field radiation patterns of the subarray at 2.325 GHz for the $\phi = 0$ and $\phi = 90$ planes are shown in Figs. 4 and 5, respectively. The measured on-axis axial ratio for the LHCP is 1.5 dB and the 3 dB beam widths are 36° in both planes. The gain of the antenna as determined

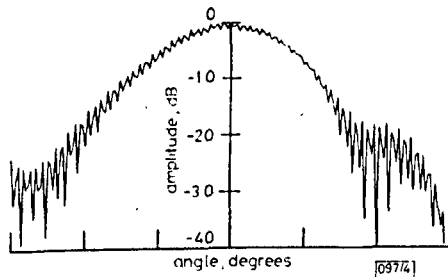


Fig. 4 Measured far field radiation pattern of subarray, $\phi = 0^\circ$ plane

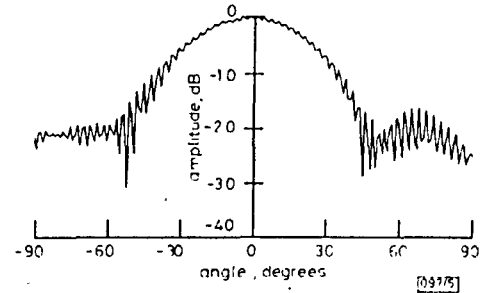


Fig. 5 Measured far field radiation pattern of subarray, $\phi = 90^\circ$ plane

from the beam widths is 13 dB. As shown in Fig. 6, the measured return loss (S_{11}) at the coaxial input port of the subarray is found to be better than 10 dB at 2.325 GHz.

Discussions and conclusions: A novel technique to couple microwave power from an inphase seven-way radial power

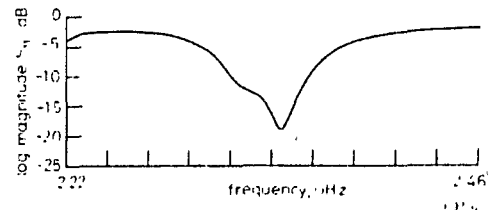


Fig. 6 Measured return loss (S_{11}) at coaxial input port

divider to a seven patch hexagonal CP subarray has been demonstrated. The post coupler which is crucial to this design has low loss and wide bandwidth. The subarray which exhibits CP patterns has thin profile and light weight, and is therefore suitable as a building block for larger arrays.

R. N. SIMONS
R. Q. LEE
G. R. LINDAMOOD

1st February 1991

Mail Stop 54-5
NASA Lewis Research Center
21000 Brookpark Road
Cleveland, OH 44135, USA

References

1. TO, Y. T., and LEE, S. W.: 'Antenna handbook' (Van Nostrand Reinhold Co., New York, 1988), Chap. 10.
2. SIMONS, R. N., and POSCHAK, G. T.: 'Coax-to-channelised coplanar waveguide in-phase N-way, radial power divider', *Electron Lett.*, 1990, **26**, (11), pp. 754-755.
3. TO, Y. T., INGSI, B., and LEE, R. Q.: 'Simple design formulas for circularly polarized microstrip antennas', *IEEE Proc. II*, 1988, **135**, (3), pp. 213-215.

NEW CHANNELISED COPLANAR WAVEGUIDE TO RECTANGULAR WAVEGUIDE POST AND SLOT COUPLERS

Indexing terms: Waveguides, Waveguide components, Waveguide couplers

Two new coplanar waveguide to rectangular waveguide couplers with coupling through a post and a slot are experimentally demonstrated. The couplers operate over the K_u -band transmission and X -band reception frequencies that are designated for satellite communications. The measured insertion loss and return loss are about 1 dB and 10 dB, respectively, for both couplers.

Introduction: Coplanar waveguide (CPW) is a very useful transmission line for microwave integrated circuits and has several advantages over conventional microstrip line.¹ The channelised coplanar waveguide (CCPW)² is a new variant of the conventional CPW. This Letter presents the design and experimental characterisation of new CCPW-to-rectangular waveguide post and slot couplers. In the post coupler, coupling is through a metal post that enters the waveguide through a circular aperture in the centre of the top broad wall. In the slot coupler, coupling is through a printed longitudinal radiative slot in the centre of the narrow wall. These couplers can inject signals directly from a circuit such as a monolithic IMPATT/Gunn diode oscillator into a waveguide. Hence these couplers have potential applications in satellite communication systems such as Very Small Aperture Terminals (VSATs).

Coupler design and fabrication: Post coupler: A CCPW-to-rectangular waveguide post coupler and a CCPW circuit board with a probe are schematically illustrated in Figs. 1 and 2, respectively. The channel width C , centre strip conductor width S , and slot width W of the CCPW for a given substrate thickness d are determined as explained in Reference 2. The waveguide height, width and wall thickness are denoted as a , b and T , respectively, and are standard for a given frequency

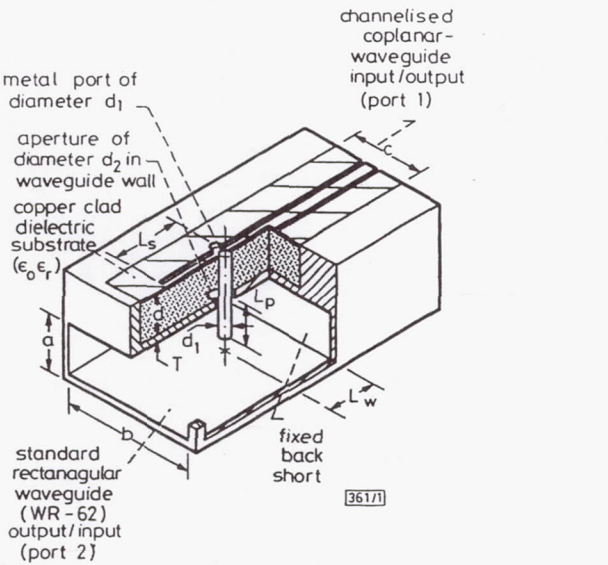


Fig. 1 Cutaway drawing of CCPW-to-rectangular waveguide post coupler

- $a = 7.8994 \text{ mm}$
- $b = 15.7988 \text{ mm}$
- $C = 5.08 \text{ mm}$
- $d = 3.175 \text{ mm}$
- $d_1 = 1.3208 \text{ mm}$
- $d_2 = 5.08 \text{ mm}$
- $L_p = 5.715 \text{ mm}$
- $T = 1.016 \text{ mm}$
- $L_w = 4.191 \text{ mm}$
- $\epsilon_r = 2.2$

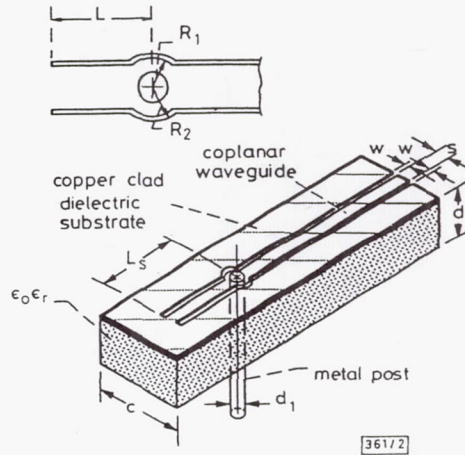
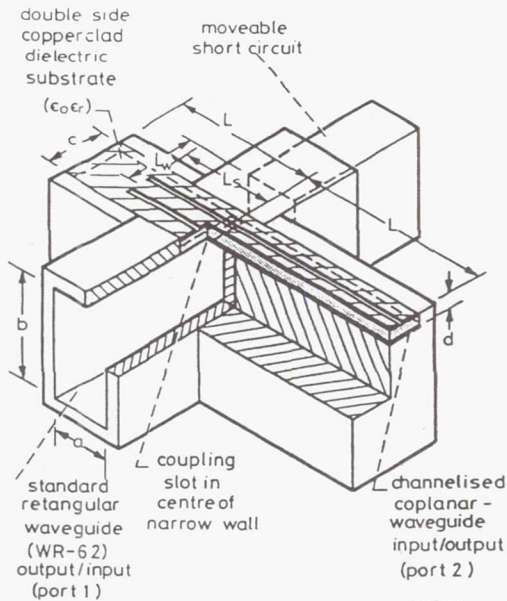


Fig. 2 CCPW circuit board with probe

- $S = 1.143 \text{ mm}$
- $W = 0.254 \text{ mm}$
- $L_s = 2.54 \text{ mm}$
- $R_1 = 0.889 \text{ mm}$
- $R_2 = 1.143 \text{ mm}$

band. The axis of the two transmission lines are parallel; however, they can be oriented at any arbitrary angle. A metal post of diameter d_1 enters the waveguide through an aperture of diameter d_2 to form an electric probe. The length of the probe extending into the waveguide is L_p . The opposite end of the post is attached through the dielectric substrate to the center strip conductor of the CCPW. The waveguide and the CCPW are terminated in a fixed short circuit which are placed at a distance L_w and L_s from the centre of the post, respectively.

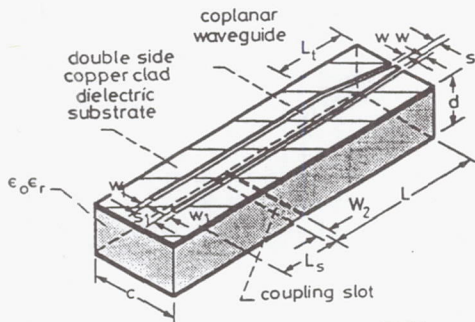
Coupler design and fabrication: Slot coupler: A CCPW-to-rectangular waveguide slot coupler and a CCPW circuit board with a coupling slot are schematically illustrated in Figs. 3 and 4, respectively. The coupling slot is flush with the inner surface of the waveguide narrow wall and consequently inter-



36173

Fig. 3 Cutaway drawing of CCPW-to-rectangular waveguide slot coupler

$a = 7.8994 \text{ mm}$
 $b = 15.7988 \text{ mm}$
 $c = 5.08 \text{ mm}$
 $d = 0.7874 \text{ mm}$
 $L = 25.4 \text{ mm}$
 $L_w = 11.43 \text{ mm}$
 $\epsilon_r = 2.2$



36174

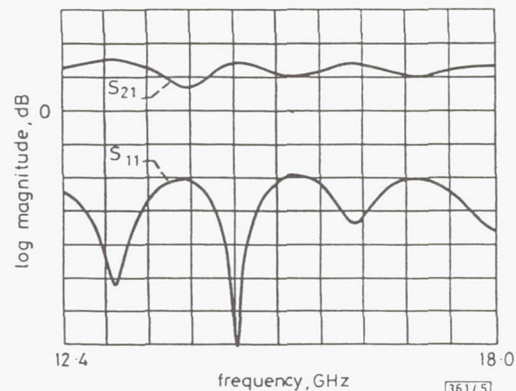
Fig. 4 CCPW circuit board with coupling slot

$S = 0.6858 \text{ mm}$
 $W = 0.3048 \text{ mm}$
 $S_1 = 1.397 \text{ mm}$
 $W_1 = 0.254 \text{ mm}$
 $L_1 = 1.143 \text{ mm}$
 $W_2 = 0.254 \text{ mm}$
 $L_s = 11.0236 \text{ mm}$

rupts the transverse surface currents. Thus power from the TE_{10} mode is coupled to the CCPW. The slot width is chosen as 0.254 mm for ease of fabrication. The slot length is equal to the channel width C . The waveguide and the CCPW are terminated in a short circuit placed at a distance L_w and L_s from the centre of the coupling slot, respectively. The length of the impedance matching taper L_1 is equal to $\lambda_{g(\text{CCPW})}/2$.

Experimental coupler performance: For the post coupler, L_w and L_s are approximately $\lambda_{g(\text{waveguide})}/6$ and $\lambda_{g(\text{CCPW})}/6$, respectively, at the centre frequency. The radii of curvature R_1 and R_2 in the CCPW centre strip conductor and the ground plane at the location of the post are approximately $0.7d_1$ and $0.7d_1 + W$, respectively. Further, d_1/b and L_p/a are equal to 0.084 and 0.723 , respectively. The above parameters, obtained through experimentation, resulted in satisfactory insertion and return loss characteristics. The measured return loss (S_{11}) at the CCPW port and the insertion loss (S_{21}) between the CCPW and the waveguide ports of the post coupler are presented in Fig. 5. The post coupler operates over the entire K_u band which includes VSAT transmission frequencies (14.0 to 14.5 GHz) and has an insertion loss of less than 1 dB and a return loss of greater than 10 dB .

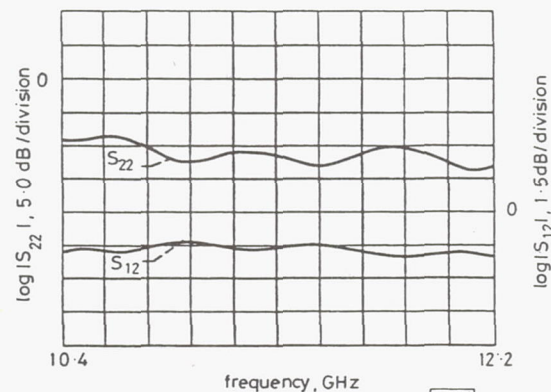
For the slot coupler, L_w and L_s are approximately $\lambda_{g(\text{waveguide})}/4$ and $\lambda_{g(\text{CCPW})}/2$, respectively, at the centre frequency. The measured return loss (S_{22}) at the CCPW port and the insertion loss (S_{12}) between the CCPW and the waveguide ports of the slot coupler are presented in Fig. 6. The slot coupler has an insertion loss of about 1.5 dB and a return loss of greater than 10 dB at VSAT reception frequencies that extend from 10.95 to 12.2 GHz .



36175

Fig. 5 Measured return loss (S_{11}) at CCPW port and insertion loss (S_{21}) between CCPW and rectangular waveguide ports of post coupler

S_{11} 5.0 dB/division
 S_{21} 1.0 dB/division



36176

Fig. 6 Measured return loss (S_{22}) at CCPW port and insertion loss (S_{12}) between CCPW and rectangular waveguide ports of slot coupler

Conclusions and discussions: Two new CCPW-to-rectangular waveguide couplers with coupling through a post and a slot are experimentally demonstrated. The measurements show that the couplers have excellent insertion loss and return loss characteristics. These couplers are very compact, efficient and inexpensive to fabricate.

R. N. SIMONS

12th March 1991

Mail Stop 54-5
NASA Lewis Research Center
21000 Brookpark Road
Cleveland, Ohio 44135, USA

References

- 1 GUPTA, K. C., GARG, R., and BAHL, I. J.: 'Microstrip lines and slot-lines' (Norwood: Artech House, Inc., 1979), Chap. 7
- 2 SIMONS, R. N., PONCHAK, G. E., MARTZAKLIS, K. S., and ROMANOFSKY, R. R.: 'Channelized coplanar waveguide: discontinuities, junctions, and propagation characteristics'. 1989 IEEE MTT-S Inter. Micro-wave Symp. Dig., III, pp. 915-918

Theoretical and Experimental Characterization of Coplanar Waveguide Discontinuities for Filter Applications

Nihad I. Dib, *Student Member, IEEE*. Linda P. B. Katehi, *Senior Member, IEEE*,
George E. Ponchak, *Member, IEEE*. and Rainee N. Simons, *Senior Member, IEEE*

Abstract—A full-wave analysis of shielded coplanar waveguide two-port discontinuities based on the solution of an appropriate surface integral equation in the space domain is presented. Using this method, frequency-dependent scattering parameters for open-end and short-end CPW stubs are computed. The numerically derived results are compared with measurements performed in the frequency range 5–25 GHz and show very good agreement. Equivalent circuit models and closed-form expressions to compute the circuit element values for these discontinuities are also presented.

I. INTRODUCTION

RECENTLY, coplanar waveguide (CPW) technology has attracted a great deal of interest for RF circuit design owing to several advantages over the conventional microstrip line, among them the capability to wafer probe at millimeter-wave frequencies [1]–[6]. Thus, several investigators have undertaken the study of the propagation characteristics of uniform CPW, and extensive data are available in the literature [7]. However, very few models are available on CPW discontinuities, which are useful in the design of circuits such as filters [8]–[12].

Filters are important blocks in microwave circuits and are among the first few circuit elements studied in any new technology. Microstrip or stripline filters have been extensively studied and very accurate design techniques have been presented in the literature [13]. However, CPW filter elements [1], [14] have been investigated only experimentally and lack accurate equivalent circuits. Two such filter elements are the short-end and open-end series stubs, which are shown in Fig. 1(a) and (b) respectively. In this figure PP' refers to the reference planes, which are coincident with the input and output ports of the discontinuity. The short-end CPW stub was modeled by Houdart [1] as a series inductor. This model cannot predict the

resonant nature of the stub as it approaches $\lambda_g/4$ or the asymmetry of the discontinuity; therefore, it is valid only in the limit as the stub length approaches zero. The model used by Ponchak and Simons [15], an ideal short-end series stub, predicts the resonant nature of the stub but not the asymmetry. The open-end CPW stub was modeled by Houdart [1] as a series capacitor, which is also too simple to predict the resonant nature of the stub or its asymmetry and is valid only for stubs with very small lengths. Williams [14] expanded this model to a capacitive Π network and selected a reference plane which removed the element asymmetry. This improved model is difficult to incorporate into CAD programs since the reference planes are not at the plane of the discontinuity, as shown in Fig. 1. The model by Ponchak and Simons [15], an ideal open-end series stub, again cannot predict the element asymmetry.

This paper attempts, for the first time, to study theoretically and experimentally the two CPW filter elements shown in Fig. 1. The theoretical method used to study these CPW discontinuities is based on a space-domain integral equation (SDIE), which is solved using the method of moments [16]. The main difference between this approach and the one used in [3] and [10]–[12] is that the boundary conditions are applied in the space domain instead of the spectral domain. Thus, in the SDIE method the Fourier transforms of the basis functions, which are used in the method of moments, are not required, which makes it simpler to handle complicated geometries. The SDIE approach has previously been applied to study several CPW discontinuities and has shown very good accuracy, efficiency, and versatility in terms of the geometries it can solve [17], [18]. Using this method, theoretical results for the scattering parameters of the two CPW discontinuities shown in Fig. 1 are computed. Extensive experiments have been performed in the frequency range 5 to 25 GHz to validate the theoretically derived scattering parameters, and a very good agreement has been found. From the scattering parameters, lumped element equivalent circuits have been derived to model the discontinuities. The inductors and capacitors of these models have been represented by closed-form equations, as functions of the stub length, which have potential applications

Manuscript received August 30, 1990; revised January 22, 1991. This work was supported by the National Science Foundation under Contract ECS-8657951.

N. I. Dib and L. P. B. Katehi are with the Department of Electrical Engineering and Computer Science, University of Michigan, Ann Arbor, MI 48109-2122.

G. E. Ponchak and R. N. Simons are with the NASA Lewis Research Center, Cleveland, OH 44135.

IEEE Log Number 9143466.

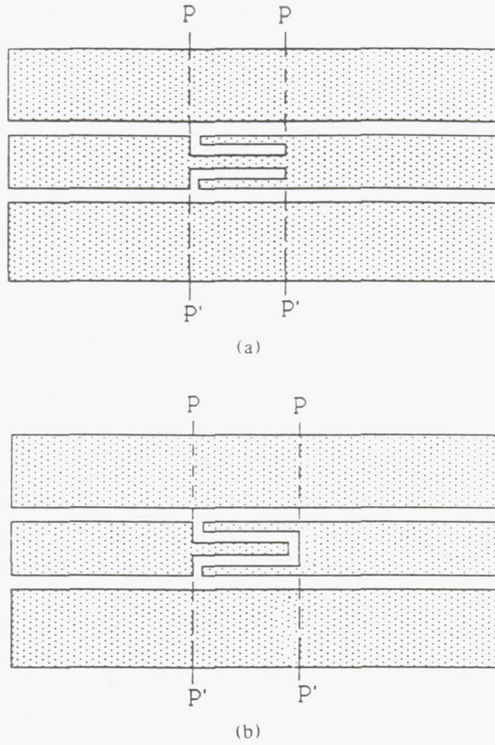


Fig. 1. Coplanar waveguide filter elements. (a) Short-end CPW series stub. (b) Open-end CPW series stub.

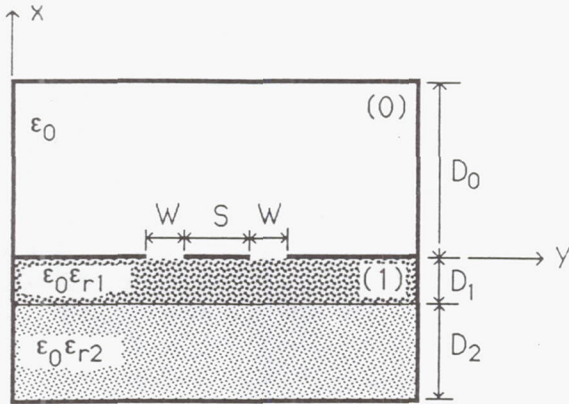


Fig. 2. A cross section of a shielded CPW.

in the design of CPW circuits. In addition, these circuits are capable of modeling the ON and OFF states of CPW p-i-n diode switches [15].

II. THEORY

A. Derivation of the Scattering Parameters

Fig. 2 shows a shielded coplanar waveguide with the cavity dimensions chosen such that the CPW fundamental mode is not affected by higher order cavity resonances. The original boundary problem is divided into two simpler ones by introducing an equivalent magnetic current, \vec{M}_s , on the slot aperture (see the Appendix). This surface

magnetic current radiates an electromagnetic field in the two waveguide regions (above and below the slots) so that the continuity of the electric field on the surface of the slots is satisfied. The remaining boundary condition to be applied is the continuity of the tangential components of the magnetic field on the surface of the slot aperture.

$$\hat{a}_y \times (\vec{H}_0 - \vec{H}_1) = \vec{J}_s \quad (1)$$

where \vec{J}_s vanishes everywhere on the plane of the slot apertures except at the position of the electric current sources exciting the CPW. $\vec{H}_{0,1}$ are the magnetic fields in the regions directly above and below the slot aperture, respectively (see Fig. 12), and can be expressed in terms of the equivalent magnetic current density, \vec{M}_s , as shown below:

$$\vec{H}_0 = \int_{S_{CPW}} \int \vec{G}_0^h(\vec{r}/\vec{r}') \cdot \vec{M}_s(\vec{r}') ds' \quad (2)$$

$$\vec{H}_1 = - \int_{S_{CPW}} \int \vec{G}_1^h(\vec{r}/\vec{r}') \cdot \vec{M}_s(\vec{r}') ds' \quad (3)$$

In (2) and (3), S_{CPW} is the surface of the slot aperture, and $\vec{G}_{0,1}^h$ is the dyadic Green's function in the two waveguide regions (see the Appendix).

In view of (2) and (3), (1) takes the form

$$\hat{a}_y \times \int_{S_{CPW}} \int [\vec{G}_0^h + \vec{G}_1^h] \cdot \vec{M}_s(\vec{r}') ds' = \vec{J}_s \quad (4)$$

To obtain the unknown magnetic current distribution, \vec{M}_s , (4) is solved by applying the method of moments [16]. First, the slot aperture is subdivided into rectangles. Then, the unknown magnetic current density is expressed as a finite double summation:

$$\begin{aligned} \vec{M}_s(\vec{r}') = & \hat{a}_y \sum_{i=1}^{N_y} \sum_{j=1}^{N_z} V_{y,ij} f_i(y') g_j(z') \\ & + \hat{a}_z \sum_{i=1}^{N_y} \sum_{j=1}^{N_z} V_{z,ij} f_j(z') g_i(y') \end{aligned} \quad (5)$$

where $\{f_i(y')g_j(z'); i=1, \dots, N_y, j=1, \dots, N_z\}$ is a family of rooftop functions [19] and $V_{y,ij}$ and $V_{z,ij}$ are the unknown coefficients for the y and z components of the magnetic current density. The subdomain basis functions (rooftop functions) for each current component have piecewise-sinusoidal variation along the longitudinal direction and constant variation along the transverse direction. Using (5), (4) can be written in the form

$$\begin{aligned} \vec{J}_s + \Delta \vec{J}_s = & \hat{a}_x \times \left\{ \sum_{i=1}^{N_y} \sum_{j=1}^{N_z} V_{y,ij} \iint [\vec{G}_0^h - \vec{G}_1^h] \right. \\ & \cdot \hat{a}_y f_i(y') g_j(z') ds' \\ & + \sum_{i=1}^{N_y} \sum_{j=1}^{N_z} V_{z,ij} \iint [\vec{G}_0^h + \vec{G}_1^h] \\ & \left. \cdot \hat{a}_z f_j(z') g_i(y') ds' \right\} \end{aligned} \quad (6)$$

where $\Delta \vec{J}_s$ represents the error introduced from the ap-

proximations made in the magnetic current distribution (eq. (5)).

Finally, Galerkin's procedure is used to minimize the error $\Delta \vec{J}_s$ resulting in the following inner products:

$$\iint (\hat{a}_x \times \Delta \vec{J}_s) \cdot \hat{a}_z f_m(y) g_n(z) ds = 0 \quad (7)$$

$$\iint (\hat{a}_x \times \Delta \vec{J}_s) \cdot \hat{a}_z f_n(z) g_m(y) ds = 0 \quad (8)$$

where f_m and g_n are weighting functions identical to the basis functions, $m = 1, \dots, N_y$ and $n = 1, \dots, N_z$. In this manner, (6) reduces into a matrix equation of the form

$$\begin{pmatrix} [Y_{yy}] & [Y_{yz}] \\ [Y_{zy}] & [Y_{zz}] \end{pmatrix} \begin{pmatrix} I_y \\ I_z \end{pmatrix} = \begin{pmatrix} I_y \\ I_z \end{pmatrix} \quad (9)$$

where $[Y_{\xi\xi}]$ ($\xi, \xi = y, z$) represent blocks of the admittance matrix whose elements are expressed in terms of multiple space integrals, involving trigonometric functions, and are given by

$$Y_{yy} = \iiint \hat{a}_y f_m(y) g_n(z) \cdot [\bar{G}_0^h + \bar{G}_1^h] \cdot \hat{a}_y f_i(y') g_j(z') dy' dz' dy dz \quad (10)$$

$$Y_{yz} = \iiint \hat{a}_y f_m(y) g_n(z) \cdot [\bar{G}_0^h + \bar{G}_1^h] \cdot \hat{a}_z f_i(z') g_j(y') dy' dz' dy dz \quad (11)$$

$$Y_{zy} = \iiint \hat{a}_z f_n(z) g_m(y) \cdot [\bar{G}_0^h + \bar{G}_1^h] \cdot \hat{a}_y f_i(y') g_j(z') dy' dz' dy dz \quad (12)$$

$$Y_{zz} = \iiint \hat{a}_z f_n(z) g_m(y) \cdot [\bar{G}_0^h + \bar{G}_1^h] \cdot \hat{a}_z f_i(z') g_j(y') dy' dz' dy dz \quad (13)$$

where $i, m = 1, \dots, N_y$ and $j, n = 1, \dots, N_z$. V_y and V_z are the subvectors of the unknown coefficients for the y and z components of the magnetic current distribution respectively and I_y and I_z are the known excitation subvectors, which are dependent on the impressed feed model.

In order to solve (9), the excitation is modeled by ideal y -directed current sources located at specific node points, as shown in Fig. 3(a), resulting in an excitation vector which has zeros everywhere except at the positions of these current sources (delta gap current generators). Although only a mathematical model, this feeding mechanism has proved to be efficient, accurate, and reliable [17], [20]. In addition, it does not introduce any unwanted numerical complications, as is the case with other excitation techniques [3], [12]. The CPW may be excited in two different ways: with the fields on the two slot apertures in phase (slotline mode) or out of phase (coplanar mode), exhibiting very different characteristics when operating in each mode. The CPW mode is excited by choosing $I'_{g1} = -I_{g1}$ and $I'_{g2} = -I_{g2}$, while the slotline mode is excited by choosing $I'_{g1} = I_{g1}$ and $I'_{g2} = I_{g2}$ (see Fig. 3(a)). However, only the CPW mode will be considered here since it tends to concentrate the fields around the slot aperture

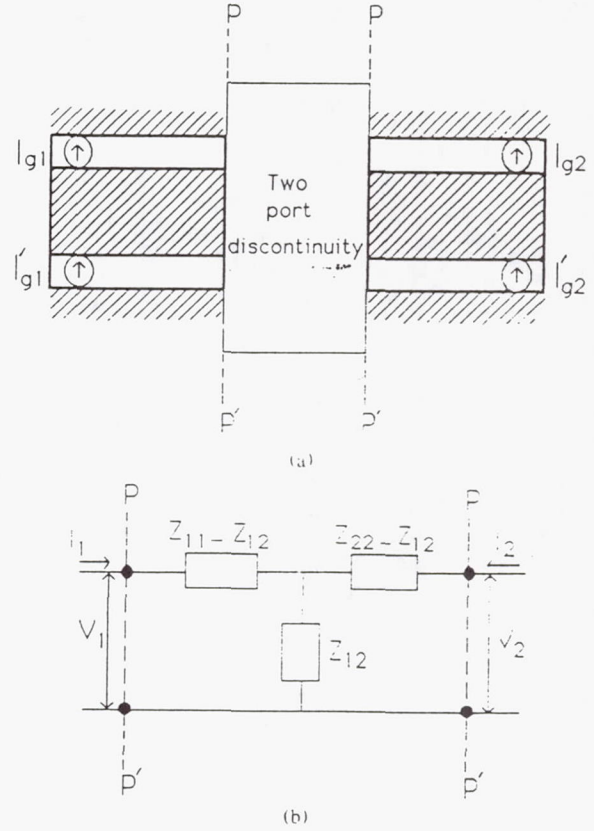


Fig. 3. (a) A general two-port CPW discontinuity with y -directed electric current sources. (b) Equivalent network representation.

(low radiation losses) and is therefore the commonly used mode in CPW circuits.

The discontinuities behave as an asymmetric two-port network with an equivalent circuit of the type shown in Fig. 3(b). For the evaluation of the network impedance matrix, three different modes of excitation are required ($I_{g1} = I_{g2} = 1, I_{g1} = -I_{g2} = 1$, and $I_{g1} = 1$ and $I_{g2} = 0$ were used). It should be noticed that the currents and voltages (I_1, I_2, V_1, V_2) shown in Fig. 3(b) are induced at the discontinuity ports as a consequence of I_{g1} and I_{g2} . The matrix equation (9) is solved to give the magnetic current distribution in the slot aperture for each mode of excitation. Then, the input impedances at ports 1 and 2 are evaluated from the positions of the minima and the maxima of the electric field standing waves in the feeding CPW lines using ideal transmission line theory. Finally, the network impedance matrix and the scattering parameters are derived using the expressions in [21].

B. Convergence Properties of Scattering Parameters

In the expressions for the Green's functions given in the Appendix, the summations over m and n are theoretically infinite. However, for the numerical solution of the matrix equation, these summations are truncated to M_{STOP} and N_{STOP} . The values of these two parameters should be chosen such that convergence of the scattering coefficient

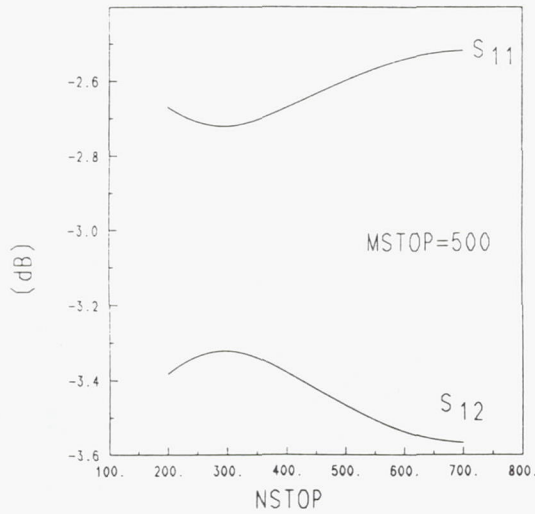
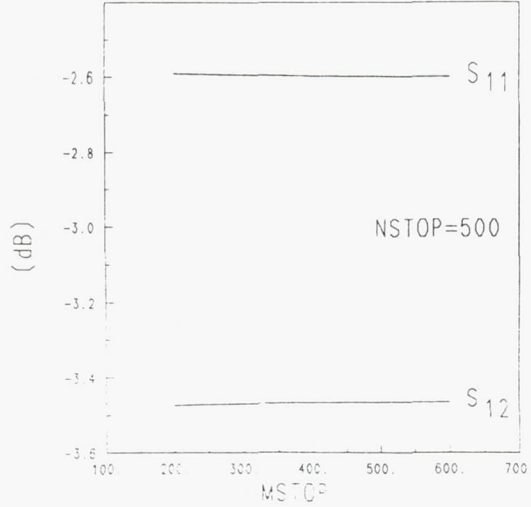


Fig. 4. Typical convergence behavior of the scattering parameters with respect to the number of modes N_{STOP} and M_{STOP} of the CPW discontinuities shown in Fig. 1.

cients is ensured. Fig. 4 shows the convergence behavior of the scattering coefficients with respect to each one of the above parameters. In (A10)–(A13), N_{STOP} and M_{STOP} correspond to the maximum values of the k_z and k_y eigenvalues considered in the summations. These eigenvalues are given by

$$k_{z \max} = \frac{(N_{STOP})\pi}{l} \quad (14)$$

$$k_{y \max} = \frac{(M_{STOP})\pi}{a}. \quad (15)$$

Since the length of the cavity, l , is larger than its width, a , the number of required k_z eigenvalues ($N_{STOP} = 700$) is much larger than the number of k_y eigenvalues ($M_{STOP} = 300$), as shown in Fig. 4.

Another critical parameter for the convergence of the results is the number of the considered basis functions N_y

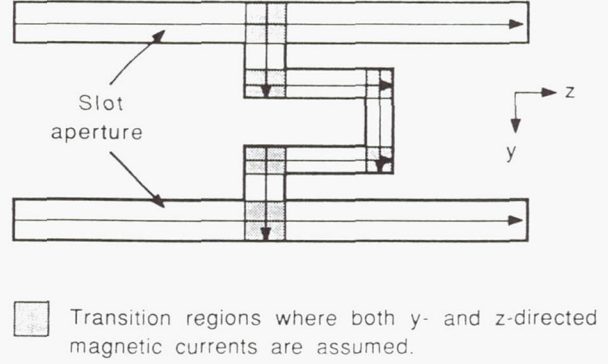


Fig. 5. The assumed magnetic current distribution in the slot aperture.

and N_z . Since the slots are assumed to be fairly thin ($W/\lambda_{CPW} < 0.1$), only a longitudinal magnetic current in the slot aperture away from the discontinuity is assumed. Furthermore, it has been found through numerical experiments that the transverse current in the feeding line around the discontinuity has a negligible effect on the current distribution and the scattering parameters. Thus, as shown in Fig. 5, both longitudinal and transverse magnetic current components are considered in the transition regions, while only the longitudinal current component is considered in the other regions. In addition, the number of basis functions N_y and N_z is chosen so that convergence of the scattering parameters of the coplanar waveguide discontinuity is achieved. The CPU time required for the evaluation of the scattering parameters depends mainly on the geometry and the electrical size of the structure. Careful consideration of the existing physical symmetries can reduce this computational time substantially.

III. RESULTS AND DISCUSSION

Using the space-domain integral equation method, the scattering parameters for the two discontinuities shown in Fig. 1 have been evaluated as a function of the stub length, L , and frequency. The theoretically derived data have been validated through extensive experiments performed in the 5 through 25 GHz frequency range. The circuits were fabricated using conventional MIC techniques on a polished alumina ($\epsilon_r = 9.9$) substrate. The plated gold thickness was $2.8 \mu\text{m}$. The RF measurements were performed on an HP 8510 ANA. A probe station with dc–26.5 GHz probes was used for providing the RF connections to the circuits. A two-tier calibration was performed: First, the system was calibrated to the 3.5 mm coaxial cable ends using coaxial open, short, load calibration standards. Then, an LRL calibration was performed to rotate the reference planes to the CPW discontinuities. The LRL calibration standards shown in Fig. 6 were fabricated on the substrate along with the circuits to eliminate errors caused by fabrication nonrepeatability. Air bridges were not needed to connect the ground planes since the discontinuities considered here are symmetric

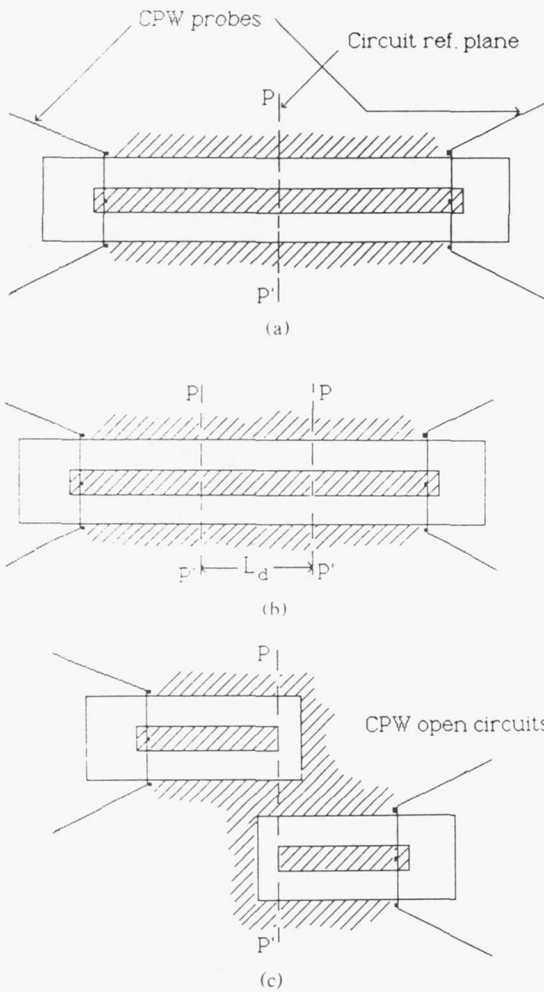


Fig. 6. CPW standards for LRL calibration: (a) Zero length thru line. (b) Delay of length L_d , where $0 \leq L_d \leq \lambda/2$. (c) Open circuit reflection standards.

about the propagation line, and the stubs are printed on the center conductor [22]. The alumina substrate was placed on a 125-mil-thick 5880 RT/Duroid ($\epsilon_r = 2.2$) substrate with copper cladding on one side to serve as the bottom ground plane.

Fig. 7 shows the scattering parameters for the short-end CPW stub of length $1500 \mu\text{m}$. It can be seen that the agreement between the theoretical and experimental results is very good. The differences are due to radiation, conductor, and dielectric losses since an unshielded structure was used in the measurements and the theoretical model did not account for losses. From the characteristic behavior of the above stub, it can be concluded that a band-stop filter can be realized by cascading several of these stubs in series.

Fig. 8 shows a comparison between theoretical and experimental values of the resonant frequency as a function of stub length. In addition, superimposed are values of the resonant frequencies for the above CPW stub operating under ideal conditions: no discontinuity effects and zero electromagnetic interactions. It can be noticed

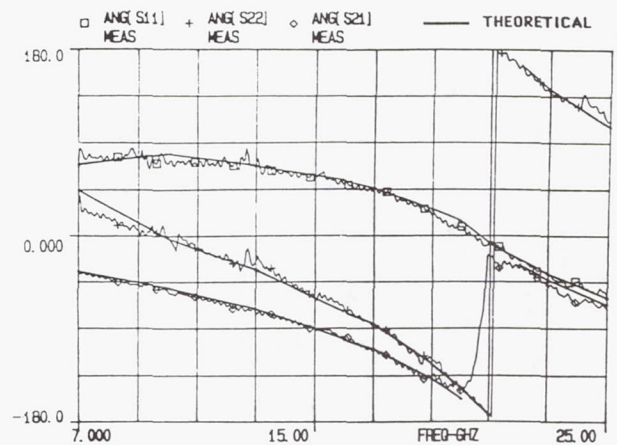
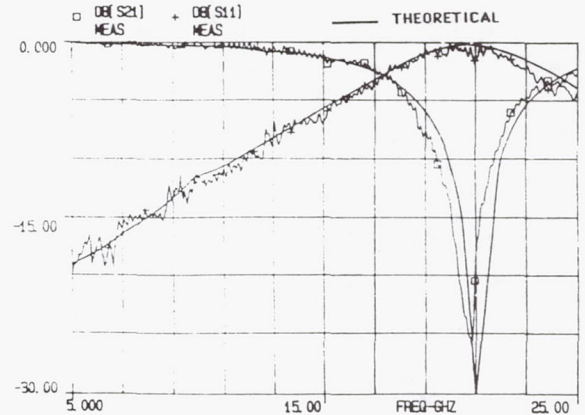
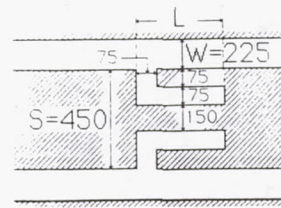


Fig. 7. Scattering parameters for the short-end CPW stub with $L = 1500 \mu\text{m}$ ($D_1 = 25 \text{ mil}$, $D_2 = 125 \text{ mil}$, $\epsilon_{r1} = 9.9$, $\epsilon_{r2} = 2.2$; other dimensions are in μm).

that the theoretically computed resonant frequencies for large stub lengths agree very well with the ones predicted for the ideal stub. This indicates that at low resonant frequencies (large stub lengths) the specific stub geometry introduces negligible discontinuity effects and is almost free of parasitic electromagnetic interactions. However, as the frequency increases, the parasitic effects become stronger, resulting in a small difference between the theoretically obtained resonant frequencies and the ones computed for the ideal stub.

Fig. 9 shows the scattering parameters for the open-end CPW stub of length $1500 \mu\text{m}$. As in the previous case, the agreement between the theoretical and experimental results is very good. Owing to its performance, such structures can be used to build band-pass filters.

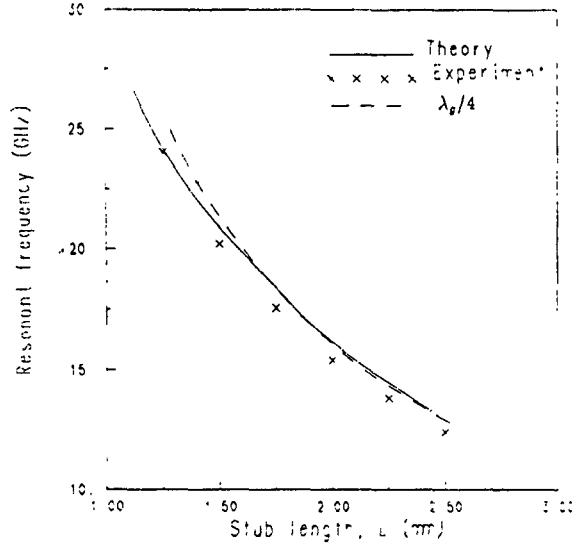


Fig. 8. Resonant frequency of the short-end CPW stub of different lengths ($D_1 = 21.5$ mil, $D_2 = 125$ mil, $\epsilon_{r1} = 9.9$, $\epsilon_{r2} = 2.2$; other dimensions are as in Fig. 10(a))

In the theoretical analysis, the CPW stubs were assumed to be inside a cavity while for the derivation of experimental data these structures were measured in open environment. The fact that there is very good agreement between theory and experiment suggests that radiation losses were very low. The loss factor of the measured stub discontinuities has been investigated and has shown a maximum value of -10 dB at the stub's resonant frequency. This indicates that it is possible to design CPW stub discontinuities with very low radiation losses.

IV. EQUIVALENT MODELS

To accurately model the short-end CPW stub over the frequency range from 5 GHz to the first band-stop resonance, the model shown in Fig. 10(b) is proposed. Using the derived scattering parameters (for Fig. 10(a)), the capacitances and inductances are evaluated using commercial optimization software. The following relations have been found, which give the values of the lumped elements in terms of the stub length, L :

$$C_s = 1.32 \times 10^{-4} L + 3.3515 \times 10^{-2} \quad (16)$$

$$C_{f1} = 1.5959 \times 10^{-2} \quad (17)$$

$$C_{f2} = 1.1249 \times 10^{-4} L + 7.522 \times 10^{-3} \quad (18)$$

$$L_1 = 2.6368 \times 10^{-4} L - 6.618 \times 10^{-3} \quad (19)$$

$$L_2 = 1.77 \times 10^{-4} L - 8.35 \times 10^{-4} \quad (20)$$

$$L_3 = 1.8656 \times 10^{-4} L - 8.34 \times 10^{-4} \quad (21)$$

where the stub length, L , is in μm , the inductances in nH, and the capacitances in pF. The above equations, which apply for the configuration shown in Fig. 10(a) only, have been verified for stub lengths, L , through 2500 μm . It should be noted that $C_{f1} = C_{f2}$ and $L_1 = L_3$ when

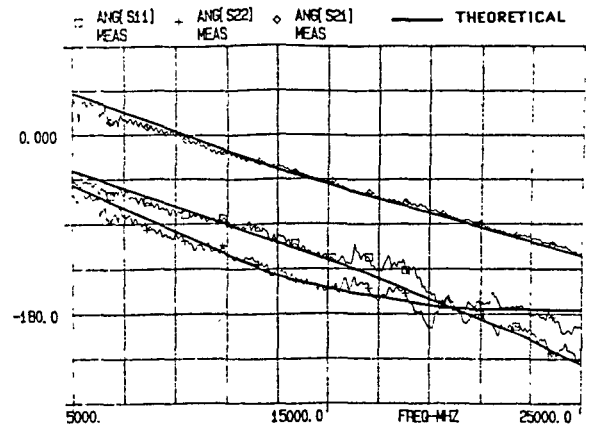
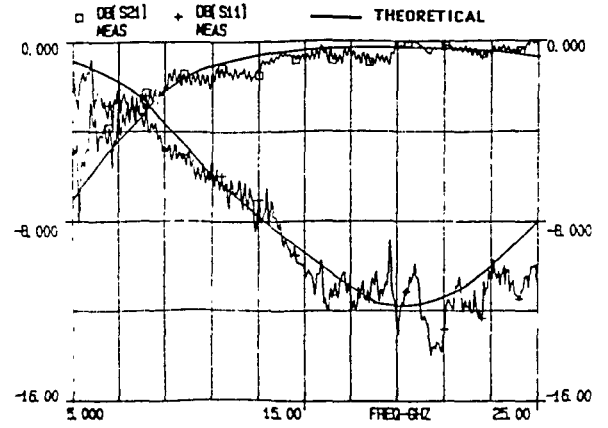
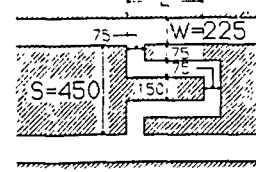


Fig. 9. Scattering parameters for the open-end CPW stub with $L = 1500 \mu\text{m}$ ($D_1 = 25$ mil, $D_2 = 125$ mil, $\epsilon_{r1} = 9.9$, $\epsilon_{r2} = 2.2$; other dimensions are in μm).

$L = 75 \mu\text{m}$ since a symmetric model is expected for a simple notch in the center conductor of the CPW.

The equivalent circuit shown in Fig. 11(b) is proposed to model the open-end CPW stub over the frequency range from 5 GHz to the first band-pass resonance. The following relations have been found, which give the values of the lumped elements in terms of the stub length, L :

$$C_s = 1.01 \times 10^{-4} L + 1.642 \times 10^{-2} \quad (22)$$

$$C_{f1} = 0.39 \times 10^{-4} L + 1.765 \times 10^{-2} \quad (23)$$

$$C_{f2} = 0.883 \times 10^{-4} L + 1.765 \times 10^{-2} \quad (24)$$

$$L_1 = 1.22 \times 10^{-4} L \quad (25)$$

$$L_2 = 1.43 \times 10^{-4} L \quad (26)$$

$$L_3 = 3.26 \times 10^{-4} L \quad (27)$$

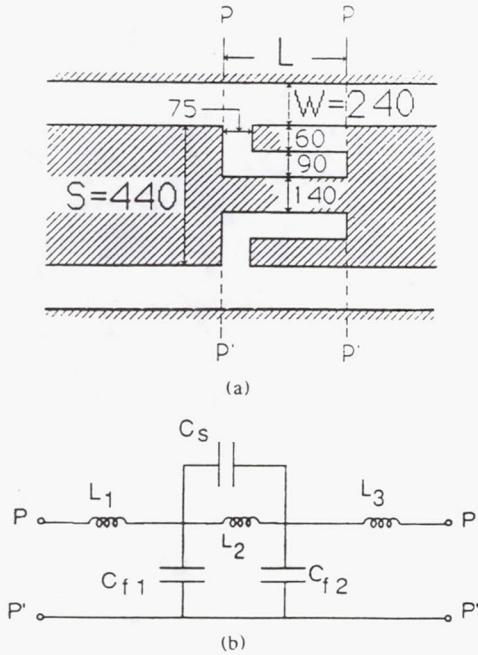


Fig. 10. Equivalent circuit for the short-end CPW stub ($D_1 = 21.5$ mil, $D_2 = 125$ mil, $\epsilon_{r1} = 9.9$, $\epsilon_{r2} = 2.2$; other dimensions are in μm).

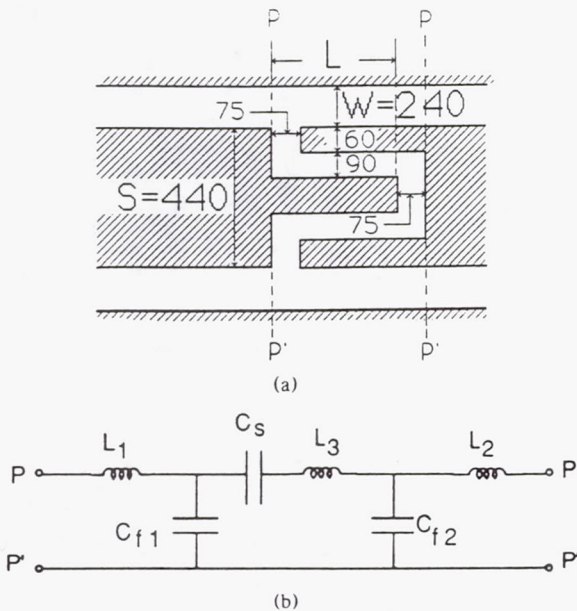


Fig. 11. Equivalent circuit for the open-end CPW stub ($D_1 = 21.5$ mil, $D_2 = 125$ mil, $\epsilon_{r1} = 9.9$, $\epsilon_{r2} = 2.2$; other dimensions are in μm).

where the stub length, L , is in μm , the inductances in nH, and the capacitances in pF. As in the previous case, the above equations, which apply for the configuration shown in Fig. 11(a) only, have been verified for stub lengths, L , through $2500 \mu\text{m}$. In the limit as L approaches zero, the inductances reduce to zero and C_{f1} becomes equal to C_{f2} , resulting in a capacitive Π network which is expected for a series gap.

The above lumped element equivalent circuits predict the response up to the first resonant frequency with a 5% accuracy. It is expected that similar linear relationships apply for a short or open-end CPW stub with any dimensions. Thus, it is enough to model two different stub lengths, from which the characteristics of other lengths can be derived.

V. CONCLUSIONS

A space-domain integral equation method solved by the method of moments in conjunction with simple transmission line theory was applied to analyze CPW circuit elements useful for band-pass and band-stop filters. An experimental setup to measure the scattering parameters of those structures has been described. The agreement between the theoretical results and the experimental data was very good; thus, the validity of both results is verified. Lumped element equivalent circuits were proposed to model the above circuit elements, and closed-form expressions to compute the values of the capacitances and inductances were given as functions of stub length.

APPENDIX

As shown in Fig. 12, a typical CPW discontinuity problem is reduced to deriving the dyadic Green's function in both regions directly above and below the slots. The transmission line theory is used to transform the surrounding layers into impedance boundaries. Using the equivalence principle, the problem is divided into four subproblems (as shown in Fig. 12), where the fields in both regions due to magnetic currents in the y and z directions have to be obtained. After this has been accomplished, the continuity of the tangential fields at the interface is used to arrive at the integral equation. The main steps in the derivation of the fields arising from an infinitesimal z -directed magnetic current inside a cavity (with impedance boundary top side) will be presented here (see Fig. 13).

In the derivations, the following vector potentials for the LSM and LSE modes are assumed:

$$A = \hat{a}_x \psi \quad F = \hat{a}_x \phi. \quad (\text{A1})$$

By using Maxwell's equations along with

$$H = \frac{1}{\mu} \nabla \times A \quad (\text{A2})$$

$$E = -\frac{1}{\epsilon} \nabla \times F \quad (\text{A3})$$

one can obtain the field components in terms of the magnetic and electric vector potentials.

The differential equations for A and F are solved in view of the pertinent boundary conditions to give the unknown field components. The boundary conditions considered for the solution of this problem are listed below (see Fig. 13, where the magnetic current dipole is raised

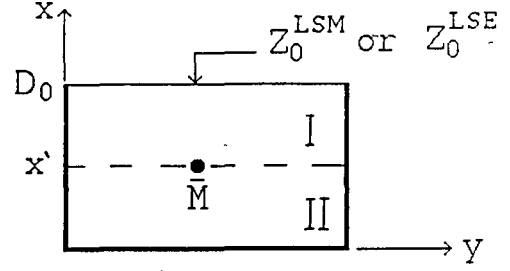
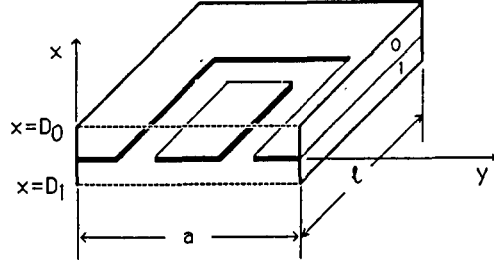


Fig. 13. A z -directed magnetic dipole inside a cavity with an impedance boundary top side.

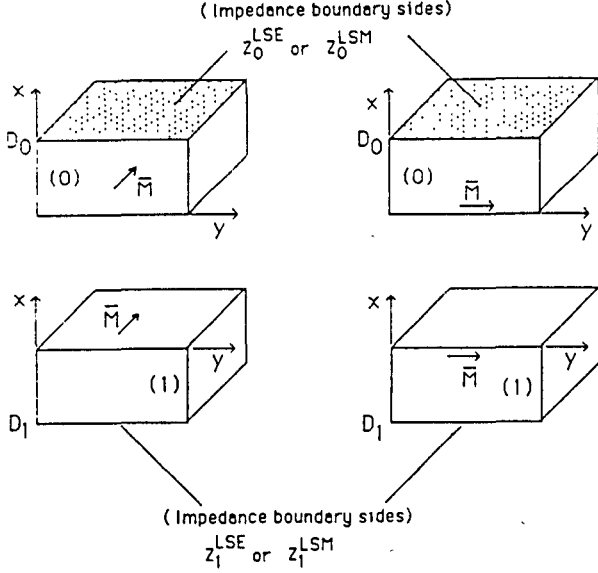


Fig. 12. A typical one-port CPW discontinuity where four subproblems are obtained using the equivalence principle. (All the sides excluding the impedance boundaries are assumed perfectly conducting.)

to simplify the application of the boundary conditions):

$$E_z^I = E_z^{II} \quad \text{at } x = x' \quad (\text{A4})$$

$$H_y^I = H_y^{II} \quad \text{at } x = x' \quad (\text{A5})$$

$$H_z^I = H_z^{II} \quad \text{at } x = x' \quad (\text{A6})$$

$$\left(\frac{E_y^I}{H_z^I} \right)^{\text{LSE}} = Z_0^{\text{LSE}} \quad \text{at } x = D_0 \quad (\text{A7})$$

$$\left(\frac{E_y^I}{H_z^I} \right)^{\text{LSM}} = Z_0^{\text{LSM}} \quad \text{at } x = D_0 \quad (\text{A8})$$

$$E_y^{II} - E_y^I = \delta(x - x')\delta(y - y')\delta(z - z'). \quad (\text{A9})$$

In (A4)–(A9), D_0 is the thickness of the layer directly above the slot apertures. Z_0^{LSE} and Z_0^{LSM} are the LSE and LSM impedances seen at the interface $x = D_0$. For the structures considered here (Fig. 3), $Z_0^{\text{LSE}} = Z_0^{\text{LSM}} = 0$ since perfect conductors are assumed. Solving (A4)–(A9), the fields in the region directly above the slot aperture caused by a z -directed magnetic dipole are obtained. In the same manner the fields due to a y -directed magnetic dipole can be derived.

The components of the dyadic Green's function for the coplanar waveguide problem are given by the following expressions:

$$G_{xx}^{(0)}(\bar{r}/\bar{r}') = \sum_{m=0}^{M_{\text{STOP}}} \sum_{n=0}^{N_{\text{STOP}}} \frac{2e_n}{al} \frac{1}{k_{x_0}^2 - k_0^2} [k_y^2 P_0 + k_z^2 Q_0] \cdot \sin(k_x y') \cos(k_z z') \sin(k_y y) \cos(k_z z) \quad (\text{A10})$$

$$G_{zy}^{(0)}(\bar{r}/\bar{r}') = \sum_{m=0}^{M_{\text{STOP}}} \sum_{n=0}^{N_{\text{STOP}}} \frac{2e_n}{al} \frac{k_y k_z}{k_{x_0}^2 - k_0^2} [P_0 - Q_0] \cdot \sin(k_x y') \cos(k_z z') \cos(k_y y) \sin(k_z z) \quad (\text{A11})$$

$$G_{yz}^{(0)}(\bar{r}/\bar{r}') = \sum_{m=0}^{M_{\text{STOP}}} \sum_{n=0}^{N_{\text{STOP}}} \frac{2e_n}{al} \frac{k_y k_z}{k_{x_0}^2 - k_0^2} [P_0 - Q_0] \cdot \cos(k_x y') \sin(k_z z') \sin(k_y y) \cos(k_z z) \quad (\text{A12})$$

$$G_{zz}^{(0)}(\bar{r}/\bar{r}') = \sum_{m=0}^{M_{\text{STOP}}} \sum_{n=0}^{N_{\text{STOP}}} \frac{2e_m}{al} \frac{1}{k_{x_0}^2 - k_0^2} [k_z^2 P_0 + k_y^2 Q_0] \cdot \cos(k_x y') \sin(k_z z') \cos(k_y y) \sin(k_z z) \quad (\text{A13})$$

where

$$P_0 = \left(\frac{k_{x_0}}{\omega \mu_0} \right) \frac{\omega \mu_0 + j k_{x_0} Z_0^{\text{LSE}} \tan(k_{x_0} D_0)}{k_{x_0} Z_0^{\text{LSE}} + j \omega \mu_0 \tan(k_{x_0} D_0)} \quad (\text{A14})$$

$$Q_0 = \left(\frac{\omega \epsilon_0}{k_{x_0}} \right) \frac{k_{x_0} + j \omega \epsilon_0 Z_0^{\text{LSM}} \tan(k_{x_0} D_0)}{\omega \epsilon_0 Z_0^{\text{LSM}} + j k_{x_0} \tan(k_{x_0} D_0)} \quad (\text{A15})$$

$$e_n = 1, \quad n = 0$$

$$= 2, \quad n \neq 0 \quad (\text{A16})$$

$$e_m = 1, \quad m = 0$$

$$= 2, \quad m \neq 0 \quad (\text{A17})$$

$$k_y = \frac{m\pi}{a} \quad (\text{A18})$$

$$k_z = \frac{n\pi}{l} \quad (\text{A19})$$

$$k_0^2 = \omega^2 \mu_0 \epsilon_0 \quad (\text{A20})$$

$$k_0^2 = k_{x_0}^2 - k_y^2 + k_z^2. \quad (\text{A21})$$

In the above expressions, a and l are the width and length of the cavity, respectively, and $G_{ij}^{(0)}$ denotes the magnetic field $H_i^{(0)}$ radiated at $x = 0$ by an infinitesimal magnetic dipole M_j located at $x' = 0$ ($i, j = y, z$).

The components of \bar{G}_1^h are essentially the same as in (A10)–(A21) with the following changes:

$$\begin{aligned} Z_0^{\text{LSE}} &\rightarrow Z_1^{\text{LSE}} \\ Z_0^{\text{LSM}} &\rightarrow Z_1^{\text{LSM}} \\ D_0 &\rightarrow D_1 \\ e_n \cdot e_m &\rightarrow e_n \cdot e_m \\ k_0 &\rightarrow k_1 \\ \mu_1 \cdot \epsilon_0 &\rightarrow \mu_1 \cdot \epsilon_1 \end{aligned} \quad (\text{A22})$$

where Z_1^{LSE} and Z_1^{LSM} are the LSE and LSM impedances seen at the interface $x = D_1$.

REFERENCES

- [1] M. Houdart, "Coplanar lines: Application to broadband microwave integrated circuits," in *Proc. 6th European Microwave Conf.* (Rome), 1976, pp. 49–53.
- [2] R. A. Pucel, "Design considerations for monolithic microwave circuits," *IEEE Trans. Microwave Theory Tech.*, vol. MTT-29, pp. 513–534, June 1981.
- [3] R. W. Jackson, "Considerations in the use of coplanar waveguide for millimeter wave integrated circuits," *IEEE Trans. Microwave Theory Tech.*, vol. MTT-34, pp. 1450–1456, Dec. 1986.
- [4] M. Riazat, E. Par, G. Zdasiuk, S. Bandy, and M. Glenn, "Monolithic millimeter wave CPW circuits," in *1989 IEEE MTT-S Int. Microwave Symp. Dig.* (Long Beach, CA), pp. 525–528.
- [5] T. Hirota, Y. Tarusawa, and H. Ogawa, "Uniplanar MMIC hybrids — A Proposed new MMIC structure," *IEEE Trans. Microwave Theory Tech.*, vol. MTT-35, pp. 576–581, June 1987.
- [6] M. Riazat, R. Majidi-Ahi, and I. Feng, "Propagation modes and dispersion characteristics of coplanar waveguides," *IEEE Trans. Microwave Theory Tech.*, vol. 38, pp. 245–251, Mar. 1990.
- [7] K. C. Gupta, R. Garg, and I. J. Bahl, *Microstrip Lines and Slotlines*. Dedham, MA: Artech House, 1979.
- [8] R. N. Simons and G. E. Ponchak, "Modeling of some coplanar waveguide discontinuities," *IEEE Trans. Microwave Theory Tech.*, vol. 36, pp. 1796–1803, Dec. 1988.
- [9] N. H. Koster, S. Koblowski, R. Bertenburg, S. Heinen, and I. Wolff, "Investigation of air bridges used for MMICs in CPW technique," in *Proc. 19th European Microwave Conf.* (London), Sept. 1989, pp. 666–671.
- [10] G. Kibuuka, R. Bertenburg, M. Naghed and I. Wolff, "Coplanar lumped elements and their application in filters on ceramic and gallium arsenide substrates," in *Proc. 19th European Microwave Conf.* (London), Sept. 1989, pp. 656–661.
- [11] C. W. Kuo and T. Itoh, "Characterization of the coplanar waveguide step discontinuity using the transverse resonance method," in *Proc. 19th European Microwave Conf.* (London), Sept. 1989, pp. 662–665.
- [12] R. W. Jackson, "Mode conversion at discontinuities in finite-width conductor-backed coplanar waveguide," *IEEE Trans. Microwave Theory Tech.*, vol. 37, pp. 1582–1589, Oct. 1989.
- [13] G. Matthaei, L. Young and E. Jones, *Microwave Filters, Impedance-Matching Networks, and Coupling Structures*. Dedham, MA: Artech House, 1980.
- [14] D. F. Williams and S. E. Schwarz, "Design and performance of coplanar waveguide band-pass filters," *IEEE Trans. Microwave Theory Tech.*, vol. MTT-31, pp. 558–566, July 1983.
- [15] G. E. Ponchak and R. N. Simons, "Channelized coplanar waveguide PIN-diode switches," in *Proc. 19th European Microwave Conf.* (London), 1989, pp. 489–494.
- [16] R. F. Harrington, *Field Computation by Moment Methods*. New York: Macmillan, 1968.
- [17] N. I. Dib and P. B. Katehi, "Modeling of shielded CPW discontinuities using the space domain integral equation method (SDIE)," *J. Electromagn. Waves and Appl.*, to be published.
- [18] N. I. Dib, P. B. Katehi, G. E. Ponchak, and R. N. Simons, "Coplanar waveguide discontinuities for p-i-n diode switches and filter applications," in *1990 IEEE MTT-S Int. Microwave Symp. Dig.*, May 1990, pp. 399–402.
- [19] A. W. Glisson and D. R. Wilton, "Simple and efficient numerical methods for problems of electromagnetic radiation and scattering from surfaces," *IEEE Trans. Antennas Propagat.*, vol. AP-28, pp. 593–603, Sept. 1980.
- [20] W. P. Harokopus and P. B. Katehi, "Characterization of microstrip discontinuities on multilayer dielectric substrates including radiation losses," *IEEE Trans. Microwave Theory Tech.*, vol. 37, pp. 2058–2065, Dec. 1989.
- [21] P. B. Katehi, "A generalized method for the evaluation of mutual coupling in microstrip arrays," *IEEE Trans. Antennas Propagat.*, vol. AP-35, pp. 125–133, Feb. 1987.
- [22] R. E. Stegens, "Coplanar waveguide FET amplifiers for satellite communications systems," *Comsat Tech. Rev.*, vol. 9, pp. 255–267, spring 1979.

*SECTION
TWO*

*DEVELOPMENT OF
HETEROJUNCTION
MATERIALS AND DEVICES*

ELLIPSOMETRIC STUDY OF InGaAs MODFET MATERIAL

S. A. ALTEROVITZ*, R. E. SIEG**, H. D. YAO†, P. G. SNYDER†, J. A. WOOLLAM†,
J. PAMULAPATI‡, P.K. BHATTACHARYA‡

*NASA-Lewis Research Center, Cleveland, Ohio 44135

**Undergraduate Student Intern at NASA-Lewis Research Center from Cleveland State University, Dept. of Electrical Engineering, Cleveland, Ohio 44115

†University of Nebraska, Department of Electrical Engineering, Lincoln, NE 68588

‡University of Michigan, Department of Electrical Engineering and Computer Science, Ann Arbor, MI 48109

ABSTRACT

In_xGa_{1-x}As based MODFET (modulation doped field effect transistor) material was grown by MBE (molecular beam epitaxy) on semi-insulating InP substrates. Several structures were made, including lattice matched and strained layer InGaAs. All structures also included several layers of In_{0.52}Al_{0.48}As. Variable angle spectroscopic ellipsometry (VASE) was used to characterize the structures. The experimental data, together with the calibration function for the constituent materials, were analyzed to yield the thickness of all the layers of the MODFET structure. Results of the ellipsometrically determined thicknesses compare very well with the RHEED (reflection high energy electron diffraction) in situ thickness measurements.

INTRODUCTION

Recently In_xGa_{1-x}As became the material of choice for MODFET devices, both on InP [1] and GaAs [2] substrates. The In_xGa_{1-x}As serves as the conduction channel, mainly due to its high electron mobility and saturated velocity. The most commonly studied indium concentration is X=0.53, the InP lattice matched composition. However, strained layer structures are now available, both on InP and GaAs. The heterostructure material used for MODFET fabrication is grown mostly by MBE. In this growth method, the thickness is measured in situ using the RHEED technique. In this paper we will describe the application of the variable angle spectroscopic ellipsometry technique to the characterization of MBE grown In_xGa_{1-x}As based MODFET structures. This non-destructive technique can estimate not only the thicknesses of all the layers within the optical penetration depth, but also the quality of the interface and possibly the indium concentration. The capabilities of VASE for complete MODFET characterization were demonstrated on the MBE grown AlGaAs/GaAs structures [3]. Detailed interface work on InGaAs/InP was performed on MOCVD (metal-organic chemical vapor deposition) grown material [4]. This paper will concentrate on MBE grown structures. In this growth technique, InP cannot be grown and it is replaced by In_{0.52}Ga_{0.48}As, which is lattice matched to InP and provides the high band gap donor layer of the MODFET.

EXPERIMENTAL

The MODFET structures studied here were grown by MBE on semi-insulating InP substrates, with continuous RHEED monitoring. The structures studied here

are shown in Fig. 1(a). Starting from the bottom, these structures nominally contain the following layers: a superlattice (S.L.) buffer made of 30 period $\text{In}_{0.53}\text{Ga}_{0.47}\text{As}/\text{In}_{0.52}\text{Al}_{0.48}\text{As}$, a 4000 Å isolation layer of $\text{In}_{0.52}\text{Al}_{0.48}\text{As}$, a complex conduction channel made of 400 Å undoped $\text{In}_{0.53}\text{Ga}_{0.47}\text{As}$, and a layer of thickness d of undoped $\text{In}_x\text{Ga}_{1-x}\text{As}$ with $d=150$ Å for $X=0.53$ and 0.65 and $d=100$ Å for $X=0.70$, a 50 Å $\text{In}_{0.52}\text{Al}_{0.48}\text{As}$ spacer layer, a 350 Å $\text{In}_{0.52}\text{Al}_{0.48}\text{As}$ donor layer with only 150 Å of doped material, and a 100 Å doped cap layer of $\text{In}_{0.53}\text{Ga}_{0.47}\text{As}$ for contacts. Ellipsometry cannot differentiate between doped and undoped material, but it will be sensitive to a surface oxide layer. Thus, the nominal structure for ellipsometric purposes will be different from the MBE nominal structure. For example, the nominal structure for ellipsometric purposes for the $X=0.53$ material is given in Fig. 1(b), on the left side of the graph. The 4000 Å $\text{In}_{0.52}\text{Al}_{0.48}\text{As}$ layer is considered the substrate for ellipsometric purposes, as the optical penetration length in most of the experimental range is smaller than the thickness shown in Fig. 1(b).

Actual Structure			Nominal		Ellips.
100 Å	n ⁺	$\text{In}_{0.53}\text{Ga}_{0.47}\text{As}$	t1	0 Å Oxide	47 ± 0.8 Å
200 Å	i	$\text{In}_{0.52}\text{Al}_{0.48}\text{As}$	t2	100 Å $\text{In}_{0.53}\text{Ga}_{0.47}\text{As}$	49 ± 1.4 Å
150 Å	n ⁺	$\text{In}_{0.53}\text{Al}_{0.48}\text{As}$ 5×10^{18}	t3	400 Å $\text{In}_{0.52}\text{Al}_{0.48}\text{As}$	424 ± 4 Å
50 Å	i	$\text{In}_{0.52}\text{Al}_{0.48}\text{As}$	t4	550 Å $\text{In}_{0.53}\text{Ga}_{0.47}\text{As}$	553 ± 6 Å
d	i	$\text{In}_x\text{Ga}_{1-x}\text{As}$		4000 Å $\text{In}_{0.52}\text{Al}_{0.48}\text{As}$	—
400 Å	i	$\text{In}_{0.53}\text{Ga}_{0.47}\text{As}$			
4000 Å	i	$\text{In}_{0.52}\text{Al}_{0.48}\text{As}$			
30 prd	30 Å/30 Å	S.L. $\text{InGaAs}/\text{InAlAs}$			
		SI InP Substrate			

Figure 1.—(a) Actual structure grown by MBE. (b) Nominal structure used for ellipsometry and the result obtained from the experiment.

The ellipsometric technique was described previously [3,5] and will not be repeated. In this study, we use a mean square error (M.S.E.) criterion based on $\tan \psi$ and $\cos \Delta$ fits of experimental data to model calculations. The variables of the fit were the thicknesses, t_i ($i=1-4$ in Fig. 1(b)), of the different layers in the structure.

Ellipsometric calibration functions (i.e. the dielectric functions) for the constituent material were taken from the following sources: $\text{In}_{0.52}\text{Al}_{0.48}\text{As}$ from previous measurements at NASA-Lewis [6], $\text{In}_{0.53}\text{Ga}_{0.47}\text{As}$ from [7], $\text{In}_x\text{Ga}_{1-x}\text{As}$ as a function of X from [8] and the oxide from [9]. The results obtained in reference [8] are for thermodynamically stable material and thus may have to be modified for application to a strained configuration. The oxide results [9] are for GaAs oxide and they may give an erroneous thickness for the oxide.

Results for the lattice matched structure are shown in Figs. 1(b) and 2 together with the 90% confidence limits. An excellent fit was obtained between the ψ and Δ values measured experimentally and the values calculated from a model that uses the thickness parameters given in Fig. 1(b), right hand side. There is also a good fit between the nominal and experimental layer thicknesses. The M.S.E. of the fit for experimental data in the range 3000-6000 Å was 2.3×10^{-4} . A marked deterioration in the M.S.E occurred when the fitting range was extended to cover our full experimental range of 3000-8000 Å, probably due to the fact that the optical penetration length becomes comparable to total thickness of our model, as shown in Fig. 1(a). We also note that the fit is not perfect for the ψ fits in the lower wavelength region (i.e. below ~ 3500 Å). This denotes a poor

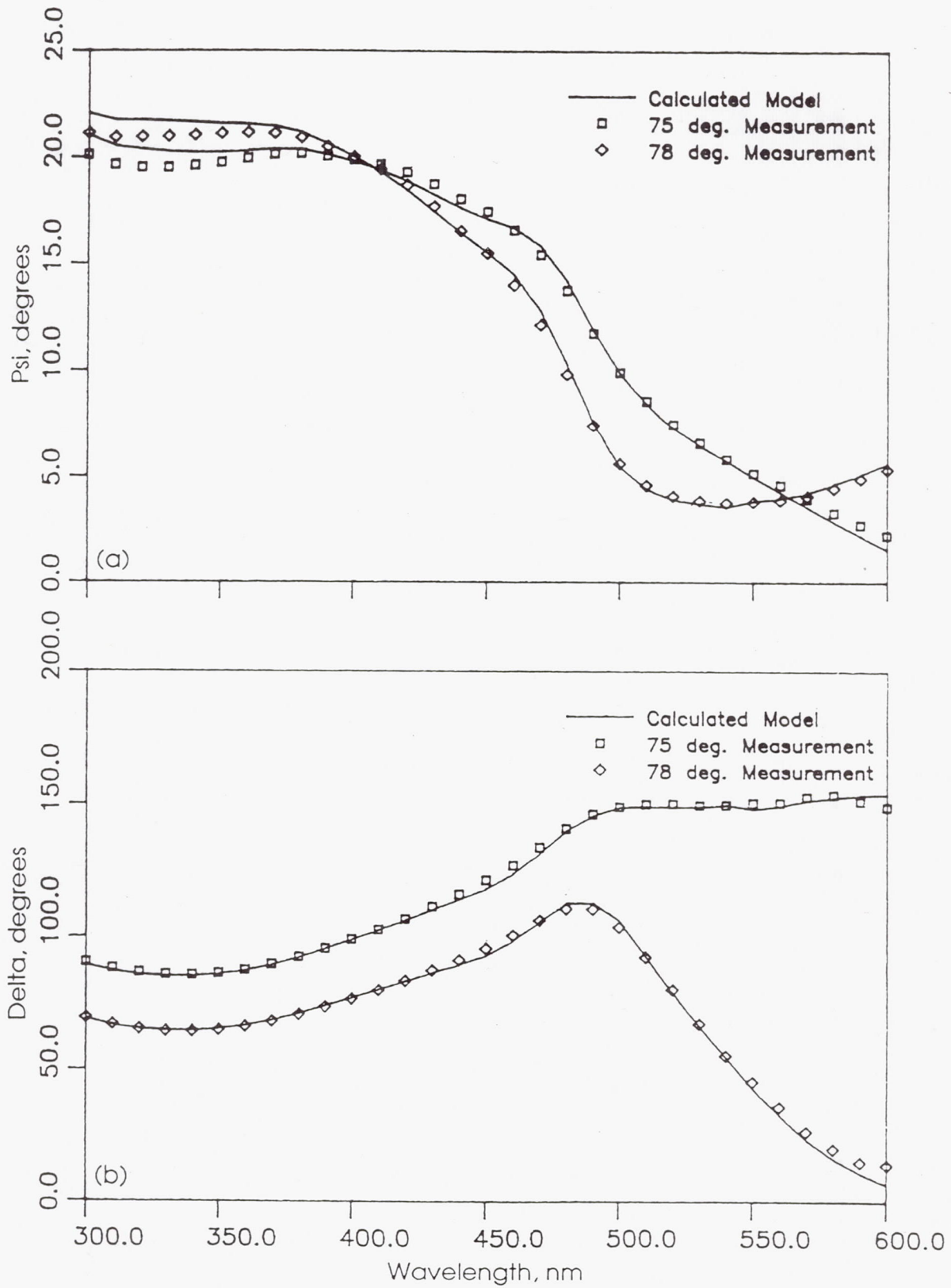


Figure 2.—Experimental and model calculation results for (a) Psi and (b) Delta for $\text{In}_{0.53}\text{Ga}_{0.47}\text{As}$ MODFET material at two angles of incidence.

fit for the surface layers. This fact can also be deduced from the anomalous thickness of the oxide layer, which is much larger than normal for compound semiconductors [3]. We believe that the approximation used here for the oxide is not very accurate. Another problem in the fit of the surface layers is the difference in the thickness of the $\text{In}_{0.53}\text{Ga}_{0.47}\text{As}$ cap layer estimated by ellipsometry as compared to the nominal thickness. This difference indicates that this layer is probably not a perfectly smooth, homogeneous, stoichiometric layer, and therefore our model is also not perfect.

Results for the samples with strained $\text{In}_x\text{Ga}_{1-x}\text{As}$ layers show only a slight dependence of the measured ψ and Δ with the indium concentration x . Thus, it is very hard to obtain the effects of strain on the dielectric function of $\text{In}_x\text{Ga}_{1-x}\text{As}$ from these MODFET structures.

REFERENCES

- ¹G. I. Ng, W. P. Hong, D. Pavlidis, M. Tutt, and P. K. Bhattacharya, IEEE Electron Device Lett. 9, 439 (1988).
- ²W. T. Masselink, J. Klem, T. Henderson, A. Ketterson, J. S. Gedjmin, H. Morkoc, and K. R. Gleason, IEDM, 755 (1985).
- ³P. G. Snyder, M. C. Rost, G. H. Bu-Abbud, J. A. Woollam, and S. A. Alterovitz, J. Appl. Phys. 60, 3293 (1986).
- ⁴M. Erman, J. P. Andre, and J. LeBris, J. Appl. Phys. 59, 2019 (1986).
- ⁵S. A. Alterovitz, R. M. Sieg, N. S. Shoemaker, and J. J. Pouch, Mat. Res. Soc. Symp. Proc. 152, 21 (1989).
- ⁶S. A. Alterovitz, R. M. Sieg, J. Pamulapati, and P. K. Bhattacharya, to be published.
- ⁷D. E. Aspnes, Private Communication.
- ⁸S. A. Alterovitz, R. M. Sieg, H. D. Yao, P. G. Snyder, and J. A. Woollam, J. Pamulapati, and P. K. Bhattacharya, ICEM-90 Proceedings, in print.
- ⁹D. E. Aspnes, G. P. Schwartz, G. J. Gualtieri, A. A. Studna, and B. Schwartz, J. Electrochem. Soc. 128, 590 (1981).

Low-Temperature Microwave Characteristics of Pseudomorphic $\text{In}_x\text{Ga}_{1-x}\text{As}/\text{In}_{0.52}\text{Al}_{0.48}\text{As}$ Modulation-Doped Field-Effect Transistors

R. LAI, PALLAB K. BHATTACHARYA, FELLOW, IEEE, S. A. ALTEROVITZ, A. N. DOWNEY, AND C. CHOREY

Abstract—Low-temperature microwave measurements of both lattice-matched and pseudomorphic $\text{In}_x\text{Ga}_{1-x}\text{As}/\text{In}_{0.52}\text{Al}_{0.48}\text{As}$ ($x = 0.53, 0.60,$ and 0.70) channel MODFET's on InP substrates have been carried out in a cryogenic measurement system. The measurements were done in the temperature range of 77 to 300 K and in the frequency range of 0.5 to 11.0 GHz at different bias conditions. The cutoff frequency (f_T) for the $\text{In}_x\text{Ga}_{1-x}\text{As}/\text{In}_{0.52}\text{Al}_{0.48}\text{As}$ MODFET's improved from 22 to 29 GHz, 29 to 38 GHz, and 39 to 51 GHz, for $x = 0.53, 0.60,$ and 0.70 , respectively, as the temperature was lowered from 300 to 77 K, which is approximately a 31% increase at each composition, and no degradations were observed in device performance. These results indicate an excellent potential of the pseudomorphic devices at low temperatures.

CRYOGENIC operation of modulation-doped field-effect transistors (MODFET's) has shown improved gain characteristics and lower noise figures compared to operation at room temperature. These have been demonstrated recently in low-noise receivers and amplifiers [1], [2]. Other potential benefits such as greater reliability and integration with high-temperature superconductors have further increased the interest in MODFET operation at cryogenic temperatures [3]. Pseudomorphic $\text{In}_x\text{Ga}_{1-x}\text{As}/\text{In}_{0.52}\text{Al}_{0.48}\text{As}$ channel MODFET's have demonstrated a performance superior to lattice-matched ones principally because of a higher band offset and improved channel transport characteristics [4], [5]. In this letter, we report on results from cryogenic (77–300 K) microwave measurements on pseudomorphic $\text{In}_x\text{Ga}_{1-x}\text{As}/\text{In}_{0.52}\text{Al}_{0.48}\text{As}$ MODFET's ($0.53 \leq x \leq 0.70$).

The MODFET structures were grown by molecular beam epitaxy (MBE) on semi-insulating InP substrates at $\sim 520^\circ\text{C}$ at a rate of $1 \mu\text{m}/\text{h}$. Standard photolithography was used to fabricate the devices. The layer structures for the devices are shown in Fig. 1. As an example of the heterostructure quality, the $\text{In}_{0.70}\text{Ga}_{0.30}\text{As}/\text{In}_{0.52}\text{Al}_{0.48}\text{As}$ MODFET exhibited a Hall mobility of about 11 900 and 53 000 $\text{cm}^2/\text{V} \cdot \text{s}$ at

100 Å	$\text{In}_{0.53}\text{Ga}_{0.47}\text{As}$	$n^+ 5 \times 10^{18} \text{ cm}^{-3}$
200 Å	$\text{In}_{0.52}\text{Al}_{0.48}\text{As}$	
150 Å	$\text{In}_{0.52}\text{Al}_{0.48}\text{As}$	$n^+ 5 \times 10^{18} \text{ cm}^{-3}$
50 Å	$\text{In}_{0.52}\text{Al}_{0.48}\text{As}$	
100-150 Å	$\text{In}_x\text{Ga}_{1-x}\text{As}$	$0.53 \leq x \leq 0.70$
400 Å	$\text{In}_{0.53}\text{Ga}_{0.47}\text{As}$	
3000 Å	$\text{In}_{0.52}\text{Al}_{0.48}\text{As}$	
1800 Å	30 Å $\text{In}_{0.53}\text{Ga}_{0.47}\text{As}/$ 30 Å $\text{In}_{0.52}\text{Al}_{0.48}\text{As}$ SL	
	SI InP Substrate	

Fig. 1. Layer schematic of pseudomorphic $\text{In}_x\text{Ga}_{1-x}\text{As}/\text{In}_{0.52}\text{Al}_{0.48}\text{As}$ ($x = 0.53, 0.60,$ and 0.70) channel MODFET's on InP substrates.

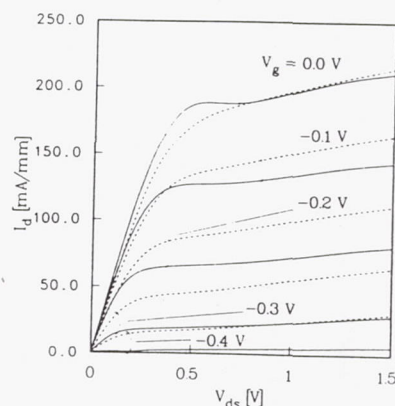


Fig. 2. I_d versus V_{ds} characteristics for a pseudomorphic $\text{In}_{0.70}\text{Ga}_{0.30}\text{As}/\text{In}_{0.52}\text{Al}_{0.48}\text{As}$ channel MODFET at 77 K (solid lines) and 300 K (dashed lines).

300 and 77 K, respectively. Gate stripes with a gate length of $1.0 \mu\text{m}$ and a gate width of $100 \mu\text{m}$ were formed by evaporating $500\text{-}\text{\AA}/3000\text{-}\text{\AA}$ Ti/Au. DC measurements at 300 and 77 K (shown in Fig. 2) of an $\text{In}_{0.70}\text{Ga}_{0.30}\text{As}/\text{In}_{0.52}\text{Al}_{0.48}\text{As}$ MODFET show an increase in transconductance from 510 mS/mm at 300 K to 680 mS/mm at 77 K and a decrease in output conductance from 40 mS/mm at 300 K to 20 mS/mm at 77 K measured at $V_{ds} = 1.5 \text{ V}$ and $V_{gs} = 0$

Manuscript received July 5, 1990; revised September 12, 1990. This work was supported by the National Aeronautic and Space Administration (Lewis Research Center) under Grant NAG-3-988 and by the Army Research Office (URI Program) under Contract DAAL03-87-K0007.

R. Lai and P. K. Bhattacharya are with the Department of Electrical Engineering and Computer Science, University of Michigan, Ann Arbor, MI 48109-2212.

S. A. Alterovitz, A. N. Downey, and C. Chorey are with the Solid State Technology, Branch, NASA Lewis Research Center, Cleveland, OH 44135. IEEE Log Number 9040699.

V. The measured gate leakage current also decreased from $9 \mu\text{A}$ at 300 K to less than $1 \mu\text{A}$ at 77 K.

For cryogenic microwave characterization, the devices were mounted and bonded to coplanar chip carriers. The devices were measured in a coplanar waveguide test fixture (Design Techniques) operating in the frequency range of 0.5–11.0 GHz. A spring loading capability was added to the test fixture to ensure repeatable contacts between the device carrier and the coaxial connectors. The cryogenic system included a helium closed-cycle refrigerator, a temperature controller, a Si diode thermometer, and the test fixture attached to the refrigerator cold finger. The system is capable of achieving and stabilizing temperatures down to 77 K. The microwave measurements were done using an HP8510B automatic network analyzer. The measurement setup was calibrated at room temperature using a set of open, short, and through standards. Shifts in the reference plane caused by the lowering of temperature (most likely due to the contraction of the cables, connectors, and the coplanar lines) were accounted for by cooling a short-circuit standard to the desired temperatures.

The microwave characteristics of each device were measured at 300, 200, 120, and 77 K from 0.5 to 11.0 GHz. The devices were measured at $V_{ds} = 1.2, 1.5,$ and 1.8 V and at five different V_{gs} values near the peak g_m point. For each of the devices, there was an observed increase in the measured magnitude of S_{21} and commensurate increase in the current gain H_{21} (shown in Fig. 3(a) and (b) for the device with an $\text{In}_{0.70}\text{Ga}_{0.30}\text{As}$ channel). The extrapolated extrinsic f_T of the $\text{In}_{0.53}\text{Ga}_{0.47}\text{As}/\text{In}_{0.52}\text{Al}_{0.48}\text{As}$ device showed an increase from 22 to 29 GHz when cooled from 300 to 77 K, while for the pseudomorphic devices having channels with $x = 0.60$ and 0.70 , the observed increases were from 28 to 37 GHz and 39 to 51 GHz, respectively. The increase in each of the devices can be attributed primarily to the increase in the average electron saturation velocity in the channel at lower temperatures [6].

A standard equivalent circuit, including models for the bond wires, was generated for each device measured at each bias condition and temperature. The bond-wire inductances were initially estimated from the length of the wires and then were further optimized in the circuit. The extracted intrinsic f_T values, given by

$$f_T = \frac{g_{m0}}{2\pi \cdot C_{gs}} \quad (1)$$

follow the same trend as the measured extrinsic f_T values. The extracted output conductance G_{ds} decreased at lower temperatures, as shown in Fig. 4, and shows the same trend as the dc measured output conductance. The main reason for this is the improved confinement of the carriers in the 2DEG channel at lower temperatures. A slight increase in the extracted gate-to-source capacitance C_{gs} was also observed. This was previously observed and modeled in GaAs/AlGaAs MODFET's [7]. It may be noted that the values of the various parameters were almost constant as the measurement temperature was lowered below 120 K.

Another observation that was made during these measure-

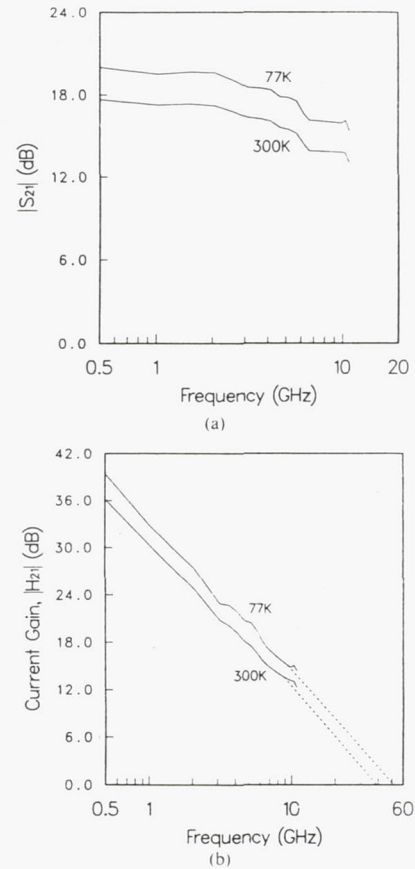


Fig. 3. Magnitude of (a) S_{21} and (b) current gain H_{21} versus frequency for a pseudomorphic $\text{In}_{0.70}\text{Ga}_{0.30}\text{As}/\text{In}_{0.52}\text{Al}_{0.48}\text{As}$ channel MODFET at 77 and 300 K with $V_{ds} = 1.5$ V and $V_{gs} = 0$ V.

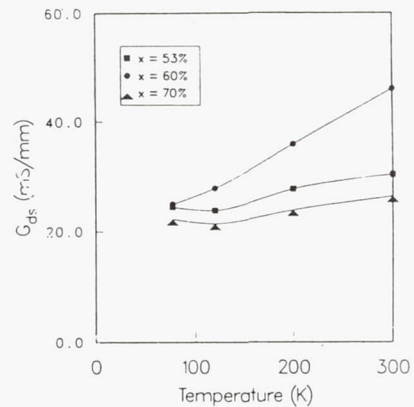


Fig. 4. Output conductance G_{ds} versus temperature for pseudomorphic $\text{In}_x\text{Ga}_{1-x}\text{As}/\text{In}_{0.52}\text{Al}_{0.48}\text{As}$ ($x = 0.53, 0.60,$ and 0.70) channel MODFET's with $V_{ds} = 1.5$ V and V_{gs} biased for peak gain.

ments was the absence of significant effects due to deep-level traps such as the collapse of $I-V$ characteristics which have been seen in AlGaAs/GaAs MODFET structures at low temperatures [8]. It should be noted that since the chamber was completely enclosed, the measurements were carried out in the dark. A small threshold shift of up to $+0.1$ V was observed in the dc characteristics for each of the devices.

This value is very small compared to the threshold shifts observed in AlGaAs/GaAs MODFET devices, which typically range from +0.2 to +0.4 V [9]. The threshold shift may occur due to a smaller concentration of deep-level traps and the small shift in the Fermi levels with temperature.

In conclusion, we have demonstrated and analyzed cryogenic measurements of pseudomorphic $\text{In}_x\text{Ga}_{1-x}\text{As}/\text{In}_{0.52}\text{Al}_{0.48}\text{As}$ MODFET's on InP substrates. Each device showed an increase in gain and cutoff frequency with decreasing temperature with no noticeable degradation in device performance. Further studies are needed to better understand the cryogenic microwave operation of these devices, such as the apparent -12-dB/octave rolloff of the maximum available gain reported by Kolodzey *et al.* [10] on lattice-matched $\text{In}_{0.53}\text{Ga}_{0.47}\text{As}/\text{In}_{0.52}\text{Al}_{0.48}\text{As}$ MODFET's. As may be noticed, our measurement frequency band was not high enough to detect this phenomenon, if present. However, the enhanced performance demonstrated in these devices at cryogenic temperatures shows that the pseudomorphic $\text{In}_x\text{Ga}_{1-x}\text{As}/\text{In}_{0.52}\text{Al}_{0.48}\text{As}$ MODFET's have great potential to be used in low-temperature high-frequency circuits.

ACKNOWLEDGMENT

The authors would like to thank K. B. Bhasin, B. T. Ebihara, and R. Simons for helpful contributions on the cryogenic system, J. Pamulapati and W. Li for MBE growth

of the samples, and G. I. Ng, M. N. Tutt, and D. Pavlidis for helpful discussions and contributions.

REFERENCES

- [1] K. H. Duh *et al.*, "32-GHz cryogenically cooled HEMT low-noise amplifiers," *IEEE Trans. Electron Devices*, vol. 36, pp. 1528-1534, Aug. 1989.
- [2] S. Weinreb, M. W. Pospieszalski, and R. Norrod, "Cryogenic HEMT low-noise receivers for 1.3 to 43 GHz range," in *1988 IEEE MTT-S Dig.*, pp. 945-948.
- [3] R. K. Kirshman, "Low-temperature electronics," *IEEE Circuit and Devices*, pp. 12-24, Mar. 1990.
- [4] G. I. Ng, W. P. Hong, D. Pavlidis, M. Tutt, and P. K. Bhattacharya, "Characteristics of strained $\text{In}_{0.65}\text{Ga}_{0.35}\text{As}/\text{In}_{0.52}\text{Al}_{0.48}\text{As}$ HEMT with optimized transport parameters," *IEEE Electron Device Lett.*, vol. 9, pp. 439-441, Sept. 1988.
- [5] U. K. Mishra, A. S. Brown, and S. E. Rosenbaum, "DC and RF performance of 0.1 μm gate length $\text{Al}_{0.48}\text{In}_{0.52}\text{As}/\text{Ga}_{0.38}\text{In}_{0.62}\text{As}$ pseudomorphic HEMT's," in *1988 IEDM Tech. Dig.*, pp. 180-183.
- [6] W. P. Hong, G. I. Ng, P. K. Bhattacharya, D. Pavlidis, and S. Willing, "Low- and high-field transport properties of pseudomorphic $\text{In}_x\text{Ga}_{1-x}\text{As}/\text{In}_{0.52}\text{Al}_{0.48}\text{As}$ ($0.53 \leq x \leq 0.65$) modulation-doped heterostructures," *J. Appl. Phys.*, vol. G4, pp. 1945-1949, Aug. 1988.
- [7] L. P. Sadwick and K. L. Wang, "A treatise on the capacitance-voltage relation of high electron mobility transistors," *IEEE Trans. Electron Devices*, vol. ED-33, pp. 651-656, May 1986.
- [8] A. Kastalsky and R. A. Kiehl, "On the low-temperature degradation of AlGaAs/GaAs modulation-doped field-effect transistors," *IEEE Trans. Electron Devices*, vol. ED-33, pp. 414-423, Mar. 1986.
- [9] M. Shur, *GaAs Devices and Circuits*. New York: Plenum, 1987, pp. 583-588.
- [10] J. Kolodzey *et al.*, "Cryogenic temperature performance of modulation-doped field-effect transistors," *Electron. Lett.*, vol. 25, pp. 777-779, Feb. 1989.

Modeling Al_xGa_{1-x}As optical constants as functions of composition

Paul G. Snyder and John A. Woollam

Department of Electrical Engineering, University of Nebraska, Lincoln, Nebraska 68588-0511

Samuel A. Alterovitz

NASA Lewis Research Center, Cleveland, Ohio 44135

Blaine Johs

J. A. Woollam Co., Lincoln, Nebraska 68508

(Received 23 May 1990; accepted for publication 21 August 1990)

Three models for the dielectric function $\epsilon_1(h\nu)$ of Al_xGa_{1-x}As are reviewed. All are based on measured optical constants at discrete compositions. The validity of each model near critical point energies, and otherwise, is evaluated. Only the energy-shift model is appropriate over the entire available spectrum (1.5–6.0 eV), including the band-gap (E_g) region.

This communication addresses the modeling of Al_xGa_{1-x}As optical constants as a function of composition x . Three different modeling approaches are described and compared. Applications include fitting spectroscopic data for heterostructure samples, e.g., in waveguide design, ellipsometric characterization, and more.

Aspnes *et al.* have measured the dielectric function $\epsilon(h\nu)$ in the range 1.5–6.0 eV for discrete nominal compositions $x = 0.0, 0.1, 0.2, 0.3, 0.4, 0.5, 0.6, 0.7,$ and 0.8 .¹ The authors noted that compositional variation can be obtained by taking the weighted average of the two spectra closest in composition after their energy scales have been shifted to bring the nearest critical point energies into coincidence. It was suggested that this would only apply to a limited spectral range around the critical point energy E_1 .

We extended this approach to obtain $\epsilon_1(h\nu)$ over the entire measured spectrum, with continuous compositional variability.² With reference to Fig. 1 (from Ref. 1), three separate critical point regions are considered: E_0 , 1.4–2.5 eV; E_1 (and $E_1 + \Delta_1$), 2.9–3.9 eV; and E_2 , 4.8 eV. The energy positions of these critical points are given in Ref. 1 as

$$E_0(x) = 1.424 + 1.594x + x(1-x)(0.127 - 1.310x) \text{ eV}, \quad (1)$$

$$E_1(x) = 2.924 + 0.965x + x(1-x)(-0.157 - 0.935x) \text{ eV} \quad (2)$$

(E_2 is approximately independent of x).

For arbitrary x ($0.01 < x < 0.8$), we construct $\epsilon_1(h\nu)$ from $\epsilon_A(h\nu)$ and $\epsilon_B(h\nu)$, which are the measured dielectric functions with compositions $x_A < x < x_B$. Thus if $x = 0.37$, then $x_A = 0.3$ and $x_B = 0.4$ (more precise estimates of the actual compositions of the measured samples are given in Ref. 1; nominal values are used here). The construction consists of shifting the ϵ_A spectrum to higher energy, and the ϵ_B spectrum to lower energy, so that the critical point features coincide at an energy interpolated between the critical point energies of ϵ_A and ϵ_B , as described below. A weighted average of the two shifted spectra is then taken. This averaging accounts, to first order, for the small variation in amplitude with x (see Fig. 1).

The required energy shift for a given x is a function of

photon energy $h\nu$. At each of the two x -dependent critical point energies, the shifts are given by

$$\delta'_{1h} = E_0(x) - E_0(x_{1B}), \quad (3)$$

$$\delta'_{1h} = E_1(x) - E_1(x_{1A}), \quad (4)$$

The energies on the right-hand sides of (3) and (4) are given by (1) and (2). For photon energies other than E_0 and E_1 , the following piecewise linear interpolation is used. Below E_0 , $\delta(h\nu)$ is constant and equal to $\delta(E_0)$. Above E_2 , $\delta(h\nu)$ is zero. Between E_0 and E_1 , $\delta(h\nu)$ varies linearly between $\delta(E_0)$ and $\delta(E_1)$, and between E_1 and E_2 it varies linearly between $\delta(E_1)$ and zero. Figure 2 summarizes the energy shifts as functions of photon energy.

At a given photon energy, then, the calculated spectrum for x is the weighted average of the two shifted spectra:

$$\epsilon_1(h\nu) = \{\epsilon_1[h\nu - \delta_1(h\nu)](x_B - x) - \epsilon_1[h\nu + \delta_2(h\nu)](x - x_A)\} / (x_B - x_A). \quad (5)$$

The accuracy of ϵ_1 computed in this algorithm depends on the accuracy of the original ϵ measurements, and the difference between x and the nearest endpoint, x_A or x_B .

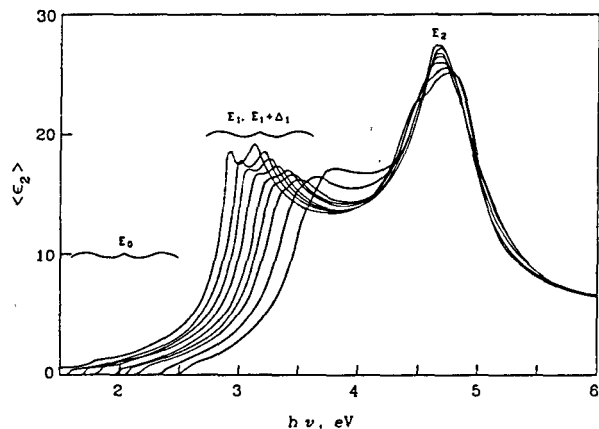


FIG. 1. Imaginary part of the dielectric function measured for Al_xGa_{1-x}As, with x increasing from 0 in steps of approximately 0.1 (from Ref. 1).

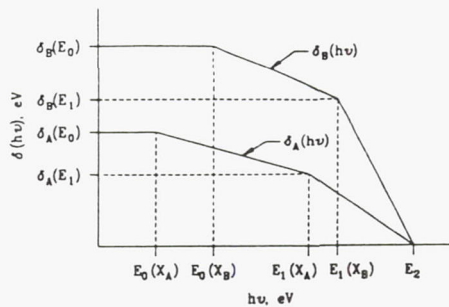


FIG. 2. Energy shifts $\epsilon(x_A)$ and $\epsilon(x_B)$, required to produce $\epsilon(x)$, are not constant over the spectrum. This is a simple scheme for smoothly varying the energy shifts, based on the known critical point energies $E_n(x)$ and $E'_n(x)$.

The measured ϵ were estimated to be accurate to within 2% of the maximum value for $x \leq 0.5$, and to within 5% for $x \geq 0.6$.¹ For x coinciding with x_A or x_B , the weighting factor in Eq. (5) causes the calculated ϵ and its accuracy to be the same as the measured ϵ . For x midway between x_A and x_B , the accuracy is slightly degraded due to the piecewise linear approximation chosen for $\delta_{A,B}(h\nu)$.

A second approach is to use several discrete harmonic oscillators (HO) to model $\epsilon_\nu(h\nu)$. For each HO, the amplitude, center photon energy, and broadening parameter can be given as continuous functions of x , allowing $\epsilon(h\nu)$ to be calculated for any x . This physically appealing and relatively simple approach was used by Erman *et al.* to model GaAs with seven oscillators.³ The result is an accurate approximation to the measured ϵ over most of the spectrum. Unfortunately, the sharp onset of absorption at the band gap is not easily modeled with discrete oscillators, so no attempt was made to model the E_0 structure by including an oscillator at E_0 . Thus the HO model is only accurate at energies above, but not including, the E_0 region.

A third approach which has been taken is to use the Bruggeman effective-medium approximation (EMA) with two constituents, ϵ_A and ϵ_B .⁴ This model is not physically realistic for the case of $\text{Al}_{1-x}\text{Ga}_x\text{As}$, however. The EMA assumes a microscopic, but not atomic, mixture of the two constituents. Each "grain" is assumed to be large enough ($> 20 \text{ \AA}$) to retain its own characteristic bulk dielectric function, but much smaller than an optical wavelength. The EMA averages the two spectra, taking into account the electrical polarization that occurs at the grain boundaries, assuming approximately spherical grains.⁵

In the AlGaAs alloy, there are no grains, and thus no microstructural polarizing field to account for. Furthermore, since the EMA is an average of two spectra which are not energy shifted, critical point features from both spectra

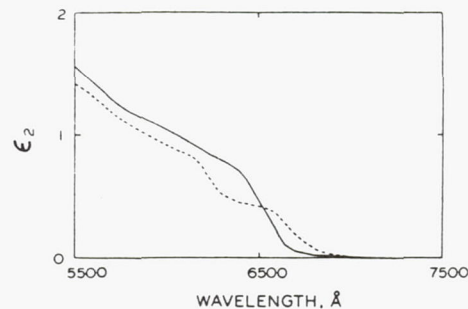


FIG. 3. ϵ_2 for $\text{Al}_{1-x}\text{Ga}_x\text{As}$ as calculated from the measured $x = 0.3$ and $x = 0.4$ spectra, using the energy-shift model (solid) and the EMA model (dashed)

will appear in an EMA composite spectrum. This will be particularly evident at E_0 .

Figure 3 shows simulated $\epsilon_2(h\nu)$ near E_0 , for $x = 0.35$, using the energy-shift and the EMA models. The HO model would simply show a smoothly decaying ϵ_2 with increasing wavelength, and no structure at E_0 . The EMA spectrum contains two absorption edges, one from each constituent ($x_A = 0.3$ and $x_B = 0.4$), but no structure at $E_0(x = 0.35)$. The energy-shift model shows a single absorption edge at the appropriate band-gap energy.

It must be emphasized that the E_0 region is the most important region for waveguide applications. In addition, sensitivity to x is highest at E_0 , making it the most important region for characterization of composition. Optical constants in this region are *not* adequately modeled by the HO or EMA models.

Our previous work with GaAs/AlGaAs heterostructures clearly showed that ellipsometric data measured near E_0 are very sensitive to layer thicknesses and compositions.² The energy-shift model is most appropriate for this region, and it also works well over the rest of the spectrum. Other work⁶ has emphasized the E_1 region, where the HO model is also valid.

This work was supported by NASA-Lewis Grant No. NAG-3-154.

¹ D. E. Aspnes, S. M. Kelso, R. A. Logan, and R. Bhat, *J. Appl. Phys.* **60**, 754 (1986).

² P. G. Snyder, M. C. Rost, G. H. Bu-Abbud, J. A. Woollam, and S. A. Alterowitz, *J. Appl. Phys.* **60**, 3293 (1986).

³ M. Erman, J. B. Theeten, P. Chambon, S. M. Kelso, and D. E. Aspnes, *J. Appl. Phys.* **56**, 2664 (1984).

⁴ J. L. Freeouf, *Appl. Phys. Lett.* **53**, 2426 (1988).

⁵ D. E. Aspnes, *Thin Solid Films* **89**, 249 (1982).

⁶ M. Erman, J. B. Theeten, N. Vojdani, and Y. Demay, *J. Vac. Sci. Technol.* **B 1**, 328 (1983).

DIELECTRIC FUNCTION OF InGaAs IN THE VISIBLE

S. A. ALTEROVITZ*, R. E. SIEG**, H. D. YAO†, P. G. SNYDER†, J. A. WOOLLAM†,
J. PAMULAPATI†, P.K. BHATTACHARYA†, P. A. SEKULA-MOISE#

*NASA-Lewis Research Center, Cleveland, Ohio 44135

**Undergraduate Student Intern at NASA-Lewis Research Center from Cleveland State University, Dept. of Electrical Engineering, Cleveland, Ohio 44115

†University of Nebraska, Department of Electrical Engineering, Lincoln, NE 68588

‡University of Michigan, Department of Electrical Engineering and Computer Science, Ann Arbor, MI 48109

#Spire Corporation, Patriots Park, Bedford, MA 01731

ABSTRACT

In this study we report, for the first time, measurements of the dielectric function of thermodynamically stable $\text{In}_x\text{Ga}_{1-x}\text{As}$ in the composition range $0.3 \leq X \leq 0.7$. The optically thick samples of InGaAs were made by molecular beam epitaxy (MBE) in the range $0.4 \leq X \leq 0.7$ and by metal-organic chemical vapor deposition (MOCVD) for $X=0.3$. The MBE made samples, usually 1 micron thick, were grown on semi-insulating InP and included a strain release structure. The MOCVD sample was grown on GaAs and was 2 microns thick. The dielectric functions were measured by variable angle spectroscopic ellipsometry in the range 1.55 eV to 4.4 eV. The data was analyzed assuming an optically thick InGaAs material with an oxide layer on top. The thickness of this layer was estimated by comparing our results for the InP lattice matched material, i.e. $X=0.53$, with results published in the literature. We removed the top oxide layer mathematically for $X=0.3$ and $X=0.53$ to get the dielectric function of the bare InGaAs. In addition, we measured the dielectric function of GaAs in vacuum, after a protective arsenic layer was removed. We used our dielectric functions for $X=0, 0.3$, and 0.53 together with the $X=1$ result from the literature to evaluate an algorithm for calculating the dielectric function of InGaAs for an arbitrary value of X ($0 \leq X \leq 1$). We compared results of the dielectric function calculated using the algorithm with experimental data.

INTRODUCTION

$\text{In}_x\text{Ga}_{1-x}\text{As}$ is a material with a variety of potential and actual applications. The most commonly studied concentration is $X=0.53$, the InP lattice matched composition. However, strained lattice configurations show great promise for applications both in optoelectronics and in electronic devices. Applications of strained layer, modulation doped, heterostructures using an InGaAs conduction channel on either GaAs [1] or InP [2] substrates, as well as special optoelectronic applications on GaAs substrates, have recently been published. It is clear that an experimental determination of the thermodynamically stable $\text{In}_x\text{Ga}_{1-x}\text{As}$ dielectric functions versus the composition, X , will be useful for several reasons. First, the results can be applied directly to the structures that are fabricated from these materials. Second, the results can be used as the starting point in calculating strain effects on the dielectric function. These effects play an important role for optoelectronic applications [3], especially near the band edge.

All published literature regarding the dielectric function of $\text{In}_x\text{Ga}_{1-x}\text{As}$ in the visible is dedicated to the concentration $X=0.53$, i.e. lattice matched to InP. Several studies were performed using the highly accurate technique of

ellipsometry [4-7]. The samples were made by liquid phase epitaxy (LPE) [4-6] or by MOCVD [7]. Presently, there are no published reports of the dielectric function of MBE made InGaAs, either lattice matched or strained layer. The most useful data available, to date, is a numerical table [8] of the results presented in [5]. These results were obtained on chemically polished $\text{In}_{0.53}\text{Ga}_{0.47}\text{As}$ made by LPE.

In the present study, we will describe an ellipsometric, experimental determination of the dielectric functions of InGaAs with several indium concentrations (X), both lattice matched and lattice mismatched to InP. We will also present an algorithm that can be used to estimate the dielectric function of InGaAs for any desired value of the concentration X.

EXPERIMENTAL

$\text{In}_x\text{Ga}_{1-x}\text{As}$ samples in the range $0.4 \leq X \leq 0.7$, with roughly 0.1 steps in X, were grown on semi-insulating InP substrates. Growth in both types of structures started with a 2000 Å lattice matched $\text{In}_{0.53}\text{Ga}_{0.47}\text{As}$ buffer layer. In the first set, hereafter called set A, this layer was followed by a ~1500 Å thick graded composition region (in multiple steps) to reach the composition of the final layer. The top $\text{In}_x\text{Ga}_{1-x}\text{As}$ layer, which is of interest, is 1 μm thick and hence the strain is relieved at the interface with the next lower layer. In the second set of samples, hereafter called set B, a 30 period superlattice (30 Å $\text{In}_x\text{Ga}_{1-x}\text{As}$ /30 Å $\text{In}_x\text{Al}_{1-x}\text{As}$) was grown at the interface before the top layer, to act as a dislocation filter. All the heterostructures were grown continuously at 520 °C at a rate of 1.2 μm/hr and with a V/III flux ratio of ~30. The MOCVD sample (X=0.3) was grown on n⁺ GaAs at Spire Corporation. The thickness was nominally 2 μm and no buffer layers were used. The $\text{In}_{0.3}\text{Ga}_{0.7}\text{As}$ layer was grown at 650 °C at a rate of 1.9 μm/hr and with a V/III flux ratio of ~75.

The GaAs sample was mounted and measured on a high temperature stage inside an ultra high vacuum (UHV) chamber. The sample consisted of a MBE grown GaAs epitaxial layer on a GaAs substrate and was covered with an amorphous arsenic layer for protection of the surface. Prior to the ellipsometric measurement, the protecting layer was evaporated by heating the sample to 350 °C in vacuum for 10 minutes [9]. This procedure [9] yielded a GaAs surface as clean and smooth as the best chemically polished surface reported previously [10].

Ellipsometric measurements were made both at NASA-Lewis and at the University of Nebraska. The technique [11,12] was described previously and will not be repeated here.

RESULTS AND DISCUSSION

The ellipsometric, experimental parameters ψ and Δ were used to find the substrate pseudo-dielectric function, i.e. without taking into account any overlayers. The results of the "pseudo" refractive index, n, for all the concentrations measured are shown in Fig. 1. The X=0.4, 0.6, and 0.7 samples belong to the set A strain release procedure, while the X=0.53 sample was grown using the set B procedure. We also measured samples with X=0.4 and 0.7 from set B. All the graphs clearly show that the E_1 critical point peak is moving to lower energies as the In concentration increases. The difference in the absolute value of n versus X is due not only to changes in the indium concentration, but also to differences in oxide overlayer thickness and surface imperfections. The results for the samples with X=0.4 and 0.7 from set B show the same values of the critical point, E_1 , as in Fig. 1, but have slightly higher values for n. This is probably due to a more perfect surface obtained for set B versus set A

samples. Results obtained for the extinction coefficient show that the optical penetration depth for all samples is well below 1000 Å, for wavelengths below 6000 Å, and below 2000 Å anywhere in the spectrum. This result reinforces our assumption that our 1-2 μm films are optically thick.

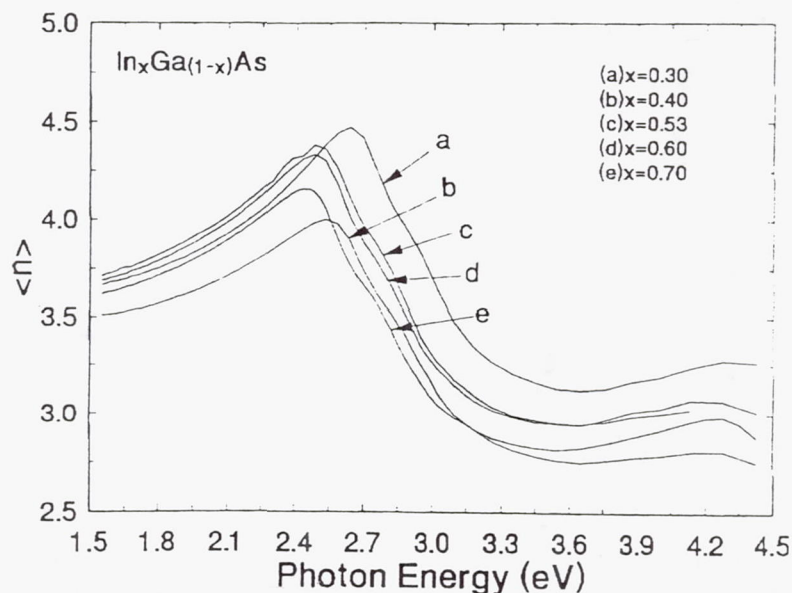


FIGURE 1. - PSEUDO REFRACTIVE INDEX OF FIVE $\text{In}_x\text{Ga}_{1-x}\text{As}$ ($0.3 \leq x \leq 0.7$) SAMPLES VERSUS THE PHOTON ENERGY.

There are several ways to remove the contribution of the top oxide layer to the dielectric function. We tried to obtain, simultaneously, the dielectric function of the InGaAs and the oxide layer thickness using our variable angle of incidence capability. However, the rather small thickness of the oxide layer and the large correlations between this thickness and the InGaAs dielectric function prevented us from obtaining reliable results using this method of analysis. A good estimate of the oxide layer thickness, for the lattice matched sample, was obtained using a model in which variable oxide thickness and constant dielectric functions for the $\text{In}_{0.53}\text{Ga}_{0.47}\text{As}$ [8] and oxide [13] were used. This one parameter fit gave an oxide layer thickness of 22.5 Å with an excellent mean square error (M.S.E.) of 0.085 for ψ and Δ fits. Assuming a constant 22.5 Å oxide thickness, we mathematically removed the oxide contribution for all samples. The result for the $X=0.53$ sample is compared to Aspnes data [8] in Fig. 2. As expected, an almost perfect agreement was obtained between the MBE and LPE grown materials. The real and imaginary parts of the dielectric functions for four indium concentrations in the range $0 \leq X \leq 1$, namely $X=0$, 0.3, 0.53, and 1, are shown in Figs. 3 and 4 respectively. The functions shown for $X=0$ [9] are the most recent results, which are very close to the generally accepted data [10]. The InAs functions were taken from the literature [10,14]. We believe that these four functions are more representative of the InGaAs material than those we obtained for other values of X due to the poorer surface quality of the latter samples. We used a numerical interpolation algorithm to calculate the value of the dielectric function for an arbitrary value of X , similar to that used for AlGaAs [15,16]. The algorithm is based on the four functions shown in Figs. 3 and 4 and uses an interpolation of the critical points and the value of the dielectric function.

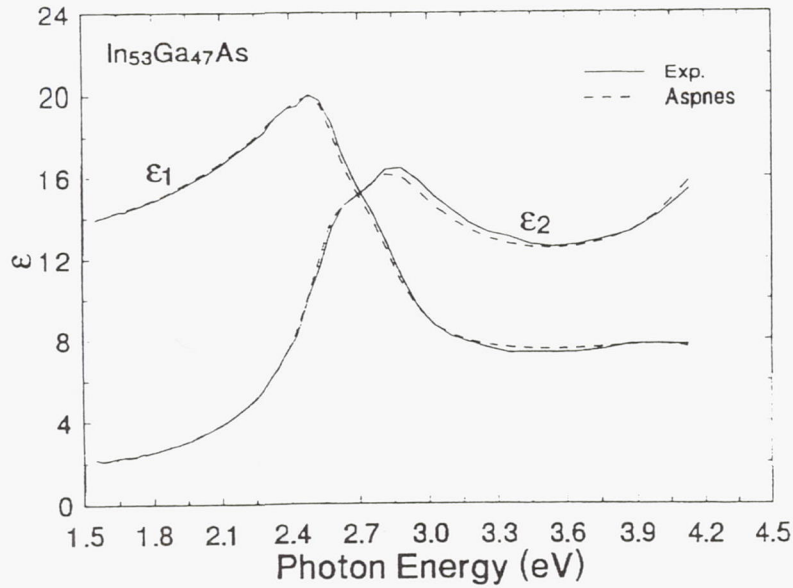


FIGURE 2. - COMPARISON OF PRESENT DATA WITH ASPNES [8] FOR THE DIELECTRIC FUNCTION OF $\text{In}_{0.53}\text{Ga}_{0.47}\text{As}$ VERSUS PHOTON ENERGY.

As a test of the algorithm, we used it to estimate the indium concentration, X , for a sample from set A with nominal concentration $X=0.4$. We applied a least squares fitting procedure to fit the experimental ellipsometric data to values calculated using the algorithm with X and the oxide overlayer thickness as variables. We obtained an oxide thickness of 31 Å, an indium concentration of $X=0.37$, and an M.S.E.=0.39 for the ψ and Δ fits. The result is shown in Fig. 5, in terms of the measured and best-fit pseudo-dielectric functions. The lower peak value of the experimental $\langle \epsilon_2 \rangle$, compared to the best-fit $\langle \epsilon_2 \rangle$, is indicative of a relatively poor surface quality for this sample.

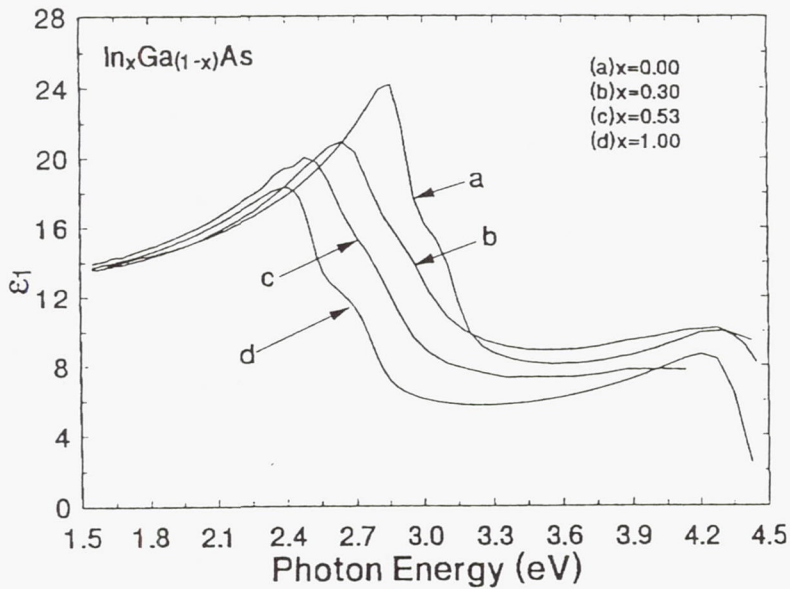


FIGURE 3. - REAL PART OF THE DIELECTRIC FUNCTION OF $\text{In}_x\text{Ga}_{1-x}\text{As}$ ($0 \leq x \leq 1$) FOR FOUR SAMPLES VERSUS ENERGY.

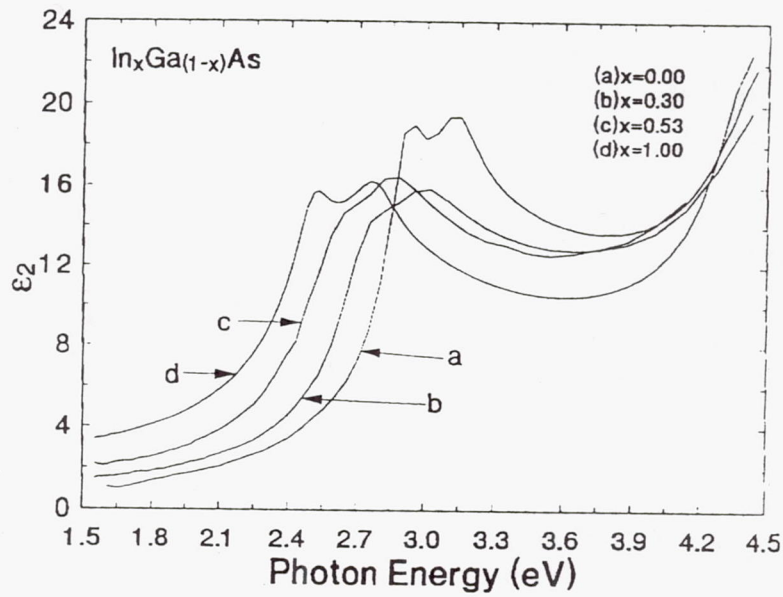


FIGURE 4. - IMAGINARY PART OF THE DIELECTRIC FUNCTION OF $\text{In}_x\text{Ga}_{1-x}\text{As}$ ($0 \leq x \leq 1$) FOR FOUR SAMPLES VERSUS ENERGY.

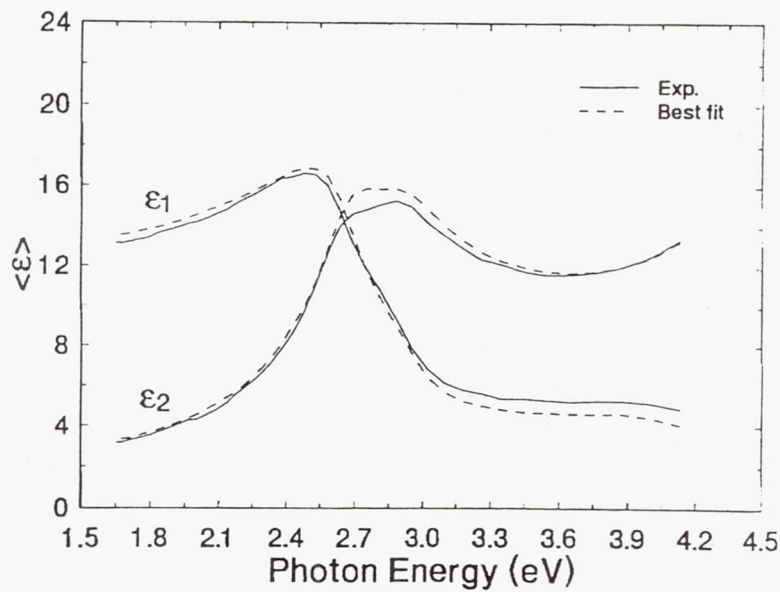


FIGURE 5. - REAL AND IMAGINARY PARTS OF THE EXPERIMENTAL AND BEST-FIT (CALCULATED) PSEUDO DIELECTRIC FUNCTION FOR THE NOMINAL $x = 0.4$ SAMPLE.

CONCLUSIONS

Thermodynamically stable $\text{In}_x\text{Ga}_{1-x}\text{As}$ samples in the range $0.3 \leq x \leq 0.7$ were grown by MBE and MOCVD. Samples were 1-2 μm thick, well above both the optical penetration depth and the dislocation range. The oxide overlayer contribution was estimated by comparison of our results with published data for $x=0.53$, the lattice matched concentration. After a mathematical removal of the oxide layer, the pseudo-dielectric functions of $\text{In}_x\text{Ga}_{1-x}\text{As}$ were obtained for several values of x . These functions were interpolated using a special algorithm to calculate the dielectric function for any value of x . The algorithm was successfully tested versus our experimental result at $x=0.4$.

ACKNOWLEDGEMENTS

Work at the University of Michigan was supported by grant NAG3-988. Work at Spire Corporation was performed under contract NAS3-25867.

REFERENCES

- ¹W. T. Masselink, J. Klem, T. Henderson, A. Ketterson, J. S. Gedjmin, H. Morkoc, and K. R. Gleason, *IEDM*, 755 (1985).
- ²G. I. Ng, W. P. Hong, D. Pavlidis, M. Tutt, and P. K. Bhattacharya, *IEEE Electron Device Lett.* **9**, 439 (1988).
- ³S. C. Hong, G. P. Kothigal, N. Debbar, P. Bhattacharya, and J. Singh, *Phys. Rev. B* **37**, 878 (1988).
- ⁴H. Burkhard, H. W. Dinges, and E. Kuphal, *J. Appl. Phys.* **53**, 655 (1982).
- ⁵D. E. Aspnes and H. J. Stocker, *J. Vac. Sci. Technol.* **21**, 413 (1982).
- ⁶S. M. Kelso, D. E. Aspnes, M. A. Pollock, and R. E. Nahori, *Phys. Rev. B* **26**, 6669 (1982).
- ⁷M. Erman, J. P. Andre, and J. LeBris, *J. Appl. Phys.* **59**, 2019 (1986).
- ⁸D. E. Aspnes, Private Communication.
- ⁹H. D. Yao, P. G. Snyder, and J. A. Woollam, *These Proceedings*.
- ¹⁰D. E. Aspnes and A. A. Studna, *Phys. Rev. B* **27**, 985 (1983).
- ¹¹S. A. Alterovitz, R. M. Sieg, N. S. Shoemaker, and J. J. Pouch, *Mat. Res. Soc. Symp. Proc.* **152**, 21 (1989).
- ¹²J. A. Woollam and P. G. Snyder, *Mat. Sci: Eng. B* **5**, 279 (1990).
- ¹³D. E. Aspnes, G. P. Schwartz, G. J. Gualtieri, A. A. Studna, and B. Schwartz, *J. Electrochem. Soc.* **128**, 590 (1981).
- ¹⁴E. D. Palik and R. T. Holm, *Handbook of Optical Constants of Solids*, 479 (1985).
- ¹⁵P. G. Snyder, J. A. Woollam, and S. A. Alterovitz, to be published.
- ¹⁶P. G. Snyder, M. C. Rost, G. H. Bu-Abbud, J. A. Woollam, and S. A. Alterovitz, *J. Appl. Phys.* **60**, 3293 (1986).

***SECTION
THREE***

***HIGH TEMPERATURE
SUPERCONDUCTIVITY***

SUPERCONDUCTING MICROWAVE ELECTRONICS AT LEWIS RESEARCH CENTER

Joseph D. Warner, Kul B. Bhasin, and Regis F. Leonard
National Aeronautics and Space Administration
Lewis Research Center
Cleveland, Ohio 44135

ABSTRACT

Over the last three years, NASA Lewis Research Center has investigated the application of newly discovered high temperature superconductors to microwave electronics. Using thin films of $\text{YBa}_2\text{Cu}_3\text{O}_{7-\delta}$ and $\text{Tl}_2\text{Ca}_2\text{Ba}_2\text{Cu}_3\text{O}_x$ deposited on a variety of substrates, including strontium titanate, lanthanum gallate, lanthanum aluminate and magnesium oxide, a number of microwave circuits have been fabricated and evaluated. These include a cavity resonator at 60 GHz, microstrip resonators at 35 GHz, a superconducting antenna array at 35 GHz, a dielectric resonator filter at 9 GHz, and a microstrip filter at 5 GHz. Performance of some of these circuits as well as suggestions for other applications are reported.

INTRODUCTION

Investigations to determine space electronics applications of high temperature superconductor (HTS) at NASA Lewis Research Center were initiated soon after the discovery of superconductivity in ceramic oxides $\text{La}_{1-x}\text{Sr}_x\text{CuO}_y$ ¹ and $\text{YBa}_2\text{Cu}_3\text{O}_{7-\delta}$ ² with transition temperatures 35 K and 93 K. Soon after their discoveries were made others found the Bi-Sr-Ca-Cu-O³ and Tl-Ca-Ba-Cu-O⁴ class of 100 K + superconductors. Since that time the properties of these superconductors became known and we concentrated our efforts on development of thin films of $\text{YBa}_2\text{Cu}_3\text{O}_{7-\delta}$ and $\text{Tl}_2\text{Ca}_2\text{Ba}_2\text{Cu}_3\text{O}_x$ for space microwave applications. The use of HTS films in a microwave system requires development of thin films on microwave substrates which then can be patterned into desired microwave circuits like filters, phase shifters, ring resonators and delay lines. Such circuits are used in space communication, radar, and sensing systems.⁵ Small size, low loss, low power and light weight are desirable features for these circuits.

In this paper, we describe the development of high quality $\text{YBa}_2\text{Cu}_3\text{O}_{7-\delta}$ (YBCO) and $\text{Tl}_2\text{Ca}_2\text{Ba}_2\text{Cu}_3\text{O}_x$ (TCBCO) thin films on microwave substrates carried out at NASA Lewis and also at various sponsored and cooperative facilities. The method of fabricating and the evaluation of various microwave passive circuits is presented. At the end future applications are also highlighted.

DEVELOPMENT OF THIN SUPERCONDUCTING FILMS

To obtain high quality superconducting thin films on suitable substrates for microwave applications the substrate lattice constants must be closely matched to those of the films and there must not be a detrimental chemical reaction between the substrates and the films. In addition, the film composition must be as close to the correct composition as possible. To date, very high quality films have been obtained by using several physical and chemical deposition techniques. Many of these techniques had required postannealing at high temperatures. This high temperature anneal causes chemical interactions at the film-substrate interface, making the film-substrate interface unsuitable for microwave application.⁶ To circumvent this problem, a laser ablation technique^{7,8} followed by an in situ annealing procedure has been pursued and developed for the growth of YBCO films. Also, for the growth of TCBCO films, sputtering and laser ablation techniques were chosen and funded at University of Cincinnati and University of Nebraska at Lincoln, respectively. Though, with both methods an ex-situ anneal with thallium over pressure was required.

Both YBCO and TCBCO films were evaluated for their microwave properties. The reasons why YBCO was selected were because it can be grown single phase easily and has no competing phases when the oxygen pressure is 1 atm or less. Its critical field can exceed 100 T at low temperatures and its critical current is greater than 2×10^6 A/cm² at 77 K. TCBCO films were chosen because the TCBCO phase has a transition of 125 K in bulk form and early properties of bulk TCBCO showed that the material had lower 1/f noise than YBCO. The progress to date on the growth and characterization of YBCO and TCBCO thin films is presented subsequently.

YBa₂Cu₃O_{7- δ} Films

At the beginning of the research three methods of producing YBCO films were investigated. They were sequential evaporation, coevaporation, and laser ablation. In the following paragraphs, we briefly describe the techniques and give references for them.

Produced by sequential evaporation. - One of the earliest attempts at The Ohio State University to produce YBCO films was by sequential evaporation of copper, barium fluoride, and yttrium and followed by a postanneal.⁹ This procedure did produce YBCO films that were mainly a-axis aligned, but the films generally were poor having low transition temperatures (T_c) and critical current density (J_c) values and high porosity.¹⁰ Nevertheless, this technique did allow us to set up the necessary equipment for investigation of the optical and microwave properties of HTS films.^{9,11,12}

Produced by coevaporation. - Coevaporation is being pursued jointly by Oberlin College and NASA Lewis. The film by this technique is grown at room temperature by coevaporating Cu, BaF₂, and Y from separate electron beam guns.¹³ Then the film is postannealed similar to the postannealed sequentially evaporated films. One of the advantages for coevaporation is that patterns with 2 μ m lines can be formed by using photoresist and a lift-off technique. So far the films produced have had a high T_c of 90 K but J_c in the 5×10^5 A/cm² range at 77 K. The low J_c is due to the high temperature annealing conditions which cause a substantial amount of a-axis growth and porosity.

Produced by laser ablation. - The laser ablation technique⁷ has given us the best YBCO films to date. Films by this technique were produced at NASA Lewis and the technique has also been set up at The Ohio State University, successfully. The basic principle of laser ablation is that a short wavelength and short pulse duration laser beam is focused onto a YBCO target. This evaporates the surface of the target and produces a plasma plume. Since the pulse duration is very short there is very little heat transferred to the target preventing thermal melting of the target and the noncongruent evaporation of the individual atoms. Therefore, a stoichiometric composition of the target is ablated from the surface.

The best films on LaAlO₃ were c-axis aligned and had a T_c around 90.6 K immediately after deposition as determined by a standard four point resistance measurement. Resistance versus temperature behavior for a YBCO film is shown in fig. 1. Critical current density J_c versus temperature is shown in fig. 2. As can be seen, the value of J_c was 2×10^6 A/cm² at 77 K. The surface of the films was very smooth with some small structure of about 0.25 μ m in size. This size of structure has been confirmed by scanning tunneling microscopy. In table I, we list the performance of YBCO and TCBCO thin films on various microwave substrates along with the microwave properties of these substrates.

Tl₂Ca₂Ba₂Cu₃O_x Films

TCBCO films on LaAlO₃ substrates have been made at University of Cincinnati and University of Nebraska at Lincoln. University of Cincinnati made their films by r.f. sputtering of a compressed 2223 powder target^{14,15} followed by an anneal in Tl vapors. The smooth, dense films have a T_c between 103 K to 107 K with a 6 K transition width. The films are a mixture of 2223 and 2212 phases. University of Nebraska made their films by laser ablation and have achieved a T_c as high as 115 K, see fig. 3, but typical T_c were around 108 K.¹⁶ But the films are not smooth and have some porosity. They used a compressed powder target of TlO₂, BaCuO₂, and CaCuO₂. Presently, they are exploring the use of a 2223 target to achieve a film that is denser and has a T_c above 120 K.

Microwave Characterization

Surface resistance (R_s) of superconducting film is a basic physical property that can be used to determine the quality of the film and is necessary for microwave device design. Currently, surface resistance values are obtained by cavity^{17,18} and stripline measurements¹⁹. These measurements are time consuming, and it would be worthwhile to correlate R_s with dc or low frequency measurements, such as dc conductivity above T_c, magnetic penetration depth, T_c, and a.c. susceptibility measurement; but so far there has been no consistent correlation reported between any of these measurements and R_s. The microwave conductivity (σ) is another physical property that can be measured. The conductivity for a superconductor is complex (σ = σ₁ + iσ₂) when the temperature is below T_c and it can be related to R_s and to the penetration depth (λ)²⁰.

Miranda et al.¹² have determined σ by measuring the microwave power transmitted through superconducting thin films in a waveguide experiment. From the value of σ₂ the magnetic penetration depth (λ) can be obtained. A summary of results of σ₁, λ_o, R_s for YBCO film on various substrates is shown in table II. The R_s for these films were calculated from σ₁ and λ. For YBCO on LaAlO₃ the R_s was 1.4x10⁻³ Ω which compares very well with other data.²¹ The surface resistance is an order of magnitude lower than that of copper up to 60 GHz.²¹ This demonstrates that with microwave transmission measurements one can obtain the R_s, λ, and σ of HTS films. These three properties are necessary for the determination of the quality of HTS films and the designing of microwave circuits.

FABRICATION

We have developed a method to fabricate microwave circuits and test devices for HTS films. The method is to use standard photolithography using negative photoresist and a "wet" chemical etchant. This etchant was either a 1 at % solution of bromine in ethanol or dilute phosphoric acid in water. In addition, circuits identical to the HTS circuits were made from patterned gold. This allows a direct comparison between HTS and gold circuits.

APPLICATION INVESTIGATIONS

The application of HTS to communication or radar systems does not only depend on the properties of HTS material but also the total system cost versus performance. The single most important issue for space communication is the possible need for cryogenic cooling. If HTS circuits must be cooled cryogenically then that cost in terms of power and weight must be considered along with the improved performance of the devices and any savings in weight and power from the replacement of standard equipment with HTS equipment. However, there are some missions, such as deep space probes that only would require passive cooling or other missions where cryogenic cooling is necessary for other functions, where this would not be an issue. Some of the

microwave applications and testing are discussed below. A brief description of each is made or referred to. The applications under investigation are resonators, filters, phase shifters, hybrid circuits, and antennae.

60 GHz Cavity

The surface resistance of HTS films can be calculated directly from the "Q" value of a resonant cavity experiment where one of the end walls of the cavity is replaced with the HTS film.¹⁸ This has been done at 60 GHz for YBCO films on LaGaO₃ and SrTiO₃. The R_s values for the two films can be seen in fig. 5. These films were approximately 1 μm thick; therefore, being polycrystalline c-axis oriented films. The results obtained agreed with other²¹ results for YBCO films grown by laser ablation and sputtering but measured at different frequencies. This agreement confirms the f^2 dependence of R_s and that the microwave properties for polycrystalline films of YBCO is independent of whether the films are grown on SrTiO₃ or LaGaO₃.

Resonator Circuits

HTS stripline ring resonators were fabricated on LaAlO₃ substrates.²² For measurement the resonators were mounted in a cosine tapered ridge waveguide to microstrip test fixture as shown in fig. 4. That structure was cooled by a closed cycle refrigerator. The resonators were measured by an HP8510 automatic network analyzer. The resonance frequency of the resonator changed rapidly with temperature just below T_c . This change was due to the change in the circuit reactance caused by the change in the magnetic penetration depth.²²

The best resonators measured to date and compared to gold is shown in fig. 6. The unloaded "Q" ranged from 2500 to 1000 at 20 and 77 K, respectively. This corresponds to a surface resistance value of 8 m Ω at 77 K at 35 GHz, a value two to three times better than copper at the same temperature and frequency.

Filters

Another candidate for application of HTS thin films is in the area of passive microwave filters. Taking advantage of the low losses for HTS film we have considered where they could be applied within a satellite transponder to improve performance. Based on results obtained to date on the performance of superconducting microstrip resonator circuits with high "Q" values as compared to an all metal microstrip resonators, we project the application of superconducting passive circuits as low loss, high "Q" filters¹³, high "Q" resonators, delay lines, power splitter, power combiners, and resonator stabilized oscillators.

Phase Shifters

In addition to these applications, extremely low loss phase shifters using superconducting switches are also feasible. In fig. 7, we show a phase shifter which utilizes superconducting-normal-superconducting switches in place of FET/diode switches. The switches are fabricated from high temperature thin films of YBCO. The switches operate in the bolometric mode with the film near its transition temperature. Radiation from a light source raises the temperature higher than the film's T_c and consequently causes the film to become resistive. When the light is "on" the microwave signal travels past the switch, but is reflected when the light is off. To achieve the desired phase shift, the pair switches on the same side is illuminated. Fig. 8 shows the predicted behavior for a 180° phase shifter with a R_s value that is the same as gold at 77 K and having a R_s of 100 $\mu\Omega$ in the normal state. It has an with exceptional narrow insertion loss envelope and excellent return loss.

Hybrid Semiconductor/Superconductor Device

The natural use of hybrid semiconductor and superconductor devices will be where III-V compound semiconductors, such as AlGaAs, InGaAs, and III-V heterojunction material, will be used at temperature around 77 K for devices that cannot operate or give the necessary performance at room temperatures. Some of these applications are for low noise amplifiers at frequencies above 22 GHz or solid state amplifiers above 70 GHz. Since these semiconducting devices will have to be cooled to 77 K there is no penalty in terms of the cost or reliability of the refrigeration to be paid to use superconductor devices. Therefore, it is natural to use HTS circuits in conjunction with III-V semiconductor devices to obtain the best performance of devices at these temperatures.

In fig. 9, we show an example of hybrid semiconductor/superconductor device for an ultra low noise receiver for satellite applications. This receiver takes the advantage of the excellent noise properties of AlGaAs HEMT technology and the low noise and resonator properties of superconducting transmission lines to achieve the ultra low noise and stable amplification.

Superconducting Phased Arrays

Superconducting antennas have long been imagined as extremely low loss devices. The use of superconductors to reduce the size of antennas to a fraction of a wavelength and to make super-directive arrays have been some of the more popular subjects. It has been shown recently, however, that of these various uses, the most practical use of superconductors in antennas will be in microwave and millimeter wave antennas.²³ To demonstrate the use of superconductors in such antennas, current research at NASA Lewis, in cooperation with Ball Aerospace, is focusing upon the fabrication and testing of a four element planar array at 30 GHz (fig. 10). The performance of this antenna will be compared to an identical array fabricated using gold instead of HTS.

CONCLUSIONS

We have demonstrated that rare-Earth oxide thin superconducting films can be deposited on various microwave substrates with critical temperature T_c above 77 K, critical current densities J_c above 10^6 A/cm², and low surface resistance. The films can be easily etched into microwave transmission line circuits. Microwave circuit ring resonator fabricated from a YBCO superconducting film on LaAlO₃ substrate showed "Q" values four times that for similar resonator made from a gold film. Several key HTS circuits such as filters, oscillators, phase shifters, and phased array antenna feeds are feasible in the near future. For technology to improve further, reproducible, large area films have to be grown on low dielectric constant, low loss microwave substrates. Tradeoffs between superconducting microwave circuits with cryogenic systems and normal metal microwave circuits will have to be quantitatively established to determine their suitability for advanced communication and sensor systems.

REFERENCES

1. Bednorz, J.G.; and Muller, K.A.: Possible High T_c Superconductivity in the Ba-La-Cu-O System. *Z. Phys. B. Condensed Matter*, vol. 64, 1986, pp. 189-193.
2. Chu, C.W., et al.: Evidence for Superconductivity Above 40 K in the La-Ba-Cu-O Compound System. *Phys. Rev. Lett.*, vol. 58, no. 4, Jan. 26, 1987, pp. 405-407.
3. Maeda, M., et al.: A New High- T_c Oxide Superconductor Without a Rare Earth Element. *Jpn. J. Appl. Phys. Lett.*, vol. 27, no. 2, Feb. 1988, pp. L209-L210.

4. Sheng, Z.Z.; and Herman, A.M.: Bulk Superconductivity at 120 K in the Ti-Ca/Ba-Cu-O System. *Nature*, vol. 332, no. 6160, Mar. 10, 1988, pp. 138-139.
5. Heinen, V.O., ed.: *Superconductivity Applications for Infrared and Microwave Devices*. Proc. SPIE Vol. 1292, SPIE, Bellingham, WA, 1990.
6. Bhasin, K.B., et al.: High-Temperature Superconducting Thin Film Microwave Circuits: Fabrication, Characterization, and Applications. *Superconductivity Applications for Infrared and Microwave Devices*, Proc. SPIE Vol. 1292, SPIE, Bellingham, WA, 1990 (Also, NASA TM-103235).
7. Warner, J.D.; Meola, J.E.; and Jenkins, K.A.: Study of Deposition of $\text{YBa}_2\text{Cu}_3\text{O}_{7-x}$ on Cubic Zirconia. NASA TM-102350, 1989.
8. Bhasin, K.B., et al.: Performance and Modeling of Superconducting Ring Resonators at Millimeter-Wave Frequencies. 1990 IEEE MTT-S International Microwave Symposium Digest, Vol. 1, IEEE, 1990, pp. 269-272.
9. Valco, G.J., et al.: Photoresponse of $\text{YBa}_2\text{Cu}_3\text{O}_{7.6}$ Granular and Epitaxial Superconducting Thin Films. NASA TM-103144, 1990.
10. Stan, M.A., et al.: Transport Measurements on Granular Y-Ba-Cu-O Films. *Physica C*, vol. 162-164, 1989, pp. 365-366.
11. Valco, G.J., et al.: Sequentially Evaporated Thin Y-Ba-Cu-O Superconducting Films on Microwave Substrates. NASA TM-102068, 1989.
12. Rohrer, N.J., et al.: Sequentially Evaporated Thin Film $\text{YBa}_2\text{Cu}_3\text{O}_{7-x}$ Superconducting Microwave Ring Resonator. NASA TM-103180, 1990.
13. Mankiewich, P.M., et al.: Reproducible Technique for Fabrication of Thin Films of High Transition Temperature Superconductors. *Appl. Phys. Lett.*, vol. 51, no. 21, Nov. 23, 1987, pp. 1753-1755.
14. Subramanyam, G., et al.: Fabrication and Chemical Composition of RF-Magnetron Sputtered Ti-Ca-Ba-Cu-O High T_c Superconducting Thin Films. *J. Appl. Phys.*, vol. 68, no. 3, 1990, pp. 1157-1163.
15. Subramanyam, G.; Radpour, F.; and Kapoor, V.J.: Fabrication of Ti-Ca-Ba-Cu-O Superconducting Thin Films on LaAlO_3 Substrates. *Appl. Phys. Lett.*, vol. 56, no. 18, Apr. 30, 1990, pp. 1799-1801.
16. Erington, K.B.; and Ianno, N.J.: Thin Films of Uniform Thickness by Pulsed Laser Deposition. To be published in *Journal of Applied Physics*.
17. Miranda, F.A., et al.: Microwave Conductivity of Superconducting Bi-Sr-Ca-Cu-O Thin Films in the 26.5 to 40.0 GHz Frequency Range. *Physica C*, vol. 168, nos. 1-2, June 1, 1990, pp. 91-98.
18. Miranda, F.A., et al.: Millimeter-Wave Surface Resistance of Laser Ablated $\text{YBa}_2\text{Cu}_3\text{O}_{7.6}$ Superconducting Films. *Appl. Phys. Lett.*, vol. 57, no. 10, Sept. 3, 1990, pp. 1058-1060.
19. Bhasin, K.B., et al.: Determination of Surface Resistance and Magnetic Penetration Depth of Superconducting $\text{YBa}_2\text{Cu}_3\text{O}_{7.6}$ Thin Films by Microwave Power Transmission Measurements. NASA TM-103616, 1990 (to be published in, *IEEE Trans. Magnetics*, 1991).

20. Bhasin, K.B., et al.: Microwave Conductivity of Laser Ablated $\text{YBa}_2\text{Cu}_3\text{O}_{7-\delta}$ Superconducting Films and its Relation to Microstrip Transmission Line Performance. AMSAHTS 1990: Advances in Materials Science and Applications of High Temperature Superconductors, Y. Flom, ed., NASA CP-10043, 1990, pp. 78-81.
21. Klein, N., et al.: Millimeter Wave Surface Resistance and London Penetration Depth of Epitaxially Grown $\text{YBa}_2\text{Cu}_3\text{O}_{7-x}$ Thin Films. Physica C, vols. 162-164, pt. II, 1989, pp. 1549-1550.
22. Miranda, F.A., et al.: Complex Permittivity of Lanthanum Aluminate in the 20 to 300 K Temperature Range from 26.5 to 40.0 GHz. Microwave Opt. Technol. Lett., vol. 3, no. 1, Jan. 1990, pp. 11-13.
23. Hansen, R.C.: Superconducting Antennas. IEEE Trans. Aerospace Electron., vol. 26, no. 2, Mar. 1990, pp. 345-355.

TABLE I. - KEY PROPERTIES OF MICROWAVE SUBSTRATE MATERIALS AND THE TRANSITION TEMPERATURE (T_c) FOR LASER ABLATED $\text{YBa}_2\text{Cu}_3\text{O}_7$ FILM ON THE VARIOUS SUBSTRATES

Material	Laser, T_c (K)	Dielectric constant	Loss tangent	Lattice size, Å
Magnesium oxide (MgO)	88	9.65	4×10^{-4}	4.178 (100)
Lanthanum aluminate (LaAlO_3)	90	22	5.8×10^{-4}	3.792 (110)
Lanthanum gallate (LaGaO_3)	88	27	2×10^{-3}	3.892 (110)
Sapphire (Al_2O_3)	73	9.4	1×10^{-6}	5.111 (011)
Yttria stabilized zirconia (ZrO)	89	11.6	6×10^{-4}	3.8795 (100)
Silicon (Si)	--	12	10×10^{-4}	5.43 (100)
Gallium arsenide (GaAs)	--	13	6×10^{-4}	5.563 (100)

TABLE II. - THE REAL PART OF THE CONDUCTIVITY $\sigma = \sigma_1 + i\sigma_2$, AND AT 77 K AND 33 GHz, THE CALCULATED R_s AT 5 GHz, THE MAGNETIC PENETRATION DEPTH (λ_o) FOR $\text{YBa}_2\text{Cu}_3\text{O}_7$ FILMS ON LaAlO_3 , MgO, AND YTTERIA STABILIZED CUBIC ZIRCONIA (YSZ)

Substrate	Thickness, nm	σ_1 , s/m	R_s (Ω), 33 GHz	R_s (Ω), 5 GHz	λ_o , nm
LaAlO_3	177	2.5×10^5	1.8×10^{-3}	41×10^{-6}	360
MgO	350	1.2×10^5	5.9×10^{-3}	135×10^{-6}	530
YSZ	120	2.4×10^5	2.5×10^{-3}	57×10^{-6}	590

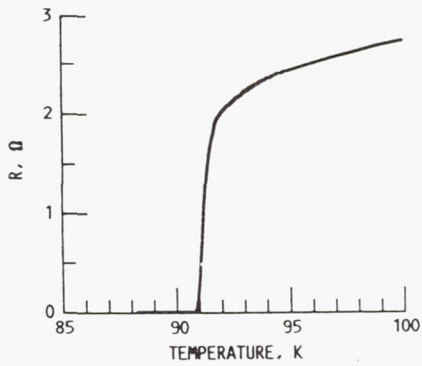


FIGURE 1. - D.C. RESISTANCE VERSUS TEMPERATURE OF LASER ABLATED $\text{YBa}_2\text{Cu}_3\text{O}_{7-\delta}$ FILM ON LaAlO_3 .

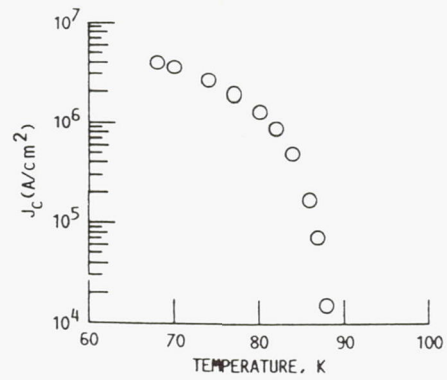


FIGURE 2. - CRITICAL CURRENT DENSITY OF LASER ABLATED $\text{YBa}_2\text{Cu}_3\text{O}_{7-\delta}$ FILM ON LaAlO_3 .

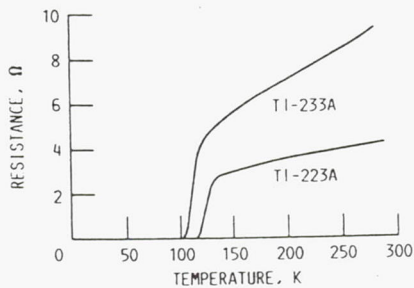


FIGURE 3. - D.C. RESISTIVITY VERSUS TEMPERATURE OF TWO $\text{Tl}_2\text{Ca}_2\text{Ba}_2\text{CuO}_x$ FILMS.

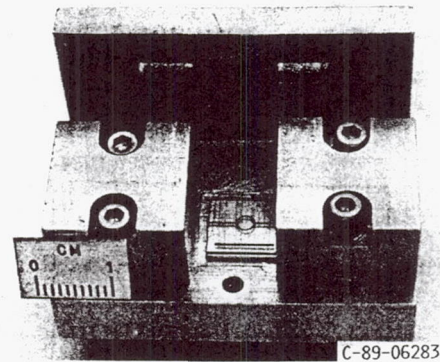


FIGURE 4. - WAVEGUIDE TEST FIXTURE USED FOR THE MEASUREMENT OF "Q" VALUES OF SUPERCONDUCTING RING RESONATORS.

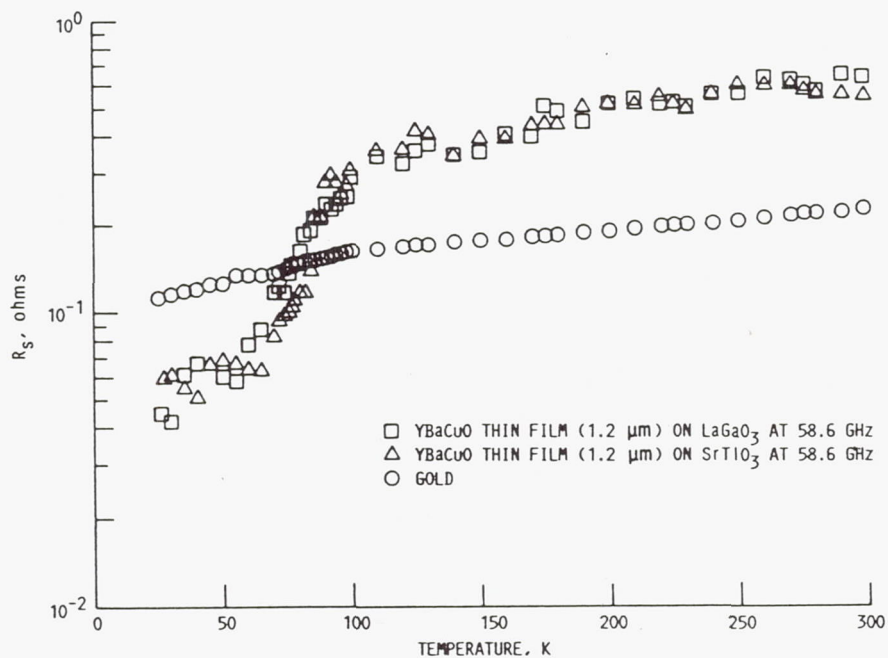


FIGURE 5. - SURFACE RESISTANCE (R_s) VERSUS TEMPERATURE FOR GOLD AND LASER ABLATED $\text{YBa}_2\text{Cu}_3\text{O}_{7-\delta}$ FILMS ON THE INDICATED SUBSTRATES AS MEASURED IN THE 58.6 GHz GOLD CAVITY.

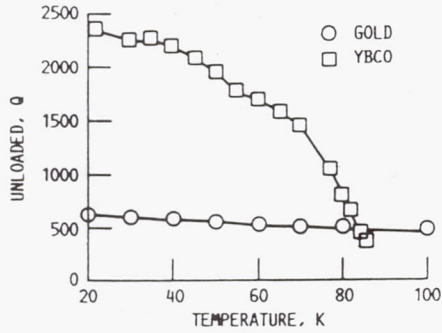


FIGURE 6. - 35 GHz RING RESONATOR UNLOAD "Q" VERSUS TEMPERATURE FOR GOLD AND LASER ABLATED $\text{YBa}_2\text{Cu}_3\text{O}_{7-\delta}$ FILM ON LaAlO_3 .

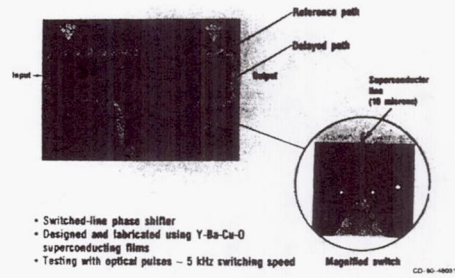
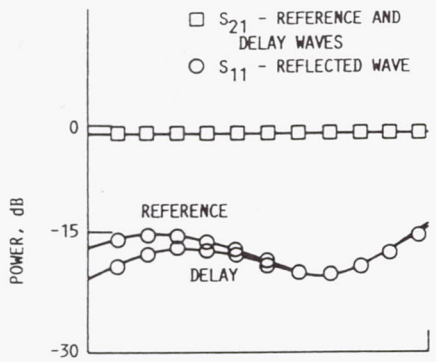
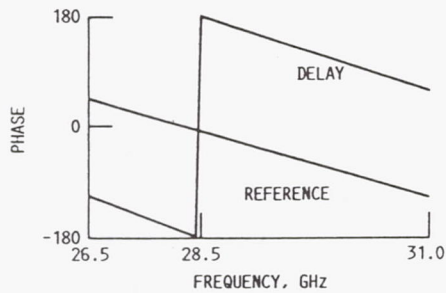


FIGURE 7. - OPTICALLY CONTROLLED SUPERCONDUCTOR PHASE SHIFTER.



(a) S_{21} AND S_{11} FOR REFERENCE, DELAY, AND REFLECTED WAVES.



(b) PHASE RESPONSE VERSUS FREQUENCY FOR REFERENCE AND DELAY PATHS.

FIGURE 8. - THEORETICAL RESPONSE FOR THE DESIGNED OPTICALLY CONTROLLED $\text{YBa}_2\text{Cu}_3\text{O}_{7-\delta}$ PHASE SHIFTER AT 77K.

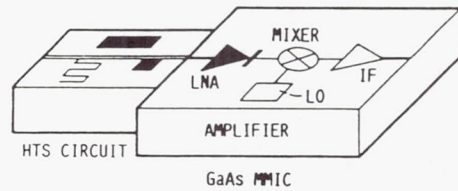
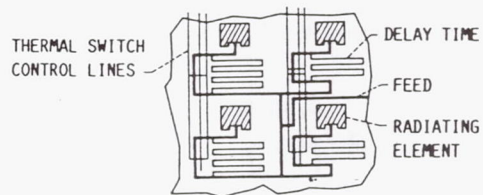


FIGURE 9. - SUPERCONDUCTING GaAs MMIC HYBRID RECEIVER.



4x4 ARRAY PRELIMINARY DESIGN

FIGURE 10. - PRELIMINARY DESIGN OF A THERMALLY SWITCHED PHASE ARRAY SUPERCONDUCTING ANTENNA FOR A 4x4 ARRAY.

High Temperature Superconductive Microwave
Technology for Space Applications

R. F. Leonard, D. J. Connolly, K. B. Bhasin,
J. D. Warner, and S. A. Alterovitz

NASA Lewis Research Center
Cleveland, Ohio 44135

ABSTRACT

Research on thin film ceramic superconductors has enjoyed success and it is now clear that this technology has advanced to the point that it is ready for application. Many of the thin film applications involve microwave passive devices and there is great interest in the development of high temperature superconductor (HTS) based active three terminal devices to provide the foundation of a complete high performance cryogenic microwave circuit technology. Of course it is widely known that because of the temperature dependence of semiconductor materials - especially III-V semiconductor materials, three terminal HTS devices may not be necessary for the development of cryogenic microwave circuits with superior performance. NASA is active in the development of HTS microwave circuit components. In order to provide, in the relatively short term, all of the elements of high performance cryogenic microwave circuits we are focusing our active device efforts on optimizing III-V material based on semiconductor active device designs for cryogenic operation. Progress in this work, and also in our HTS microwave passive device development effort is reviewed.

1. BACKGROUND

Immediately upon the announcement of the discovery of high temperature superconductors early in 1987^{1,2} NASA Lewis Research Center initiated an investigation of their application to microwave electronics, particularly for use in communications, radar, or radiometry systems. In the absence of commercially available sources of materials, however, the necessary first step in this research was the fabrication of appropriate films. This activity has concentrated mainly on the $\text{YBa}_2\text{Cu}_3\text{O}_{7-x}$ (YBCO) system, since it was the first "high temperature" material discovered and its properties are best known. In addition, however, NASA sponsors activities aimed at the evaluation of $\text{Tl}_2\text{Ca}_2\text{Ba}_2\text{Cu}_3\text{O}_x$ (TCBCO). For either system, the next critical step was the identification of substrates which would be useful for microwave applications. Most initial investigations of YBCO films for example, were conducted on strontium titanate substrates, which offered the advantages of being nearly lattice-matched with YBCO and displaying little or no chemical interaction at the interface.

Strontium titanate, however, has an unacceptably large dielectric constant for use as a microwave substrate. On the other hand, the most commonly used microwave substrates, such as silicon and MgO, appear to be incompatible with the YBCO. A major step toward the resolution of this difficulty was taken with the identification of lanthanum aluminate as a useful substrate. Although its loss tangent is larger than one would like, it has served as a useful demonstration substrate for most of the circuitry developed to date.

In addition to film deposition, other critical areas requiring work included rf evaluation, microwave circuit fabrication, and rf testing of cryogenic circuits. All of these have been addressed with considerable success, and the fabrication of passive superconducting microwave circuits has now been conclusively demonstrated.

In the course of these investigations, however, it became clear that the growth of complex multilayer structures, such as are necessary for the fabrication of three terminal devices would require a considerably longer effort. It seemed prudent therefore to consider semiconductor materials and devices which might be suitable for incorporation into amplifiers, switches, phase shifters, and other microwave circuitry which utilizes HTS technology and operates at cryogenic temperatures. Such devices would be easily integrable with superconducting circuits based on microstrip or coplanar waveguide transmission lines. They would in fact offer some advantages, such as graceful degradation in the event of a cooling failure. An example of such a circuit, a hybrid low noise receiver is shown in Figure 1. To develop appropriate devices, an investigation of low band gap materials such as indium-rich InGaAs was undertaken in collaboration with the University of Michigan.

2. FILM FABRICATION AND EVALUATION

2.1 Film deposition

2.1.1 YBCO films

In general it has been observed that the most useful films for microwave applications are those deposited by methods which require no post annealing.³ Such a high temperature post anneal is thought to induce chemical reactions at the film-substrate interface to the detriment of the microwave properties. This has been verified by work at NASA Lewis, where three methods of deposition were investigated. These included sequential evaporation, co-evaporation, and laser ablation.

The first superconducting films produced under the NASA program were grown at Ohio

State University by means of sequential evaporation of copper, barium fluoride, and yttrium.⁴ These films played an important role in the program in that they were useful in the development of characterization methods. However, the films required post-annealing and exhibited low transition temperatures, low critical currents, high porosity, and were strongly a-axis aligned.⁵

A second technique currently under investigation for growth of YBCO films is co-evaporation.⁶ This work is being carried out at Oberlin College in cooperation with NASA Lewis personnel, and deposits films at room temperature by co-evaporating Cu, BaF², and Y from separate electron guns. Films grown by this technique exhibit high critical temperatures (90K), but reduced critical currents, apparently due again to high temperature post-annealing which produces a-axis alignment. However, coevaporation does offer the advantage that it is amenable to conventional photoresist/lift-off techniques for patterning. Using such methods, pattern features as small as 2 microns have been produced.

Unquestionably, the most successful method for production of thin films of YBCO has been laser ablation.⁷ The geometry of the process is shown in Figure 2. Pulses from an excimer laser (248 nm) are focused onto a YBCO target, supplying an instantaneous power density of 100 to 200 megawatts/cm² at the target surface, and producing a plasma plume whose composition closely reflects the stoichiometry of the target. Following the deposition, which takes place with the substrate heated to 775°C, a 2-hour in-situ anneal in oxygen at the reduced temperature of 450°C is carried out. The DC properties of films produced by laser ablation are shown in Figures 3 and 4. Critical temperatures as high as 90.6 K and critical currents as high as 2x10⁶ amperes/cm² at 77 K have been observed. In addition, X-ray studies indicate that the films are strongly c-axis aligned.

2.1.2 TCBCO films

The development of high quality films of thallium-based material is less mature than the work on YBCO. However, promising results have been obtained from NASA-sponsored work both at the University of Nebraska, where efforts have focused on laser ablation, and at the University of Cincinnati, where investigations concentrate on the rf-sputtering of a compressed powder target followed by annealing in thallium vapor. Nebraska has achieved a critical temperature as high as 115K, but films generally are rather rough and porous.⁸ Cincinnati has produced dense films with T_c between 103K and 107K, but the films are clearly a mixture of 2223 and 2212 phases.^{9,16} Thallium films have also been produced by Superconductive Technology Incorporated under NASA's Small Business Innovative Research (SBIR) program, and have in fact been patterned and incorporated into simple microwave circuits.

2.2 RF characteristics of films

The superconducting films produced here have been extensively studied to determine their intrinsic RF properties, which in turn are useful in assessing their potential for use in microwave circuits. The basic experiment involves measuring the relative magnitude and phase of RF power transmitted through a thin film of the material under study. Measurements were made under vacuum in a specially designed chamber. The sample was clamped between two waveguide flanges mounted on top of the cold head of the refrigerator. Waveguides were made of thin walled stainless steel to minimize heat conduction. From the transmission data, assuming a two-fluid model, one may extract the complex conductivity, the magnetic penetration depth, and the RF surface resistance. Typical experimental data are shown in Figure 5. The results of the analysis are given in reference 11. In addition, evaluations have been carried out using a resonant cavity at 58 GHz.¹²

3. PASSIVE MICROWAVE CIRCUITS

3.1 Overview

A number of microwave circuits have been fabricated and tested at this time. For the most part, these were selected either on the basis of the fundamental information which they could yield, or on the likelihood of their use in a realistic system. In most cases, in addition, ease of design and fabrication was a consideration. As a result, at this time, simple microstrip circular resonators have been investigated fairly intensively. In addition to being relatively easy to design and fabricate, they are an invaluable tool for obtaining realistic information on the microwave performance of film-substrate combinations. Other, more complex circuits which have been investigated include an optically activated phase shifter, a 7 GHz microstrip filter (in collaboration with COMSAT Laboratories), a 10 GHz dielectric resonator filter (in collaboration with Ford Aerospace), a 10 GHz patch antenna element (in collaboration with NASA Johnson Space Center, and a patch array antenna (in collaboration with Ball Aerospace).

3.2 Circuit fabrication

For passive circuits using YBCO films standard photolithography with negative photoresist and wet chemical etching was used. The etchant was either a 1 at% solution of bromine in ethanol or a dilute phosphoric acid in water. For all of the microstrip circuits described here, a normal metal ground plane consisting of 1 micron of gold atop 10 nm of titanium was used.

3.3 Circuit evaluation

3.3.1 Cryogenic apparatus

Testing of microstrip circuits at cryogenic temperatures was carried out using the experimental test fixture shown in Figure 6. It was placed in a cryostat with closed-cycle cooling and waveguide input for RF signals via a cosine tapered ridge waveguide transition to microstrip. The RF measurements used conventional calibration methods and an automatic network analyzer.

3.3.2 Microstrip resonators

Microstrip ring resonators of the type shown in Figure 6 have been studied over the frequency range 34 to 36 GHz and at temperatures from 21K to above T_c .¹³ Such circuits have been fabricated and tested, using both YBCO and TCBCO circuits, a lanthanum aluminate substrate, and a normal metal ground plane. Typical data (return loss versus frequency) for a YBCO circuit at several temperatures are shown in Figure 7. From these data, it is possible to extract unloaded Q-values for the resonator. These are shown in Figure 8 as a function of temperature for YBCO circuits, TCBCO circuits and gold circuits. It can be seen that the Q for the YBCO resonator ranges from 2500 at 20 K to 1000 at 77 K. This corresponds to a surface resistance of approximately 8 milliohms at 77 K and 35 GHz, a value two to three times better than copper at the same temperature and frequency. For the TCBCO devices fabricated under NASA's SBIR program by Superconductor Technologies Incorporated, the Q-values are somewhat lower than for YBCO, except of course in the temperature region above the critical temperature of YBCO. It seems likely that the poorer performance is in part due to the fact that the techniques for production of the TCBCO films include post-annealing.

3.3.3 Phase shifters

In principle, considerable improvement in performance, especially insertion loss, could be obtained simply by substituting a superconducting patch for an active device such as a FET or diode in a switched line, true time delay phase shifter. The layout for such a device is shown in Figure 9. For the device fabricated at NASA Lewis, switching between normal and superconducting states is induced bolometrically, heating the superconducting switch with optical energy delivered via optical fiber. Preliminary tests indicate that switching times achievable in this manner are on the order of 200 microsec, which is likely too slow for

many applications. Thermal analysis of the device also indicates that faster switching times are unlikely unless substrates with smaller thermal conductivities are employed. At the present time, a substrate with both the ideal thermal and microwave characteristics has not been found.

3.3.4 Microstrip filter

The fabrication of a microstrip filter has been carried out in conjunction with COMSAT Laboratories. Based on the lower surface resistance of the superconducting material, it should be possible to obtain such a filter with a reduced in-band insertion loss and sharper passband edges than could be obtained with normal metals. Using a COMSAT design, NASA Lewis personnel have fabricated a 2-pole, 7 GHz microstrip filter. A photo of the finished filter is shown in Figure 10. The filter is presently undergoing testing at COMSAT. Its preliminary frequency response is shown in Figure 11.

3.3.5 Dielectric resonator filter

A 3-pole dielectric resonator filter for operation at 9.2 GHz has been fabricated in conjunction with Ford Aerospace. The filter, which was designed and built by Ford, uses NASA-supplied superconducting films as cavity walls, thereby reducing in-band insertion loss. A schematic diagram of the filter is shown in Figure 12. The filter is intended as one of the experiments to be tested in space as part of the Naval Research Laboratory's High Temperature Superconductor Space Experiment (HTSSE). To date Ford has delivered 5 modules to NRL, where they have been subjected to vibration and thermal testing. The HTSSE launch is scheduled for 1992. Complete data for the Ford superconducting filter is not yet available.

3.3.6 Superconducting antennas

Two investigations of the application of HTS materials to antennas are presently being pursued under NASA sponsorship, with active participation by Lewis personnel. The first of these involves the application of superconducting materials (YBCO) to a simple patch radiator and its associated feed microstrip feed lines. The 10 GHz radiating element, which was designed by Johnson Space Center and fabricated at Lewis, is presently undergoing testing (radiation patterns and efficiency) at JSC. For this application reduced conductor losses should increase the radiation efficiency of such a device, and thereby increase the

overall gain of the antenna. No experimental results are available at this time.

A parallel investigation of the use of HTS films for antennas is studying their advantages in arrays, where excessive conductor losses in the power divider/feed network can significantly limit the real gain of an array. This work is being carried out in cooperation with Ball Aerospace, and is also supported by NASA through its SCAR program. As with Ford and JSC, a first design of a 30 GHz 2x2 array has been carried out by Ball and the device has been fabricated at NASA Lewis. The finished design, including power divider and feed network, is shown in Figure 13 and is presently undergoing testing at Ball.

4. SEMICONDUCTOR DEVICES FOR CRYOGENIC CIRCUITS

In collaboration with the University of Michigan, NASA Lewis has systematically investigated the performance of FETs based on an $\text{In}_x\text{Ga}_{1-x}\text{As}/\text{InP}$ structure. As shown in Figure 14, the InGaAs system offers the possibility of exceptionally low band gaps. Such materials may not be practical for use in room temperature devices due to thermally generated leakage current, however, this should not be a problem at cryogenic temperatures. The structure, shown in Figure 15, consists of an active channel of InGaAs on an InP substrate. By using active layer indium concentrations higher than 53% percent, one creates a "pseudomorphic" structure, in which the active layer is strained due to the lattice mismatch between InGaAs and InP. In addition, however, the higher indium concentration and lower band gap energy of the InGaAs result in better charge containment, higher mobility, higher cutoff frequencies, and greater performance enhancement at reduced temperatures. Also, such devices should avoid the problems arising from the presence of DX centers in similar devices using AlGaAs active layers.

Michigan has grown material and fabricated FET devices with 1 micron gate lengths for indium concentrations from 53% to 80%. The devices have been tested as a function of frequency (1-26 GHz) and temperature (55-300 K) at NASA Lewis. The results are shown in Figure 16. It is clear that a sizeable improvement in performance is obtained by cooling these devices to approximately 120K, although further improvement below that point is marginal. In addition, it would appear that indium concentrations higher than approximately 70% do not yield further improvement in performance. Michigan researchers, however, have attributed this to the development of "islands" of nonuniform growth during the molecular beam epitaxial deposition of the InGaAs layer. Efforts are planned to remedy this problem by means of migration-enhanced epitaxy, which will control growth parameters in such a way as to prohibit initiating the growth of any layer until the preceding one has achieved full coverage of the substrate. If true monolayer epitaxy can be achieved thereby,

it seems likely that devices can be further improved by using indium concentrations higher than 70%.

5. CONCLUSIONS

At the present time, a variety of passive microwave circuits have been fabricated using high temperature superconductor technology. Their performance in most cases, particularly at frequencies below 10 GHz, represents a significant improvement over normal metal components. In addition, NASA Lewis will soon begin efforts to integrate semiconductor materials with passive superconducting components. It is clear, however, that specific system studies are necessary to determine whether the performance enhancement achieved offsets the obvious complication introduced by the cooling requirements. Clearly, this trade-off would be affected dramatically if components could be fabricated from TCBCO, whose 110K critical temperature makes it a strong candidate for passive cooling in space. At the present time, however, it would appear that improvements in TCBCO processing are required in order to obtain surface resistances comparable to YBCO.

6. REFERENCES

1. J. G. Bednorz and K. A. Muller, *Z. Phys. B.* 64, 189(1986)
2. C. W. Chu, Ph. Hor, R. L. Meng, L. Gao, Z. J. Huang, and Y. Q. Wang, *Phys. Rev. Lett.*, 58, 405 (1987)
3. K. B. Bhasin and V. O. Heinen, *SPIE Proceedings* 1292, 1990
4. G. Valco, P. C. Claspy, J. D. Warner, N. C. Varaljay and K. B. Bhasin, *NASA TM* 103144, 1990
5. M. A. Stan, S. A. Alterovitz, D. Ignjatovic, and K. B. Bhasin, *Physica C* 162-164, 365 (1989)
6. P. M. Mankiewich, J. H. Scoffield, W. J. Skoepol, P. E. Howard, D. H. Dayem and E. Good, *Appl. Phys. Lett.*, 51, 1753
7. J. D. Warner, J. E. Meola and K. A. Jenkins, *NASA TM* 102350, 1990
8. K. B. Erington, and N. J. Ianno,, to be published in *Journal of Applied Physics*
9. G. Subramanyam, F. Radpour, V. J. Kapoor, and G. H Lemon, *J. Appl. Phys.* 68, 1157 (1990)
10. G. Subramanyam, F. Radpour, and V. J. Kapoor, *Appl. Phys. Lett.* 56, 1799 (1990)
11. K. B. Bhasin, J. D. Warner, F. A. Miranda, W. L. Gordon, and H. S. Newman, *NASA TM* 103616, 1990 (to be published in *IEEE Transactions in Magnetics* (March 1991)
12. F. A. Miranda, W. L. Gordon, K. B. Bhasin, and J. D. Warner, *Appl. Phys. Lett.* 57, 1058 (1990)
13. K. B. Bhasin, J. D. Warner, R. R. Romanofsky, W. O. Heinen, and C. M. Chorey, 1990 *IEEE MTT-S International Microwave Symposium Digest*, Vol. 1, IEEE, 1990, pp. 269-272

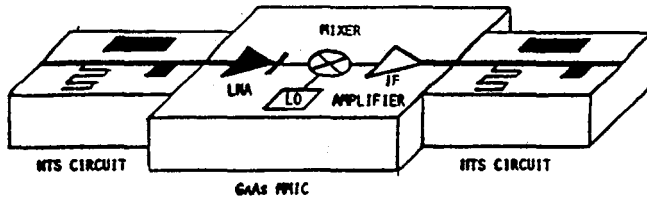


FIGURE 1. CONCEPTUAL HYBRID SUPERCONDUCTING-SEMICONDUCTING RECEIVER CIRCUIT

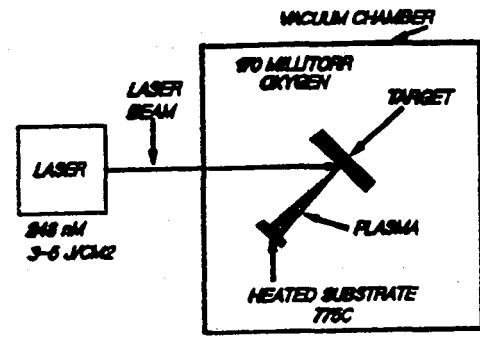


FIGURE 2. LASER ABLATION TECHNIQUE

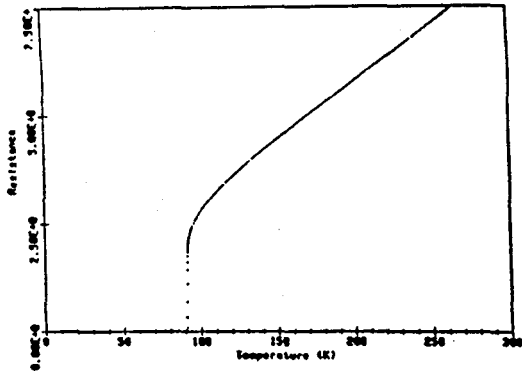


FIGURE 3. DC RESISTANCE OF A LASER-ABLATED YBCO FILM ON LANTHANUM ALUMINATE

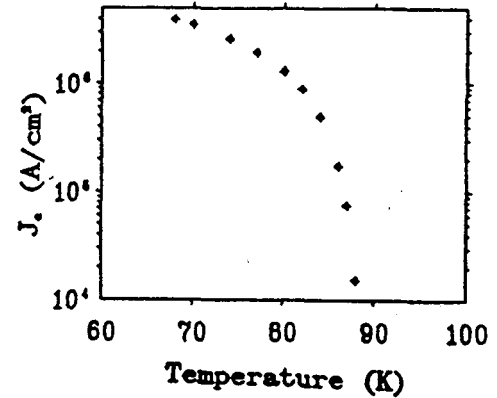


FIGURE 4. DC CRITICAL CURRENT FOR LASER-ABLATED YBCO FILM ON LANTHANUM ALUMINATE

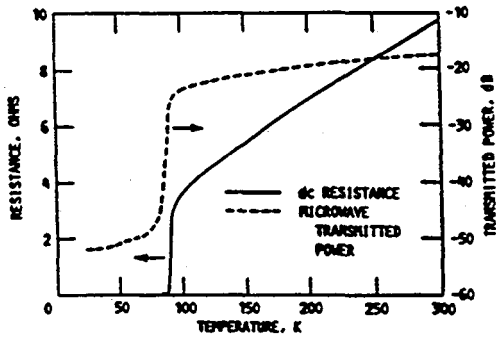


FIGURE 5. DC RESISTANCE AND MICROWAVE TRANSMITTED POWER AT 35 GHz YBCO FILM ON LANTHANUM ALUMINATE

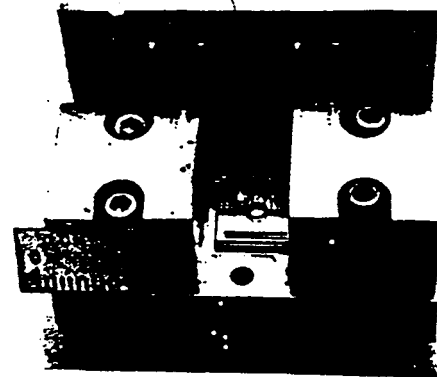


FIGURE 6. TEST FIXTURE AND YBCO MICROSTRIP RING RESONATOR

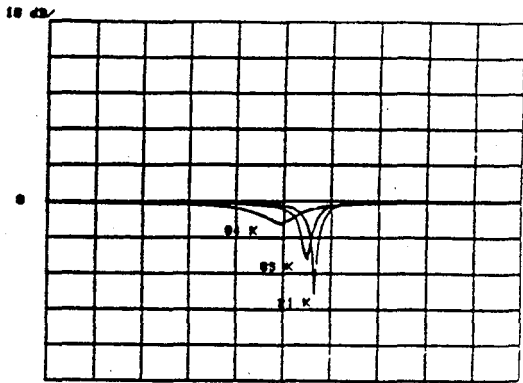


FIGURE 7. RETURN LOSS, S₂₁, OF YBCO MICROSTRIP RING RESONATOR FROM 34 TO 36 GHz

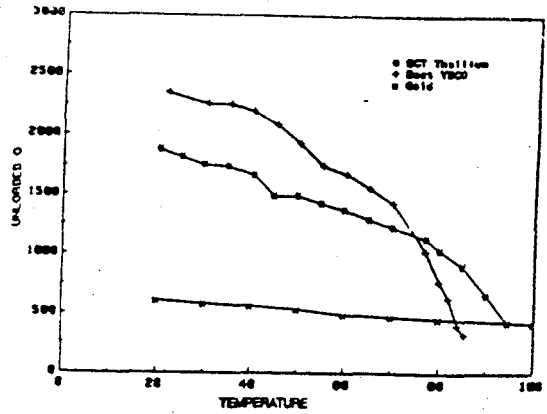


FIGURE 8. RELATIVE PERFORMANCE OF YBCO, TBCO, AND GOLD MICROSTRIP RING RESONATORS

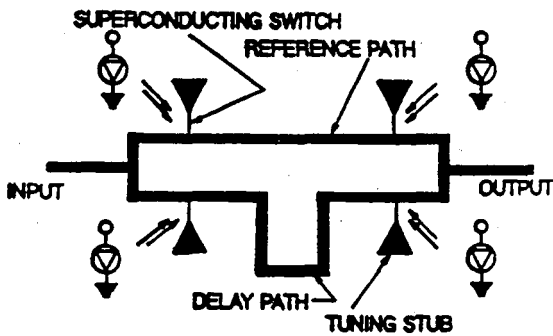


FIGURE 9. OPTICALLY CONTROLLED SUPERCONDUCTING PHASE SHIFTER

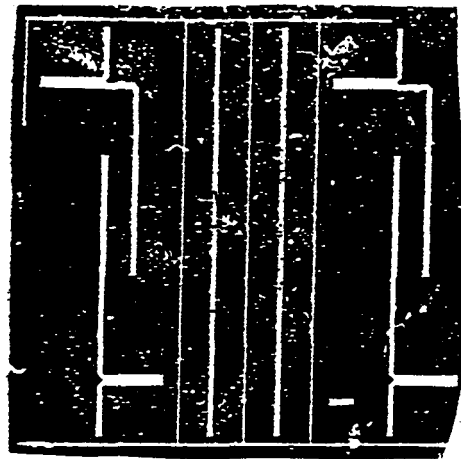


FIGURE 10. NASA/COMSAT SUPERCONDUCTING 7 GHz 2-POLE FILTER

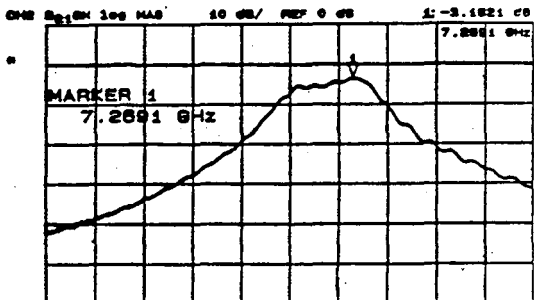


FIGURE 11. RESPONSE OF COMSAT SUPERCONDUCTING FILTER - S₂₁ FROM 7 TO 9 GHz

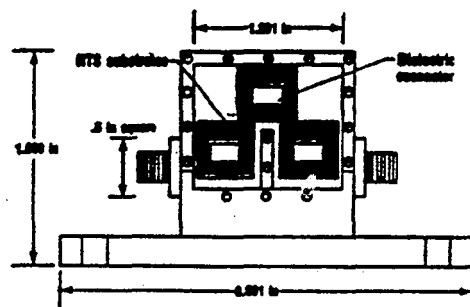


FIGURE 12. 3-POLE HIGH T_c SUPERCONDUCTING DIELECTRIC RESONATOR FILTER

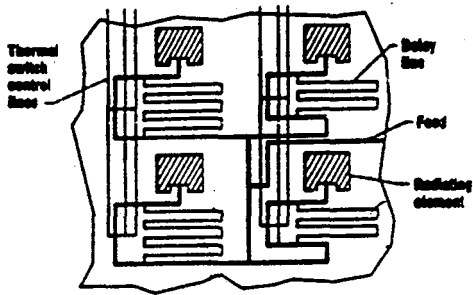


FIGURE 13. PRELIMINARY DESIGN FOR A 4x4 HIGH-T_c SUPERCONDUCTING ANTENNA

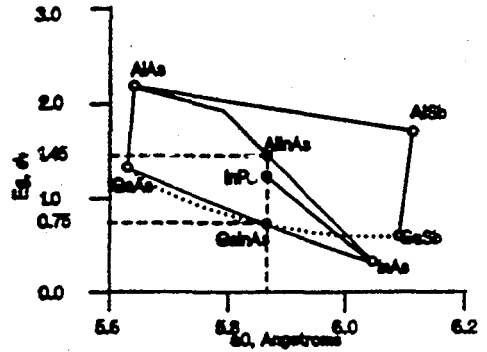


FIGURE 14. ENERGY GAP vs LATTICE CONSTANT

100 Å	In _{0.57} Ga _{0.43} As	n ⁺ (5×10 ¹⁸ cm ⁻³)
200 Å	In _{0.57} Al _{0.43} As	i
150 Å	In _{0.57} Al _{0.43} As	n ⁺ (5×10 ¹⁸ cm ⁻³)
50 Å	In _{0.57} Al _{0.43} As	i
54-150 Å	In _{0.57} Ga _{0.43} As	i
400 Å	In _{0.57} Ga _{0.43} As	i
4000 Å	In _{0.57} Al _{0.43} As	i
InAlAs/InGaAs Superlattices		i
S. I. InP (100) Substrate		

FIGURE 15. CRYOGENIC HEMT STRUCTURE

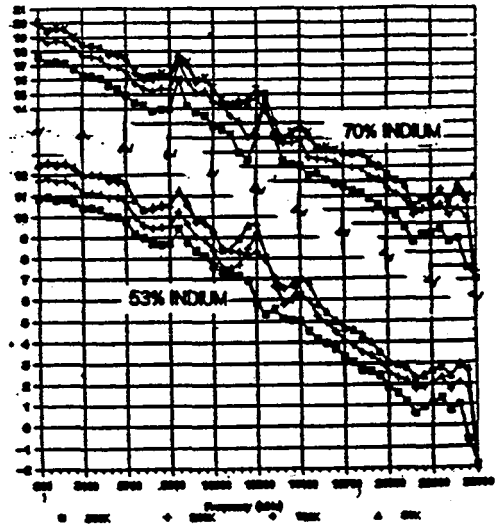


FIGURE 16. POWER GAIN, S₂₁, FOR 1-MICRON InGaAs/InP HEMT FETs WITH 53% AND 70% INDIUM

EMERGING APPLICATIONS OF HIGH-TEMPERATURE SUPERCONDUCTORS

FOR SPACE COMMUNICATIONS

Vernon O. Heinen, Kul B. Bhasin, and Kenwyn J. Long
National Aeronautics and Space Administration
Lewis Research Center
Cleveland, OH 44135

SUMMARY

Proposed space missions require longevity of communications system components, high input power levels, and high speed digital logic devices. The complexity of these missions calls for a high data bandwidth capacity. Incorporation of high temperature superconducting (HTS) thin films into some of these communications system components may provide a means of meeting these requirements. Space applications of superconducting technology has previously been limited by the requirement of cooling to near liquid helium temperatures. Development of HTS materials with transition temperatures above 77 K along with the natural cooling ability of space suggest that space applications may lead the way in the applications of high temperature superconductivity.

In order for HTS materials to be incorporated into microwave and millimeter wave devices, the material properties such as electrical conductivity, current density, surface resistivity and others as a function of temperature and frequency must be well characterized and understood. The millimeter wave conductivity and surface resistivity have been well characterized, and at 77 K are better than copper. Basic microwave circuits such as ring resonators have been used to determine transmission line losses. Higher Q values than those of gold resonator circuits were observed below the transition temperature. Several key HTS circuits including filters, oscillators, phase shifters and phased array antenna feeds are feasible in the near future. For technology to improve further, good quality, large area films must be reproducibly grown on low dielectric constant, low loss microwave substrates. Tradeoffs between superconducting microwave circuits with cryogenic systems and normal metal microwave circuits will have to be quantitatively established to determine the suitability for advanced communications systems.

INTRODUCTION

Space application of superconducting technology has previously been limited by the requirement of cooling to near liquid helium temperatures. The discovery of HTS materials with transition temperatures above 77 K along with the natural cooling properties of space suggest that space operations may lead the way in the applications of high temperature superconductivity. Proposed space missions require longevity of communications system components, high input power levels, and high speed digital logic devices. The complexity of these missions calls for a high data bandwidth capacity. To ensure adequate efficiencies, the microwave surface resistance of the component materials must be reduced to as low a level as possible. Incorporation of high critical temperature superconducting (HTS) thin films into some of these communications system components may provide a means of meeting these requirements as well as

offering enhanced efficiency and reductions in size and weight.

The use of high T_c superconductors in a microwave system requires development of thin films on microwave substrates which can be patterned into desired microwave circuits such as filters, phase shifters, ring resonators and delay lines. The superconducting thin films for microwave circuits need to be deposited on low-dielectric-constant and low-loss substrates, have smooth morphology, high critical temperature T_c , high critical current density J_c , and low surface resistance R_s . Furthermore, films on the substrates must be evaluated in devices such as microstrip or ring resonator circuits to determine the quality factor, Q , and various loss factors before appropriate microwave circuit applications can be developed.

STATUS OF HIGH- T_c SUPERCONDUCTOR PROPERTIES

To obtain high quality YBaCuO films on suitable substrates, the lattice constants of the substrate must be matched to those of the film, and there must be no detrimental chemical reactions between the substrate and the film. In addition, the film composition must be as close as possible to the desired stoichiometry. Many of the physical and chemical deposition techniques used to obtain high quality films require post-annealing at high temperatures. This high-temperature anneal causes undesirable chemical interactions at the film-substrate interface, making it unsuitable for microwave applications (ref. 1). To circumvent this problem, an in situ annealing procedure, which allows lower growth temperatures, has been used to grow epitaxial films using a laser ablation technique (ref. 2).

The best laser-ablated film had a T_c of 89.8 K immediately after deposition, as determined by a standard four-point resistance measurement. From x-ray diffraction data, the film was determined to be c-axis aligned. In table I, we list the performance of $YBa_2Cu_3O_7$ thin films on various microwave substrates along with physical properties of these substrates. As can be seen, the value of J_c was greater than 10^6 A/cm² at 77 K.

Surface resistance characterization of superconducting films offers valuable information on the film quality for microwave surface applications. Currently, surface resistance values are obtained by cavity (refs. 3 and 4) and stripline measurements (ref. 5). Correlation between material properties (i.e., T_c , dc conductivity above T_c , and penetration depth) and surface resistance are still not well understood for new high T_c superconducting films. Conductivity is a complex quantity, $\sigma = \sigma_1 + j\sigma_2$. For $\sigma_2 \gg \sigma_1$ one can obtain the surface resistance of superconducting film

$$R_s = 0.5\sigma_1\mu/\sigma_2^{3/2} \quad (1)$$

where σ_2 is related to the penetration depth λ by

$$\sigma_2 = 1/\omega\mu\lambda^2 \quad (2)$$

To obtain superconducting film surface resistance values that are lower than those of a normal metal, the smallest values of σ_1 and λ are desired. Miranda, et al., (ref. 6) have measured microwave transmission in a waveguide for superconducting films. From the transmission data, using the two-fluid models, σ_1 and λ have been obtained. The surface resistance for films deposited on LaAlO_3 was calculated. In figure 1, which is adopted from reference 7, we show the quadratic variation of the surface resistance for laser-ablated YBaCuO films on microwave substrates. The surface resistance is several orders of magnitude lower than that of copper. Surface resistance, penetration depth, and microwave conductivity measurements provide valuable information on the quality of these films for microwave circuits.

Microstrip resonators patterned from thin films on microwave substrates allow direct measurement of microstrip losses. We have fabricated microstrip ring resonators operating at 35 GHz from laser-ablated YBaCuO thin films deposited on lanthanum aluminum substrate (ref. 8). Several groups have studied resonator circuits at lower frequencies (refs. 5, 9 to 11). The resonator circuits we fabricated were patterned by standard photolithography using negative photoresist and a "wet" chemical etchant. These resonators were characterized using a Hewlett-Packard 8510 Automatic Network Analyzer, operating in a WR-28 waveguide. Two features are apparent: (1) the coupling changes with temperature (the coupling coefficient increases with decreasing temperature), and (2) the resonant frequency shifts with temperature. This change is a consequence of the dependence of internal impedance of the strip on the varying normal and superconducting electron densities.

The best resonators measured to date have shown unloaded Q values ranging from 2500 to 1000 at 20 and 77 K, respectively. This corresponds to a surface resistance value of, at most, 15 m Ω at 77 K at 35 GHz, a value two to three times better than that of copper at the same temperature and frequency. The 33 to 37 GHz YBaCuO ring resonator circuit developed at NASA Lewis is viewed as a precursor to frequency-selective filters and may have potential application in enhancing the efficiency of radiating antenna elements. Such HTS resonating circuits have a high Q as compared to equivalent normal metal circuits and may afford reduction in size and mass of electronically-steered millimeter wave antennas.

POTENTIAL APPLICATIONS

Passive Microwave Circuits

High T_c superconducting thin films have shown lower surface resistance than copper. Low conductor losses have been demonstrated for a high T_c superconducting ring resonator circuit. Low surface resistance and conductor losses are desirable in passive microwave circuits used in communication and radar systems since they offer increased bandwidth, reduction in loss and size, and provide low noise. A complete system analysis of the impact of high T_c superconducting microwave circuits remains to be undertaken. From a block diagram of a satellite transponder (fig. 2), we have considered several potential applications of HTS microwave circuits in satellite communications system components. Based on results obtained to date on the performance of

superconducting microstrip resonator circuits with high Q values, one can easily project the application of superconducting passive circuits as low loss, high Q filters (ref. 12), high Q resonators, delay lines, power splitter combiners, and resonator stabilized oscillators.

HTS materials may be most effective in enhancing the efficiency of phased-array antennas when incorporated into interconnects and power dividers. Thin films of YBaCuO offer a reduction in resistive heating loss relative to gold and copper, and could conceivably be designed into microstrip lines. This frequency-dependent resistive heating loss effect is most significant at frequencies below Ka-band (~ 20 to 30 GHz). However, as frequency increases individual elements become smaller. The number of required elements increases, necessitating more complex interconnects, thereby making the overall savings from HTS materials more significant.

At submillimeter frequencies ($f \geq 300$ GHz), RF ohmic losses in antenna elements of normal metals are on the order of a fraction of a decibel. HTS antenna patch elements would thus yield only a slight advantage over normal metal components in this frequency range. However at millimeter-wave operation ($30 \text{ GHz} \leq f < 300 \text{ GHz}$), ohmic losses in antenna elements and interconnects are significant in normal metals, making benefits from HTS materials appreciable. The small antenna sizes required at these frequencies are more readily encapsulated in cryogenic envelopes than are microwave-frequency elements. The critical current density of HTS thin films should exceed the current densities in proposed space communication antenna systems, which is expected to be on the order of 10^5 A/cm^2 or less.

Granular YBaCuO and BiCaSrCuO detectors have been fabricated and tested at 77 K, between 24 and 110 GHz (ref. 13). Superconducting microstrip lines were used as IF and/or video output lines. All detectors showed a dramatic increase in sensitivity below 77 K. The theoretical high-frequency limit (determined from the superconductor energy gap) for these detectors is in the low terahertz range. However, the experimental video response decreases by about one order of magnitude when the carrier frequency is increased from 100 to 300 GHz. This research determined that the properties of HTS ceramics, and thus the resulting detector performance, are highly dependent upon the substrate material and are most likely tied to the dielectric properties of the substrate.

In addition to these applications, extremely low loss phase shifters using superconducting switches are also feasible. In figure 3, we show a phase shifter which utilizes superconducting-normal-superconducting switches in place of FET/diode switches. The switches are fabricated from high T_c thin films of YBaCuO. The switches operate in the bolometric mode with the film held near its transition temperature. Radiation from a light source raises the temperature and consequently causes the film to become resistive. If the switches in the reference path are illuminated, they too will become resistive. The switches on the opposite side of the device are superconducting. Since each switch is positioned one quarter of a wavelength from the junction, the signal will be reflected from the delay path in phase. A similar phenomenon occurs at the output port. To achieve the desired phase

shift, the opposite set of switches is illuminated. Figure 3 shows the predicted behavior for a 180° phase shifter, with an exceptionally narrow insertion loss envelope and excellent return loss.

Figure 4 illustrates an example of a hybrid semiconductor/superconductor device. It is possible that by combining the excellent low noise properties of GaAs devices with the low loss and low noise properties of superconducting transmission lines, one can achieve ultra-low-noise receivers for satellite communications applications. If these promising concepts of high T_c superconducting devices are actually brought to fruition, then one can conceive of their use in low loss, low noise superconducting phased array antennas in space communications systems such as shown in figure 5. HTS transmission lines can provide low loss feed networks for antenna arrays.

E-BEAM DEVICES

There are several areas for possible application of HTS material in electron beam devices. These include the slow-wave circuit, the cathode, and the focusing magnet. Superconducting slow-wave circuits are likely only in very limited applications due to the heating caused by interception of the electron beam by the slow-wave circuit. Another possible area of application of HTS material is in the cathode. Electron field emission from the cathode may be enhanced when the cathode surface is in the superconducting state. Research in this area is in its very early stages and not likely to be applied in the near future.

What is likely to be the first application of HTS material in e-beam devices is for use as the focusing magnet. At the present time most traveling wave tubes used in space employ periodic permanent magnet (PPM) focusing to confine the electron beam because PPM focusing is lightweight and requires no power. The disadvantage of it is that the attainable magnetic fields are less than that required for optimum performance of the tube. This results in reductions in frequency stability, gain flatness, attainable output power, and overall efficiency. A larger solenoidal field can be used for confined flow focusing to overcome these problems resulting in a much improved tube. Because of the large number of potential applications of HTS magnets there are many groups working toward their development.

CONCLUSIONS

Microwave components have been fabricated from HTS materials which have superior performance over similar nonsuperconducting components. The development of HTS devices has large potential impact on the communication system for future space missions. There remains a significant amount of progress to be made in the development of materials and devices to the extent of applications

of HTS technology to microwave systems. System studies must be performed to determine any overall advantage of HTS system along with the necessary coolers over conventional technology.

REFERENCES

1. Valco, G.J., et al.: Sequentially Evaporated Thin Y-Ba-Cu-O Superconducting Films on Microwave Substrates. NASA TM-102068, 1989.
2. Warner, J.D., et al.: Growth and Patterning of Laser Ablated Superconducting $\text{YBa}_2\text{Cu}_3\text{O}_{7-x}$ Films on LaAlO_3 Substrates. NASA TM-102436, 1989.
3. Klein, N., et al.: Millimeter Wave Surface Resistance of Epitaxially Grown $\text{YBa}_2\text{Cu}_3\text{O}_{7-x}$ Thin Films. Appl. Phys. Lett., vol. 54, no. 8, Feb. 20, 1989, pp. 757-759.
4. Miranda, F.A., et al.: Millimeter Wave Surface Resistance of Laser Ablated Y-Ba-Cu-O Superconducting Films. Accepted for publication in Appl. Phys. Lett., Sept. 1990.
5. Fathy, A., et al.: Microwave Properties and Modeling of High T_c Superconducting Thin Film Meander Line. 1990 IEEE MTT-S International Symposium Digest, IEEE, 1990, pp. 859-862.
6. Miranda, F.A., et al.: Microwave Conductivity of Superconducting Bi-Sr-Ca-Cu-O Thin Films in the 26.5 to 40.0 GHz Frequency Range. Physica C., vol. 168, nos. 1-2, June 1, 1990, pp. 91-98.
7. Inam, A., et al.: Microwave Properties of Highly Oriented $\text{YBa}_2\text{Cu}_3\text{O}_{7-x}$ Thin Films. Appl. Phys. Lett., vol. 56, no. 12, Mar. 19, 1990, pp. 1178-1180.
8. Bhasin, K.B., et al.: Performance and Modeling of Superconducting Ring Resonators at Millimeter-wave Frequencies. 1990 IEEE MTT-S International Microwave Symposium Digest, IEEE, 1990, pp. 269-272. (Also, NASA TM-102526).
9. Valenzuela, A.A.; and Russer, P.: High-Q Coplanar Transmission Line Resonator of $\text{YBa}_2\text{Cu}_3\text{O}_{7-x}$ on MgO. Appl. Phys. Lett., vol. 55, no. 10, Sept. 4, 1989, pp. 1029-1031.
10. McAvoy, B.R., et al.: Superconducting Stripline Resonator Performance. IEEE Trans. Magn., vol. 25, no. 2, Mar. 1989, pp. 1104-1106.
11. Takemoto, J.H., et al.: Microstrip Ring Resonator Technique for Measuring Microwave Attenuation in High T_c Superconducting Thin Films. IEEE Trans. Microwave Theory Tech., vol. MTT-37, no. 10, Oct. 1989, pp. 1650-1652.

12. Fiedziuszko, S.J., Holme, S., and Heidmann, P.: Novel Filter Implementations Using HTS Materials. To be published.
13. Konopka, J., et al.: Microwave Detectors Based on Granular High- T_c Thin Films. IEEE Trans. Microwave Theory Techniques, vol. 38, no. 2, Feb. 1990, pp. 160-165.

TABLE I. - KEY PROPERTIES OF MICROWAVE SUBSTRATES MATERIALS

Material	Highest T_c achieved	Dielectric constant	Loss tangent	Lattice size, Å
Magnesium oxide (MgO)	88	9.65	4×10^{-4}	4.178 (100)
Lanthanum aluminate (LaAlO ₃)	90	22	5.8×10^{-4}	4.792 (110)
Lanthanum gallate (LaGaO ₃)	88	27	2×10^{-3}	3.892 (110)
Sapphire (Al ₂ O ₃)	71	9.4	1×10^{-6}	5.111 (011)
Yttria stabilized zirconia (ZrO)	89	27	6×10^{-4}	3.8795 (100)
Silicon (Si)	--	12	10×10^{-4}	5.43 (100)
Gallium arsenide (GaAs)	--	13	6×10^{-4}	5.653 (100)

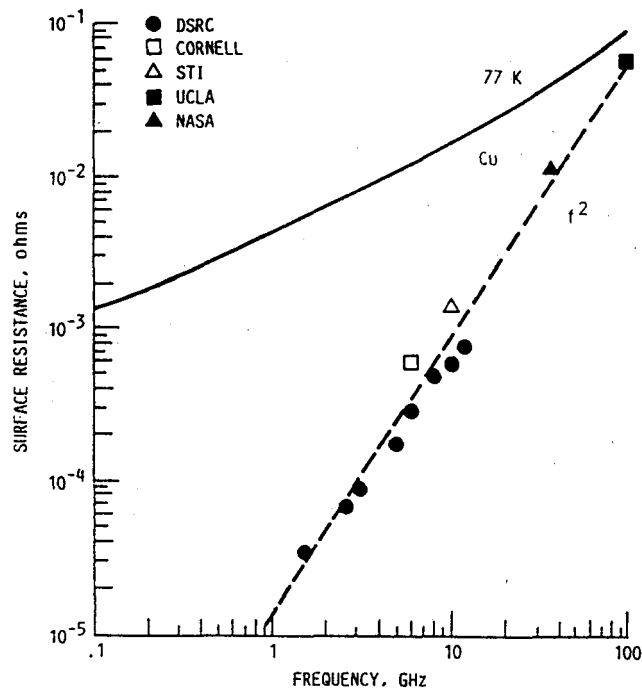


FIGURE 1. - SURFACE RESISTANCE OF LASER ABLATED Y-Ba-Cu-O FILMS ON LaAlO₃ SUBSTRATE VERSUS FREQUENCY. ADOPTED FROM APPLIED PHYSICAL LETTERS VOLUME 56, P.P. 1178-1180. NASA DATA OBTAINED BY MICROWAVE CONDUCTIVITY MEASUREMENTS.

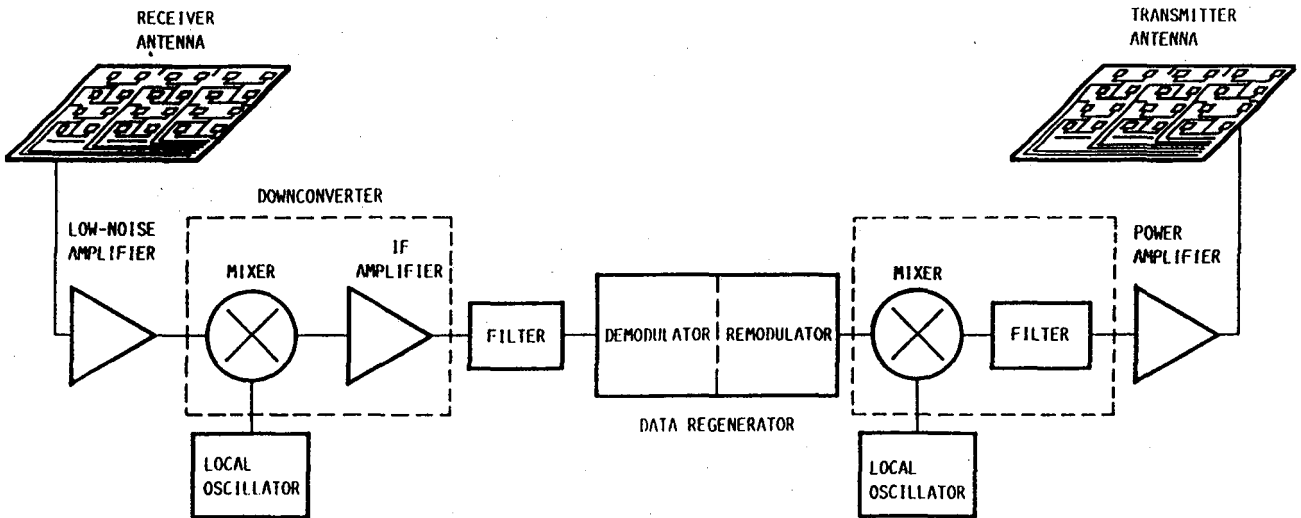
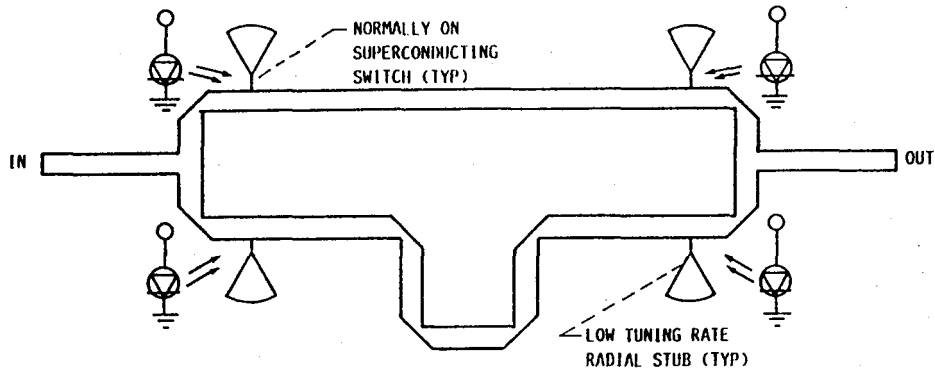
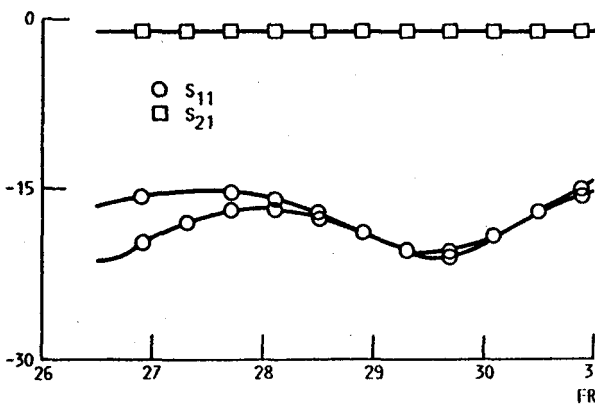


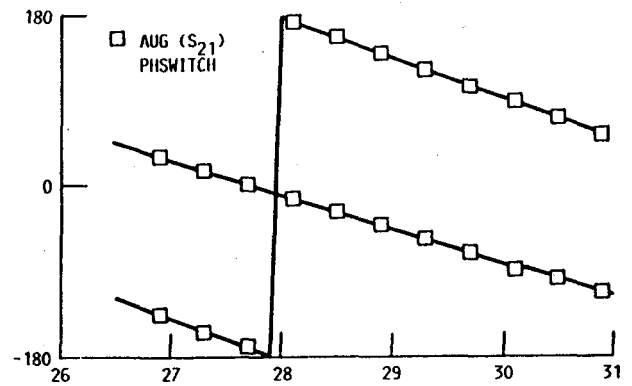
FIGURE 2. - BLOCK DIAGRAM OF A SATELLITE TRANSPONDER.



(a) OPTICALLY CONTROLLED HIGH- T_c SUPERCONDUCTING SWITCH-LINE PHASE SHIFTER.



(b) INSERTION LOSS AND RETURN LOSS FOR BOTH REFERENCE AND DELAY STATES.



(c) INSERTION PHASE FOR REFERENCE AND DELAY STATES.

FIGURE 3.

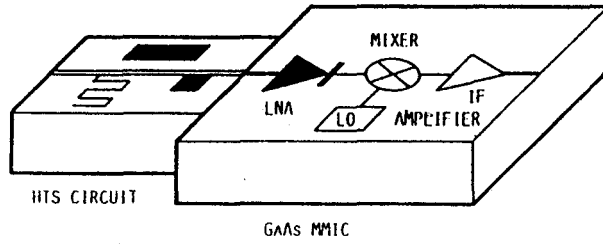


FIGURE 4. - SUPERCONDUCTING GaAs MMIC HYBRID RECEIVER.

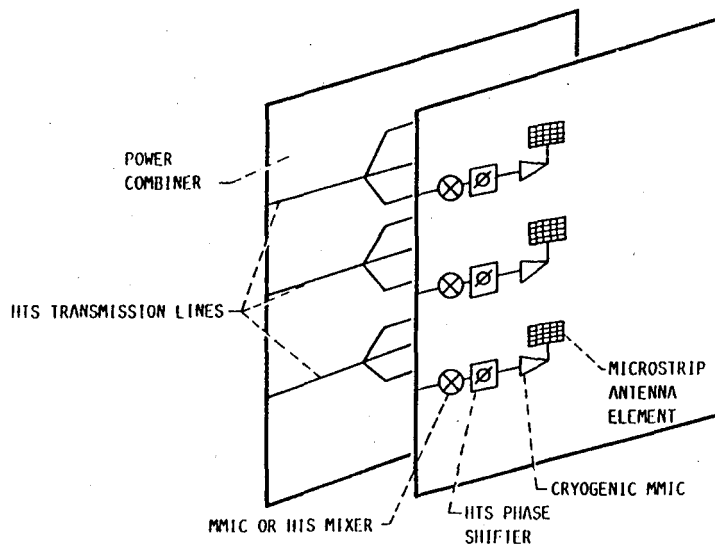


FIGURE 5. - CONCEPTUAL DIAGRAM OF A MMIC-SUPERCONDUCTING HYBRID PHASE ARRAY ANTENNA.

ANALYSIS OF MICROSTRIP LINES WITH ALTERNATIVE IMPLEMENTATIONS OF CONDUCTORS AND SUPERCONDUCTORS

K.-S. Kong, H.-Y. Lee*, C.M. Chorney†, and K.B. Bhasin‡*

**Department of Electrical and Computer Engineering
The University of Texas at Austin, Austin, TX 78712
U.S.A.*

*†Sverdrup Technology, Inc., LeRC Group
Brook Park, OH 44142
U.S.A.*

*‡NASA Lewis Research Center
Cleveland, OH 44135
U.S.A.*

Abstract

This paper presents analysis of microstrip line structures in which either the strip or the ground plane or both are made of a high T_c superconductor. The effect of implementation of a superconductor to the strip and the ground plane is explained with the calculation of a conductor loss of the structure by the Phenomenological Loss Equivalence Method (PEM). The theoretical values are compared with the experimental results from a ring resonator which is made of a gold ground plane and a high T_c superconductor, $YBa_2Cu_3O_{7-x}$ strip.

Introduction

In this paper, we calculate and compare Q values of the microstrip line structures in which either the strip or the ground plane or both are a high T_c superconductor. The motivation for this study is to provide the theoretical basis for the effective application of a superconductor to the microstrip line as well as other planar transmission lines. The analytical method in this paper is based on the Phenomenological Loss Equivalence Method (PEM) [1,2] and the introduction of the superposition principle of the internal impedances from the strip and the ground plane of the microstrip line. By using this method, we calculate the Q value of the ring resonator which has a superconducting strip and a normal conducting ground and compare the results with the experimental data.

Analysis of Various Superconducting Microstrip Line Structure

We analyze the various superconducting microstrip line structures that have alternative implementations of a superconductor and a normal conductor into the strip or the ground plane as shown in Fig.1. There are field penetrations even inside of the superconductor. These field penetrations contribute to the internal impedance and cause the conductor loss in the microstrip line structure as shown in Fig.2. The internal impedances from strip conductor and the ground plane are separately calculated by PEM. Then, the total internal impedance is obtained by using the superposition of internal impedances. The internal impedance of each case is obtained by considering the cases where either strip or the ground plane is perfect.

When the ground plane is assumed to be perfect, the field penetration occurs only in the strip conductor. In this case, the geometric factor, say G_1 , of the microstrip line is obtained from the magnetic field penetration inside of the strip conductor. The equivalent strip [1,2] is obtained from G_1 . The internal impedance of microstrip line under the assumption of a perfect ground plane can be obtained as $Z_{i1} = G_1 \cdot Z_{s1} \cdot \coth(Z_{s1} \cdot \sigma_1 \cdot A \cdot G_1)$ where Z_{s1} , σ_1 and A are the surface impedance, the conductivity of the material and the cross section ($w \cdot t$) of the strip, respectively. Next, we consider the case where the field penetration occurs only in the ground plane. In this case, the geometric factor, G_2 , is obtained from the field penetration in the ground plane. The internal impedance from the ground plane is obtained as $Z_{i2} = G_2 \cdot Z_{s2} \cdot \coth(Z_{s2} \cdot \sigma_2 \cdot A \cdot G_2)$ where Z_{s2} and σ_2 are surface impedance and conductivity of the ground, respectively. Then, the total internal impedance is obtained by adding Z_{i1} and Z_{i2} . We calculate the propagation constant of the microstrip line structure by adding this internal impedance to the external impedance and by using the transmission line model. Since our method is based on the PEM, this can be applied to any field penetration depth compared with the conductor thickness as demonstrated in reference [1, 2].

Comparison Between Microstrip Lines with Various Superconductor Implementation

The conductor losses of each microstrip line in Fig.1 are calculated by applying the method explained above. Then, we calculate Q values of each strip line

by additional consideration of substrate loss [3]. This will give us insight to the effects of an application of superconductor on microstrip line. The dimensions of the structure are shown in Fig.3 (a). For the calculation, we use the measured conductivity values of the $\text{YBa}_2\text{Cu}_3\text{O}_{7-x}$ film obtained from the power transmitted through the film and a two fluid model [4]. The calculated Q values of each structure at 35 GHz are shown and compared in Fig.3. In this calculation, the value of 5.8×10^{-4} is used for loss tangent. Since the current is more concentrated on the strip, the implementation of a superconductor in the strip gives more influence on the loss as expected. The extent of an effect of the implementation of a superconductor in the microstrip line can be different for different geometric structures of the microstrip line.

Next, we compare our calculated results with the experimental results from the ring resonator structure shown in Fig.4. This ring resonator has the resonant frequency of 35.0 GHz. The details of the fabrication of this structure and the measurements are presented elsewhere [5]. The strip of this ring resonator is a thin film of $\text{YBa}_2\text{Cu}_3\text{O}_{7-x}$ deposited on LaAlO_3 by a laser ablated technique. The ground plane consists of Ti/Au. A thin Ti layer is employed to make the deposition of the gold on the substrate and its effect on the structure is negligible because it is thin compared with a gold layer. Fig.5 shows the experimental Q values and the calculated Q values with the variation of loss tangent of the substrate. The calculated values of Q are higher than the experimental results. There are several factors for this discrepancy between the experimental and theoretical results. The ring resonator was built with a $\text{YBa}_2\text{Cu}_3\text{O}_{7-x}$ film different from the film on which the conductivity values were measured. The $\text{YBa}_2\text{Cu}_3\text{O}_{7-x}$ film used in the ring resonator has lower T_c and lower quality than the one used in the conductivity measurement. Also, it is more affected by the surface roughness because it is patterned. Another factor can be the edge current effect on the superconducting ring resonator. Also, since the conductor loss from the gold and superconductor decreases at the low temperature region, the substrate loss becomes more dominant. However, the information on the loss tangent of the substrate is not available at low temperature region. As we can observe in Fig.5, the Q values depend on the value of loss tangent of the substrate used in the calculation. The accurate characteristics of the substrate should be done in order to make it meaningful to compare the theoretical and experimental results.

Conclusion

In this paper, we presented a theoretical analysis of the superconducting microstrip lines with the various implementations of a superconductor and a normal conductor into the strip or the ground plane of the microstrip line. By using the method presented, we calculated the Q values of a ring resonator with the thin $\text{YBa}_2\text{Cu}_3\text{O}_{7-x}$ strip and the gold ground plane. This theoretical results are compared and discussed with

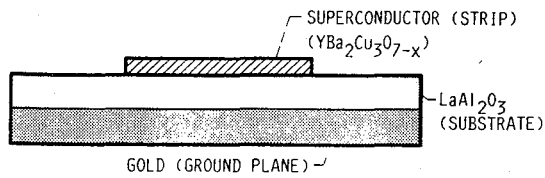
experimental results of a ring resonator with the thin $\text{YBa}_2\text{Cu}_3\text{O}_{7-x}$ strip and the gold ground plane. It was found that the substrate loss becomes very critical at the superconducting microstrip line.

Acknowledgement

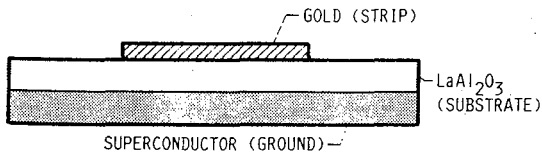
The authors at the University of Texas were supported by the cooperative agreement NCC-3154 from NASA and the Texas Advanced Technology Program. The PEM method was originally developed under support by grant N00014-89-J-1006 at The University of Texas at Austin from the U.S. Office of Naval Research.

References

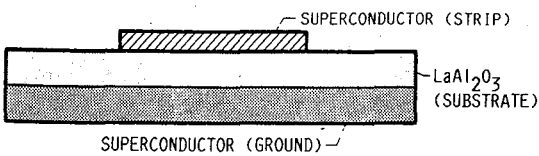
- [1] H.-Y. Lee and T. Itoh, "Phenomenological loss equivalence method for planar quasi-TEM transmission line with a thin normal conductor or superconductor," *IEEE Trans. Microwave Theory Tech.*, Vol. MTT-37, Number 12, December 1989.
- [2] H.-Y. Lee, K.-S. Kong, T. Itoh, "Conductor loss calculation of superconducting microstrip line using a phenomenological loss equivalence method," 19th European Microwave Conference, London, England, September 1989.
- [3] K. C. Gupta, R. Garg, and I. J. Bahl, "Microstrip lines and slotlines", Artech House, Inc., (1979).
- [4] NASA Technical Memorandum, "Millimeter Wave Transmission Studies of $\text{YBa}_2\text{Cu}_3\text{O}_{7-x}$ Thin Films in the 26.5 to 40.0 GHz Frequency Range", to be published in *Proceeding of Third Annual Superconductor application*, 1990.
- [5] K.B. Bhasin, C.M. Chorey, J.D. Warner, K.-S. Kong, H.-Y. Lee and T. Itoh, "Performance and Modeling of Superconducting Ring Resonators at Millimeter-Wave Frequencies", *IEEE MTT-S Int. Microwave Symposium*, pp 269-272, May 1990.



(a) SUPERCONDUCTING STRIP, NORMAL CONDUCTING GROUND.



(b) SUPERCONDUCTING GROUND, NORMAL CONDUCTING STRIP.



(c) SUPERCONDUCTING STRIP, SUPERCONDUCTING GROUND.

FIGURE 1. - SUPERCONDUCTING MICROSTRIP LINES.

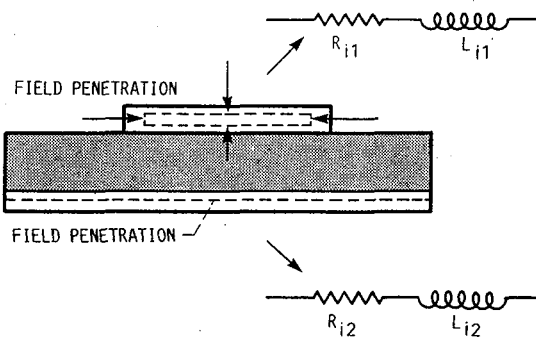
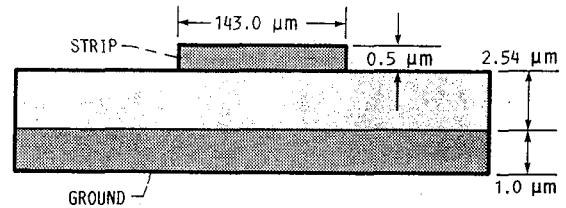
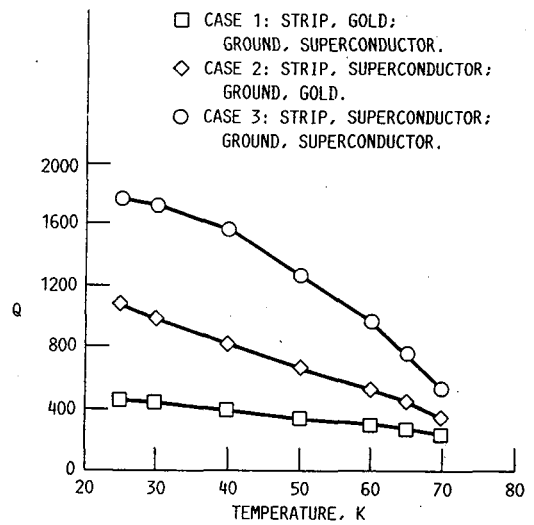


FIGURE 2. - FIELD PENETRATION IN THE STRIP AND THE GROUND PLANE.



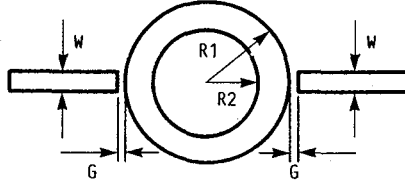
(a) MICROSTRIP LINE.



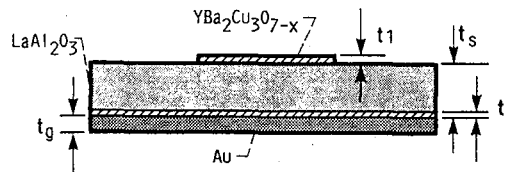
(b) Q-VALUES OF SUPERCONDUCTING MICROSTRIP LINES.

FIGURE 3. - DIMENSIONS AND Q-VALUES OF SUPERCONDUCTING STRIP LINES.

R1: 918 μm
 R2: 1061 μm
 W: 143 μm
 G: 36 μm



(a) TOP VIEW OF THE RING RESONATOR.



t_t : (TITANIUM LAYER) t_1 : 0.5 μm
 t_s : 254 μm
 t_t : 0.1 μm
 t_g : 1.0 μm

(b) SIDE VIEW OF THE RING RESONATOR.

FIGURE 4. - SUPERCONDUCTING RING RESONATOR.

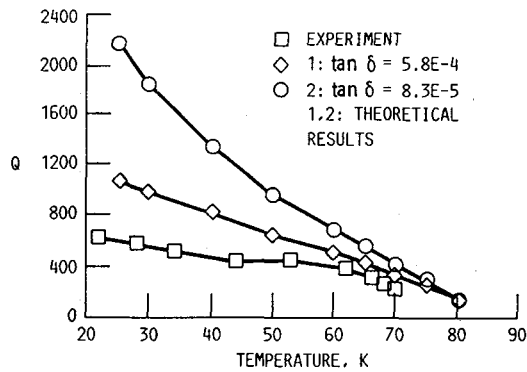


FIGURE 5. - EXPERIMENTAL AND THEORETICAL VALUES OF Q IN SUPERCONDUCTING RING RESONATOR.

AN EXPERIMENTAL STUDY OF HIGH TC SUPERCONDUCTING MICROSTRIP TRANSMISSION LINES AT 35 GHZ AND THE EFFECT OF FILM MORPHOLOGY.

C. M. Chorey
Sverdrup Technology, LeRC Group
20001 Aerospace Prky
Brook Park, Ohio 44142

K. B. Bhasin, J. D. Warner
NASA, Lewis Research Center
21000 Brookpark Rd
Cleveland, Ohio 44135

J. Y. Josefowicz, D. B. Rensch, C. W. Nieh
Hughes Research Labs
3011 Malibu Canyon Rd
Malibu, California 90265

Abstract

Microstrip transmission lines in the form of ring resonators have been fabricated from a number of in-situ grown laser ablated films and post-annealed co-sputtered $\text{YBa}_2\text{Cu}_3\text{O}_{7-x}$ (YBCO) films. The properties of these resonators have been measured at 35 GHz and the observed performance is examined in light of the critical temperature (T_c) and film thickness and also the film morphology which is different for the two deposition techniques. We find that T_c is a major indicator of the film performance for each growth type with film thickness becoming important as it decreases towards 1000\AA . We find that the films with a mixed grain orientation (both 'a' axis and 'c' axis oriented grains) have poorer microwave properties as compared with the primarily 'c' axis oriented material. We speculate that this is due to the significant number of grain boundaries between the different crystallites, which may act as superconducting weak links and contribute to the surface resistance.

Introduction

Numerous papers to date have demonstrated the applicability of thin films of the oxide-based high temperature superconductors to passive microwave circuits. Cavity studies^{1,2}, conductivity measurements³ and patterned resonator⁴ studies have all demonstrated that high quality epitaxial films of these superconductors can have surface resistances significantly lower than normal metals typically used in microwave applications (i.e. gold and copper). Despite these encouraging results, there is still no definite understanding of which film properties are most important in determining the microwave characteristics of a thin film of these materials. It had been our observation, that films produced by processes that involved a high temperature anneal typically did not perform as well in a microstrip ring resonator as in-situ

grown films. In an attempt to address this issue, we have undertaken a study comparing the performance of post-annealed and in-situ grown $\text{YBa}_2\text{Cu}_3\text{O}_{7-x}$ (YBCO) films on lanthanum aluminate (LaAlO_3) using a patterned microstrip ring resonator with a 3λ resonance at 35 GHz. The morphology of the films produced by the two growth methods is determined by X-ray diffraction (XRD) and scanning electron microscopy (SEM). We examine the unloaded Q vs temperature of each film type and note the effect of T_c and thickness on the performance. We compare the results from the resonators of the two growth types and observe the effect that the morphology has on the performance. Finally we propose an explanation of the observed differences based on the different film morphologies brought about by the different growth techniques.

Film Growth and Resulting Morphology

Two growth techniques were used to produce thin films of YBCO on LaAlO_3 with different film morphologies; these were in-situ laser ablation and co-sputtering with a high temperature anneal. The laser ablated films were formed by the ablation of a sintered YBCO pellet by a 248 nm excimer laser⁵. The substrate was mounted on a stainless steel block which was heated to 775°C in a background pressure of 170 mtorr for growth. The laser was pulsed at a rate of 4 pps and rastered over the target by means of an external lens. Following deposition, the sample block temperature was lowered to 450°C , the oxygen pressure raised to 1 atmosphere and the sample allowed to anneal for 2 hours. Then the block was allowed to slowly cool in oxygen to room temperature before removing the superconducting film from the growth chamber.

The post-annealed samples were prepared by simultaneous co-sputtering of Y, Cu, and BaF_2 targets onto a rotating LaAlO_3 substrate at ambient temperature⁶. This resulted in a non-superconducting amorphous film which was then annealed at 850°C in an H_2O saturated oxygen atmosphere for .5 hours to

Manuscript received September 24, 1990.

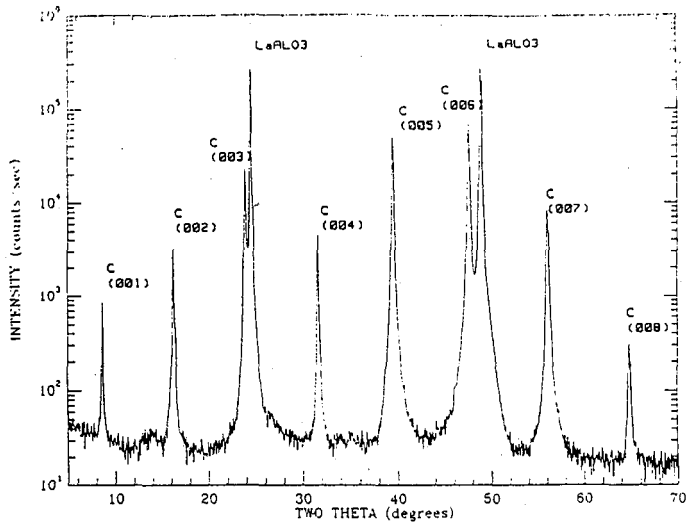


Figure 1. X-ray diffraction analysis of a laser ablated film on LaAlO_3 .

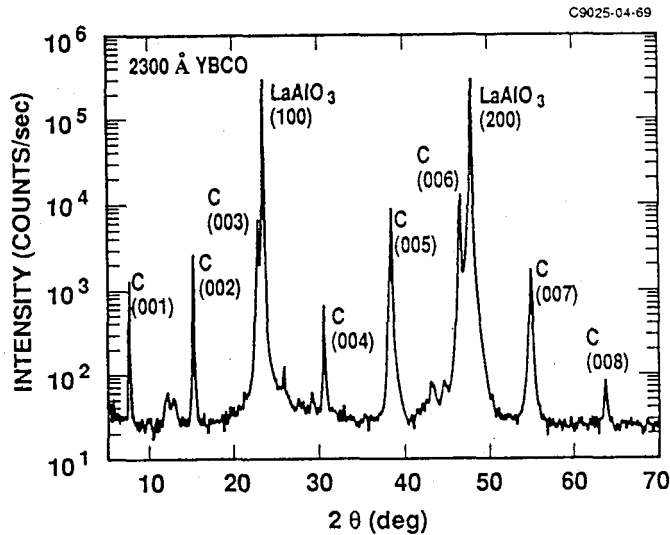


Figure 2. X-ray diffraction analysis of a co-sputtered post-annealed YBCO film on LaAlO_3 .

produce the oriented superconducting film.

The morphology of the resulting films was examined using X-ray diffraction (XRD) and scanning electron microscopy (SEM). Typical XRD results from each type of film are shown in figures 1 and 2. Both show strong c-axis peaks and few spurious peaks indicating predominantly 'c' axis oriented material ('c' axis normal to the substrate). The co-sputtered films, however, tend to show the presence of extraneous phases more frequently than the laser ablated films.

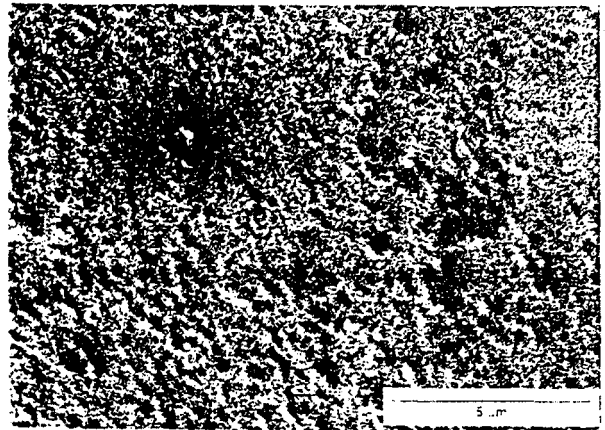


Figure 3. SEM micrograph of the surface of a laser ablated YBCO film on LaAlO_3 . Note the absence of misoriented grains. This film shows some surface roughness and particulates; the best films are virtually feature-less.

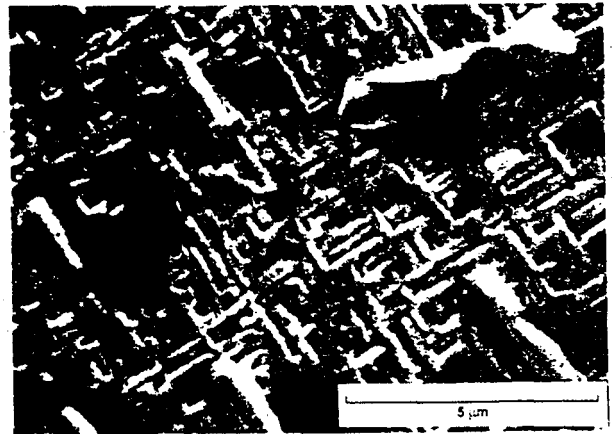


Figure 4. SEM micrograph of a 3000 Å thick co-sputtered post-annealed YBCO film on LaAlO_3 . The 'basket weave' structure is composed of YBCO grains with either the 'a' or 'b' axis normal to the substrate.

SEM investigation of the films (figures 3 and 4) shows a marked difference in the morphology of the two growth methods. The laser ablated films, in the best cases, are smooth and feature-less but sometimes (fig.3) show some surface roughness and particulates. These films show no evidence of large grains of misoriented material or secondary phases. TEM studies of other laser ablated films⁷ seem to confirm that this deposition process produces mainly 'c' axis oriented material with few misoriented grains, though these same studies indicate that the 'c' material contains a high density of crystal defects. The post-annealed films, however (fig.4).

in all cases show the development of a 'basket weave' structure indicative of material oriented with either the 'a' or 'b' axis normal to the substrate (referred to in the following as 'a' axis material or 'a' grains). That these grains have the 'a' axis normal to the substrate has been established by TEM studies⁸ using electron microdiffraction and cross sectional microscopy. That study of the microstructure of films produced in the same growth chamber has shown that for the post-annealed films the 'a' oriented material extends from the substrate upwards and that as the film grows thicker the upper portion of the material contains a higher fraction of 'a' material due to differential growth rates along the a,b, and c axes.

Fabrication and Testing

The superconducting films were patterned into microstrip ring resonators using standard photolithography. A positive photoresist was spun on, exposed through a UV contact mask aligner and developed. The resonator pattern was defined by etching in a dilute (<1%) solution of phosphoric acid which resulted in a well defined pattern with little undercutting. Finally a gold ground plane was evaporated on the reverse side of the circuit.

The circuits were fabricated on lanthanum aluminate 10 mils thick to avoid substrate modes at 35 GHz. The microstrip line width was 5.6 mil and the mean ring diameter was 77 mil and supported a 3λ mode near 35 GHz. The calculated impedance of the line was 45 ohms. The circuits were tested using an HP 8510B network analyzer in WR-28 waveguide. The Q's were extracted from the reflection response of the one port resonator.

Results and Discussion

The measured resonators showed a wide range of performance depending on film thickness, growth method and Tc. Figure 5 summarizes the Q data obtained from the laser ablated films and includes the performance of a gold resonator as a comparison. For films produced by a particular growth method, Tc appears to be a major indicator of the resonator performance. The best laser ablated film, #LA1, had the highest Tc. Two other films, #LA2 and #LA3 which were of thickness 2500Å and 4000Å but approximately the same Tc, 84°K, have similar performance further indicating that Tc is an important controlling factor in the film's microwave performance. Film #LA4 with a Tc of 87.2°K seems to deviate from this scaling trend as its Q values fall below the 84°K films. However, this film is only 1200Å thick and the lower Q values are most likely a reflection of the thinness of this film. It is expected that at some point film thickness will become a dominant factor in determining the microstrip losses just as in normal conducting strips, due to increased current density.

Figure 6 summarizes results from the post annealed films. Again, an examination of the data indicates the importance of film Tc on performance. The measured results scale quite well with the film Tc. However, the

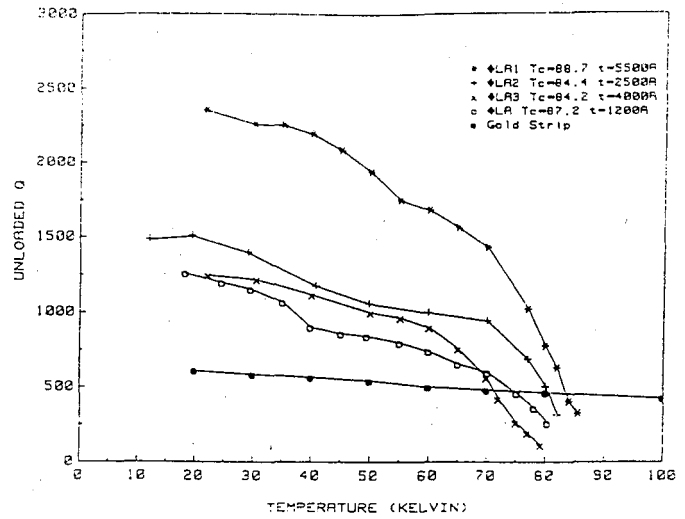


Figure 5. Unloaded Q vs temperature for several laser ablated films on LaAlO_3 . All films eventually perform better than the gold implementation of the resonator. The best film is four times better at 20°K than the gold resonator.

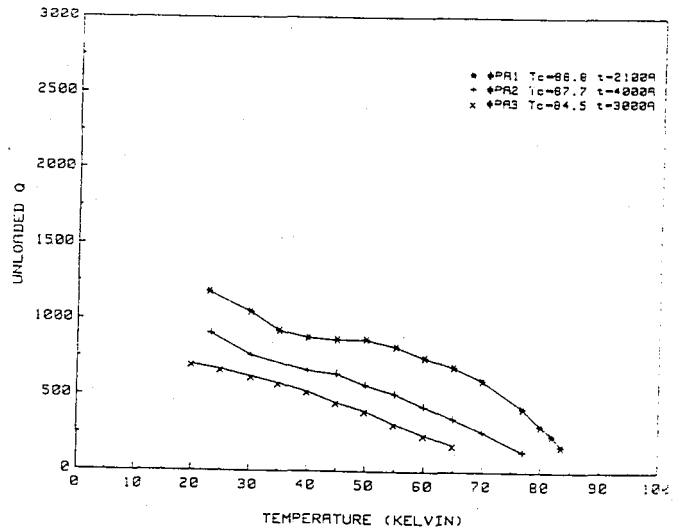


Figure 6. Unloaded Q vs temperature for several co-sputtered post-annealed YBCO films on LaAlO_3 . The scale is the same as figure 5 to facilitate comparison between the two film types.

interpretation of the post annealed films and the relative importance of Tc vs film thickness for them is more involved. As discussed earlier, the most striking feature of the post annealed film morphology is the presence of a high density of 'a' axis oriented material. The presence of these 'a' grains and the resulting "basket weave" structure leads to a large number of grain boundaries.

These must act as either superconducting weak links or imbedded normal conducting material, either of which will cause additional loss in the film. The higher the number of grain boundaries, the more lossy the material would tend to be. Comparing performance by this criterion, it is significant that the film #PA1, with the best performance is also the film with the lowest density of 'a' axis oriented material.

The effect of the 'a' grains becomes more apparent when the post annealed and laser ablated films are compared. It is seen that as a group the post annealed films have lower Q's than the laser ablated films. The best post-annealed ring resonator, fabricated from a 2100Å film had a Q which was about half of that of the best laser ablated resonator, fabricated from a 5500Å film. Although some of the reduced performance in the post annealed resonator was probably due to the relatively thin film, the presence of 'a' axis grains also have an effect on the surface resistance. Because of the complexities of comparing films of different thickness and Tc's we have extracted values for the surface resistance of the films. This was accomplished by separately accounting for the dielectric loss (assuming $\tan \delta = 1E-4$) and the normal ground plane loss and matching the experimental Q values with values for the strip surface resistance. The strip and ground plane losses were calculated using the PEM method which takes into account the conductor thickness. The results are tabulated in Table 1 and Table 2 with three temperature values for each film. The laser ablated films consistently show a surface resistance of approximately one half the value exhibited by the post annealed films.

Conclusions

We have measured several 35 GHz microstrip ring resonators fabricated from laser ablated and co-sputtered post annealed YBCO films. It was found that for a particular film type (growth method) Tc is a strong indicator of the resonator performance. Thickness effects on the performance of the resonators become apparent as the film decreases towards 1000Å; for thicknesses greater than this the performance is more dependent on the intrinsic properties of the material as indicated in Tc. Comparison of resonators fabricated from films of the two growth methods shows that the superconducting films with primarily 'c' axis orientation have better performance than the films with mixed grain orientation. We believe that weak links associated with the grain boundaries formed by the intersection among the 'a' grains and between the 'a' and 'c' material add an additional loss mechanism which limits the performance of circuits fabricated from this material.

ACKNOWLEDGEMENT

The authors would like to thank Donna Bohman, Chuck Hulbert and Nick Varaljay of the Micro-Circuits Fabrication Facility at NASA, Lewis Research Center; also, Frans Krajenbrink and Richard Miles of Hughes Research Labs for the film growth and X-Ray analysis.

Table 1. Data for Laser Ablated Films.

Film	Tc	Thickness	Rs (milliohms)		
			20 K	40 K	70 K
#LA1	88.7 K	5500A	5.3	5.5	8.3
#LA2	84.4 K	2500A	8.4	9.2	15.9
#LA3	84.2 K	4000A	7.0	8.5	9.0
#LA4	87.2 K	1200A	4.0	5.9	7.7

Table 2. Data for Post-annealed Films.

Film	Tc	Thickness	Rs (milliohms)		
			20 K	40 K	70 K
#PA1	88.8 K	2100A	10.5	14.2	19
#PA2	87.7 K	4000A	8.0	10.9	24
#PA3	84.5 K	3000A	10.3	13.7	-

1. F.A. Miranda, W.L. Gordon, K.B. Bhasin and J.D. Warner, "Millimeter-wave surface resistance of laser-ablated $YBa_2Cu_3O_{7-x}$ superconducting films", Appl. Phys. Lett., 57(10), 1058-1060, 1990.
2. N. Klein, G. Muller, H. Piel, B. Roas, L. Shultz, U. Klein and M. Peiniger, "Millimeter wave surface resistance of epitaxially grown YBaCuO thin films", Appl. Phys. Lett., 54(8), 757-759, 1989.
3. K.B. Bhasin, J.D. Warner, F.A. Miranda, W.L. Gordon, H.S. Newman, "Determination of Surface Resistance and Magnetic Penetration Depth of Superconducting $YBa_2Cu_3O_{7-x}$ Thin Films by Microwave Power Transmission Measurements", IEEE Trans. Magnetics, This Issue.
4. A.A. Valenzuela and P. Russer, "High Q coplanar transmission line resonator of $YBa_2Cu_3O_{7-x}$ on MgO", Appl. Phys. Lett., 55(10), 1029-1031, 1989.
5. J.D. Warner, K.B. Bhasin, N.C. Varaljay D.Y. Bohman and C.M. Chorey, "Growth and Patterning of Laser Ablated Superconducting YBaCuO Films on $LaAlO_3$ Substrates", NASA TM-#102346, 1989.
6. E. Wiener-Avneer, J.E. Cooper, G.C. Kerber, J.W. Spargo, A.G. Toth, J.Y. Josefowicz, D.B. Rensch, B.M. Clemens and A.I. Hunter, "Laser Patterning of YBaCuO Weak Link Bridges", IEEE Trans. Mag. vol.25 no.2, 935-938, 1989.
7. D.M. Hwang, T. Venkatesan, C.C. Chang, L. Nazar, X.D. Wu, A. Inam and M.S. Hedge, "Microstructure of in situ epitaxially grown superconducting Y-Ba-Cu-O thin films", Appl. Phys. Lett., 54(17), 1702-1704, 1989.
8. C.W. Nieh, L. Anthony, J.Y. Josefowicz, F.G. Krajenbrink, "Microstructure of epitaxial $YBa_2Cu_3O_{7-x}$ thin films", Appl. Phys. Lett., 56(12), 2138-2140, 1990.

9. . H.Y. Lee and T. Itoh, "Phenemenological Loss
Equivalence Method for Planar Quasi-TEM Transmission
Lines with a Thin Normal Conductor or Superconductor",
IEEE MTT, vol.37, 1904-1909, 1989.

MICROWAVE RESPONSE OF HIGH TRANSITION TEMPERATURE SUPERCONDUCTING THIN FILMS

Abstract

by

FELIX ANTONIO MIRANDA

We have studied the microwave response of $\text{YBa}_2\text{Cu}_3\text{O}_{7-\delta}$, Bi-Sr-Ca-Cu-O, and Tl-Ba-Ca-Cu-O high transition temperature superconducting (HTS) thin films by performing power transmission measurements. These measurements were carried out in the temperature range of 300 to 20 K and at frequencies within the range of 30 to 40 GHz. Through these measurements we have determined the magnetic penetration depth (λ), the complex conductivity ($\sigma^* = \sigma_1 - j\sigma_2$), and the surface resistance (R_s). An estimate of the intrinsic penetration depth ($\lambda \sim 121$ nm) for the $\text{YBa}_2\text{Cu}_3\text{O}_{7-\delta}$ HTS has been obtained from the film thickness dependence of λ . This value compares favorably with the best values reported so far (~ 140 nm) in single crystals and high quality c-axis oriented thin films. Furthermore, it was observed that our technique is sensitive to the intrinsic anisotropy of λ in this superconductor. Values of λ are also reported for Bi-based and Tl-based thin films.

We observed that for the three types of superconductors, both σ_1 and σ_2 increased when cooling the films below their transition temperature. This indicates that the temperature dependence of σ_1 is not consistent with that expected from

the two-fluid model, and also deviates from the values obtained using the Mattis-Bardeen equations based on the BCS theory.

Values of R_s comparable to or lower than that for copper at the same frequency and at 77 K were obtained for the $\text{YBa}_2\text{Cu}_3\text{O}_{7-\delta}$ thin films. However, the R_s for the Bi-based and Tl-based films was larger than that of copper for all the measured temperatures. Our R_s measurements were consistent with those performed at 36 GHz on the same films using resonant cavity techniques. We have fabricated a resonant cavity to measure R_s . The measured R_s are in good agreement with other reported R_s values obtained using resonant cavity techniques if we assume a quadratic frequency dependence for R_s .

Our analysis shows that, of the three types of HTS films studied, the $\text{YBa}_2\text{Cu}_3\text{O}_{7-\delta}$ thin films, deposited by laser ablation and off-axis magnetron sputtering are the most promising for microwave applications.

DETERMINATION OF SURFACE RESISTANCE AND MAGNETIC
PENETRATION DEPTH OF SUPERCONDUCTING $\text{YBa}_2\text{Cu}_3\text{O}_{7-x}$ THIN FILMS BY
MICROWAVE POWER TRANSMISSION MEASUREMENTS

K. B. Bhasin and J. D. Warner
National Aeronautics and Space Administration
Lewis Research Center
Cleveland, Ohio 44135

H. S. Newman
Naval Research Laboratory
Washington, DC 20375

F. A. Miranda and W. L. Gordon
Department of Physics
Case Western Reserve University
Cleveland, Ohio 44106

Abstract

A novel waveguide power transmission measurement technique has been developed to extract the complex conductivity ($\sigma^* = \sigma_1 - j\sigma_2$) of superconducting thin films at microwave frequencies. We obtained the microwave conductivity of two laser-ablated $\text{YBa}_2\text{Cu}_3\text{O}_{7-x}$ thin films on LaAlO_3 with transition temperatures (T_c) of approximately 86.3 and 82 K, respectively, in the temperature range 25 to 300 K. From the conductivity values we calculated the penetration depth (λ) to be approximately 0.54 and 0.43 μm , and the surface resistance (R_s) to be approximately 24 and 36 m Ω at 36 GHz and 76 K for the two films under consideration. We further compared the R_s values with those obtained from the change in the Q-factor of a 36 GHz TE_{011} -mode (OFHC) copper cavity by replacing one of its end walls with the superconducting sample. We found that this technique allows noninvasive characterization of high- T_c superconducting thin films at microwave frequencies.

Introduction

Microwave measurements of the high-transition-temperature superconductors provide a convenient probe to be used in attempting to identify the conduction mechanisms and the nature of the superconducting state of these compounds.¹ Whereas dc resistance measurements provide information about the normal state above the transition temperature (T_c) and other techniques, such as magnetization measurements, give information on the superconducting state below T_c , microwave measurements can give useful information on both the superconducting and normal states.² Another main objective of the microwave studies of these high- T_c superconductors is to evaluate the potential of these materials for microwave device applications.³ In an attempt to uncover the intrinsic properties and the ultimate performance of these oxides at microwave frequencies, surface resistance measurements of very high-quality thin films have been carried out by different researchers.^{4,5} Another parameter of fundamental importance in the characterization of these new materials is the microwave conductivity. Nevertheless, reports on

measurements of this parameters are scarce, probably because more painstaking techniques are necessary to measure it directly. In this paper we report on the characterization of laser-ablated $\text{YBa}_2\text{Cu}_3\text{O}_{7-x}$ thin films by a power transmission measurement technique. We obtained values for the microwave conductivity ($\sigma^* = \sigma_1 - j\sigma_2$) in the normal and superconducting states and calculated the magnetic penetration depth (λ) and the surface resistance (R_s) from the conductivity values. Finally, we compared the R_s values with those obtained from the change in the Q-factor of a 36 GHz TE_{011} -mode (OFHC) copper cavity, by replacing one of its end walls with the superconducting sample, to estimate the agreement between the two techniques in determining R_s .

Experimental Procedures

We used a pulsed-laser ablation technique to deposit the $\text{YBa}_2\text{Cu}_3\text{O}_{7-x}$ thin films onto 508- μm -thick LaAlO_3 substrates. The deposition was performed at a substrate temperature of 755 $^\circ\text{C}$ and at an ambient oxygen pressure of 170 mtorr. The laser wavelength was 248 nm, the pulse length was 20 to 30 ns, and the pulse rate was 2 pulses per second. During deposition the distance between the target and the sample was kept at 7.5 cm, and the laser fluence on the target was maintained at 2.0 J/cm² per pulse. For the deposition of the films we used $\text{YBa}_2\text{Cu}_3\text{O}_{7-x}$ stoichiometric targets with a density greater than 95% of theoretical. During this process the laser beam was scanned 1 cm across the target by using an external lens on a translator. At the end of the deposition process the oxygen pressure was raised to 1 atm, and the temperature was slowly lowered to room temperature. A more detailed description of the deposition technique can be found elsewhere.⁶

We analyzed the films by x-ray diffraction, dc resistance versus temperature measurements, and scanning electron microscopy (SEM). The T_c was 86.3 K for one of the films (hereinafter called sample 1) and at 82.0 K for the other (hereinafter called sample 2). The dc resistance versus temperature for sample 1 is shown in Fig. 1. The x-ray diffraction pattern revealed that both films are single phased with a predominantly c-axis orientation. The SEM's showed the presence of

randomly distributed particulate inhomogeneities whose average size was $\approx 1/4 \mu\text{m}$.

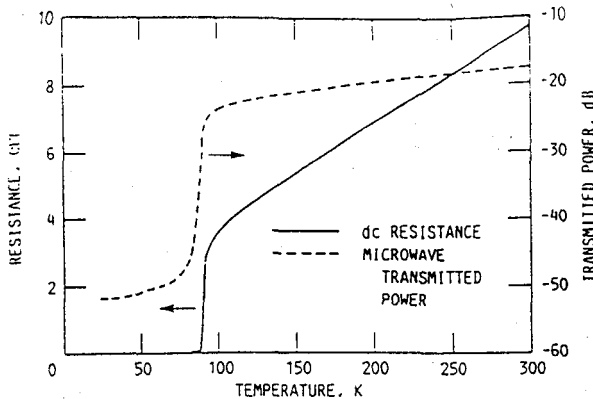


FIGURE 1. - dc RESISTANCE AND MICROWAVE TRANSMITTED POWER AT 35 GHz VERSUS TEMPERATURE FOR A $\text{YBa}_2\text{Cu}_3\text{O}_{7-\delta}$ THIN FILM (2655 Å) ON A LaAlO_3 SUBSTRATE.

We performed the power transmission and phase measurements on a Hewlett-Packard 8510 automatic network analyzer connected to a helium gas closed-cycle refrigerator by Ka-band (26.5 to 40.0 GHz) waveguides. All the measurements were made under vacuum ($< 10^{-6}$ torr) in a custom-designed vacuum chamber. Inside the vacuum chamber the sample was clamped between two waveguide flanges mounted on top of the cold head of the refrigerator. The waveguides were made of thin-wall stainless steel to minimize heat conduction, and their inner surfaces were gold plated to reduce microwave energy losses. The flanges were made of brass; their inner surfaces were also gold plated. Inside the waveguides there were vacuum sealed mica windows. The temperature of the sample was monitored with silicon diode sensors mounted on the waveguide flanges that supported the sample.

The measured temperature dependence of the power transmission coefficient (T) (ratio of transmitted power to incident power) corresponding to sample 1 is given in Fig. 1. In the normal state the behavior of the transmitted power with decreasing temperature was similar to that of the dc resistance. At temperatures just below the onset temperature the transmitted power dropped abruptly, falling monotonically with decreasing temperature, until a lower limit was reached. This behavior was typical for both films.

Surface Resistance and Magnetic Penetration Depth

We calculated the surface resistance R_s and the magnetic penetration depth λ from the microwave complex conductivity. The real and imaginary parts of the complex conductivity are given in terms of the power transmission coefficient T and the phase shift ϕ by

$$R = \frac{\{(2n/T^{1/2})[\text{ncos}(k_0nt)\sin(k_0t + \phi) - \sin(k_0nt)\cos(k_0t + \phi)] - n(n^2 - 1)\sin(k_0nt)\cos(k_0nt)\}}{k_0d[n^2\cos^2(k_0nt) + \sin^2(k_0nt)]} \quad (1)$$

and

$$I = \frac{\{(2n/T^{1/2})[\text{ncos}(k_0nt)\cos(k_0t + \phi) + \sin(k_0nt)\sin(k_0t + \phi)] - 2n^2\cos^2(k_0nt) - (n^2 + 1)\sin^2(k_0t)\}}{k_0d[n^2\cos^2(k_0nt) + \sin^2(k_0nt)]} \quad (2)$$

where k_0 is the wave number of the normal incident transverse electric wave propagating in the rectangular waveguide, d is the film thickness, t is the thickness of the substrate with refraction index n , $R = 1 + 4\pi\sigma_2/\omega\epsilon$, $I = 4\pi\sigma_1/\omega\epsilon$, $\omega/2\pi = f$ is the frequency of the wave, and ϵ is the relative dielectric constant of the material.

Figure 2 shows the temperature dependence of σ_1 and σ_2 for sample 1 at 35 GHz. The conductivity at room temperature ($\sim 3.9 \times 10^5$ S/m) compared reasonably well with reported values of dc conductivities in this type of film⁷. The change of σ_1 with decreasing temperature exhibited a metallic behavior down to the onset temperature, at which $\sigma_1 \sim 1.3 \times 10^6$ S/m. In the normal state σ_2 was close to zero, as expected for a good conductor. Note that both σ_1 and σ_2 increased upon going through the onset temperature, with σ_1 reaching values of 4.0×10^6 and 4.8×10^6 S/m at 76 and 50 K, respectively, and σ_2 reaching values of approximately 1.3×10^7 and 1.8×10^7 S/m at these same temperatures.

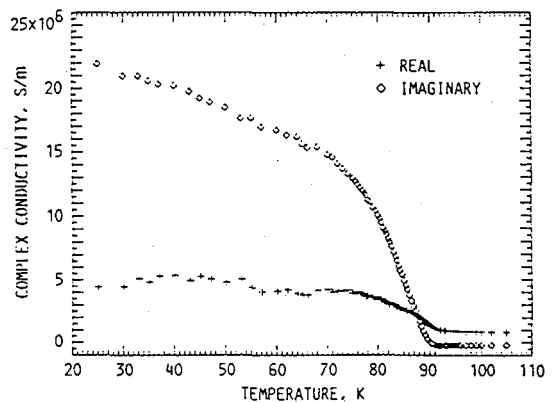


FIGURE 2. - REAL AND IMAGINARY PARTS OF THE MICROWAVE CONDUCTIVITY VERSUS TEMPERATURE AT 35 GHz FOR A $\text{YBa}_2\text{Cu}_3\text{O}_{7-\delta}$ THIN FILM (2655 Å) ON A LaAlO_3 SUBSTRATE.

We calculated the values of the magnetic penetration depth λ from the values of σ_2 and London's expression $\lambda = (\mu_0\omega\sigma_2)^{-1/2}$. For sample 1, λ of 0.57 and 0.40 μm were obtained at 76 and 25 K, respectively. Figure 3 shows a plot of λ versus temperature for this sample. For sample 2, λ of 0.43 and 0.26 μm were obtained at 76 and 25 K, respectively.

The values of λ obtained in this study were higher than the best reported values for strongly c-axis-oriented $\text{YBa}_2\text{Cu}_3\text{O}_{7-x}$ thin films on SrTiO_3 ($\lambda \approx 0.14 \mu\text{m}$).⁸ These larger λ values can be explained in terms of the existence of residual inhomogeneities. It has been shown⁹ that these inhomogeneities can produce grain boundary Josephson junctions, which will increase the effective penetration depth. Furthermore, although the x-ray diffraction pattern for the films revealed

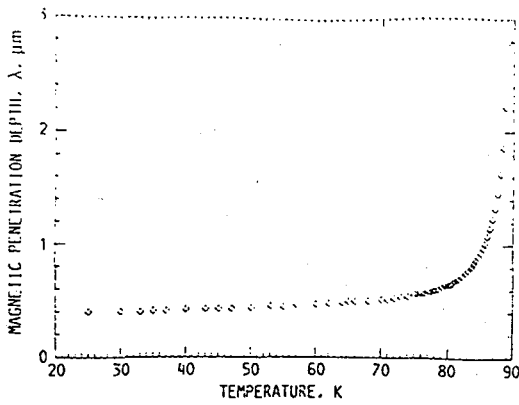


FIGURE 3. - MAGNETIC PENETRATION DEPTH VERSUS TEMPERATURE FOR A $\text{YBa}_2\text{Cu}_3\text{O}_{7-\delta}$ THIN FILM (2655 Å) ON A LaAlO_3 SUBSTRATE.

predominantly c-axis orientation, SEM micrographs revealed randomly distributed grains protruding through the surface that may be a-axis-oriented grains. The presence of a-axis oriented grains in a film increases the value of λ , since the penetration depth for shielding currents along the c-axis is greater than that for shielding currents in the a-b plane.¹⁰

The surface resistance R_s for films in the superconducting state can be obtained by using the expression^{11,12}

$$R_s = R_N \left\{ \frac{[(\sigma_1/\sigma_N)^2 - (\sigma_2/\sigma_N)^2]^{1/2} - \sigma_2/\sigma_N}{(\sigma_1/\sigma_N)^2 + (\sigma_2/\sigma_N)^2} \right\}^{1/2} \quad (3)$$

where $R_N = (\omega \mu_0 / 2\sigma_N)^{1/2}$ and σ_N are the surface resistance and the conductivity, respectively, at the onset temperature as determined from microwave power transmission measurements. The R_s values at 36 GHz were obtained assuming a T^2 dependence for R_s . The change in R_s for sample 1 with decreasing temperature is shown in Fig. 4. At 76 K, R_s of 24 and 36 mΩ were obtained for samples 1 and 2, respectively. At 25 K, an R_s of 12 mΩ was obtained for both samples. The surface resistance for the samples was also measured by looking at the change in Q of a TE_{011} -mode (OFHC) copper cavity resonant at 36 GHz when one of its end walls was replaced with the superconducting sample. Values for R_s at 76 K of 25 and 303 mΩ were measured for samples 1 and 2, respectively. The R_s values for sample 1 as measured by the cavity technique are plotted in fig. 4. We have also plotted the R_s of copper for comparison.

Note that both techniques give an R_s that decreases rapidly when the sample is cooled through the transition temperature and then levels off at lower temperatures, showing a residual surface resistance that changes very slowly with decreasing temperature. Observe that although there is a considerable discrepancy between the R_s values obtained by the two techniques at temperatures not far below T_c , they compare better at lower temperatures. The same feature was observed for sample

2. The normal skin depth $\delta_N = 2R_N/\omega\mu_0$ for sample 1 calculated from the R_s value at 87 K as measured by the cavity technique is approximately 5.4 μm. The largeness

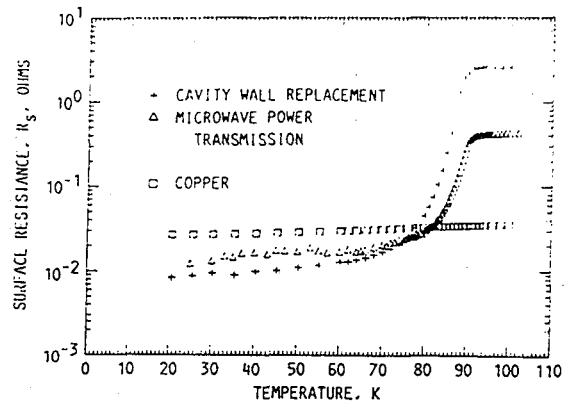


FIGURE 4. - SURFACE RESISTANCE VERSUS TEMPERATURE AT 36 GHz FOR A $\text{YBa}_2\text{Cu}_3\text{O}_{7-\delta}$ THIN FILM (2655 Å) ON LaAlO_3 AS MEASURED BY A CAVITY WALL REPLACEMENT METHOD AND BY A MICROWAVE POWER TRANSMISSION METHOD. THE R_s FOR COPPER IS ALSO PLOTTED FOR COMPARISON.

of this value relative to the film thickness of approximately 2655 Å suggests that a great deal of energy could be leaking through the substrate, an effect that would result in an overestimation of R_s . Because of the inhomogeneous nature of these films, it is very probable that some leakage can persist at temperatures lower than T_c but not at temperatures far below T_c since at these temperatures most of the film is superconducting. The increasing agreement between the R_s values obtained by the two techniques at lower temperatures seems to be consistent with this argument.

The results obtained by the microwave power transmission technique were strongly influenced by the intrinsic behavior of the superconducting intragranular material as well as by nonintrinsic losses due to normal inclusions and grain boundary effects in the interior of the film. Therefore, the R_s values obtained with this technique may be affected more by the nonintrinsic properties of the films than those measured by the cavity technique, which is only sensitive to the surface properties of the film. However, in view of the good correspondence obtained in this study for the R_s values at low temperatures, we believe that the microwave power transmission measurement technique provides an alternative way for determining R_s , particularly at temperatures far below T_c .

Conclusions

We have used a microwave power transmission measurement technique to determine the surface resistance R_s and the magnetic penetration depth λ of $\text{YBa}_2\text{Cu}_3\text{O}_{7-\delta}$ superconducting thin films. The calculated λ values were higher than the best reported values perhaps because of the effect of the film's inhomogeneities. Comparing the R_s values obtained by this technique with those measured by using a cavity wall-replacement technique suggests the suitability of the

microwave power transmission measurement technique for estimating R_s values of superconducting thin films.

References

1. K. Khachatryan, E. R. Weber, P. Tejedor, A. M. Stacey, and A.M. Portis, "Microwave observation of magnetic field penetration of high- T_c superconducting oxides", *Phys. Rev. B*, 36, 8309-8314, 1987.
2. Tyagi, S., et al., "Low-field ac susceptibility and microwave absorption in YBaCuO and BiCaSrCuO superconductors", *Physica C* 156, 73-78, 1988.
3. S. Sridhar and W. L. Kennedy, "Novel technique to measure the microwave response of high T_c superconductors between 4.2 and 200 K", *Rev. Sci. Instrum.* 59, 531-536, 1988.
4. J. P. Carini, A. M. Awasthi, W. Beyermann, G. Gruner, T. Hylton, K. Char, M. R. Beasley and A. Kapitulnik, "Millimeter-wave surface resistance measurements in highly oriented YBa₂Cu₃O_{7- δ} thin films", *Phys. Rev. B.*, 37, 9726-9729, 1988.
5. N. Klein, G. Muller, H. Piel, B. Roas, L. Shultz, U. Klein, and M. Peiniger, "Millimeter wave surface resistance of epitaxially grown YBa₂Cu₃O_{7- x} thin films", *Appl. Phys. Lett.*, 54, 757-759, 1989.
6. J. D. Warner, J. E. Meola, and K. A. Jenkins "Study of Deposition of YBa₂Cu₃O_{7- x} on Cubic Zirconia" *NASA TM 102350* (1989).
7. Q. Hu and P. L. Richards, "Design and analysis of a high T_c superconducting microbolometer", *Appl. Phys. Lett.* 55, 2444-2446, 1989.
8. A. T. Fiory, A. F. Hebard, P. M. Mankiewich, and R. E. Howard, "Renormalization of the mean-field superconducting penetration depth in epitaxial YBa₂Cu₃O₇ films", *Phys. Rev. Lett.* 61, 1419-1426, 1988.
9. L. Drabeck, J. P. Carini, G. Gruner, T. Hylton, K. Char, and M. R. Beasley, "Power-law temperature dependence of the electrodynamic properties in oriented YBa₂Cu₃O_{7- δ} and Y₂Ba₄Cu₃O_{16- δ} films", *Phys. Rev. B.*, 39, 785-788, 1989.
10. S. M. Anlage, H. Sze, H. J. Shortland, S. Tahara, B. Langley, C. B. Eom, M. R. Beasley, and R. Taber, "Measurements of the magnetic penetration depth in YBa₂Cu₃O_{7- δ} thin films by the microstrip resonator technique", *Appl. Phys. Lett.*, 54, 2710-2712, 1989.
11. J. I. Gittleman and B. Rosenblum, "Microwave Properties of Superconductors", *IEEE Proc.*, 52, 1138-1147, 1964.
12. J. I. Gittleman and J. R. Matey, "Modeling the microwave properties of the YBa₂Cu₃O_{7- x} superconductors", *J. Appl. Phys.*, 65, 688-691, 1989.

Properties of large area $\text{ErBa}_2\text{Cu}_3\text{O}_{7-x}$ thin films deposited by ionized cluster beams

L. L. Levenson

Department of Physics and Energy Science, University of Colorado, Colorado Springs, Colorado 80933-7150

M. Stan and K. B. Bhasin

Lewis Research Center National Aeronautics and Space Administration, Cleveland, Ohio 44135

(Received 17 September 1990; accepted 8 October 1990)

$\text{ErBa}_2\text{Cu}_3\text{O}_{7-x}$ films have been produced by simultaneous deposition of Er, Ba, and Cu from three ionized cluster beam (ICB) sources at acceleration voltages of 0.3–0.5 kV. Combining ozone oxidation with ICB deposition at 650 °C eliminated any need of post anneal processing. The substrates were rotated at 10 rotations per minute during the deposition which took place at a rate of about 3 to 4 nm. $\text{ErBa}_2\text{Cu}_3\text{O}_{7-x}$ films with areas up to 70 mm in diameter have been made by ICB deposition. These films, 100-nm thick, were deposited on SrTiO_3 (100) substrates at 650 °C in a mixture of 6 at. % O_3 in O_2 at a total pressure of 4×10^{-4} Torr. They had T_c ranging from 84.3 to 86.8 K over a 70 mm diameter and J_c above 10^6 A/cm² at 77 K. Another set of three samples, deposited within a 50 mm diameter, was examined by magnetization measurements. These samples had J_c ranging from 8.2×10^6 to 1.1×10^7 A/cm² at 4.2 K and from 2.4×10^5 to 5.1×10^5 A/cm² at 70 K. X-ray diffraction measurements of the three samples showed preferential *c*-axis orientation normal to the substrate surface. Rocking curves showed small variation in grain misorientation with sample position relative to the center of the substrate holder. Scanning electron micrographs (SEM) of the three samples also show some texture dependence on sample position. For the three samples, there is a correlation between SEM texture, full width at half-maximum of rocking curves and J_c versus temperature curves.

I. INTRODUCTION

Since the discovery of cuprate high temperature superconductors (HTS) by Bednorz and Muller¹ in 1986, a large number of investigations have been devoted to the development of HTS thin film deposition.² Of particular importance are the issues of surface roughness and the difficulties of fabricating large area, mirror smooth films with uniform physical properties. In general, smooth surfaces can be produced only if medium temperature deposition processes are used. The substrate temperature during deposition significantly influences the critical temperature T_c .³ The substrate temperature also strongly influences the orientation of the film crystal structure relative to the crystal plane of the substrate.³ Substrate temperature, deposition rate, and film composition all influence surface smoothness.⁴ For large area HTS films all of these factors must be well controlled to achieve high quality films for a variety of electronic applications.

Obviously, it is important to use a deposition technique which is able to produce single crystal HTS films on a wide range of substrate materials, especially those which do not have an ideal lattice match with 123 type ceramics. It has been known for some time that ionized cluster beam (ICB) deposition allows epitaxial film growth to be achieved even in cases of large lattice mismatch.⁵ Therefore, the recent application of ICB deposition to the fabrication of 123 type films is a logical development in HTS thin film research.⁶ At this time, it is of interest to survey some physical properties of ICB deposited 123 films since these films have good prospects for thin film electronic device applications.⁷ The data

presented here concern films produced in an experimental ICB apparatus. This ICB equipment was fabricated by Mitsubishi Electric Corporation in Amagasaki, Japan, and is presently being used at the University of Colorado at Colorado Springs.

II. EXPERIMENTAL

Three ICB sources⁵ were used to deposit 123 thin films on a variety of substrate materials. The base pressure of the vacuum system was 5×10^{-9} Torr. Load-lock mechanisms were used to introduce samples into the chamber, and to reload refractory metal source crucibles. The sample holder platten was 100 mm in diameter and was heated to 650 °C by thermal radiation from Ta wire heaters located above it. During film deposition, the sample holder was rotated at 10 rpm to obtain uniform film properties. Ionization of the cluster beams was produced by electron impact, and the acceleration voltage for deposition was between 0.3 and 0.5 kV. Quartz crystal deposition monitors were used to determine the deposition rate from each source before and during deposition. The film deposition rate was 3 to 4 nm/min. A shutter was opened and closed to start and stop deposition. The substrate temperature was monitored by optical pyrometry during film deposition. The oxidation gas was composed of 6 at. % ozone in oxygen. This gas was introduced into the chamber through a narrow tube located in proximity to the substrate holder. The oxidizing gas pressure was raised to 4×10^{-4} Torr after the substrate temperature was stabilized

and held constant during deposition and during the sample cool down.

III. RESULTS

YBCO and ErBCO thin films have been deposited by ICB onto a variety of substrates. These films have very similar properties. However, Er has a vapor pressure that is significantly higher than the vapor pressure of Y at any temperature.⁸ Thus, the source temperature for the deposition of Er is significantly lower than for Y at the same deposition rate. This is an advantage for ErBCO deposition. Therefore, in this paper we will limit our discussion to ErBCO films deposited by ICB.

Figure 1 shows the resistance-temperature relationship for an ErBaCuO film on SrTiO₃(100). This curve shows essentially a linear decline of resistance until the steep drop to zero resistance at 87 K. A typical J_c versus temperature curve of an ICB deposited ErBaCuO film on SrTiO₃ is shown in Fig. 2. At 77 K, J_c is greater than 1×10^6 A/cm², and J_c increases to over 3×10^6 A/cm² at 65 K.

Some work has been done to determine the properties of large area ErBCO films. Three ErBCO films deposited simultaneously on SrTiO₃(100). The positions of the substrates on the sample holder are shown in Fig. 3. The center of sample A was 25 mm from the center of the sample holder, the center of sample B was 18 mm from the center, and sample C was centered in the holder. The films were deposited at a nominal substrate temperature of 650 °C and were 100-nm thick. These films were examined by scanning electron micrographs (SEM). The micrographs of films A, B, and C are shown in Fig. 4. As seen in these micrographs, the film structure becomes more textured as the distance to the center of the sample holder becomes smaller.

The T_c for films A, B, and C were 86.3, 84.9, and 84.8 K, respectively, as measured by the four point probe method. The widths ΔT_c of the conductor to superconductor transition were 2.1, 2.6, and 2.8 K, respectively. Zero field magne-

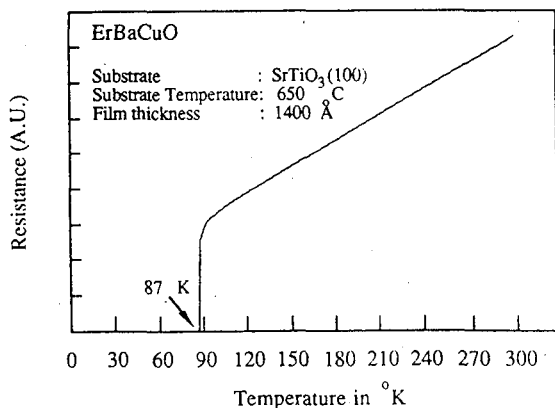


FIG. 1. Resistance-temperature curve for 100-nm thick ErBaCuO film (sample A).

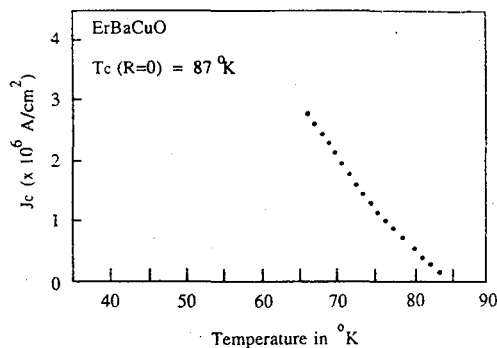


FIG. 2. Critical current density (J_c) vs temperature for an ErBaCuO film having $T_c = 87$ K.

tization (ZFC) and magnetization hysteresis measurements of these samples were made in a Quantum Design magnetic property measurement system (MPMS). All magnetization measurements were performed with the SrTiO₃ substrate face perpendicular to the applied magnetic field. The ZFC curve for sample A is shown in Fig. 5. The onset of diamagnetism occurs at approximately 85 K, in agreement with the direct current measurement of zero resistance at 86.3 K. The hysteresis curve for sample A at 4.2 K is shown in Fig. 6. The current density J_c at the temperature at which the hysteresis curve is measured can be calculated from the model of Bean.⁹ This calculation is an approximation since we are working with thin films and the Bean theory is based on cylindrical samples. However, this approach allows one to make comparisons between samples, and furthermore, the J_c calculated from hysteresis curves can be compared to direct current measurements of J_c at higher temperatures. The values of J_c versus T derived from hysteresis curves for samples A, B, and C at various temperatures are shown in Fig. 7. These values of J_c are very close except at 70 K, where J_c for sample C is significantly lower than the J_c for samples A and B. At 70 K, the calculated J_c for these samples is somewhat lower than J_c found by direct current measurements by roughly a factor of 2. However, given the approximations made to calculate J_c and the uncertainties in the sample dimensions (thickness and area), the agreement between the results found for J_c by two distinct methods is fairly good.

The x-ray spectrum of sample A is shown in Fig. 8. The x-ray diffraction spectra of samples A, B, and C are virtually identical. Since diffraction peaks only from (00 l) planes are visible in the spectra, it appears that the films have nearly

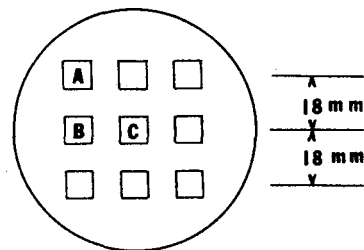


FIG. 3. Dimensions of sample holder used for samples A, B, and C.

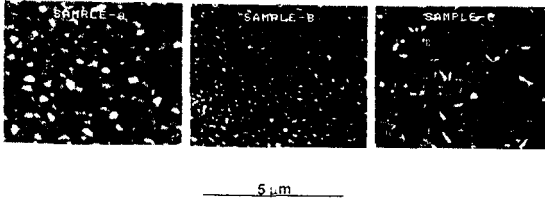


FIG. 4. SEM micrographs of a: sample A; b: sample B; c: sample C.

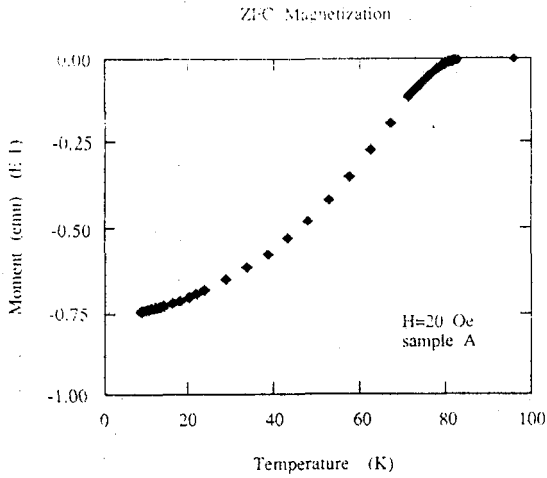


FIG. 5. Zero field cooling magnetization curve for sample A.

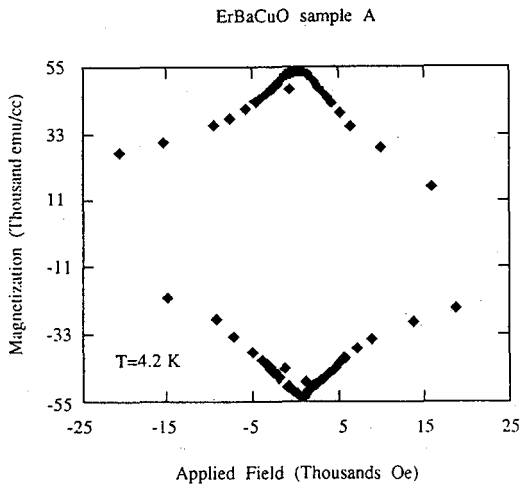


FIG. 6. Magnetization hysteresis curve at 4.2 K for sample A.

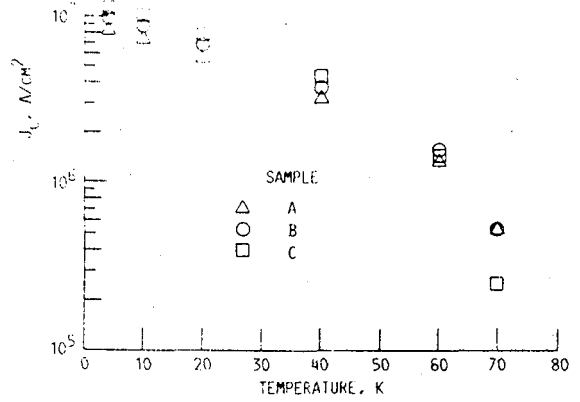


FIG. 7. J_c vs T derived from magnetization hysteresis curves for samples A, B, and C.

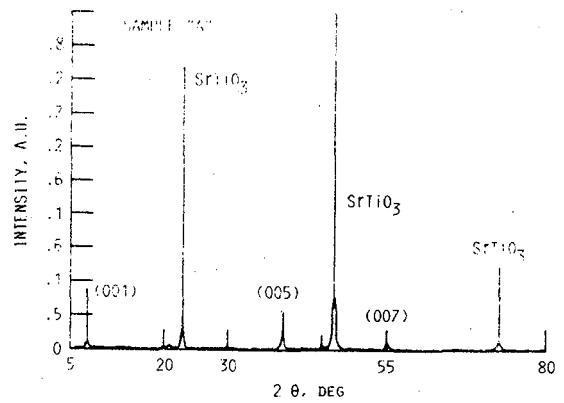


FIG. 8. X-ray spectrum of sample A. The (006) peak is hidden by the SrTiO₃ peak.

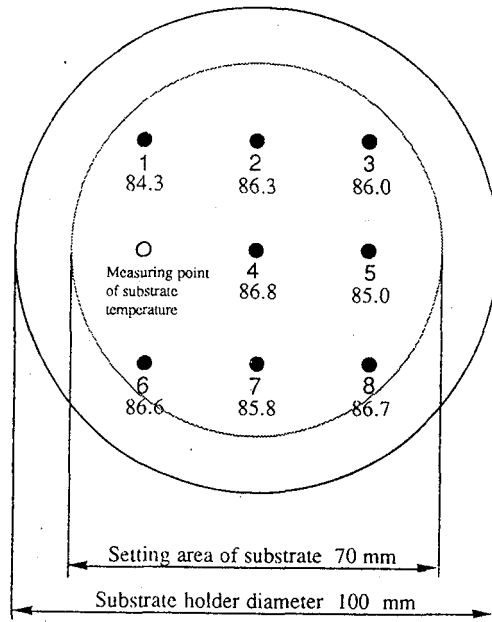


FIG. 9. Dimensions of sample holder used for large area deposition test. The values of T found for each sample inserted at each sample position.

TABLE I. Variation of T_c of eight $\text{ErBa}_2\text{Cu}_3\text{O}_{7-x}$ Films on SrTiO_3 substrates.

Measuring point	1	2	3	4	5	6	7	8
Measured T_c	84.3	86.3	86.0	86.8	85.0	86.6	85.8	86.7

perfect c -axis orientation normal to the substrate surface. However, the diffraction peaks characteristic of a -axis and b -axis growth may be obscured by the SrTiO_3 peaks: Therefore one must look for reflections, such as the (102) and (012) reflections, which do not overlap with the SrTiO_3 peaks. This type of measurement requires a four-circle diffractometer, which we have not used.

X-ray rocking curves give another indication of crystal perfection. Rocking curves were made of the (005) peaks for samples A, B, and C. These rocking curves gave full width at half-maximum (FWHM) values of 0.46° , 0.60° , and 0.63° for samples A, B, and C, respectively. It is evident that the film of sample A has a higher degree of crystal perfection than the other two samples. The x-ray rocking curve results correlate well with the higher T_c , the smaller ΔT_c , and the nominally higher J_c of sample A.

For samples A, B, and C the SEM micrographs, the x-ray rocking curves, and measured T_c and J_c show variations of film properties as a function of distance from the center of the sample holder. These variations in film properties were caused, in part, by a temperature gradient in the sample holder. Using thermocouples spot welded to the sample holder, we found a temperature 35°C lower at the edge of the sample holder when the temperature was 650°C at the center. Therefore, when large area HTS films are deposited, it is important to take steps to make the substrate temperature as uniform as possible.

Further information on this subject was developed by simultaneously depositing $\text{ErBa}_2\text{Cu}_3\text{O}_{7-x}$ on eight 1×1 cm SrTiO_3 substrates uniformly distributed on a circular substrate holder. Figure 9 shows the center positions of the eight SrTiO_3 (100) substrates on a sample holder. The outer diameter of the substrate group was 70 mm. The measured T_c of the ErBCO films is given in Table I.

There is a 2.5 K variation in T_c for the eight samples. This variation appears to be random. This randomness may be caused by a combination of small temperature and deposition rate nonuniformities. More work is required to correlate film structure, T_c and J_c with ICB film deposition conditions, especially for large area HTS films.

Although SrTiO_3 is an excellent substrate material for the epitaxial growth of 123 type HTS films, it has a large dielectric constant. This makes SrTiO_3 a poor candidate among substrates considered for high frequency applications of HTS films. In spite of its less than ideal lattice match with 123 films, MgO has been shown to be a good candidate as a substrate for high frequency applications.¹⁰ Another material of interest is LaAlO_3 which has a good lattice match with 123 films and good power transmission properties at millimeter wavelengths.^{10,11} ICB deposition of ErBCO films on these materials has produced T_c of 86 and 83–84 K and J_c of 3×10^5 and 1×10^5 A/cm² at 77 K on MgO(100) and

LaAlO_3 (100), respectively.¹² These results were obtained for films of thickness ranging from 0.1 to $0.14 \mu\text{m}$ and deposited on 650°C substrates. Because the number of depositions on MgO and LaAlO_3 substrates has been limited, these results should be considered as preliminary. Streaked reflection high-energy electron diffraction (RHEED) patterns from as-grown ErBCO films show that the surfaces of ErBCO films on MgO(100) substrates can be made extremely smooth by ICB deposition.¹²

IV. CONCLUSIONS

The ICB deposition of $\text{ErBa}_2\text{Cu}_3\text{O}_{7-x}$ films on various substrates has been demonstrated to produce high quality films without need of post-annealing processes. Large area (70 mm diameter) films have been grown in a mixture of ozone and oxygen on SrTiO_3 (100) at nominal substrate temperatures of 650°C . T_c for these films are generally in the range of 84–87 K, while J_c is commonly near 1×10^6 A/m² at 77 K. Preliminary x-ray diffraction data show that the films grown on SrTiO_3 are epitaxial with the c -axis perpendicular to the plane of the substrate surface. However, more detailed x-ray diffraction measurements are needed to determine the proportion of a -axis and b -axis perpendicular growth. Measurements of film properties in the U.S.A. have confirmed similar measurements made at Mitsubishi Electric Corporation in Japan. Therefore, it has been established that large area, smooth, stable HTS films having high J_c and very good T_c can be routinely produced by ICB.

ACKNOWLEDGMENTS

Thanks are due to K. Yamanishi and S. Yasunaga of Mitsubishi Electric Corporation for providing the authors with detailed information concerning the properties of ICB deposited HTS films made in their laboratory.

¹J. G. Bednorz and K. A. Muller, Z. Phys. B 23, 189 (1986).

²M. Leskela, J. K. Truman, C. H. Mueller, and P. H. Holloway, J. Vac. Sci. Technol. A 7, 3147 (1989).

³W. Shi, J. Shi, J. Shu, W. Yao, and Zh. Qi, Appl. Phys. Lett. 57, 822 (1990).

⁴A. Schuhl, R. Cabanel, S. Lequien, B. Ghyselen, S. Tyc, and G. Cruzet, Appl. Phys. Lett. 57, 819 (1990).

⁵I. Yamada, H. Inokawa, and T. Takagi, J. Appl. Phys. 56, 2746 (1984).

⁶K. Yamanishi, S. Yasunaga, K. Imada, K. Sato, and Y. Hashimoto, Mat. Res. Soc. Symp. Proc. 99, 343 (1988).

⁷K. Char, N. Newman, S. M. Garrison, R. W. Barton, R. C. Tabor, S. S. Laderman, and R. D. Jacowitz, Appl. Phys. Lett. 57, 409 (1990).

⁸R. E. Honig, RCA Rev. 23, 574 (1962).

⁹C. P. Bean, Rev. Mod. Phys., Vol. 36, 31 (1964).

¹⁰F. A. Miranda, W. L. Gordon, K. B. Bhasin, V. O. Heinen, and G. L. Valco, NASA Techn. Memor. 102345 (1989).

¹¹R. W. Simon, Appl. Phys. Lett. 53, 2677 (1988).

¹²K. Yamanishi and S. Yasunaga, Mitsubishi Electric Corporation, Amagasaki, Hyogo 661, Japan (private communication).

TEMPERATURE DEPENDENCE OF THE ANISOTROPY IN MAGNETIC RELAXATION

IN $\text{YBa}_2\text{Cu}_3\text{O}_{7-x}$ THIN FILMS

Satish Vitta, M. A. Stan and S. A. Alterovitz

NASA Lewis Research Center

Cleveland, OH 44135

Abstract

The relaxation of diamagnetic magnetization in the *c*-axis aligned $\text{YBa}_2\text{Cu}_3\text{O}_{7-x}$ thin film is studied as a function of orientation and temperature in the range 5-50 K at $H = 0.2$ T. The magnetization $M(T,H)$ in both the orientations $H \parallel c$ and $H \perp c$ and at all the temperatures is found to decrease logarithmically with time t . An activation energy for the movement of flux lines U can be obtained using the relation $U = -kT \{1/M_0, dM/d\ln t\}^{-1}$ and is found to be 30-110 meV in the range 5-50 K. For $H \parallel c$, U increases continuously with T , where as for $H \perp c$, U has two apparent maxima: at $T = 10$ K and $T > 50$ K. These results are discussed in terms of the thermally activated flux motion model.

Introduction

Among the different magnetic properties of the high temperature superconductors, the magnetic flux relaxation or creep has been extensively studied to determine the flux pinning energy, the nature of flux line configuration and motion. In the case of $\text{YBa}_2\text{Cu}_3\text{O}_7$, when $H \parallel c$, the reported values for the pinning energy in single crystals ranges from 20 meV to 17 eV and for thin films they vary from 25 meV to 4 eV.¹ The large variation is partly due to the different types of measurement techniques used. The flux relaxation and thus the pinning energy are generally discussed in terms of thermal activation combined with the various critical state models.² The flux relaxation rate for $H \perp c$ was found to be higher as compared to that for $H \parallel c$ by Rice et al.³ in disagreement with the results of Yeshurun et al.⁴ This anisotropy in relaxation has not been extensively investigated.

In this paper we report the diamagnetic relaxation in $\text{YBa}_2\text{Cu}_3\text{O}_{7-x}$ thin film as a function of field orientation and temperature in the range 5-50 K. The results are discussed in terms of the thermally activated flux motion model as modified by Beasley et al.⁵ Although a qualitative explanation for the temperature variation of the activation energy U can be obtained using this model, it is found to be insufficient to explain the results completely.

Experimental Procedures

The $\text{YBa}_2\text{Cu}_3\text{O}_{7-x}$ thin film (0.5 μm thick) was prepared by co-evaporation of Y, Cu and BaF_2 onto (100) SrTiO_3 substrate in an oxygen partial pressure followed by annealing in wet O_2 at 850 C. The film texture, analysed by

the standard x-ray diffraction and rocking curve techniques indicates that it is highly oriented with the *c*-axis perpendicular to the film plane. The grain morphology observed using scanning electron microscope shows that the grains are elongated rod like and the typical grain size is $\approx 0.5 \mu\text{m} \times 10 \mu\text{m}$. The superconducting transition temperature was determined by the dc four probe resistance method and is found to be 90 K with a transition width < 2 K.

The magnetic relaxation results reported here were obtained using the Quantum Design SQUID magnetometer. A clear plastic straw which has a negligible moment compared to the sample was used as the sample holder. In order to keep the spatial inhomogeneity in the applied field to $< 0.5 \%$ during the measurements, a short scan length of 3.6 cm is used. During each measurement, the sample was warmed up to 100 K, well above the transition temperature, and held for 5 min before cooling to the required temperature. The magnetic field was then set to the desired value, 3 min after the temperature reached a stable value ($\pm 0.5 \%$ of the set value). The magnetic relaxation data was recorded for 4000 s after the field was stabilized and a 3 min wait period.

Results and Discussion

The diamagnetic relaxation is studied as a function of temperature T and field H orientation with respect to the *c*-axis of the $\text{YBa}_2\text{Cu}_3\text{O}_{7-x}$. A fixed field of 0.2 T was used in all the cases. The magnetization was found to relax logarithmically with time t (for $t > 100$ s) both for $H \parallel c$ and $H \perp c$ in the temperature range 5-50 K, indicating that the sample was in the critical state. The rate of relaxation or flux creep $dM/d\ln t$ suitably modified by the demagnetization factor is shown in fig.1(a). For both the orientations $dM/d\ln t$ has a maximum, but at different temperatures. The creep rate normalised with the initial magnetization M_0 (M at $t = 100$ s), however does not exhibit a clear maximum for either of the directions and is shown in fig.1(b). This shows that the variation of M_0 with T is significant and that it can not be ignored.

The high rates of flux creep observed in the high temperature superconductors are generally attributed to the extremely short coherence lengths, thus low energy barriers, and discussed in terms of the thermally activated flux motion

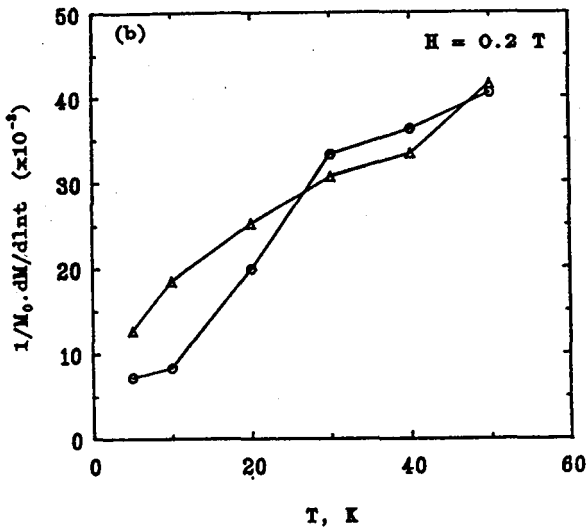
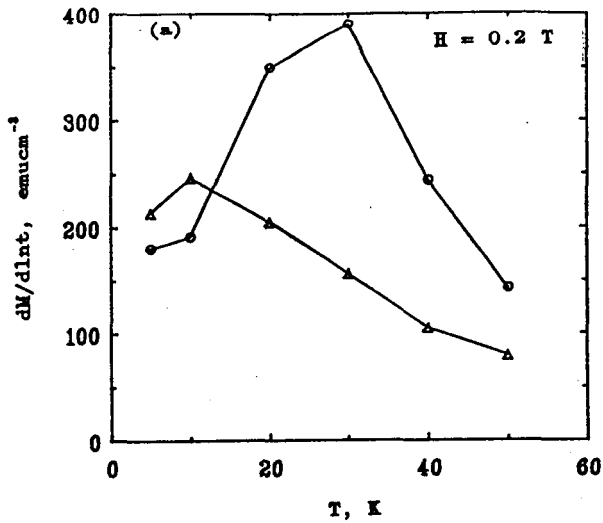


Figure 1. (a) The diamagnetic flux creep rate $dM/dlnt$ in the temperature range 5-50 K at $H = 0.2$ T. For $H \parallel c$ (Δ) the demagnetization factor $N = 0.98$ and for $H \perp c$ (\circ) $N \approx 0.6$.
 (b) The normalised flux creep rate $1/M_0 \cdot dM/dlnt$; $M_0 = M(t = 100 \text{ s})$.

model. According to this model, the flux lines move as a result of the driving force which is due to the combination of flux line density gradient and thermal activation. The activation energy for flux line motion is given as,⁵
 $U = -kT \{1/M_0 \cdot dM/dlnt\}^{-1}$. The activation energies for flux line motion determined using this relation are shown in fig.2.

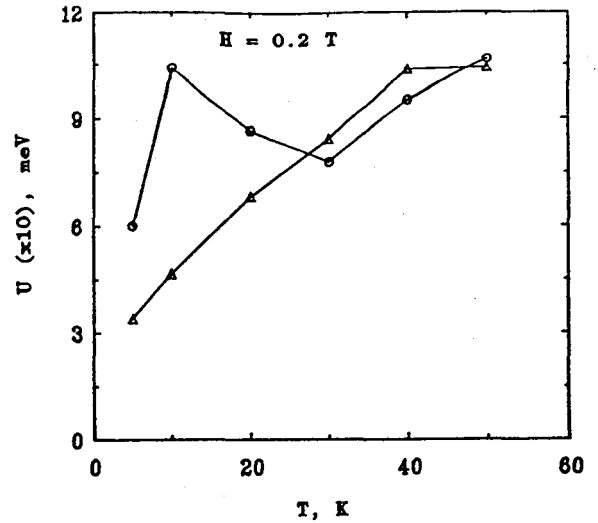


Figure 2. The activation energy $U(T)$ for $H \parallel c$ (Δ) and $H \perp c$ (\circ) at $H = 0.2$ T. (The lines through the data points in both the figures is only an aid to the eye and does not indicate any particular behaviour).

For $H \parallel c$, U increases monotonically from ~ 34 meV at 5 K to ~ 104 meV at 40 K and saturates. This behaviour can be understood qualitatively using the formalism given in ref.5. The activation energy U is assumed to be a linear function of the driving force F and is given as
 $U = U_0 - FVX$, where V is the activation volume and X is the pinning length. The driving force $F \propto H\nabla B$ or HJ_c , where J_c is the critical current density at t_0 . Hence $U(T)$ can be represented as $U(T) \approx U_0(T, \nabla B) - HVXJ_c(T, \nabla B)$. The intercept U_0 is merely a tangential intercept of the true pinning potential U_p versus the field gradient ∇B curve. As the temperature increases, ∇B and J_c decrease while U_0 increases and as a consequence the observed value of U increases with T .

As mentioned earlier, the model offers only a qualitative explanation for $U(T)$. The serious limitations of the model are as follows; (i) although U_p is treated as a nonlinear function of ∇B , the net activation energy U is assumed to be a linear function of F ; (ii) the treatment is valid only in the limit $U \gg kT$, i.e. the flux line motion is only along the field gradient ∇B , which is valid only at low temperatures and high U_p ; and (iii) it does not take into account material anisotropy and variation in the pinning strengths.

For $H \parallel c$, the dM/dI_{nt} curve [fig.1(a)] exhibits a peak at ≈ 30 K. This is generally interpreted as the temperature at which the flux fronts meet at the center of the sample.³ The activation energy U is found to increase with T only for $T > 30$ K, (fig.2) consistent within the description of thermally activated flux creep. However the values of U for $T < 30$ K cannot be understood even qualitatively using the above discussed model. The values of U for both the orientations are in the same range, contrary to the observation in a $YBa_2Cu_3O_7$ single crystal.⁴ A plausible reason for the low effective anisotropy is the density and type of defects in the film. Recently Daemuling et al.⁷ have reported point defects as the sources for pinning in single crystal $YBa_2Cu_3O_{7.6}$.

In conclusion, we find that the magnitude of the apparent pinning potential U is independent of the crystallographic orientation and is similar to that reported earlier.¹ In order to completely understand the nature of pinning and flux line motion, the field and temperature dependence of U together with the field dependence of the irreversibility temperature are required. The flux pinning in polycrystalline materials also depends on the method of sample preparation and hence a knowledge of the microstructure is needed to determine U_p unambiguously. Preliminary measurements of U as a function of H indicates that it decreases with increasing H ,⁸ contrary to the model proposed by Beasley et al.

Acknowledgements

SV acknowledges the National Research Council for an Associateship and MAS acknowledges the NASA Lewis Research Center for support through grant no. 440751.

* National Research Council Associate

Department of Physics, Kent State University,
Kent OH 44242

References

- 1) Y. Xu, M. Suenaga, A.R. Moodenbaugh and D.O. Welch, *Phys. Rev.B*, **40**, 10882 (1989); I.A. Campbell, L. Fruchter and R. Cabanel, *Phys. Rev. Lett.* **13**, 1561 (1990).
- (2) D. Shi, M. Xu and A. Umezawa (to be published).
- (3) J.P. Rice, D.M. Ginsberg, M.W. Rabin, K.G. Vanderwoot, G.W. Crabtree and H. Claus (to be published).
- (4) Y. Yeshurun, A.P. Malozemoff, F. Holtzberg and T.R. Dinger, *Phys. Rev.B*, **39**, (1988).
- (5) M.R. Beasley, R. Labusch and W.W. Webb, *Phys. Rev.* **181**, 682 (1969).
- (6) H. Zijlstra, *Experimental methods in magnetism* (North-Holland, Amsterdam, 1967).
- (7) M. Daemuling, J.M. Seuntjens and D.C. Larbal stier, *Nature*, **346**, 332 (1990).
- (8) Satish Vitta, M.A. Stan and S.A. Alterovitz (to be published).

Dependence of the critical temperature of laser-ablated $\text{YBa}_2\text{Cu}_3\text{O}_{7-\delta}$ thin films on LaAlO_3 substrate growth technique

Joseph D Warnert, Kul B Bhasin† and Felix A Miranda‡

† National Aeronautics and Space Administration, Lewis Research Center, 21000 Brookpark Road, Cleveland, OH 44135, USA

‡ Case Western Reserve University, Department of Physics, Cleveland, OH 44106, USA

Received 23 July 1990

Supercond. Sci. Technol. 3 (1990) 437-439. Printed in the UK

Abstract. Samples of LaAlO_3 made by flame fusion and the Czochralski method were subjected to the same temperature conditions that they have to undergo during the laser ablation deposition of $\text{YBa}_2\text{Cu}_3\text{O}_{7-\delta}$ thin films. After oxygen annealing at 750 °C, the LaAlO_3 substrate made by the two methods experienced surface roughening. The degree of roughening on the substrate made by the Czochralski method was three times greater than that on the substrate made by flame fusion. This excessive surface roughening may be the origin of the experimentally observed lowering of the critical temperature of a film deposited by laser ablation on a LaAlO_3 substrate made by the Czochralski method with respect to its counterpart deposited on a LaAlO_3 substrate made by flame fusion.

1. Introduction

High-temperature superconducting (HTS) thin films have been grown on LaAlO_3 (100) substrates because of its lattice match with $\text{YBa}_2\text{Cu}_3\text{O}_{7-\delta}$ and its possible suitability for the fabrication of microwave devices [1-3]. Since the surface quality of the substrate is very important in determining the quality of the HTS film to be deposited, it is necessary to know what kind of changes, if any, can take place on the substrate's surface during HTS film growth. For LaGaO_3 substrates, Miyazawa has shown that their surface roughened during the thermal cycling of growing $\text{YBa}_2\text{Cu}_3\text{O}_{7-\delta}$ thin films [4]. Since LaAlO_3 is isomorphic with LaGaO_3 and undergoes a second-order phase transition at 400 °C, one might expect that its surface would roughen as well. It is well known that for metal-substrate interfaces, the substrate's surface roughness increases the microwave losses [5]. Therefore, it is worthwhile to see if this same effect in the $\text{YBa}_2\text{Cu}_3\text{O}_{7-\delta}$ - LaAlO_3 interface would cause any degradation of the superconducting properties of the film.

At present there are two different commercial methods of making single crystals of LaAlO_3 . These are the Czochralski and the flame fusion methods. The method of substrate preparation could possibly determine the extent of surface roughening during thermal cycling of the substrate. Motivated by this possibility, substrates made by the two methods and obtained from different suppliers were subjected to the same thermal cycling conditions that they would have to undergo

during the growth of $\text{YBa}_2\text{Cu}_3\text{O}_{7-\delta}$ films by laser ablation. In addition, to determine the effect of the surface roughening on the critical temperature of the superconducting films, films of $\text{YBa}_2\text{Cu}_3\text{O}_{7-\delta}$ were grown on each type of substrate, with identical growth conditions, by laser ablation.

2. Experimental procedures and results

The substrates measured were from two commercial vendors. Each 500 μm thick substrate was polished on both sides. The surface roughness of the substrate made by the Czochralski method (hereinafter called Czochralski substrate) and of the substrate made by the flame fusion method (hereinafter called flame fusion substrate) was compared before and after annealing. The roughness was measured by a profilometer and calculated by taking the root mean square deviation of the distribution of data points from a smooth curve fitted through the profilometer's data. For measurements before the annealing, a piecewise, continuous, second-order function was fitted to the data; for measurements after annealing, a straight line was fitted to the data. The substrates were annealed together at 750 °C for 1 h with a slow cool to room temperature in oxygen.

As can be seen from figure 1, both substrates roughened after annealing, although the Czochralski substrate roughened considerably more than the flame fusion substrate. For the flame fusion substrate, the average

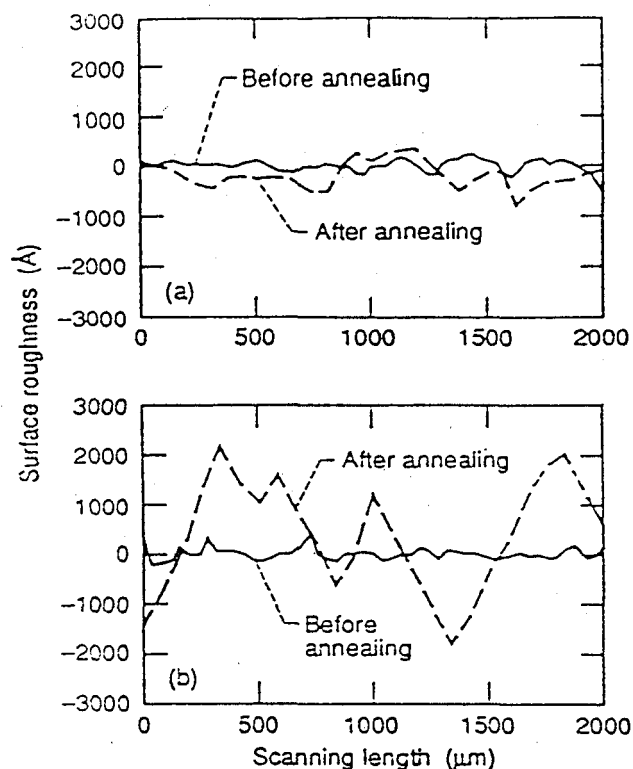


Figure 1. Surface roughness of LaAlO_3 as measured with a profilometer before and after annealing for (a) flame fusion substrate and (b) Czochralski substrate.

surface roughness before the annealing was $\sim 100 \text{ \AA}$, and after annealing it was $\sim 530 \text{ \AA}$. On the other hand, for the Czochralski substrate the average surface roughness before the annealing was $\sim 130 \text{ \AA}$ and after annealing an order of magnitude greater, $\sim 1490 \text{ \AA}$.

Thin films of $\text{YBa}_2\text{Cu}_3\text{O}_{7-\delta}$ ($\sim 0.6 \mu\text{m}$ thick) were grown on the two substrates by a laser ablation technique [6–8]. The growth conditions of films on the two substrates were the same (see table 1). The T_c of the film made on a flame fusion substrate was 89.8 K and exhibited a narrow transition region ($\sim 0.6 \text{ K}$); while the film made on the Czochralski substrate had a T_c of 85.9 K, a broad transition region ($\sim 4 \text{ K}$), and a tail, as can be seen in the inset of figure 2. The difference in the T_c , 4.1 K, of the two films is approximately eight times the run-to-run repeatability normally observed for $\text{YBa}_2\text{Cu}_3\text{O}_{7-\delta}$ films grown on SrTiO_3 or cubic zirconia.

Table 1. Deposition and *in situ* annealing parameters of high-temperature $\text{YBa}_2\text{Cu}_3\text{O}_{7-\delta}$ superconducting thin films grown by laser ablation.

Growth temperature ($^{\circ}\text{C}$)	750
Oxygen pressure (Torr)	0.17
Laser energy density per pulse at target (J cm^{-2})	2
Pulses per second	4
<i>In situ</i> annealing oxygen pressure (atm)	1
<i>In situ</i> annealing time to cool down to 50°C (h)	5

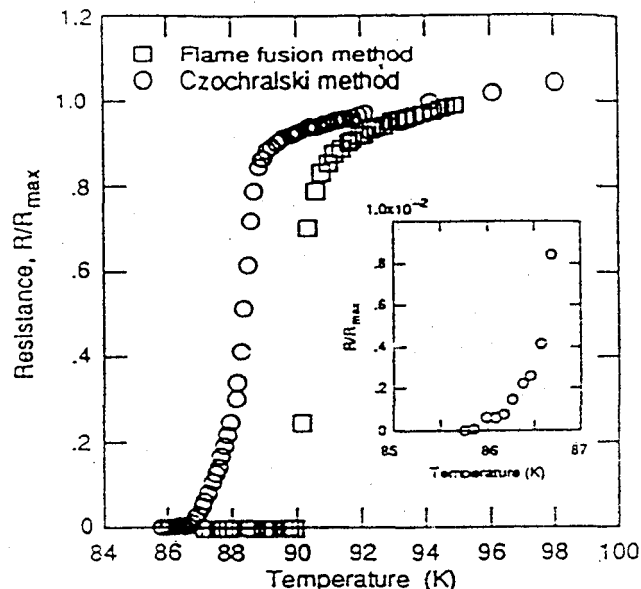


Figure 2. Plots of relative resistance against temperature for $\text{YBa}_2\text{Cu}_3\text{O}_{7-\delta}$ films on (100) LaAlO_3 made by flame fusion and by the Czochralski method.

Since two roughening behaviours were observed in LaAlO_3 substrates made by the flame fusion method and the Czochralski method, we believe that the roughening is not due to the intrinsic properties of LaAlO_3 . The relatively large post-anneal roughening observed in the Czochralski substrate could have been caused by relief of stress created during the growth process or during the sawing or polishing of the substrate. Since the stress could be manufacturing dependent, no conclusion about LaAlO_3 substrates made by the Czochralski method from other manufacturers can be drawn from this study.

3. Conclusions

We have shown that there is roughening of the surface of LaAlO_3 substrates when subjected to an annealing process similar to the one that the substrate undergoes during the deposition of $\text{YBa}_2\text{Cu}_3\text{O}_{7-\delta}$ thin films by laser ablation. The extent of the roughening was much greater in the sample made by the Czochralski method than in the sample made by flame fusion. The roughening of the surface of the flame fusion substrate had no noticeable effect on the T_c of the film deposited on it. However, we believe that the 4 K decrease in T_c for the film deposited on the Czochralski substrate may be a direct consequence of the enormous surface roughness developed by the substrate during the thermal cycling involved in the deposition process. Therefore, a careful testing of LaAlO_3 substrates must be performed, before the deposition of HTS films by laser ablation, to determine if their surface roughens as a result of the heating and cooling cycle involved in the deposition method.

References

- [1] Simon R W, Platt C E, Lee A E, Lee G S, Daly K P, Wire M S, Luine J A and Urbanik M 1988 *Appl. Phys. Lett.* 53 2677
- [2] Inam A *et al* 1990 *Appl. Phys. Lett.* 56 1178
- [3] Miranda F A, Gordon W L, Bhasin K B, Heinen V O, Warner J D and Valco G J 1990 NASA TM-102345 (to appear in *Proc. 3rd Ann. Conf. on Superconductivity and Applications* (New York: Plenum) to be published)
- [4] Miyazawa S 1989 *Appl. Phys. Lett.* 55 2230
- [5] Bhasin K B, Warner J D, Liu D C and Romanofsky R R 1985 *J. Vac. Sci. Technol. A* 3 778
- [6] Dijkamp D, Venkatesan T, Wu X D, Shaheen S A, Jisrawi N, Min Lee Y H, McLean W L and Croft M 1987 *Appl. Phys. Lett.* 51 619
- [7] Roas B, Schultz L and Endres G 1988 *Appl. Phys. Lett.* 53 1557
- [8] Warner J D, Meola J E and Jenkins K A 1989 NASA TM-102350

Electromigration failure in $\text{YBa}_2\text{Cu}_3\text{O}_{7-x}$ thin films

Satish Vitta,^{a)} M. A. Stan,^{b)} J. D. Warner, and S. A. Alterovitz
NASA Lewis Research Center, Cleveland, Ohio 44135

(Received 13 September 1990; accepted for publication 12 November 1990)

Electromigration failure in highly oriented $\text{YBa}_2\text{Cu}_3\text{O}_{7-x}$ thin films below the superconducting transition temperature is reported here for the first time. The film on SrTiO_3 failed at 86 K, $2.3 \times 10^5 \text{ A cm}^{-2}$; while that on LaAlO_3 failed at 84 K, $9.3 \times 10^5 \text{ A cm}^{-2}$. Scanning electron microscopy and energy dispersive x-ray analysis of the films after failure shows that Cu migrates preferentially away from the failure region towards the electrode.

The phenomenon of electromigration (EM) has been extensively studied in metals and alloys of Al, Au, and Cu because of their usage in semiconductor integrated circuits.¹ The study of EM in oxide materials had not been possible earlier because of their poor electrical conductivity. The recently discovered oxide superconductors, however, exhibit metallic conduction behavior in the normal state and when fabricated into stripes of thin film, were found to carry current densities $> 10^6 \text{ A cm}^{-2}$ in the superconducting state.² It is also known that holes and not electrons are the major charge carriers,³ and the oxygen atoms are highly mobile in these compounds.⁴ Hence the study of EM in these materials is important both for basic understanding and practical applicability. Recently, EM at 200 and 350 °C in $\text{YBa}_2\text{Cu}_3\text{O}_{7-\delta}$ sintered rods has been reported.⁵ In this letter, results obtained from EM below the superconducting transition temperature in $\text{YBa}_2\text{Cu}_3\text{O}_{7-x}$ thin films on SrTiO_3 and LaAlO_3 substrates are reported.

In the present work, thin films of $\text{YBa}_2\text{Cu}_3\text{O}_{7-x}$ were deposited onto SrTiO_3 and LaAlO_3 single-crystal substrates by pulsed excimer laser ablation.⁶ The films, $\approx 0.25 \mu\text{m}$, were patterned using conventional optical lithography and chemical etching into stripes of size $40 \mu\text{m}$ wide and 2.0 mm long between the voltage contact pads. Very low resistivity ohmic contacts to the film were obtained by a thorough cleaning of the film surface followed by an evaporation of $0.3 \mu\text{m}$ Ag onto the pads. The $T_c(R=0)$ for the film on LaAlO_3 is 88.6 K as compared to 90 K for the film on SrTiO_3 . The transition width in both the films however, is $< 2 \text{ K}$ and the critical current density at 77 K defined by $1.0 \mu\text{V cm}^{-1}$ is $> 10^6 \text{ A cm}^{-2}$.

Following the critical current measurements, the current voltage (I - V) characteristics of the two films were studied. During these studies the samples were biased with currents which resulted in the development of electric fields as high as 50 mV cm^{-1} along the stripe. However the time for which such high electric fields were sustained was very short ($< 60 \text{ s}$). The films were subjected to repeated temperature and current cycles during these observations. Since the temperature range of cycling was only between 30 and 90 K, thermal stress failure can be ruled

out. The films on both the substrates failed after $\approx 40 \text{ h}$. The film on SrTiO_3 substrate failed at $\approx 86 \text{ K}$. The current density at this temperature was $2.3 \times 10^5 \text{ A cm}^{-2}$ corresponding to a field of 50 mV cm^{-1} between the two voltage contacts. The film on LaAlO_3 on the other hand failed at $\approx 84 \text{ K}$; $9.3 \times 10^5 \text{ A cm}^{-2}$ and 20 mV cm^{-1} . The surface morphology of the films after they failed was studied both by optical and scanning electron microscopy and is shown in Figs. 1 and 2. In both films, failure occurred both across the main stripe and at the junction between one of the large current pads and the main conductor stripe where there is a large change in the cross-sectional area of the film. The failure pattern at the pad stripe junction is similar to that observed in the mechanical failure of materials—initiation and propagation of a crack. The tendency of the crack-like feature to extend radially outward towards a current pad is reminiscent of the EM failure pattern in metals. Close observation of the scanning electron micrographs reveals a macroscopic material displacement at both the failed regions. A clear material buildup can be seen along the sides of the crack-like feature and also away from it. This is similar to that observed in electromigration failure of metals and alloy thin films—formation of hillocks and voids.⁷ In the case of metals and alloys, voids or cracks are observed at the cathode and material buildup in the form of hillocks is found both at the anode and along the length of the conductor stripe. In the present case of $\text{YBa}_2\text{Cu}_3\text{O}_{7-x}$ a clear distinction between voids and hillocks as seen in metals is not observed.

The composition analysis of the film using energy dispersive x-ray analysis technique at different points along the length of the stripe shows several salient features. Far away from the failure region and towards the seemingly unaffected current pad, a contour mapping of the three cations, Y, Ba, and Cu, shows that they are uniformly distributed over the entire area. However, at the regions of failure, a clear segregation of the three elements is observed. A very noticeable fact is that there is a relative depletion of Cu at the failed region on the stripe as compared to that near the current pad.

In the EM studies of $\text{YBa}_2\text{Cu}_3\text{O}_{7-\delta}$ at 200 and 350 °C,⁵ it was found that the material decomposes into a number of phases at the anode accompanied by an oxygen enrichment at the cathode. This has been attributed to the nature of charge carriers (holes) and also the ease of oxygen diffusion. It is well known from the crystallographic

^{a)}National Research Council Associate.

^{b)}Department of Physics, Kent State University, Kent, Ohio, 44242.

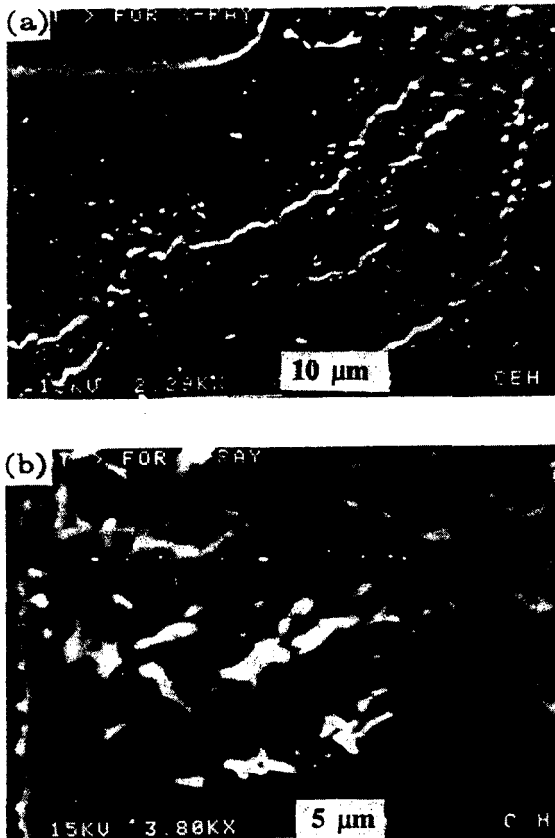


FIG. 1. Scanning electron microscope (SEM) micrographs of electromigration failure in the $\text{YBa}_2\text{Cu}_3\text{O}_{7-x}$ film on (100) SrTiO_3 substrate: (a) at the current pad-main conductor stripe junction, (b) across the main conductor stripe.

studies⁸ that the O atoms are primarily in the Cu and Ba planes. Hence migration of the anion (O) towards the cathode should lead to the migration of Cu and/or Ba. The relative depletion of Cu in the middle and an enrichment at the pad observed in the present work clearly indicates that the migrating cation is Cu. The diffusion studies of ^{63}Ni in $\text{YBa}_2\text{Cu}_3\text{O}_{7-x}$ thin films in the temperature range 500–650 °C yielded activation energies and diffusion coefficients similar to those of Cu self-diffusion,⁹ further indicating that Cu is the migrating cation. The $\text{YBa}_2\text{Cu}_3\text{O}_{7-x}$ compound is known to be unstable below an oxygen concentration of 5.8 and decomposes into various phases.¹⁰ The conductivity of the decomposed phases varies from metallic to insulating values. Decomposition of $\text{YBa}_2\text{Cu}_3\text{O}_{7-x}$ by EM into various low conductivity phases in the presence of the high current densities used in these experiments could lead to a thermal failure known as thermomigration. The rounding of the walls of the crack-like feature is evidence for possible heating.

Electromigration of atoms, in general, is due to diffusion of the atomic species in the presence of an external driving force. In the case of thin polycrystalline films, diffusion will be along the grain boundaries and the surface as the bulk diffusivity will be negligible at low temperatures.

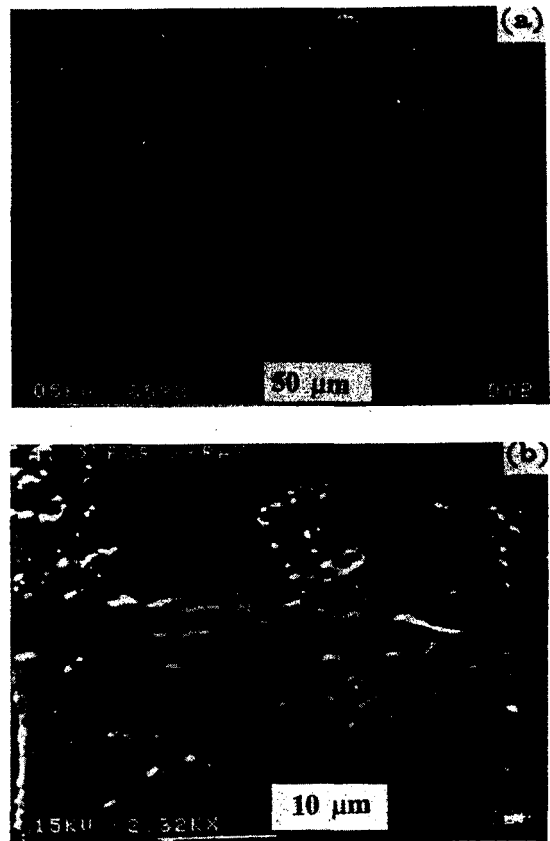


FIG. 2. SEM micrographs of electromigration failure in the $\text{YBa}_2\text{Cu}_3\text{O}_{7-x}$ film on (100) LaAlO_3 substrate: (a) at the current pad-main conductor stripe junction, (b) across the main conductor stripe.

The driving force for electromigration in the free electron-gas description of a conductor is typically assumed to have two components: (i) direct force on the charge of the migrating ion due to the applied electric field (E), and (ii) force due to momentum transfer from the charge carriers to the migrating atom “wind force.”

The average grain size in both the films is $< 0.25 \mu\text{m}$, which is comparable to the film thickness, and the grains are preferentially aligned with the c axis perpendicular to the film plane. However the in-plane alignment of the grains is known to be random. These factors are known to enhance electromigration. The residual resistivity fraction, which contributes to the wind force at the failure temperature obtained by extrapolating the normal-state resistance, is found to be 0.14 and 0.19, respectively for the films on SrTiO_3 and LaAlO_3 . These relatively high values, as compared to metals and alloys together with the microstructural features, lead to electromigration failure in the high-temperature superconducting materials.

In conclusion, electromigration-related failure in $\text{YBa}_2\text{Cu}_3\text{O}_{7-x}$ thin films has been reported here for the first time. The phenomenon of EM in oxide superconductors in general is complex due to the associated phase changes and decomposition as a function of oxygen con-

centration. The grain boundary diffusivity and its anisotropy, if any, are not currently known. Also, since the normal-state conduction in these materials is completely different, the driving force for EM cannot be estimated using the models applicable to metals and alloys. A detailed understanding of the charge distribution and screening effects is necessary to estimate the driving force. Detailed investigation of these factors is currently in progress.

SV wishes to acknowledge the National Research Council for an Associateship and MAS wishes to acknowledge NASA Lewis Research Center for support through grant No. 440751. The authors also wish to acknowledge D. Bohman and G. Kitchen for their assistance.

¹See, R. E. Hummel and H. B. Huntington, eds. *Electro- and Thermotransport in Metals and Alloys* (The Metallurgical Society, New York,

1977), p. 2.

²J. Mannhart, P. Chaudhari, D. Dimos, C. C. Tsuei, and T. R. McGuire, *Phys. Rev. Lett.* **61**, 2476 (1988).

³N. P. Ong, Z. Z. Wang, J. Clayhold, J. M. Tarascon, L. H. Green, and W. R. McKinnon, *Phys. Rev. B* **36**, 7222 (1987).

⁴Hans-Ulrich Krebs, *J. Less-Common Metals* **150**, 269 (1989).

⁵K. Govinda Rajan, P. Parameshwaran, J. Janaki, and T. S. Radhakrishnan, *J. Phys. D: Appl. Phys.* **23**, 694 (1990).

⁶J. D. Warner, J. E. Meola, and K. A. Jenkins, NASA Technical Memorandum-102350, 1989.

⁷A. Gangulee and F. M. D'Heurle, *Thin Solid Films* **25**, 317 (1975).

⁸J. D. Jorgensen, *Jpn. J. Appl. Phys. Suppl.* **26**, 2017 (1987).

⁹D. Gupta, R. B. Laibovitz, and J. A. Lacey, *Phys. Rev. Lett.* **64**, 2675 (1990).

¹⁰Y. Hariharan, C. S. Sundar, J. Janaki, A. K. Sood, M. P. Janawadkar, A. Bharathi, V. Sankara Sastry, R. Baskaran, and T. S. Radhakrishnan, in *Studies in High Temperature Superconductors*, edited by A. V. Narlikar (Nova Science, New York, 1989), p. 255.

ELLIPSOMETRIC STUDY OF $\text{YBa}_2\text{Cu}_3\text{O}_{7-x}$ LASER ABLATED AND CO-EVAPORATED FILMS

S. A. ALTEROVITZ*, R. M. SIEG**, J. D. WARNER*, M. A. STAN+, S. VITTA**

*NASA-Lewis Research Center, Cleveland, Ohio 44135

**Undergraduate Student Intern at NASA-Lewis Research Center from Cleveland State University, Dept. of Electrical Engineering, Cleveland, Ohio, 44115

+Kent State University, Department of Physics, Kent, Ohio 44242

**NRC Research Associate

ABSTRACT

High temperature superconducting films of $\text{YBa}_2\text{Cu}_3\text{O}_{7-x}$ (YBCO) were grown on SrTiO_3 , LaAlO_3 , and YSZ substrates using two techniques: excimer laser ablation with in-situ annealing and co-evaporation of Y, Cu, and BaF_2 with ex-situ annealing. Film thicknesses were typically 5000 Å, with predominant c-axis alignment perpendicular to the substrate. Critical temperatures up to $T_c(R=0)=90\text{K}$ were achieved by both techniques. Ellipsometric measurements were taken in the range 1.6-4.3 eV using a variable angle spectroscopic ellipsometer. The complex dielectric function of the laser ablated films was reproducible from run to run, and was found to be within 10% of that previously reported for (001) oriented single crystals. A dielectric overlayer was observed in these films, with an index of refraction of approximately 1.55 and nearly zero absorption. For the laser ablated films the optical properties were essentially independent of substrate material. The magnitude of the dielectric function obtained for the co-evaporated films was much lower than the value reported for single crystals, and was sample dependent.

INTRODUCTION

Ellipsometry of thin films is a non-destructive technique used to characterize the properties and morphology of thin film materials. It is particularly suitable for thin films since it is non-destructive, highly accurate, and self-normalizing. Recently several investigators have used ellipsometry to study the dielectric function of sintered pellets [1-4] made from superconducting materials such as YBCO, $\text{CaBi}_2\text{Sr}_2\text{Cu}_2\text{O}_8$, and $\text{M}\text{Ba}_2\text{Cu}_3\text{O}_7$, where M is a lanthanide, as well as single crystal YBCO [1,4]. In general, their results show that the oxygen content has a strong effect on the imaginary part (ϵ_2) of the dielectric function $\epsilon(E)$, but the absolute values depend on the sample. For instance, the measured values of the dielectric function of single crystal samples when compared show very different values in the literature [1,4]. Thus, there is no calibration spectrum that can be used for further ellipsometric studies of morphology and/or overlayers. This fact has essentially prevented any meaningful application of ellipsometry to high temperature superconductors in the last two years.

In this study we will present the application of ellipsometry to the study of sample surface, and overlayer nature and growth rate mainly on laser ablated YBCO superconducting films deposited on several substrates. First, we demonstrate the detection of the presence of a thin overlayer on laser ablated films, its refractive index, thickness, and time evolution. Second, we compare, using SEM and ellipsometry, the surface morphology of YBCO thin films made by two techniques: laser ablation with in-situ oxygen anneal and co-evaporation

with ex-situ anneal. Thus, we show that ellipsometry is a valid technique for the evaluation of surface quality in thin HTS films. It is expected that the above study should lead to extensive application of ellipsometry to the investigation of the surface properties of high temperature superconductors.

EXPERIMENTAL

Samples were prepared by two methods: laser ablation and co-evaporation. The laser ablation technique [5] was based on an excimer laser working at 248 nm, energy density of 1.5 J/cm²/pulse with 4 pulses per second. The target was a sintered 25 mm diameter YBCO pellet located 8 cm from the sample at 45° to the laser beam. The beam was rastered up and down 1 cm over the target using an external lens on a translator. The substrates used in this study, namely SrTiO₃, YSZ (yttria stabilized ZrO₂), and LaAlO₃, were mounted on a stainless steel plate with a diameter of 63 mm. The plate was heated from the backside by resistive heating, while a type K thermocouple, welded to the plate, was used for thermometry. After a preheat to 500 °C, oxygen was introduced into the chamber and the samples were heated to temperatures at or near 775 °C. During deposition an oxygen pressure of 170 mTorr was maintained. After deposition the oxygen pressure was raised to 1 atm and the temperature was lowered slowly (at a rate of 2 °C/min) to 450 °C, maintained there for 2 hours, then lowered slowly to 250 °C and finally cooled below 40 °C for removal. The co-evaporation method was essentially the same as the one described in reference [6]. Two electron guns were used to evaporate Y and Cu while thermal evaporation was used for BaF₂. The ex-situ anneal step started with wet oxygen for 1 hour at 875 °C, followed by a dry oxygen anneal, 1 hour step down to 550 °C, 1 hour at 550 °C, and finally oven cool down. The critical temperature, T_c, was measured resistively using a four point technique. In some cases the actual samples were tested, while other times samples made in the same run were measured. The ellipsometric technique was described elsewhere [7] and will not be repeated here. Analysis of the results was done mainly using a substrate and ambient model, while in some cases a substrate, film, and ambient model was applied. Rough surfaces were modeled by a combination of voids and substrate material using the effective medium approximation (EMA) [8].

RESULTS

Results reported here were obtained on samples prepared in separate runs on both the laser ablation and co-evaporation techniques. All samples show c-axis alignment, with only (001) peaks present in the X-ray diffraction pattern. Altogether 12 laser ablated and 5 co-evaporated films were measured. Data will be reported only for samples with a T_c(R=0) higher than 82 K. This is essentially all of the films since a T_c(R=0) higher than 85 K was characteristic of most of the films, especially in the case of the laser ablated films. The thickness of the films was typically 5000 Å, thus ensuring that it was much larger than the optical penetration depth. Several measurements at different angles of incidence, in the range 65°-75°, were performed for all samples. The measured ellipsometric parameters tan(ψ) and cos(Δ) were used to calculate the dielectric function, ϵ , directly. The results gave essentially the same value of the dielectric function, ϵ , independent of the angle of incidence for the samples shown here. Results for ϵ for four representative samples made by laser ablation are compared with that of single crystal YBCO [4] in Fig. 1.

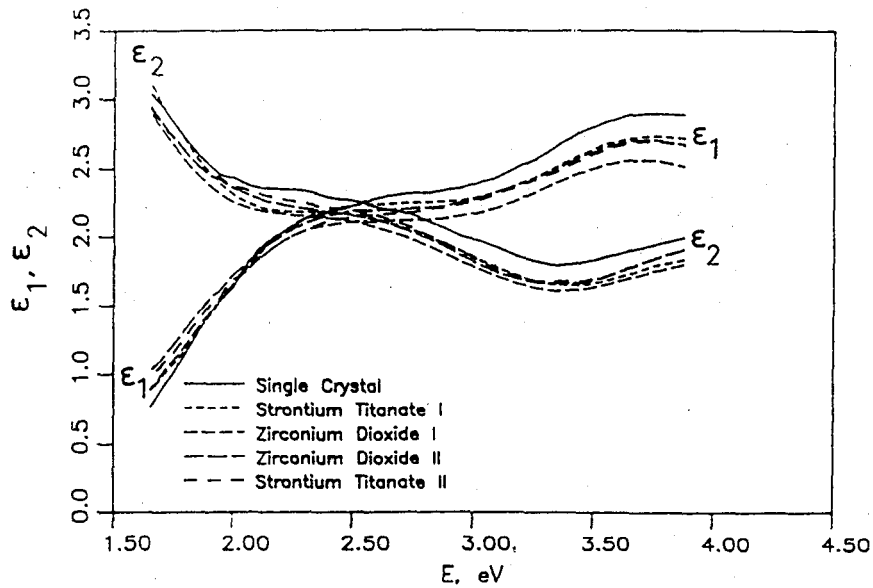


FIGURE 1. - DIELECTRIC FUNCTION OF FOUR LASER ABLATED FILMS AND A SINGLE CRYSTAL YBCO [4].

All laser ablated samples, irrespective of the substrate material, gave dielectric functions with very similar shapes. However, some of them gave absolute values lower than the majority. The lowest $\epsilon(E)$ values obtained for any laser ablated sample are shown in Fig. 2, labeled "before Q tip cleaning".

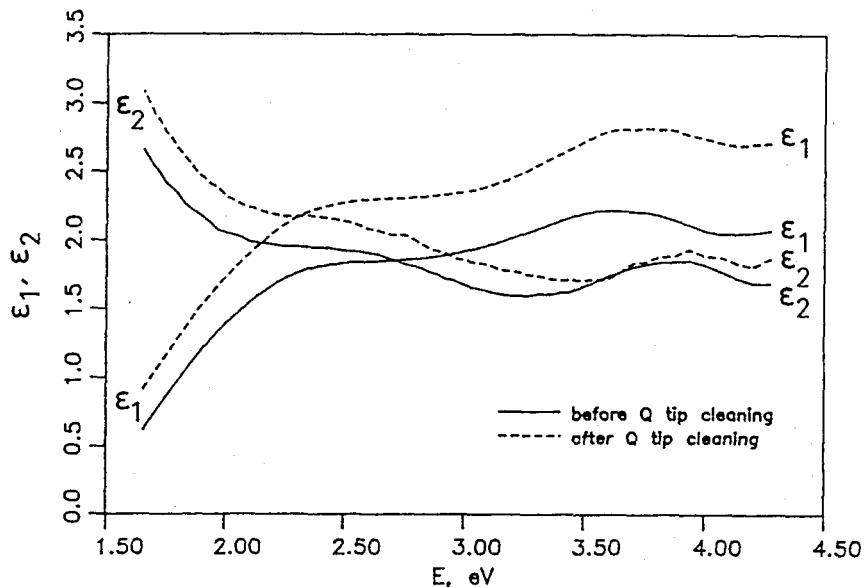


FIGURE 2. - DIELECTRIC FUNCTION OF A LASER ABLATED FILM BEFORE AND AFTER MECHANICAL CLEANING.

In the course of making electrical contacts to the laser ablated films, we found that the quality of the contacts is poor. A solution to this problem was mechanical cleaning of the surface. This fact is related to the result previously reported for YBCO, namely the interaction with air to produce BaCO_3 and Ba(OH)_2 [9-11]. The Ba(OH)_2 is formed only as an intermediate step to the BaCO_3 formation, with grain boundaries covered primarily by BaCO_3 [9-11]. Mechanical cleaning with a Q tip removed a small amount of white film from the samples with low values of the dielectric function. Fig. 2 displays ϵ before and after mechanical cleaning. Cleaning was done with the sample in the ellipsometer, with dry nitrogen flowing for the measurement. The difference between these two spectra was analyzed as follows: $\epsilon(E)$ after mechanical cleaning was assumed as the calibration $\epsilon(E)$, while the result for $\epsilon(E)$ before cleaning was analyzed as substrate-dielectric film-ambient. The refractive index of the 72 Å film was found to be 1.55. Moreover, it is not a function of energy, i.e., it does not have dispersion in the visible. This fact shows that the overlayer is an insulator. This value of the refractive index and the color are in good agreement with published data [12] for BaCO_3 , not Ba(OH)_2 . The BaCO_3 film growth rate in air, at temperatures around 20 °C, was studied by measuring the film thickness versus time. Measurements started immediately after the mechanical cleaning and lasted 480 hours. The final thickness was 35 Å, showing a rather slow growth rate, of the order of 1.5 Å/day, for this sample. We found that the quality of electrical contacts made by silver evaporation and annealing in oxygen depends on the thickness of the dielectric layer. In the worst cases, the silver contact would peel off the sample when a small force was applied. Results of $\epsilon(E)$ functions of cleaned samples show much less variation in absolute value versus the original measurements.

Dielectric functions of two co-evaporated samples are shown in Fig. 3. $\epsilon(E)$ in this case is sample dependent and bear small similarity to the single crystal result. SEM micrographs of the films show the presence of voids on otherwise dense films. In addition, the films show more roughness on the surface as compared to the laser ablated films which have $<0.25 \mu\text{m}$ surface roughness as seen by SEM.

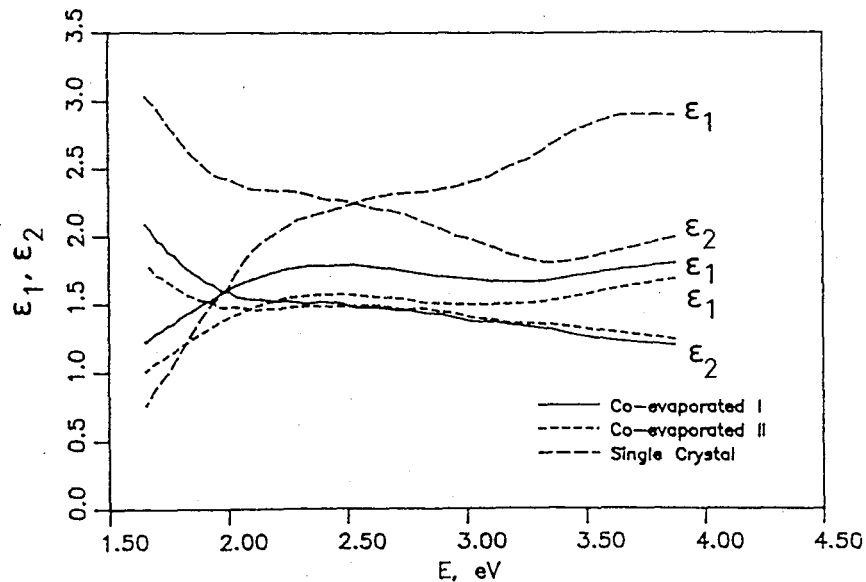


FIGURE 3. - DIELECTRIC FUNCTION OF TWO COEVAPORATED FILMS AND A SINGLE CRYSTAL YBCO [4].

We tried to describe the morphology by the EMA method [8], i.e. using a combination of voids and YBCO. The free parameter used was the void volume fraction, f . A test of the quality of this model is given in Fig. 4, where the best value of f (25.8%) was used to generate ψ and Δ , and compared with the experimental results. The quality of the fit is only moderate, showing that this model is marginally applicable. We obtained large void fractions typically around 20-25%.

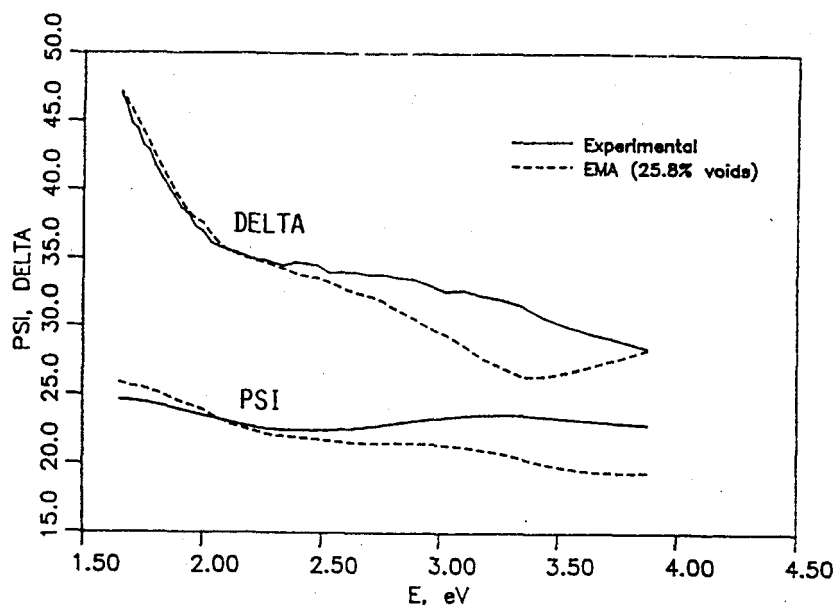


FIGURE 4. - CALCULATED AND EXPERIMENTAL PSI AND DELTA VERSUS ENERGY FOR A COEVAPORATED YBCO FILM.

DISCUSSION

Evaluation of a dielectric function for ellipsometric characterization purposes requires an absolutely perfect surface. As YBCO reacts with air, and the surface morphology of this new type of material is not completely under control, the $\epsilon(E)$ determination is not a simple matter. Our results show a scatter just below 10% among themselves and versus the single crystal result. The best analysis of the overlayers, which are below 10 Å in many cases, is reached when the $\epsilon(E)$ of the cleaned sample is used as the substrate $\epsilon(E)$, i.e. not by using a universal $\epsilon(E)$ function. In this way surface irregularities do not interfere with the overlayer analysis. The fact that our results are so similar to the single crystal result of reference [4] shows that the laser ablation technique gives smooth crystalline films and that the $\epsilon(E)$ given in [4] is for a good quality single crystal. The overlayer, probably BaCO_3 , was shown to grow very slowly. However, we believe that the growth rate depends on the stoichiometry of the material on the top surface layer. Thus, the experimental growth rate measured here is only for one particular case, obtained for a high quality crystalline film.

The EMA analysis of the co-evaporated films was not completely successful. The reasons for this, in our opinion, are mainly the complex nature of the surface roughness, and, to a lesser extent, the imperfect stoichiometry on the surface of these films. We expect the void fraction to be a function of depth, with lower values of f as we move into the film. These facts, along with the

anisotropy of the material, result in a dielectric function that is probably different from our calibration function.

CONCLUSIONS

We obtained reproducible results for the dielectric function on fully c-axis aligned samples. In absolute value, this result is very similar to the function obtained for (001), platelet-like, free-grown, single crystals [4]. The differences are smaller than 10% at any value of the spectrum. We used our result as the calibration spectrum for subsequent studies, although the single crystal result of reference [4] is probably just as reliable. An overlayer of BaCO₃ was measured on top of these films and its growth rate was determined. Results of the overlayer properties analysis compare favorably with the literature. The comparison of the ellipsometry and SEM studies shows that smoothness and density of the film surface are the crucial parameters in the ellipsometric results on YBCO films. At present, ellipsometry has been shown to be useful to the study of laser ablated YBCO films. More work is needed to assess the application of this technique to the study of co-evaporated films.

ACKNOWLEDGEMENT

We are indebted to John H. Scofield for allowing us to use his co-evaporation system.

REFERENCES

- ¹M. Garriga, J. Humlicek, J. Barth, R. L. Johnson, and M. Cardona, J. Opt. Soc. Am. B6, 470 (1989).
- ²M. K. Kelly, Siu-Wai Chan, K. Jenkin II, D. E. Aspnes, P. Barboux, and J. M. Tarascon, Appl. Phys. Lett. 53, 2333 (1988).
- ³M. K. Kelly, D. E. Aspnes, P. Barboux, J. M. Tarascon, Siu-Wai Chan, and K. Jenkin II, SPIE Conf. Proc. 1056, 212 (1989).
- ⁴M. K. Kelly, P. Barboux, J. M. Tarascon, D. E. Aspnes, W. A. Bonner, and P. A. Morris, Phys. Rev. B 38, 870 (1988).
- ⁵J. D. Warner, J. E. Meola, and K. A. Jenkins, NASA TM-102350 (1989).
- ⁶P. M. Mankiewich, J. H. Scofield, W. J. Skocpol, R. E. Howard, A. H. Dayem, and E. Good, Appl. Phys. Lett. 51, 1753 (1987).
- ⁷S. A. Alterovitz, R. M. Sieg, N. S. Shoemaker, and J. J. Pouch, Mat. Res. Soc. Symp. Proc. 152, 21 (1989).
- ⁸D. E. Aspnes, J. B. Theeten, and F. Hottier, Phys. Rev. B 20, 3292 (1979).
- ⁹M. F. Fan, R. L. Barns, H. M. O'Brian Jr., P. K. Gallagher, R. C. Sherwood, and S. Jin, Appl. Phys. Lett. 51, 532 (1987).
- ¹⁰Narottam P. Bansal and Ann L. Sandkuhl, Appl. Phys. Lett. 52, 323 (1988).
- ¹¹R. P. Vasquez, B. D. Hunt, and M. C. Foote, Appl. Phys. Lett. 53, 2692 (1988).
- ¹²CRC Handbook of Chemistry and Physics, 65th Edition, Robert C. Weast ed., CRC Press, Boca Raton, Florida (1984).

Millimeter-wave surface resistance of laser-ablated $\text{YBa}_2\text{Cu}_3\text{O}_{7-\delta}$ superconducting films

F. A. Miranda and W. L. Gordon

Department of Physics, Case Western Reserve University, Cleveland, Ohio 44106

K. B. Bhasin and J. D. Warner

National Aeronautics and Space Administration, Lewis Research Center, Cleveland, Ohio 44135

(Received 16 April 1990; accepted for publication 6 July 1990)

We have measured the millimeter-wave surface resistance of $\text{YBa}_2\text{Cu}_3\text{O}_{7-\delta}$ superconducting films in a gold-plated copper-host cavity at 58.6 GHz between 25 and 300 K. High quality laser-ablated films of 1.2 μm thickness were deposited on SrTiO_3 and LaGaO_3 substrates. Their transition temperatures (T_c 's) were 90.0 and 88.9 K, with a surface resistance at 70 K of 82 and 116 $\text{m}\Omega$, respectively. These values are better than the values for the gold-plated cavity at the same temperature and frequency.

The characterization of the new high transition temperature (T_c) superconductors at millimeter-wave frequencies is necessary in order to determine their suitability for practical microwave applications. A parameter of these new materials which directly provides this information is the surface resistance (R_s). The R_s of high quality $\text{YBa}_2\text{Cu}_3\text{O}_{7-\delta}$ superconducting films deposited on various microwave substrates has been measured at different frequencies and temperatures by several researchers.¹⁻⁴ To the best of our knowledge, however, no measurements have been reported at frequencies around 60 GHz. In this letter we report on the first measurements of the millimeter-wave surface resistance at 58.6 GHz of two predominantly *c*-axis oriented polycrystalline $\text{YBa}_2\text{Cu}_3\text{O}_{7-\delta}$ films deposited on SrTiO_3 and LaGaO_3 by pulsed laser ablation.

The pulsed laser ablation technique is similar to that used by other researchers.^{5,6} The deposition was performed at a substrate temperature of 750 °C and an ambient oxygen pressure of 170 mTorr. The laser wavelength was 248 nm, the pulse length was 20–30 ns, and the pulse rate was 4 pulses per second. The distance between the target and the sample was kept at 7.5 cm, and the laser fluence on the target was maintained at 2.0 J/cm^2 per pulse. During the deposition process, the laser beam was scanned up and down 1 cm over the target using an external lens on a translator. At the end of the deposition process, the oxygen pressure was raised to 1 atm, and the temperature was lowered to 450 °C at a rate of 2 °C/min. The temperature was held at 450 °C for 2 h before it was lowered to 250 °C, also at a rate of 2 °C/min. The heater power was turned off, and the sample was allowed to cool down to 40 °C or less before it was removed from the chamber. A more detailed explanation of the deposition technique can be found in Ref. 7.

The films were analyzed by x-ray diffraction, dc resistance versus temperature measurements, and scanning electron microscopy (SEM). The dc resistance was measured using a standard four-probe technique. Zero dc resistance was attained at 90.0 and 88.9 K for the films on SrTiO_3 and LaGaO_3 , respectively (see Fig. 1). A typical critical current density for films on SrTiO_3 at 77 K was 2×10^6 A/cm^2 when using the 1 $\mu\text{V}/\text{cm}$ measurement criteria. The resistivity at 300 K for the films on SrTiO_3 and LaGaO_3 was 130 ± 30 and 220 ± 50 $\mu\Omega$ cm, respectively. The uncertainties arise from the irregular geometry of the samples and uncertainties in the film thicknesses. The x-ray diffraction pattern revealed that both films are predominantly *c*-axis oriented. Figure 2 shows SEM micrographs for the two films under study, which indicate that both films are polycrystalline.

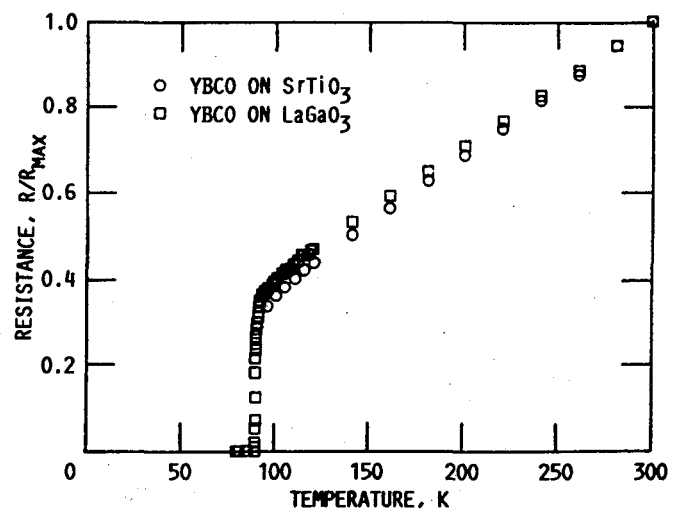


FIG. 1. dc resistance vs temperature measurement of laser-ablated $\text{YBa}_2\text{Cu}_3\text{O}_{7-\delta}$ superconducting films on SrTiO_3 and LaGaO_3 substrates.

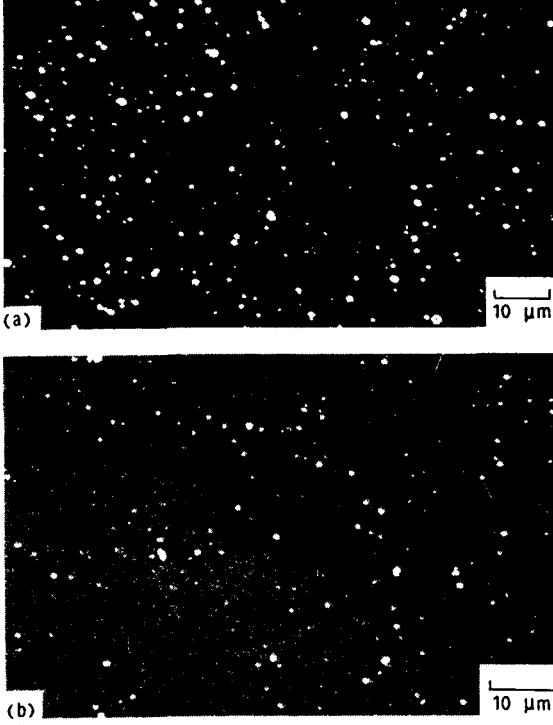


FIG. 2. Scanning electron micrographs of laser-ablated $\text{YBa}_2\text{Cu}_3\text{O}_{7-\delta}$ superconducting films on SrTiO_3 (a) and LaGaO_3 (b) substrates.

The surface resistance R_s is measured by looking at the change in the Q factor of a cylindrical, TE_{013} mode, gold-plated copper cavity operational at 58.6 GHz when one of its end walls is replaced by the superconducting film sample. Using an HP-8510 network analyzer and the Ginzton's impedance method,^{8,9} the Q factor for the cavity is determined from the reflection coefficient. The Q factor is defined as

$$Q = \omega_0 (\text{maximum energy stored}) / \text{power loss}$$

$$= \frac{1}{2} \omega_0 \epsilon \int_V |E|^2 dV / \frac{1}{2} R_s \int_S |H_t|^2 dS, \quad (1)$$

where R_s is the surface resistance of the cavity walls, S is the inner surface of the cavity, V is the volume of the cavity, and H_t is the tangential field. Integrating Eq. (1) we obtain that the Q for the bare cavity is given by

$$Q_1 = \frac{(2\pi l a f)^3 \epsilon \mu_0^2 [-J_0(q_{01}) J_2(q_{01})]}{R_s [2l^3 q_{01}^2 J_0^2(q_{01}) - 4\pi^2 a^3 n^2 J_0(q_{01}) J_2(q_{01})]}, \quad (2)$$

where l is the length of the cavity, a is the radius of the cavity, f is the frequency, J_0 and J_1 are normal Bessel functions, $q_{01} = 3.8317$ is the first zero of J_1 , and n is the longitudinal mode number. When one of the cavity's end walls is replaced with the sample, the Q factor becomes

$$Q_2 = \frac{(2\pi l a f)^3 \epsilon \mu_0^2 [-J_0(q_{01}) J_2(q_{01})]}{R_{s1} [2l^3 q_{01}^2 J_0^2(q_{01})] - 2(\pi n)^2 a^3 J_0(q_{01}) J_2(q_{01}) (R_{s1} + R_{s2})}, \quad (3)$$

where R_{s2} is the surface resistance of the superconducting sample and R_{s1} is the surface resistance of the other cavity walls. Hence, the surface resistance R_{s1} of the metal is obtained from Eq. (2) by measuring the Q factor of the bare cavity (Q_1), and then R_{s2} is computed from Eq. (3) by measuring the Q factor with the sample in place (Q_2).

In Fig. 3 the measured $R_s(T)$ curves for the two films under consideration are shown. Also plotted is the experimental surface resistance of the gold-plated reference cavity for comparison. The R_s for the two films is comparable in the normal state, while the R_s of the film on SrTiO_3 decreases faster than that for the film on LaGaO_3 at temperatures just below T_c . Using the normal skin depth formula $R_s = (\omega \mu_0 \rho / 2)^{1/2}$, we obtained values for the resistivity, ρ , and skin depth, δ , at 300 K of approximately 118 $\mu\Omega$ cm and 2.3 μm for the film on SrTiO_3 and 158 $\mu\Omega$ cm and 2.7 μm for the film on LaGaO_3 . Note that the strong "oscillatory" behavior of R_s as a function of temperature in the normal state, observed for films on SrTiO_3 by other researchers,³ was not observed in our case. This is not unexpected due to the greater film thicknesses employed here.

In the superconducting state, the films on SrTiO_3 and LaGaO_3 exhibit a drop of R_s to effective values of 103 ± 15 and 144 ± 20 m Ω at 77 K, and 82 ± 15 and 116 ± 20 m Ω at 70 K, respectively. The surface resistance at 77 K for the film on SrTiO_3 is less than that of the gold-plated cavity, while for the film on LaGaO_3 , R_s is the same as for the

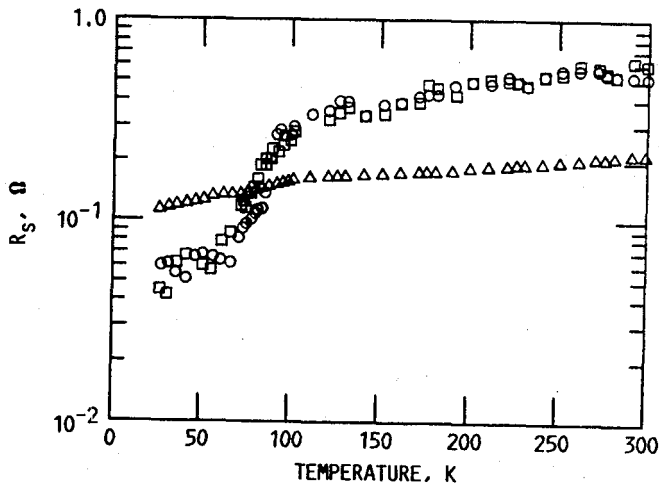


FIG. 3. Surface resistance (R_s) at 58.6 GHz vs temperature for $1.2 \mu\text{m}$ films of $\text{YBa}_2\text{Cu}_3\text{O}_{7-\delta}$ deposited by laser ablation onto SrTiO_3 (\circ) and LaGaO_3 (\square) substrates, and for the gold-plated cavity (\triangle).

gold-plated cavity. Since we are operating at a fixed frequency, we cannot study the frequency dependence of R_s directly from our measurements. Nevertheless, a comparison with R_s values reported by other researchers in similar types of films and at different frequencies, may be helpful to formulate a frequency dependence trend for R_s . Thus, using the results obtained by Klein *et al.*¹⁰ for *c*-axis textured layered samples of $\text{YBa}_2\text{Cu}_3\text{O}_{7-\delta}$, and fitting their data to a quadratic frequency dependence for R_s , give an R_s value of 102 m Ω at 58.6 GHz and 77 K. This value agrees very well with our experimentally obtained value of 103 m Ω at the same temperature. An analog approach was used for our film on LaGaO_3 . Using the data reported by Cooke *et al.*⁴ for a $\text{YBa}_2\text{Cu}_3\text{O}_{7-\delta}$ superconducting film deposited by magnetron sputtering on LaGaO_3 , an interpolation of R_s between their reported values measured at 22, 86, and 148 GHz and at 70 K was performed. The resulting R_s value of 106 m Ω at 58.6 GHz compares favorably, within experimental error, with our value of 116 m Ω at the same frequency and temperature. This result indicates that our value fits well with the nearly quadratic dependence for R_s ($R_s \propto \omega^n$, $n = 2.06 \pm 0.14$), as reported in Ref. 4. The results obtained from this correlation are very consistent with the experimental behavior observed in low T_c superconductors and also with the predictions of the Bardeen-Cooper-Schrieffer (BCS) theory.

In conclusion, the surface resistance of preferentially *c*-axis oriented polycrystalline $\text{YBa}_2\text{Cu}_3\text{O}_{7-\delta}$ superconducting laser-ablated films has been measured at 58.6 GHz via a TE_{013} cavity wall replacement technique. The

values of R_s obtained for the films on SrTiO_3 and LaGaO_3 at 77 K are less or equal to that of the gold-plated cavity. A comparison of the R_s values obtained for both films with values for similar films measured by other researchers at different frequencies shows that our values are consistent with the frequency dependence for R_s observed in classical superconductors and with the predictions of the BCS theory.

¹J. S. Martens, J. B. Beyer, and D. S. Ginley, *Appl. Phys. Lett.* **52**, 1822 (1988).

²J. P. Carini, A. M. Awasthi, W. Beyermann, G. Gruner, T. Hylton, K. Char, M. R. Beasley, and A. Kapitulnik, *Phys. Rev. B* **37**, 9726 (1988).

³N. Klein, G. Muller, H. Piel, B. Roas, L. Schultz, U. Klein, and M. Peiniger, *Appl. Phys. Lett.* **54**, 757 (1989).

⁴D. W. Cooke, E. R. Gray, R. J. Houlton, H. H. S. Javadi, M. A. Maez, B. L. Bennett, B. Rusnak, E. A. Meyer, P. N. Arendt, J. G. Beery, D. R. Brown, F. H. Garzon, I. D. Raistrick, A. D. Rollett, B. Bolmaro, N. E. Elliott, N. Klein, G. Muller, S. Orbach, H. Piel, J. Y. Josefovicz, D. B. Rensch, L. Drabeck, and G. Gruner, *Physica C* **162-164**, 1537 (1989).

⁵A. Inam, M. S. Hegde, X. D. Wu, T. Venkatesan, P. England, P. F. Miceli, E. W. Chase, C. C. Chang, J. M. Tarascon, and J. B. Wachtman, *Appl. Phys. Lett.* **53**, 908 (1988).

⁶B. Roas, L. Schultz, and G. Endres, *Appl. Phys. Lett.* **53**, 1557 (1988).

⁷J. D. Warner, J. E. Meola, and K. A. Jenkins, "Study of Deposition of $\text{YBa}_2\text{Cu}_3\text{O}_{7-\delta}$ on Cubic Zirconia," NASA-TM 102350 (1989).

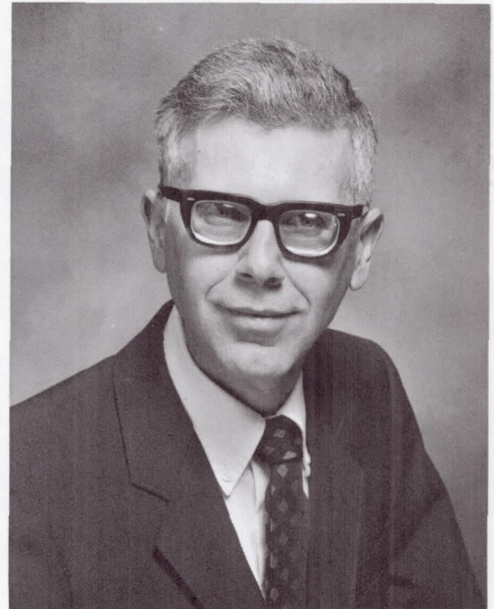
⁸E. L. Ginzton, *Microwave Measurements* (McGraw-Hill, New York, 1957), p. 406.

⁹R. R. Romanofsky, "Analytical and Experimental Procedures for Determining Propagation Characteristics of Millimeter-Wave Gallium Arsenide Microstrip Lines," NASA TP-2899 (1989).

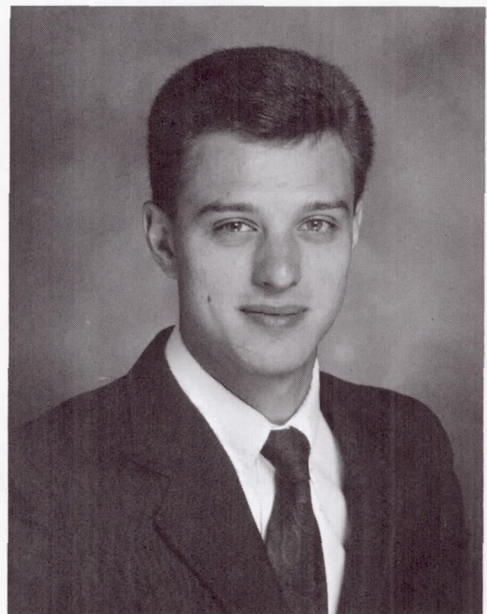
¹⁰N. Klein, G. Muller, S. Orbach, H. Piel, H. Chaloupka, B. Roas, L. Schultz, U. Klein, and M. Peiniger, *Physica C* **162-164**, 1549 (1989).

BIOGRAPHIES

Samuel A. Alterovitz earned his Ph.D. in Solid State Physics in 1971 from Tel Aviv University, Israel. After a two-year postdoctoral appointment at the University of Illinois, he joined the staff of the Physics Department at Tel Aviv University where he achieved the status of tenured associate professor. His work there focused on properties of superconducting materials, emphasizing critical currents and critical fields. In 1981, he accepted an appointment as senior engineering research scientist in the Electrical Engineering Department of the University of Nebraska, where he worked to develop the ellipsometric technique. In 1983, he transferred to NASA Lewis Research Center where he is now a senior research scientist in the Solid State Technology Branch. He played a key role in developing materials (e.g. InGaAs) for a new generation of electronic devices for high-speed, low-noise, high-efficiency space applications. Dr. Alterovitz also developed ellipsometry for novel and multilayer structures, specializing in insulators, superconductors, and semiconductor materials. Dr. Alterovitz is now working on materials for cryogenic electronics applications, including semiconductors, superconductors, and their combination. He is also working on furthering applications of the ellipsometric technique. Dr. Alterovitz has authored 103 papers in referred journals, 101 meeting presentations, and has edited two books. He is an active postdoctoral advisor for the National Research Council.



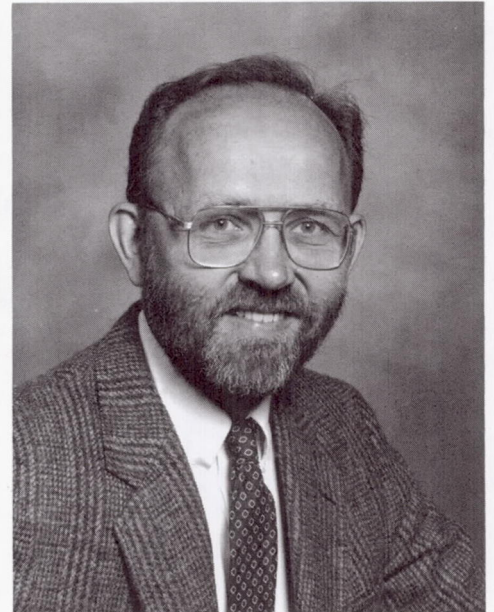
Christopher M. Chorey earned a Master's degree in Materials Science in 1987, and a Bachelor's degree in Electrical Engineering in 1984 from Case Western Reserve University. With the support of NASA Lewis Research Center, he performed two years of additional graduate work at Case Western Reserve University in 1987 and 1988. His work focused on fabrication and testing of AlGaAs based, high-frequency, electro-optic modulators.



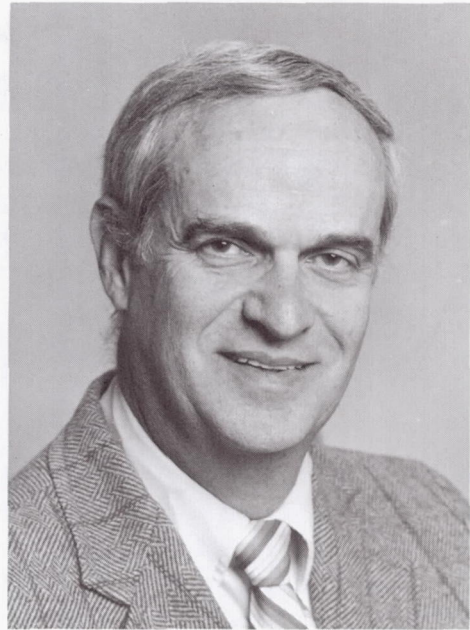
Alan M. Downey earned his B.E.E. from Cleveland State University in 1979, and his M.S.E.E. from the University of Toledo in 1983. He joined NASA Lewis Research Center in 1977 as a co-op student. In 1979 he joined the Space Communications Division. From 1979 to 1985, he was engaged in microwave measurements and solid state technology research, followed by a three-year hiatus in the Communications Projects Branch as Experiments Manager for the Applications Technology Satellites Program. Mr. Downey returned to the Solid State Technology Branch in July 1989. His current research interests include the measurement of novel HEMT structures at cryogenic temperatures, coplanar waveguide circuit design, and MMIC applications.



Edward J. Haugland earned his B.S. degree in Physics from the University of Minnesota, and M.S. and Ph.D. degrees in Solid State Physics from Case Western Reserve University. He joined NASA Lewis Research Center in 1980 as a member of the Solid State Technology branch. Since that time, he has been involved with experimental research on electrical properties of III-V semiconductor materials, heterostructures, and SiC. He was responsible for contracts concerning development of high-power IMPATT diodes and MMIC power amplifiers. Dr. Haugland is a member of the American Physical Society.



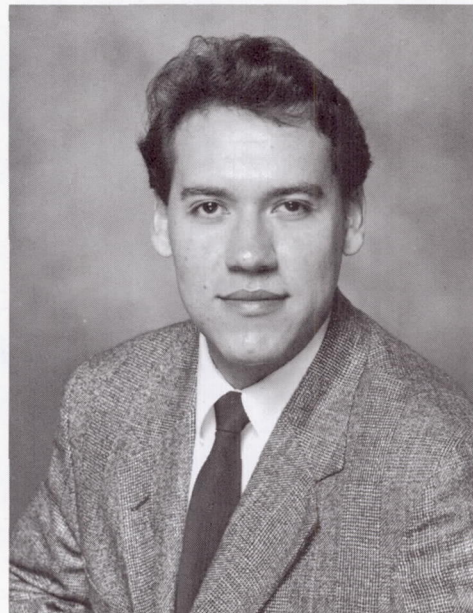
Thomas J. Kascak earned a B.S.E.E. degree from Case Western Reserve University in 1959 and joined Union Carbide Corporation where he worked with performance and reliability aspects of dry cell and alkaline batteries. Mr. Kascak received an M.S. degree in Physics in 1965 from John Carroll University, Cleveland, OH. From 1966 to the present, he has been employed at NASA Lewis Research Center. He has been involved in several work areas from research on thermionic heat to electric power conversion devices. In 1973, he transferred to the Space Electronics Division where he has been involved in various aspects of microwave and millimeter wave solid state devices and circuits. He was responsible for formulating and managing several NASA sponsored contractual efforts involving MMIC development programs. One of these efforts, a 20-GHz MMIC Transmit Module, resulted in the R&D Magazine IR-100 award. For the last few years, he has been responsible for the set-up of the division's in-house solid state facilities. Mr. Kascak has authored papers on thermionic direct energy conversion devices, 20- and 30-GHz MMIC devices, and MMIC-based phased array antennas. Mr. Kascak is a member of the American Vacuum Society.



Regis F. Leonard earned his Ph.D. in Physics from the Carnegie Institute of Technology in 1963 and came to NASA Lewis Research Center that same year. Since that time, he has completed 10 years of basic research concerning the physics of nuclear structures. For six years, Dr. Leonard worked towards the development of a unique Lewis facility that uses neutron radiation to treat cancer patients. For the last 11 years, he has helped develop technology in support of NASA's communications programs. This assignment includes work on the ACTS proof-of-concept technology program and, as head of the RF Systems Section, the development of an in-house communications system test capability for the ACTS POC hardware. For the last six years he has served as Chief of the Solid State Technology Branch. Dr. Leonard is responsible for NASA's MMIC technology development program; an active, in-house, solid state, research program; and a sizeable university grant program which supports basic research as applicable to solid state electronics.



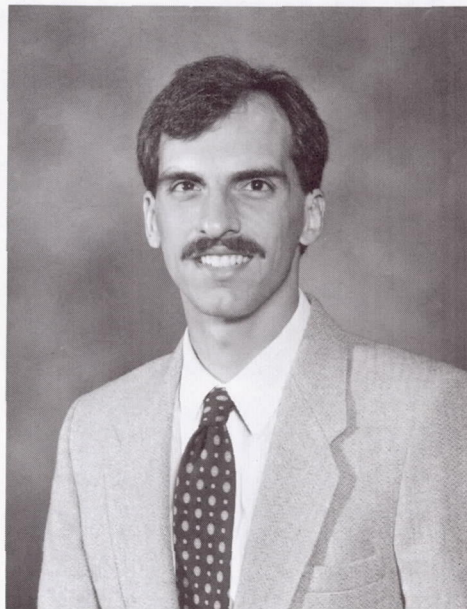
Rafael A. Mena earned his B.S. degree in Electrical Engineering in 1988 from the University of Texas at El Paso and an M.S. degree in Solid State Physics in 1990 from Arizona State University. While at Arizona State, he made theoretical calculations on the effect of a magnetic field on the optical properties of semiconductor alloys. While pursuing his degree, he participated in several co-op programs. In the summer of 1987, while with the Arizona Public Service, he conducted an economic study on the installation of underground power lines. The following summer, he was accepted into the NASA Lewis Summer internship program. During that time, he was involved in a research program to investigate the magnetic field penetration depth of superconducting materials. He returned to NASA Lewis in the summer of 1989 where he assisted in the development of automation software for a secondary ion mass spectrometer. In 1990, he joined the Solid State Technology Branch at NASA Lewis Research Center as a full-time employee. His current interests lie in both the theoretical and experimental investigation of the electrical properties of novel semiconductor materials. Mr. Mena has authored a paper on his work conducted at Arizona State University.



Carlos R. Morrison, a native of Jamaica, earned his B.S. (Honorary) degree in Physics in 1986 from Hofstra University where he was elected to the Sigma Pi Sigma National Physics Honor Society, the Kapa Mu Epsilon National Mathematics Honor Society, and the Society of Physics Students. He received a Master's degree in Physics in 1989 from the Polytechnic Institute of New York. He joined NASA Lewis Research Center in September of 1989. He worked for a short time in Reliability and Quality Assurance, then transferred to the Solid State Technology Branch in January of 1990. Currently Mr. Morrison is involved in thin film deposition and ellipsometry.



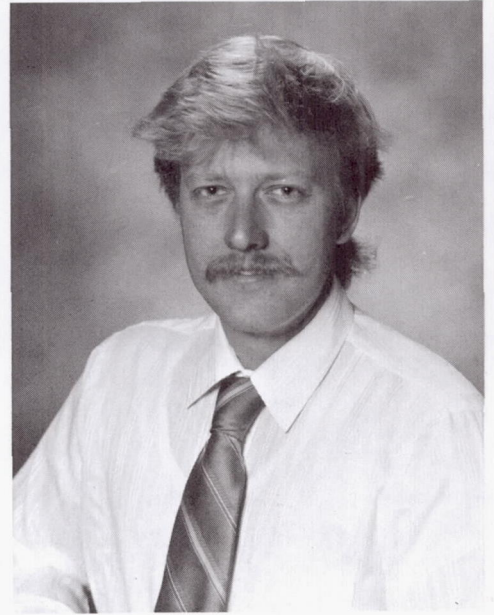
George E. Ponchak earned his B.E.E. from Cleveland State University in 1983, and his M.S.E.E. from Case Western Reserve University in 1987. He joined the Space Electronics Division at NASA Lewis Research Center in July, 1983. Since joining NASA, he has been responsible for research of microwave and millimeter wave transmission lines and managing the development of monolithic microwave integrated circuits. Mr. Ponchak has coauthored 22 papers on these topics. In September of 1990, Mr. Ponchak attended the University of Michigan for one year to complete coursework towards a Ph.D. in Electrical Engineering.



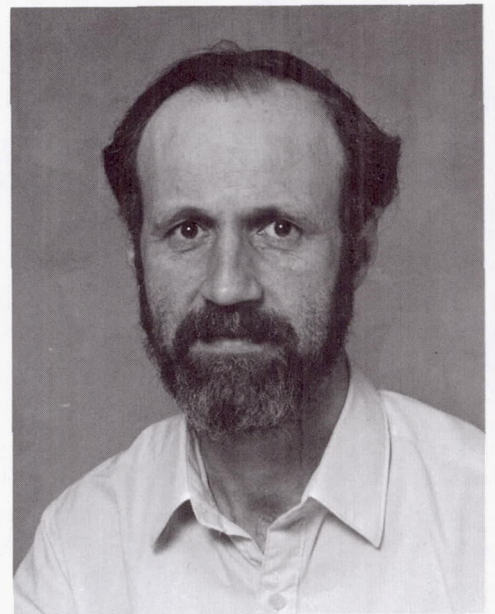
John J. Pouch earned his Ph.D. in Solid State Physics from Wayne State University, Detroit, MI, in 1981. His research activities at NASA Lewis Research Center include surface analysis of thin films for microelectronic applications, plasma and reactive ion etching, and plasma deposition.



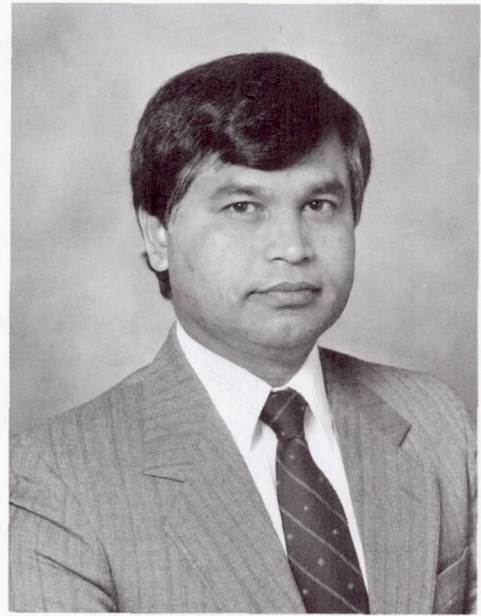
Robert R. Romanofsky earned a Bachelor of Science Degree in Electrical Engineering from Pennsylvania State University, and a Master of Science Degree in Electrical Engineering from the University of Toledo. He has been employed in the Space Electronics Division of NASA Lewis Research Center since 1983. He spent one year at NASA Headquarters in Washington, D.C., as the acting program manager for superconductivity and RF communications. His work has involved microwave transmission line research and device characterization and modeling. Recently, he has been investigating microwave applications of high-temperature superconductivity.



Samuel E. Schacham earned his B.S. degree in Mathematics and Physics with honors in 1971, and an M.S. degree in Physics in 1973 from Bar Ilan University, Ramat-Gan, Israel. He performed research work on nonlinear optical effects in liquid crystals at the Weizmann Institute and Bar Ilan University. He received a Ph.D. degree in Biomedical Engineering in 1978 from Northwestern University, Evanston, IL, working on applications of lasers to microendoscopy. From 1978 to 1981, he was the manager of the optic group at Fibronics Ltd., Haifa, Israel. From there he joined the Department of Electrical Engineering at the Technion in Haifa. In 1988 he was a visiting scientist at MCNC Research, Triangle Park, NC, working on optical interconnects as part of the packaging group. Presently, he is with NASA Lewis Research Center as a National Research Council Senior Research Associate. His present research interests are in the physical properties of quantum structures and narrow bandgap semiconductors. His list of publications includes 40 papers in international scientific journals and referred conferences.



Ajit K. Sil earned his B.S. degree from Calcutta University, India. He emigrated to the United States and was employed by Oakwood Downriver Medical Center. He received his second B.S. degree in Electronic Engineering Technology in 1988 from Wayne State University, Detroit, MI. He joined the NASA Lewis Research Center in July of 1989 as a member of the Solid State Technology Branch where he is working with microwave integrated circuits and solid state devices. He is currently working toward his M.S.E.E. at Cleveland State University.



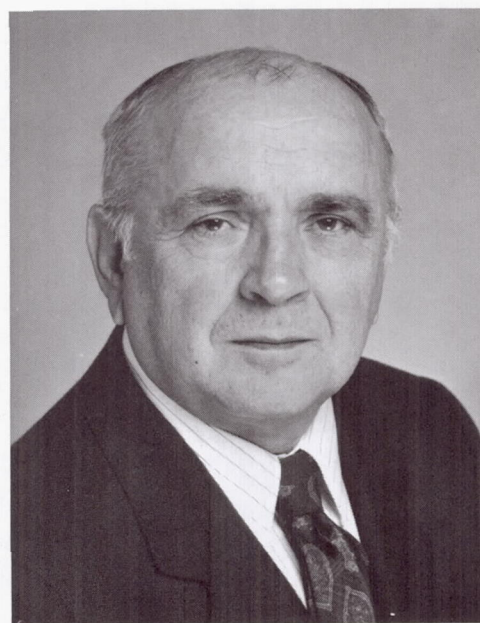
Rainee N. Simons earned a B.E. degree in Electronics and Communications from the Mysore University in 1972, and an M. Tech. degree in Electronics and Communications from the Indian Institute of Technology, Kharagpur, in 1974, and a Ph.D. in Electrical Engineering from the Indian Institute of Technology, New Delhi, in 1983, where he was a Senior Scientist Officer. From 1985 to 1987, Dr. Simons was a National Research Council Research Associate and investigated the direct optical control of GaAs microwave semiconductor devices and circuits. Since 1990, he has been with Sverdrup Technology, Inc., NASA Lewis Research Center Group. His research interest include GaAs microwave semiconductor devices, optical control, and superconductivity. Dr. Simons is the author of a book entitled "Optical Control of Microwave Devices" published by Artech House. He has received the Distinguished alumni award from his alma mater and is a senior member of IEEE.



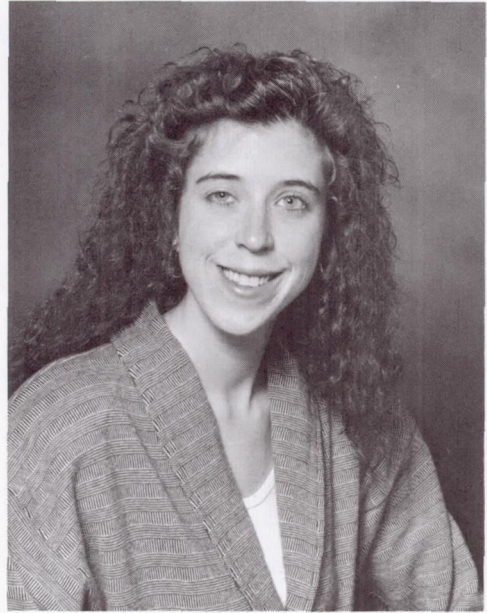
Mark A. Stan earned his B.S.E.E. degree in 1978 from the University of Akron. He was employed by the Allen-Bradley Company as a digital circuit design engineer until 1980. He then returned to graduate school at Case Western Reserve University to study the physics of melting in two-dimensional systems, completing work for his Master's degree in 1982 and a Ph.D. degree in 1988. In 1987 he began research work at NASA Lewis Research Center in the areas of characterization and growth of high-temperature superconductors. Currently Dr. Stan is a Resident Research Associate. He is a member of the American Physical Society (APS), the Materials Research Society (MRS), and the Institute of Electrical and Electronic Engineers (IEEE).



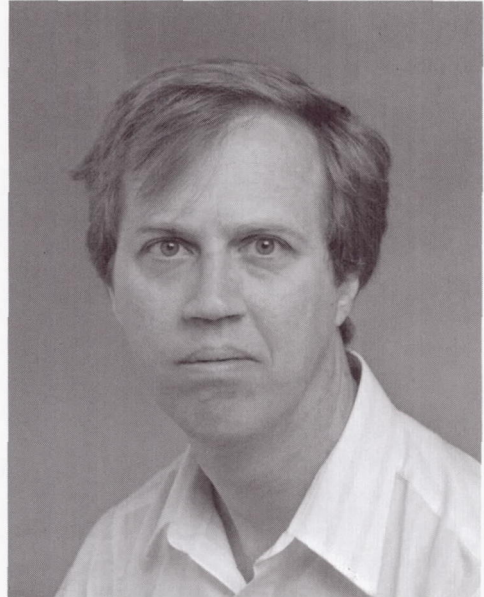
Stephan Stecura earned an M.S. degree in Physical Chemistry in 1957 from Western Reserve University, and a Ph.D. in Solid State Reaction Kinetics-Thermodynamics in 1965 from Georgetown University. From 1958 to 1965, at College Park Metallurgy Center, he studied the kinetics of crystallographic transformation and the high-temperature properties of oxides by high-temperature, x-ray diffraction techniques. He designed and built high-temperature, x-ray diffraction equipment and was invited to present the high-temperature, x-ray diffraction, arc-image furnace, capable of reaching 3000 degrees Celsius in air, at the International Crystallographic Society meeting. Since 1965, he has been with NASA Lewis Research Center. His work on heat pipes led him to determine the corrosion mechanism and the true solubilities of containment metals and alloys in alkali metals. He developed thermal barrier systems for the protection of alloy components at very high temperatures, up to 1600 degrees Celsius, on air-cooled components. Currently, he is studying the properties of superconducting materials and is trying to identify substrate materials for superconducting films. Dr. Stecura is recognized as an authority on the thermal barrier system technology that he developed. For his work in this field, he has received two IR-100 awards, one major Space Act award, and three major patents. He has written more than 30 original publications and is a member of the American Ceramic Society.



Susan R. Taub earned her B.S. degree in Electrical Engineering Technology in 1988, and a Master of Science degree in Electrical Engineering in 1990 from Temple University. In 1988 and 1989, she worked for AT&T Bell Laboratories, Reading, PA, developing PSPICE compatible models for power MOSFET's. She joined the Solid State Technology Branch of NASA Lewis Research Center in 1990, and is currently involved in the design and characterization of MMIC's and the investigation of HEMT performance at cryogenic temperatures. Ms. Taub is a member of IEEE.



Joseph D. Warner earned an M.S. in Physics from Carnegie Melon University in 1977. From 1977 to 1981, he performed research at C.M.U. on magnetic phase transition at low temperature. Since that time, he has been with NASA Lewis Research Center where he characterized various insulators on GaAs and was among the first to demonstrate growth of GaAs by laser-assisted OMCVD at temperatures below 500 degrees Celsius. Presently, he has set up a laser ablation experiment to grow high-temperature superconducting thin films. In 1989, he received a NASA Achievement Award for his part in establishing a high-temperature superconductor program at NASA Lewis. Mr. Warner has authored papers on magnetic phase transitions, electrical properties of insulation films on III-V compounds, laser assisted growth of GaAs and AlGaAs, and properties and growth of high-temperature superconductors. Mr. Warner is a member of the American Physical Society (APS), the American Vacuum Society (AVS), and the Materials Research Society (MRS). Currently, he is on a one-year assignment to the Jet Propulsion Laboratory where he participates in the development of Photonic intergrated circuits.



REPORT DOCUMENTATION PAGEForm Approved
OMB No. 0704-0188

Public reporting burden for this collection of information is estimated to average 1 hour per response, including the time for reviewing instructions, searching existing data sources, gathering and maintaining the data needed, and completing and reviewing the collection of information. Send comments regarding this burden estimate or any other aspect of this collection of information, including suggestions for reducing this burden, to Washington Headquarters Services, Directorate for Information Operations and Reports, 1215 Jefferson Davis Highway, Suite 1204, Arlington, VA 22202-4302, and to the Office of Management and Budget, Paperwork Reduction Project (0704-0188), Washington, DC 20503.

1. AGENCY USE ONLY (Leave blank)		2. REPORT DATE	3. REPORT TYPE AND DATES COVERED Technical Memorandum	
4. TITLE AND SUBTITLE Solid State Technology Branch of NASA Lewis Research Center Third Annual Digest June 1990-June 1991			5. FUNDING NUMBERS WU-506-59-4C	
6. AUTHOR(S)				
7. PERFORMING ORGANIZATION NAME(S) AND ADDRESS(ES) National Aeronautics and Space Administration Lewis Research Center Cleveland, Ohio 44135-3191			8. PERFORMING ORGANIZATION REPORT NUMBER E-6447	
9. SPONSORING/MONITORING AGENCY NAMES(S) AND ADDRESS(ES) National Aeronautics and Space Administration Washington, D.C. 20546-0001			10. SPONSORING/MONITORING AGENCY REPORT NUMBER NASA TM-105159	
11. SUPPLEMENTARY NOTES Responsible individual, Kimberly J. McKee (216) 433-3514.				
12a. DISTRIBUTION/AVAILABILITY STATEMENT Unclassified - Unlimited Subject Category 32			12b. DISTRIBUTION CODE	
13. ABSTRACT (Maximum 200 words) The digest is a collection of papers written by the members of the Solid State Technology Branch of NASA Lewis Research Center from June 1990-June 1991. The papers cover a range of topics relating to superconductivity, MMIC's, coplanar waveguide, and material characterization.				
14. SUBJECT TERMS Microwave; Superconducting materials; Thin films			15. NUMBER OF PAGES 171	
			16. PRICE CODE A08	
17. SECURITY CLASSIFICATION OF REPORT Unclassified	18. SECURITY CLASSIFICATION OF THIS PAGE Unclassified	19. SECURITY CLASSIFICATION OF ABSTRACT Unclassified	20. LIMITATION OF ABSTRACT	

National Aeronautics and
Space Administration

Lewis Research Center
Cleveland, Ohio 44135

Official Business
Penalty for Private Use \$300

FOURTH CLASS MAIL

ADDRESS CORRECTION REQUESTED



Postage and Fees Paid
National Aeronautics and
Space Administration
NASA-451

NASA
